FACULDADE DE ENGENHARIA DA UNIVERSIDADE DO PORTO

Fatigue Reliability Analysis of a Rail Vehicle Axle

Pedro Jorge Ferreira Borges Da Costa

Mestrado Integrado em Engenharia Mecânica

Advisor:
José António Fonseca de Oliveira Correia
(University of Porto)

Co-Advisors:
Shun-Peng Zhu
(University of Electronic Science and Technology of China)
Abílio Manuel Pinho de Jesus
(University of Porto)

Porto, 2020

The work presented in this dissertation was developed at
Faculdade de Engenharia da Universidade do Porto
Rua Dr. Roberto Frias s/n,
4200-465 Porto
Portugal

Pedro Jorge Ferreira Borges Da Costa
E-mail: pedrojfbc@gmail.com | up201404682@fe.up.pt

Abstract

Nowadays, new challenges are arising all over the world related with climate changes. One of these many challenges has to do with urban mobility planning and management. In order to decrease mankind's environmental impact due to air pollution caused by on-road vehicles, all transportation system has to be re-thought.

There are multiple solutions that can be adopted to solve this situation. One of them has to do with an increased usage of railway infrastructures to transport people and freight.

Nevertheless, rail infrastructures have to be carefully managed and maintained in order to be a feasible alternative.

In Europe and in particular in Portugal, rail infrastructures have been a concern of government agencies. The Portuguese government has been dealing with some accidents that took place in railway infrastructures in recent years. These accidents demonstrate a dramatic deterioration of the conditions of circulation in the Portuguese national rail network.

As so, the development of studies related with the fatigue life prediction of rail axles, wheels and rails' steels is extremely important and relevant.

In this dissertation, four main topics were addressed: railway vehicles; fatigue; fracture mechanics; reliability analysis. Several papers, reports, books, dissertations and standards concerning these topics were analysed.

A study on fatigue life prediction for fatigue crack initiation and propagation phases of a railway vehicle axle based on a numerical analysis using the finite element method as well as analytical solutions, was done. A local stress approach based on Neuber rule and Ramberg-Osgood relation was also considered.

Fatigue design standards for railway vehicle axles were analysed.

Experimental data was collected for fatigue strength characterization and crack propagation rates of steel grade EA4T, typically used in railway vehicle axles in Europe.

Structural reliability techniques, such as Monte Carlo simulation, and a probabilistic framework were employed for the fatigue analysis.

At the end, the importance and relevance of all the developed work was discussed.

Keywords: Rail vehicle axle; Fatigue; Fracture mechanics; Reliability analysis; Monte Carlo Simulation; Neural Networks.

Resumo

Nos dias de hoje, novos desafios têm vindo a surgir em todo o mundo devido às alterações climáticas. Um destes desafios está relacionado com o planemanto e gestão da mobilidade urbana. De maneira a reduzir o impacto ambiental do ser humano causado pela poluição do ar por intermédio dos veículos rodoviários, todo o sistema de transportes deve ser repensado.

Várias soluções podem ser adoptadas de maneira a resolver esta situação. Uma delas prende-se com um aumento do uso da ferrovia para o transporte de pessoas e mercadorias.

No entanto, as infraestruturas ferroviárias devem ser cuidadosamente geridas de maneira a que possam constituir uma alternativa viável.

Na Europa e em particular, em Portugal, as infraestruturas ferroviárias têm sido objecto de preocupação por parte das entidades governamentais. Nestes últimos anos, o governo português tem-se deparado com a ocorrência de alguns acidentes ferroviários. Estes acidentes demonstram que tem havido uma degradação das condições de circulação dos comboios da rede ferroviária nacional.

Assim sendo, o desenvolvimento de estudos que se debrucem sobre a previsão da vida à fadiga de eixos e rodados de veículos ferroviários, bem como carris, são de grande importância e relevância.

Nesta dissertação, quatro grandes tópicos foram abordados: veículos ferroviários; fadiga; mecânica da fratura; análise de fiabilidade. Foram analisados inúmeros artigos, relatórios, livros, dissertações e normas relacionados com estes tópicos.

Foi realizado um estudo sobre a previsão da vida à fadiga de um eixo de um veículo ferroviário para as fases de iniciação e propagação de fendas de fadiga. Este estudo baseou-se na análise de um modelo numérico que tem por base o método dos elementos finitos, bem como soluções analíticos. Uma abordagem local baseada na regra de Neuber e na relação de Ramberg-Osgood foi também considerada.

As normas que se aplicam a eixos de veículos ferroviários foram também analisadas.

Foram analisados resultados experimentais para caraterização da vida à fadiga e propagação de fendas para o aço EA4T, tipicamente usado em eixos de veículos ferroviários na Europa.

Foram utilizadas técnicas de fiabilidade estrutural, como por exemplo o método de Monte Carlo, e abordagens probabilísticas para a análise da vida à fadiga.

No final, a importância e a relevância de todo o trabalho desenvolvido foi discutida.

Palavras-chave: Eixo de veículo ferroviário; Fadiga; Mecânica da fratura; Análise de fiabilidade; Simulação de Monte Carlo; Redes neuronais.

Acknowledgements

Several people have contributed for the execution and completion of this dissertation.

But first, I shall start by the beginning. I have to pay a tribute to my family, specially to my mother, that have always supported me and are definitely the main reason for my academic pathway and success and to whom I will be forever grateful.

Next, I would like to express my gratitude to all my friends for their friendship and for always believing in me.

I am also grateful to Professor Wu Shengchuan and to the State Key Laboratory of Traction Power (TPL) on Southwest Jiaotong University, in China, that gently provided me a numerical model to conduct my analysis and data from experimental results.

I also have to express my gratitude to Professor Behrooz Keshtegar for his collaboration on the structural reliability implementation that was employed in this scientific research.

Furthermore, I would like to thank my co-advisors, Professor Shun-Peng Zhu and Professor Abílio de Jesus, for all their contributions for this master's thesis.

Moreover, I also have to mention Anis Mohabeddine and Bruno Pedrosa, PhD students, that helped me dealing with the numerical model of the railway axle.

Last but not least, I have to praise all the support, cooperation and fundamental advice given by my main advisor, Professor José Correia. His contribution was crucial for the development of this dissertation. Professor José Correia taught me that if we stay calm and work hard, there is no reason why we can't reach the goals we set for ourselves.

Pedro Jorge Costa

"Success is not final, failure is not fatal:
it is the courage to continue that counts."

Winston Churchill

Contents

List of Figures

List of Tables

Abbreviations and Symbols

ANN	Artificial Neural Networks
CDF	Cumulative Distribution Function
CP	Comboios de Portugal
EMEF	Empresa de Manutenção de Equipamento Ferroviário
EN	European Standards
FOD	Foreign Object Damages
FORM	First Order Reliability Method
FOSPA	First Order Saddlepoint Approximation
HCF	High Cycle Fatigue
HRR	Hutchinson-Rice-Rosengred
IH	Induction Hardening
IMT	Instituto da Mobilidade e dos Transportes
IP	Infraestruturas de Portugal
JIS	Japanese Industrial Standards
KDE	Kernel Density Estimation
LCF	Low Cycle Fatigue
LDA	Linear Damage Accumulation
LSF	Limit State Function
MCMC	Markov Chain Monte Carlo
MCST	Monte Carlo Simulation Technique
MPI	Magnetic Particle Inspection
MPP	Most Probable Point
MSE	Mean Square Error

NDT	Non-Destructive Testing
NOP	Number of Particles
PI	Propagation Index
PNA	Piecewise Newman Approach
PoD	Probability of Detection
PSE	Plastic Strain Energy
RATB	Railway hollow Axle with a Tapered Bore
RBD	Reliability Based Design
RCF	Rolling Contact Fatigue
REFER	Rede Ferroviária Nacional
RKE	Rice-Kujawski-Ellyin
SAFT	Synthetic Aperture Focusing Technique
SF	Safety Factor
SIF	Shiratori stress Intensity Factor
SORA	Sequential Optimization and Reliability Assessment
SORM	Second Order Reliability Analysis
SOSPA	Second Order Saddlepoint Approximation
TPL	State Key Laboratory of Traction Power
UIC	International Union of Railways
US	Ultrasonic testing
UTP	Uniaxial Tensile Properties

Chapter 1

Introduction

1.1 Motivation

The evidences of the existence of climate changes are practically everywhere. Mankind has basically two ways to address them: either people embrace this reality together and try to find strategies to fight climate changes or they can ignore them and suffer the consequences sooner or later.

Previous studies have shown that the impact of on-road vehicles on air pollution has been tremendous. On its turn, air pollution has a direct impact on climate changes. Therefore, re-thinking the way people and goods are moving all over the world is urgent to combat and try to reverse the damages caused by climate changes.

Rail infrastructures can be a good alternative to on-road vehicles. However, in order for them to be a feasible alternative, they have to be carefully maintained and managed.

Rail infrastructures in Europe and in particular in Portugal have been a concern of government agencies. The Portuguese Institute for Mobility and Transport has identified accidents in railway infrastructures, related to broken rails and excessive rail deformation. The government institute reports that this situation has to be thoroughly analysed and urgently corrected, as it indicates a deterioration of the conditions of circulation in the national rail network, possibly due to deficiencies in its maintenance. In addition, the government institute identified the existence of 9 accidents caused by technical failures in axles and wheels of the railway vehicles in the period between 2007 and 2016. In this sense, the development of technical and scientific studies on the fatigue life prediction of axles and wheels of railway vehicles as well as of rails' steels is of great relevance.

During the development of this dissertation, the main topics that were addressed were railway vehicles, fatigue, fracture, probabilistic prediction models and structural reliability techniques.

Concerning axles, they are very important components as their failure can lead to catastrophic consequences. As so, they are designed with an infinite life approach. At the same

time, a good and accurate maintenance of these components is demanding to avoid accidents and optimize costs.

Aspects such as a correct design of the axle according to the standards, the mechanical properties of the material, the establishment of the load history, calculating the stress intensity factors on the critical stress regions of the axle, crack initiation and propagation phases and axle's inspections are of great importance.

A study on the fatigue life prediction of railway axles should be conducted based on a numerical analysis using the finite element method. This study should be supported by experimental results. Moreover, in order to evaluate fatigue crack propagation, crack growth rates should be evaluated in the Paris law region by processing experimental data. Last but not least, probabilistic prediction models and structural reliability techniques should be used for reliability analysis.

1.2 Objectives

The main objectives of this master's thesis are the following ones:

- Fatigue life prediction of a rail axle based on a local approach;
- Collecting and processing experimental data resultant from rotating bending high cycle fatigue tests for steel EA4T;
- Fatigue design curve assessment for the hollow rail axle based on small-scale EA4T specimens and EN 13103/13104 standards methods;
- Probabilistic fatigue life fields for the EA4T steel used in rail vehicle axles based on ASTM E739 standard;
- Fatigue crack growth characterization of the EA4T steel in mode I, for different stress ratios;
- Residual fatigue life evaluation based on BS7910 standard of a rail axle;
- Using structural reliability techniques for fatigue analysis such as the Monte Carlo Simulation Technique (MCST) and Artificial Neural Networks (ANN);
- A comparison between fatigue curves obtained by standardised method and numerical simulation combined with reliability techniques.

1.3 Structure of the Thesis

The research work carried out during this dissertation is described from Chapter 2 to 7.

Chapter 2 corresponds to the state of the art. This chapter consists on an extensive review on railway, fatigue, fracture mechanics and probabilistic prediction models.

Chapter 3 includes the fatigue strength characterization and fatigue life prediction of a rail axle made in EA4T steel, based on a numerical analysis using the finite element method as well as the Neuber rule.

The following chapter, Chapter 4, contains the rotating bending high cycle fatigue tests data as well as the probabilistic fatigue S-N curves estimated based on ASTM E739-91 standard and EN13103/EN13104 methodologies.

Chapter 5 deals with fatigue crack growth characterization of steel EA4T in mode I, for different stress ratios. Crack growth rates were evaluated in the Paris law region by processing experimental data. Additionally , the residual fatigue life estimations based on the standard and fracture mechanics approach for several nominal stresses were made.

Then comes Chapter 6 which covers the effects of structural reliability techniques for fatigue analysis - Monte Carlo Simulation Technique and Artificial Neural Networks.

Finally, Chapter 7 comprehends the conclusions that were drawn from this research work as well as some suggestions for future works.

The Appendix contains true stress-strain data for monotonic and cyclic characterization of EA4T steel.

Chapter 2

State of the Art

2.1 A Review on Railway

A bogie is an undercarriage with four or six wheels pivoted beneath railway vehicles. The wheels are typically press-fitted to axles. Axles are one of the most important components in a railway vehicle. Typically, railway axles are manufactured by forging. Presumed life-cycle of railway axles is up to 30 years. Changes in operational conditions and applied subsequent treatments influence the amount of broken railway axles.

The main aspects that are of extreme importance for high speed railway are the prevention of hunting, curve negotiation using tilting control, brake technology and acceleration of lightweight [1].

Figure 2.1 contains the history of maximum train speeds since 1980.

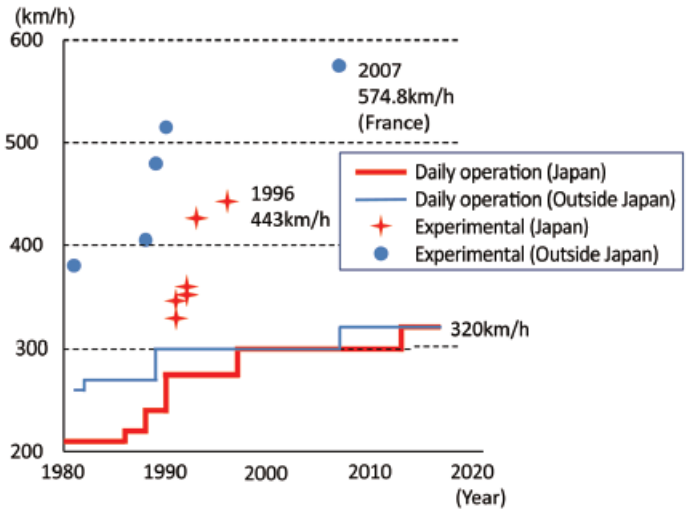

Figure 2.1: History of maximum train speeds since 1980 [1].

2.1.1 International Rail Entities

International Union of Railways (UIC), European Standards (EN) and Japanese Industrial Standards (JIS) have their own methods to inspect static and fatigue strength for railway vehicles. They all provide strength evaluation methods for bogie frames. However, they do not establish detailed fatigue life assessment approaches [2].

2.1.1.1 EN13103/13104 - Design Method for Non-powered/Powered Axles

European standards EN13103 and EN13104 establish the procedures for design and calculation of railway axles. Knowing the values of the loading forces, bending strains on the axle can be calculated. And bending moments enable to calculate bending stresses in all cross sections of the axle which have to be smaller than allowable stresses.

These standards provide a fatigue assessment for railway axles typically considering a constant amplitude approach under extreme load conditions [29].

2.1.1.2 EN13749 - Method of Specifying the Structural Requirements of Bogie Frames

EN13749 codifies static and fatigue load assumptions, calculations and test methods that verify the static and fatigue resistance of bogie frames. It also demands that fatigue life has to be evaluated by track tests [37].

Figure 2.2 depicts the step-by-step load conditions of fatigue test according to EN13749.

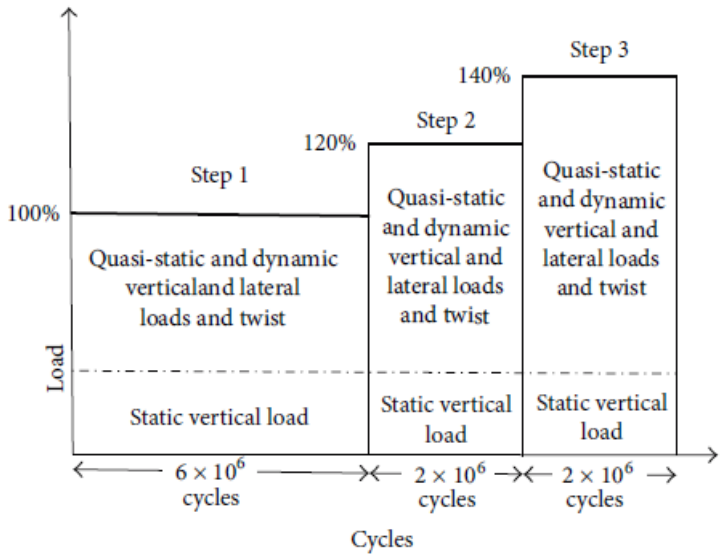

Figure 2.2: Step-by-step load conditions of fatigue test according to EN13749 [2].

There are some important aspects that are still not defined in the standard. One of them is the methodology to use for FEM simulation and for fatigue assessment in the welded joints. Another one is the definition of a standard calculation methodology to evaluate the fatigue strength in multi-axial stresses situations (common for railway applications) [37].

Fatigue calculation according to EN13749 for bogie structures should comprehend the following steps:

- Bogie's frame structural analysis done with FEM calculations;
- Structural analysis of the attachments components-bogie frame also done with FEM calculations.

.

The standard proposes two different approaches for fatigue calculation:

1. Endurance limit

   Stresses σ_{max} and σ_{min} generated by all load cases are calculated on each point of the bogie frame. With these values, σ_m and the fatigue cycle amplitude can be defined in order to establish comparisons with the fatigue limit of the material. This can be done using, for instance, the Goodman diagram (see Figure 2.3).

   The major advantage of this one methodology is that the fatigue limits for typical steels of bogies are well known (see Table 2.1), while the main disadvantage has to do with the rough simplification that is made.

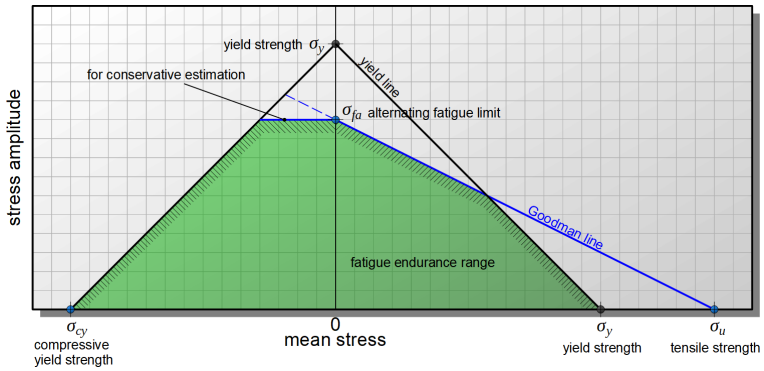

Figure 2.3: Example of a Modified Goodman diagram [3].

Table 2.1: Fatigue endurance limit for different railway structures and materials [35].

Application	Fatigue endurance limit (amplitude), (MPA)	Material and details	Reference number
Wheel seat	147	Hardened carbon steel Powered solid axle with press-fit	11
Wheel seat	120	EA1N carbon steel Powered solid axle with press-fit	12
Wheel seat	145	EA4T alloy steel Powered solid axle with press-fit	12
Wheel	300	SAE 1050	13
Wheel	295	SAE 1060	13
Wheel web	180	Steel Machined web	14
Wheel web	145	Steel Non-machined web	14
Fillet and groove of axle	200	EA1N carbon steel Powered solid axle with press-fit	12
Fillet and groove of axle	240	EA4T alloy steel Powered solid axle with press-fit	12
Axle	166	Steel	12
Axle	120	Steel Valid for steels with ultimate stresses in the range 550–650 MPa	15
Axle	220	EA1N carbon steel Press-fit.	16
Axle	180	EA4T alloy steel Press-fit	16
Axle	200	34CrNiMo6 steel Press-fit.	16
Axle	100	A1N steel Subjected to corrosion Endurance limit obtained at $4x10^7$ cycles cut-off	17
Coupler	138	Cast steel ASTM E90-60	18
Coupler	90	EN-GJS-800-8	19

2. Cumulative damage

   All the effects generated by combinations of load cases are considered. It is necessary to know the estimated number of cycles applied on the bogie for each load cases. This is used to verify the fatigue resistance with the help of a Wöhler diagram (S-N) of the material (see Figure 2). Then, in agreement with a hypothesis for damage accumulation (Palmgren-Miner rule, for instance), total damage can be calculated. The use of a load spectra close to reality is an advantage of this method as it allows to optimize structural strength and weight of the bogie frame.

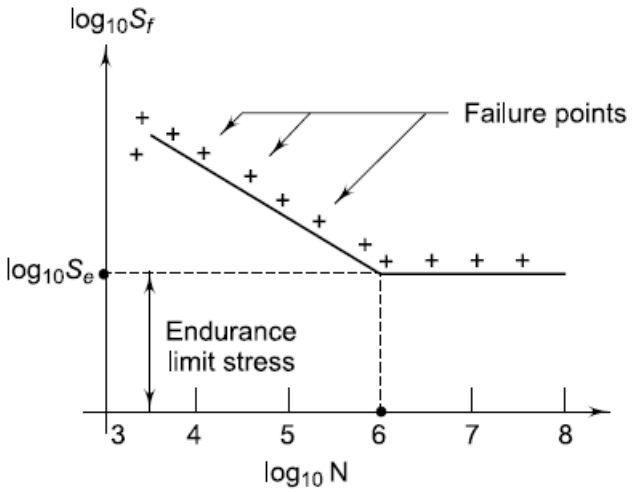

Figure 2.4: Example of a Wöhler diagram (S-N) [4].

2.1.1.3 GM/RT2100 and GM/RT2400

Newly designed European railway vehicles have to follow the group standards GM/RT2100 and GM/RT2400. These standards aim to decrease the risks associated with structural integrity [35].

2.1.1.4 ISO 1143:2010

This standard establishes the method for rotating bar bending fatigue testing of metallic materials.

2.1.1.5 ISO 12107

ISO 12107 defines the procedure for the statistical staircase method for the 50% probability of failure.

2.1.2 Portuguese Railway Model

The idea of introducing the railway in Portugal came in 1840 [38].

Railways in Portugal and Spain posses a track gauge of 1668 *mm* which is larger than the international standard gauge of 1435 *mm* [38].

The Portuguese railway model is divided into several entities:

- IMT - Regulation, supervision and development of the sector;
- IP - All duties and competences of REFER were transfered to IP which is responsible for the management of infrastructures;
- CP, Fertagus, Medway (CP Carga), Takargo, Comsa - Passengers and freight transportation [38].

The 4000 series is usually referred to an electric railcar used by the Portuguese company CP (Alfa Pendular). The 4000 series was built by *Fiat Ferroviaria* and assembled in Portugal. These railcars are composed by 10 carriages. They can reach a velocity of 220 *km/h* in commercial service.

Alfa Pendular is the name of the high-speed tilting train owned by the Portuguese state railway company CP. Alfa Pendular belongs to an Italian family of tilting trains - Pendolino.

A tilting train has a mechanism that allows increased velocity on regular rail tracks. The mechanism consists in an axis that has the ability to tilt up to 8 degrees in relation to the rails. This allows the curves to be done at higher speeds.

A tilting system can be hydraulic or mechanical. It allows the trains to tilt on curves in order to minimize the effects of centrifugal force.

2.1.3 Rolling Stock

A railcar is a railway vehicle that consists of a single coach and has a driver's cab at one or both ends of the unit. Railcars are exclusively used for passenger transport.

A locomotive is a railway vehicle that provides the necessary power to move the coaches (passenger transport) or wagons (freight transport). Locomotives do not have their own transport capacity. There are several reasons and advantages from isolating the power unit from the rest of the train.

2.1.4 Load Capacity

A vehicle's payload capacity is the amount of weight that the vehicle can carry within its cabin or on the truck bed.

The sprung mass is the portion of the vehicle's total mass that is supported by the suspension (in most applications half of the weight of the suspension itself is included). It contains the body, frame, internal components, passengers and cargo, but not the other components at the end of the suspension.

On another hand, the unsprung mass is the mass of the suspension, wheels or tracks and other components directly connected to them.

Figure 2.5 comprehends different load arrangements according to the type of bogie.

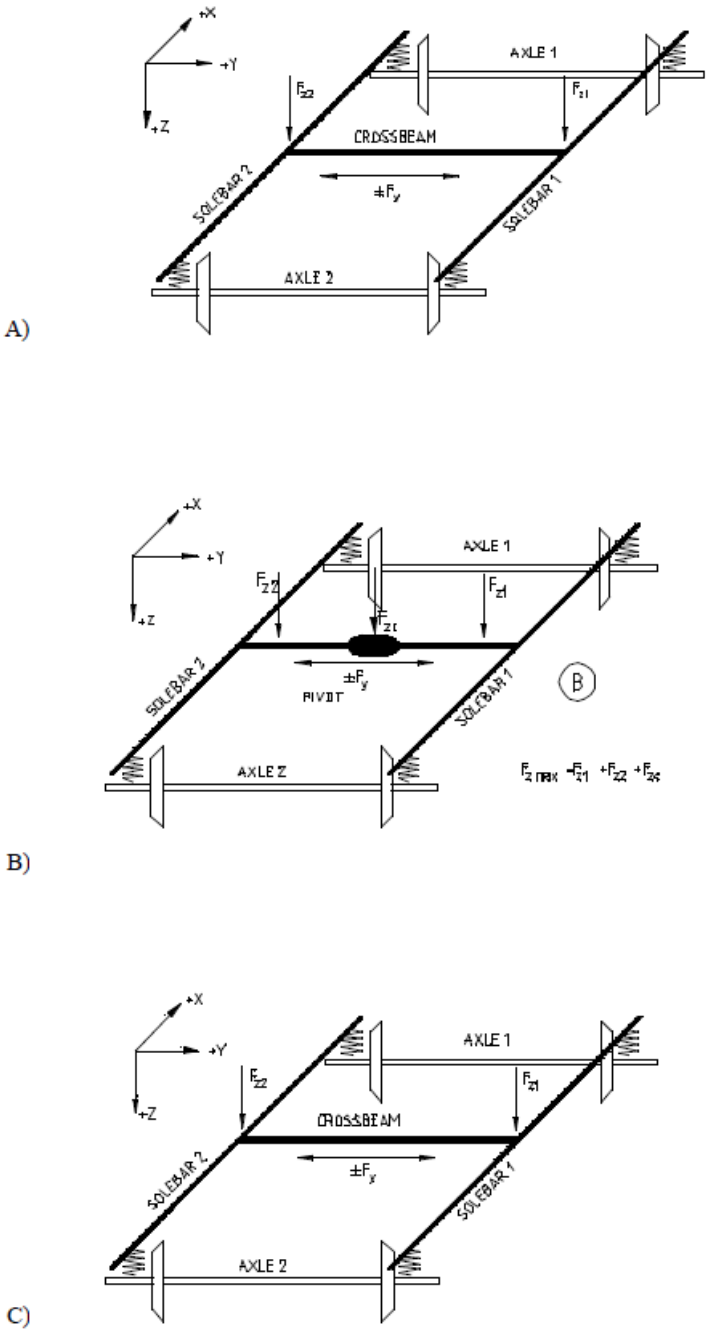

Figure 2.5: Bogie vertical and transverse loading arrangement, A) passenger and semitrailer bogie, B) freight bogie, C) powered bogie [5].

2.1.5 Bogies

Bogies play an important role in keeping the stability of vehicles at high speed, safe passing when curving and comfort during journeys [1]. Generally, a bogie frame is subject to fatigue load caused by repetitive vibration forces and landing during service. This way, ensuring enough structural strength to withstand static and fatigue load is mandatory [6].

Steels used for bogie frames are structural steels [10].

Bogies' weight approximately accounts for 37% of the weight of the whole vehicle. This means that finding a way to reduce the weight of bogie's components is of extreme importance for companies trying to reach a lightweight design for their vehicles. The use of polymer-based composite materials has been attempted [6].

Moreover, weigh reduction of the unsprung parts of bogies is essential for decreasing loads on rails, diminishing dynamic changes in wheel loads (which can cause track deformation), and reducing noise/vibration [1]. Ways to decrease the unsprung weight can be:

- Usage of bolsterless bogies;
- Weight reduction design via strength analysis applying FEM;
- Application of aluminum alloys to axle boxes and gear boxes;
- Hollow axles.

Concerning the main parts of bogies, they are the following ones (see also Figure 2.6):

- Bogie frame;
- Bogie bolster;
- Center Pivot Arrangement;
- Wheel set assembly;
- Roller bearing assembly;
- Brake beam assembly;
- Brake head;
- Brake block;
- Brake levers;
- Brake cylinder;
- Primary suspension (a rubber spring can be used as the primary suspension);
- Secondary suspension (an air spring can be used as the secondary suspension);
- Lower spring beam;
- Equalizing stay rod. [6]

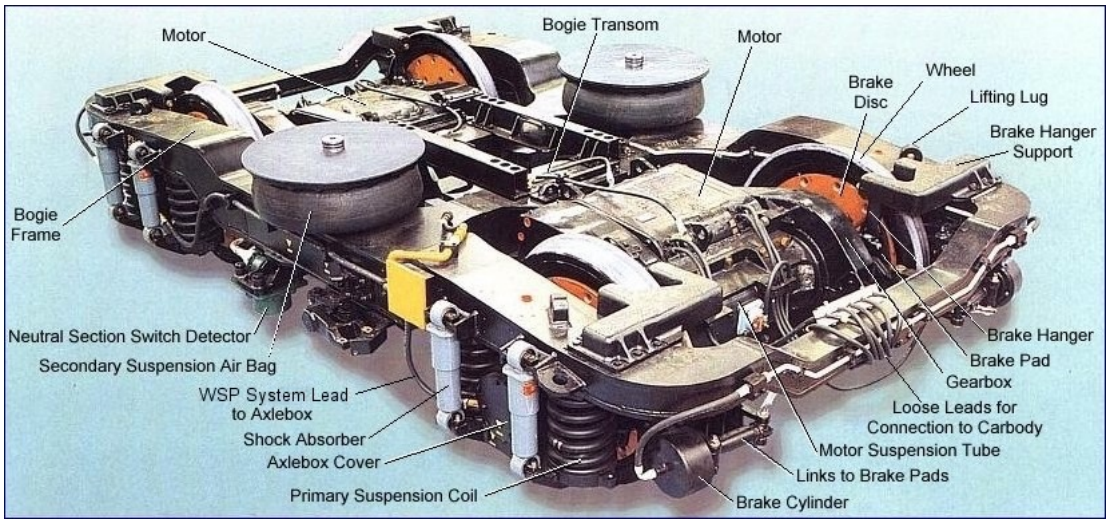

Figure 2.6: Components of a bogie [6].

There are different types of bogies such as passenger, semitrailer, locomotive, metro and tram bogies [5].

Bogies are structurally classified by the usage or not of a bolster (see Figure 2.7). A bolster is like a beam. The bearers support the bolster. The bogie bolster is welded to the body of the coach and it transfers the dead weight of the coach to the bogie frame. It is a free-floating member which allows the bogie to turn with respect to the body [6][1].

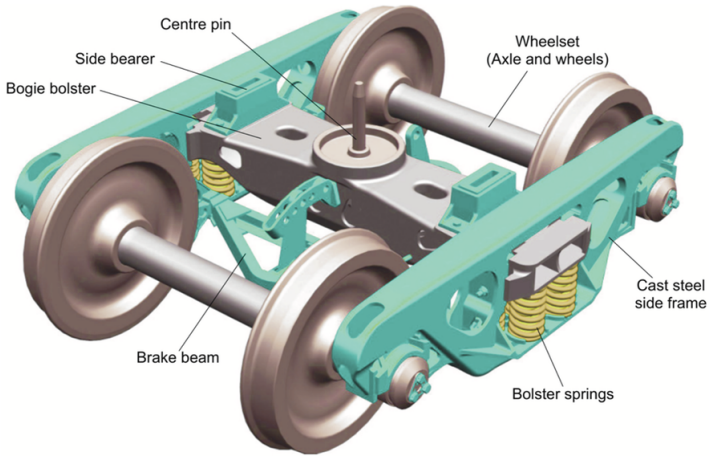

Figure 2.7: Bogie bolster [7].

The side frame takes vibrational load through dashpot of the guide of wheel due to track irregularities. Dashpot arrangement consists of a cylinder and a piston (axle box guide). It also transfers the load of the shell to the rail through the wheel, when the vehicle is static. [6] The headstock carries brake attachment foe transferring brake force from the brake cylinder to the wheel (Figure 2.8).

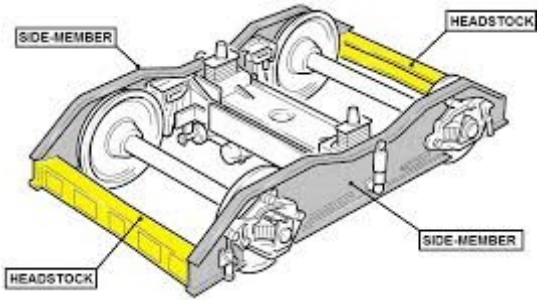

Figure 2.8: Headstock [8].

The transom takes horizontal inertial forces of the shell during motion through bolster. There are also longitudinal heads, right (RH) and left heads (LH), that are used to transfer load from the transom to the headstock. A guide is used to transfer the shell weight to rail [6].

There are multiple external forces that act on the bogie frame. They come from wheel-rail contact points and from the interfaces with the car body. They are generated from:

- Double sprung masses, including payload;
- Track irregularities;
- Lateral accelerations caused by curve riding;
- Longitudinal accelerations caused by traction and braking [6].

Vertical and transverse forces should be considered for fatigue calculation. Longitudinal forces caused from sliding between wheel and rail and track twist should also be considered [37].

According to standards, vertical forces coming from sprung masses are constituted by three components:

- A static component that comes from the sprung masses (normal service payload);
- A quasi-static component taking into account the car body rolling motion in curve riding;
- A dynamic component related with car body vertical acceleration in curve riding [6].

The amplitudes of the quasi-static and dynamic components are calculated as a percentage of the static component. For the quasi-static component, roll coefficient α is used. The roll coefficient indicates the load at the curve track. For the dynamic component, bounce coefficient β is used. [6]

Transversal forces coming from each axle:

- A quasi-static component equal to $0.063 \cdot (F_{vertical} + mg)$ which is due to non compensated acceleration;
- A dynamic component equal to $0.063 \cdot (F_{vertical} + mg)$ which appears because of track irregularities[6].

During service, there are operative and inertial loads that act on the attachments of bogie's frames:

- Inertial forces due to masses attached to the bogie frame or axle box;
- Loads resulting from damper, braking or the traction motor;
- Loads applied on the anti-roll system [6] [37].

2.1.6 Axles

An interference fit, also known as a press fit or friction fit is a fastening between two parts which is achieved by friction after the parts are pushed together (Figure 2.9). A wheel set consists in an axle press fitted with wheels 2.10.

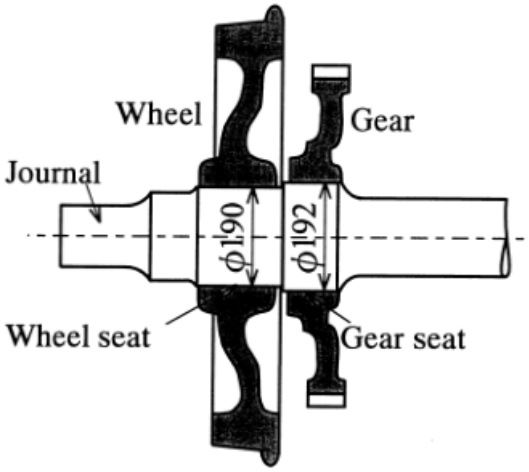

Figure 2.9: Closely fitted part of axles [9].

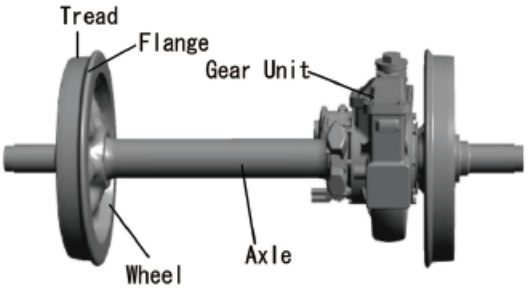

Figure 2.10: Wheel set scheme [1].

The diameter ratio of a railway axle is the ratio between the diameter D of the press-fitted portion to the diameter d of the non-press-fitted portion. When the diameter ratio of a railway axle(D/d) is increased, the fillets become the critical parts and the interference surfaces are less important. Therefore, increasing the difference in diameter (increasing the diameter ratio) should help improve the fatigue strength of press-fitted parts as it can be seen in Figure 2.11 [11].

Measurement	Shinkansen	TGV	ICE
Diameter			
D (mm)	209	212	190
d (mm)	190	184	160
Diameter ratio			
D/d	1.10	1.15	1.19
Radius			
ρ (mm)	100	15 and 75	15 and 75

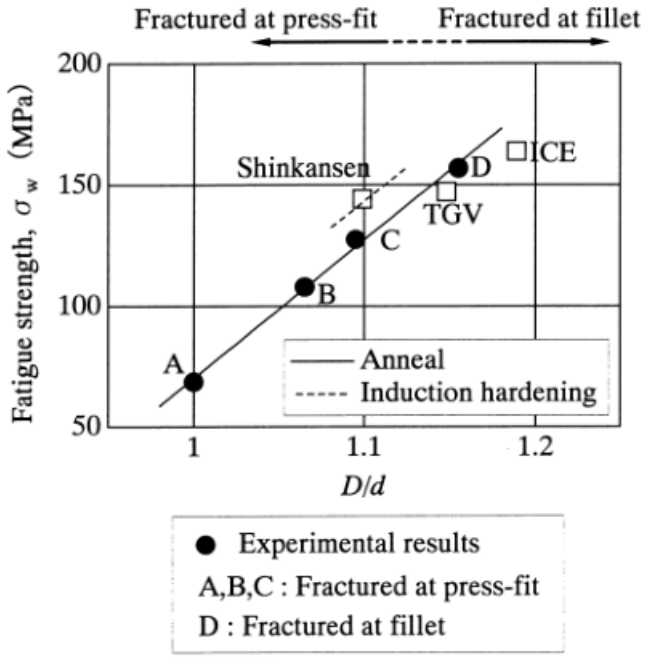

Figure 2.11: The effect of diameter ratio on the press-fit fatigue strength [9].

2.1.6.1 Axle design method

Figures 2.13 to 2.14 show the external forces that act upon a wheel set. A vertical force is applied close to each end of the axle. A reaction force is applied to the surface of contact between the axle and rail. In a curved railway section, a lateral force is applied toward the outer rail [11].

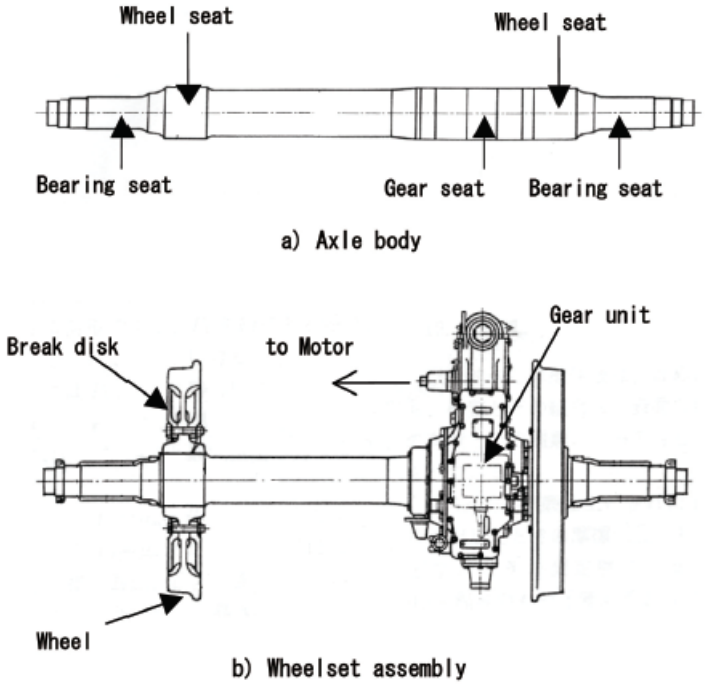

Figure 2.12: Example of a railway axle [10].

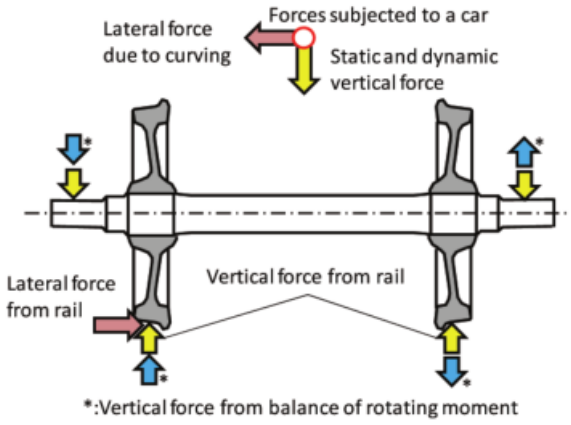

Figure 2.13: Forces acting on a wheel-axle assembly [11].

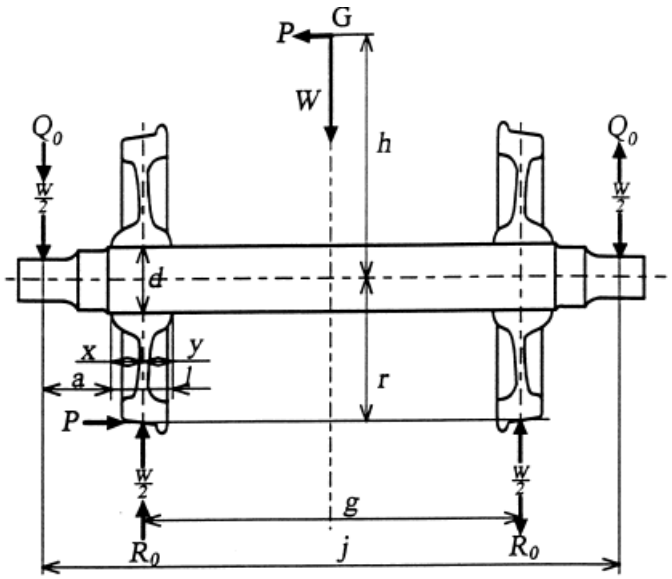

Acting forces of railway axle assembly

W	Wagon dead weight per wheel-set
P	$= \alpha_L \cdot W$ Horizontal force
α_L	Horizontal acceleration coefficient
Q_0	$= P\ (h/j)$ Vertical force of journals by P
R_0	$= (h+r)\ P/g$ Vertical force of treads by P

Dimension of railway axle assembly

d	Axle diameter	j	Distance between journal center
r	Wheel radius	g	Wheel tread distance
a	Distance between journal center and the end of wheel seat		
h	Height from axle to gravity center		
x	Distance from the outside wheel hub to contact load		
y	Distance from the inside wheel hub to contact load		
l	$x+y$		

Another symbol

G	Gravity center

Bending stress of the axle at the wheel seat σ_b

$$M_1 = (j-g)\ W/4 \quad (1)$$

$$M_2 = \alpha_V \cdot M_1 \quad (2)$$

$$M_3 = P \cdot r + Q_0\ (a+l) - R_0 \cdot y \quad (3)$$

$$\sigma_b = m\ (M_1+M_2+M_3)\ /Z \quad (4)$$

α_V	Vertical acceleration coefficient
m	Safety factor
Z	Section modulus of axle at the wheel seat

Figure 2.14: Acting forces on a railway axle assembly [9].

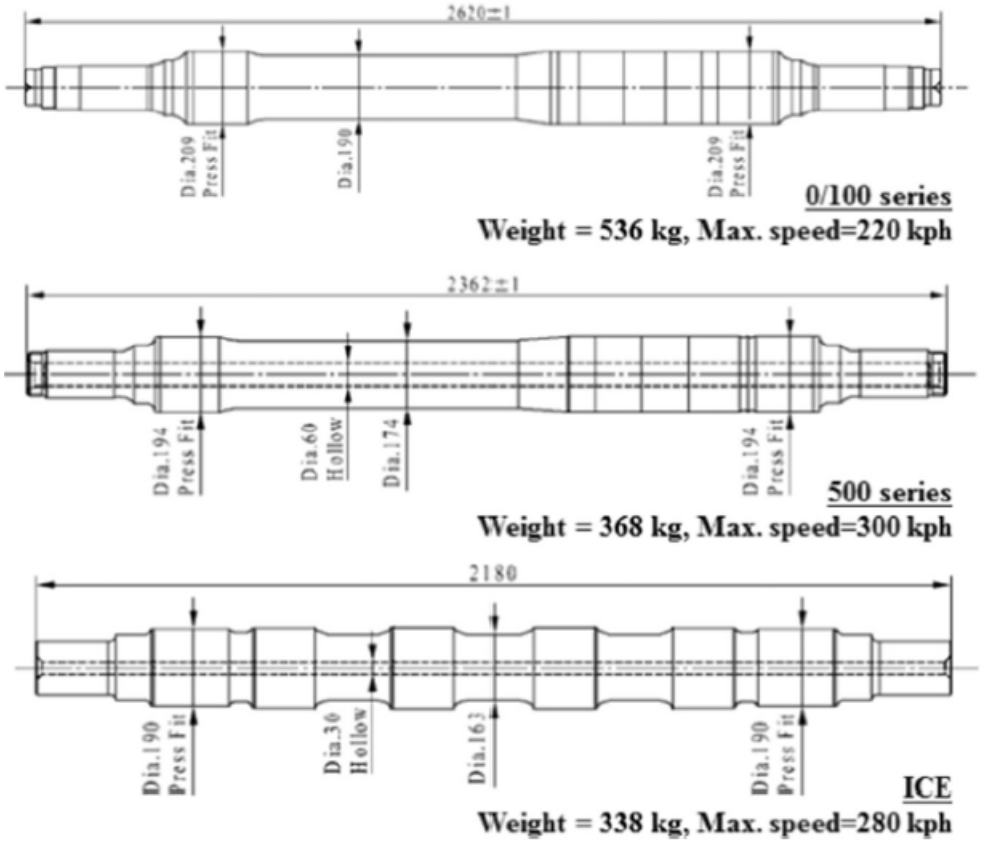

Figure 2.15: Existing hollow axle designs for high-speed trains (Shinkansen and ICE) [12].

For hollow axles, the bending stresses increases due to reduced cross-sectional area [12]. Using hollow axles can help to reduce shaft weights. Figure 2.15 contains existing hollow axle designs for high-speed trains.

2.1.6.2 Materials

European railway axles are usually made from steel grades EA1N and EA4T. Steel grade 34CrMo4 is also used. Other steels are used for high speed trains, such as steel 30CrNiMo6 [13] [14]. Materials like EA1T are also used for railway axles [12].

2.1.7 High-speed trains

There are three main aspects that are of keen importance for high-speed:

- Adhesion to transfer the traction force from the wheels to the rails without slipping;
- High-speed running stability of bogies (vibration control - dealing with hunting);
- Power collection with pantographs [1].

Generally speaking, it can be said the the most essential issue in design of bogies for high-speed trains is stability [1].

2.1.8 Trade-off between Speed Increase and Curve Negotiation

Diminishing travel times can be done raising the maximum train speed. However, what is most important for decreasing travel time is to increase train speed at curves. Nevertheless, when train speed at curves is excessively high, the centrifugal force becomes so high that passengers feel uncomfortable.

The tread is the wheel's surface that directly contacts with the rail. The tread is tapered for reasons that will be explained next. When curving, a wheel set shifts toward the outer rail. This way, the effective diameters of the outer and inner wheels automatically become different from each other and consequently, the curve can be made smoothly. The larger the tread conicity, the easier it is to deal with curves [1]. A large tread conicity is desired for subway railcars since they usually have to ride through many tight curves and the train speed is not that high. On the other hand, small conicity is desired for high-speed bullet trains. Typically, these trains have few tight curves and running stability at high speeds is crucial. Nevertheless, the tread conicity can bring along some problems such as unstable vibration (boogie hunting) [1].

In Japan, in order for maintaining a comfortable ride, lateral acceleration shouldn't exceed $0.8\ m/s^2$. Train tracks are inclined towards the inside of a curve. This way, gravitational force will push toward the inside of a curve and cancel the centrifugal force toward the outside. The inclination of train tracks is called cant. The magnitude of a cant is normally given as the height difference between the outer and inner rails. Curve radius and train speed are important for defining the size of a cant. Factors such as different kinds of trains passing at different speeds, their possible stop at a curve, lateral wind and velocity also have to be considered [1].

In Japan, an advanced controlled body-tilting system was developed. The motion of the tilting bolster is pneumatically assisted before entering a curve. However, since these body-tilting mechanisms are complex, a simpler air-spring tilting system was developed and commercially applied (Figure 2.16). With this system, the body is tilted by pneumatically differentiating the heights of the air springs on both sides of the bogies. This method only allows a limited train speed increase. This happens because the maximum tilting angle is set at 2°. Nevertheless, its simple structure is a significant advantage. The simple air-spring tilting system is of low costs of installation and maintenance [1].

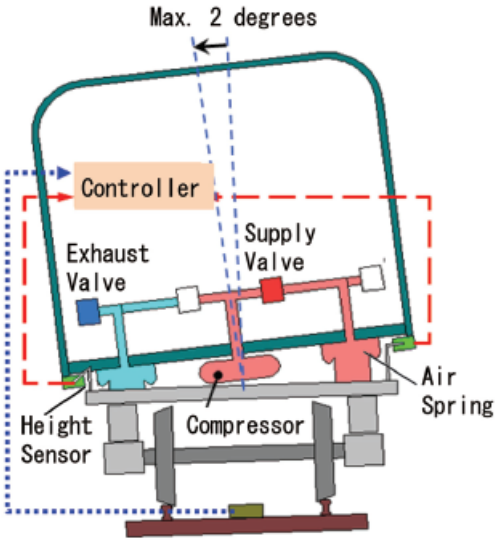

Figure 2.16: Structure of an air spring tilting system [1].

Steering bogies with the ability of steering wheel sets in the direction of curves have been developed and commercially used (Figures 2.17 and 2.18) [1].

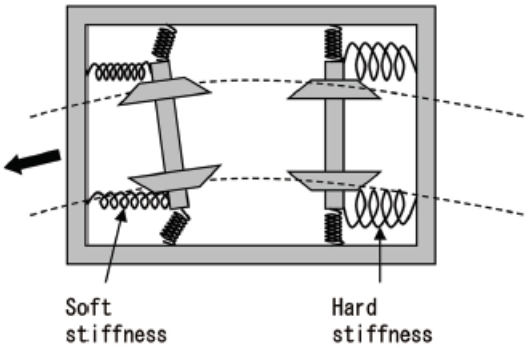

Figure 2.17: Structure of asymmetric-stiffness, self-steering bogie [1].

Figure 2.18 contains a semi-forced steering bogie. When the bogie turns with respect to the body while curving, the turning angle is transferred through linkages to the axle boxes to steer the wheel set in the direction of a curve [1].

Figure 2.18: Steering bogie for Tokyo Metro Ginza Line [1].

Steering bogies help to improve running safety at curves (lateral force is decreased). They also help reducing noise and wear of rails and wheels due to their friction and creeping.

However, the decrease in wheel loads can be a serious problem. For instance, at the gradual cant-decreasing zone at both ends of a curve where the track is twisted to match the cant.

There are bogies which have vertically elastic primary suspensions to allow wheel sets to easily follow the twisting track. Other bogies have a frame that twists [1].

Standards and regulations demand that vehicles are design so that the weight of the body is distributed equally to all wheels.

It is also known that the derailment coefficient is related to the coefficient of friction between a wheel and a rail. The degree of friction depends on multiple aspects:

- Weather;
- Atmospheric conditions (temperature, humidity and others);
- Frequency of traffic.

Although decreasing the friction coefficient can be helpful to increase safety against derailment, it may cause other problems such as slipping and skidding [1].

2.1.9 Braking

Nowadays, electric trains decelerate until stop almost depending only on electric brakes. Drive motors are used as generators and the braking force comes from the conversion of train's kinetic energy into electric energy. The generated electric energy is consumed in the train itself or used somewhere else. Nevertheless, railway vehicles are also obligated to possess a mechanical brake system. Figure 2.19 contains a center-connection type wheel mounted disc.

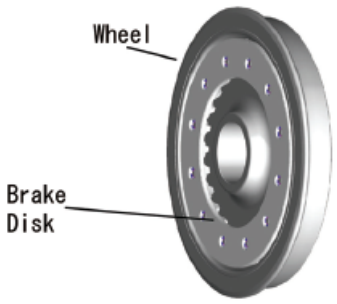

Figure 2.19: Center-connection type wheel mounted disc [1].

2.1.10 Safety Against Derailment

Running safety is evaluated using an indicator called the derailment coefficient. It is the ratio Q/P of the lateral force Q that a wheel applies to the rail to the vertical force P, or the wheel load (Figure 2.20). A curve or a vehicle is considered safe against derailment when Q/P is of 0.8 or less [1]. Figure 2.21 illustrates a modified arc wheel profile for conventional lines.

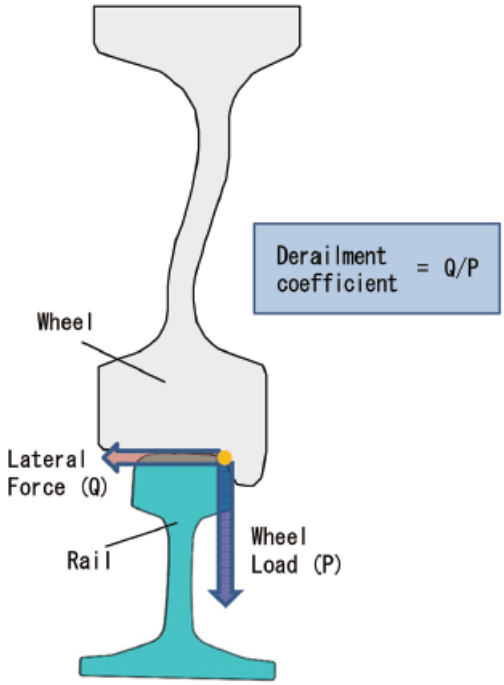

Figure 2.20: Derailment coefficient [1].

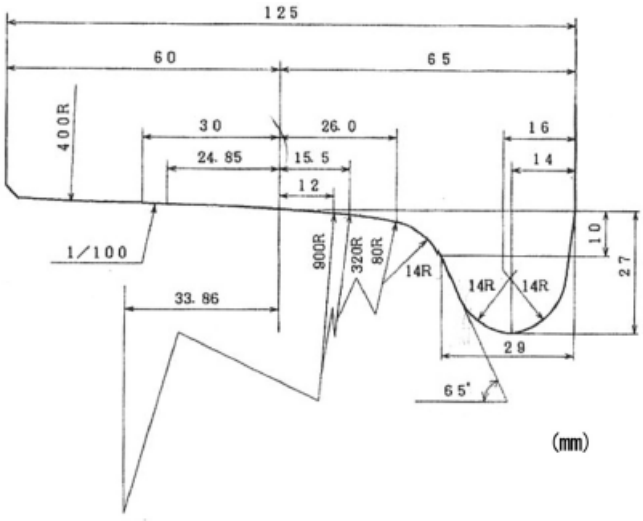

Figure 2.21: Modified arc wheel profile for conventional lines [1].

2.1.11 Ride Comfort

Suspensions are designed to insulate the body from vibration caused by disturbances from the track. Nowadays, multi-body dynamic analysis is often used for vibration analysis (Figure 2.22).

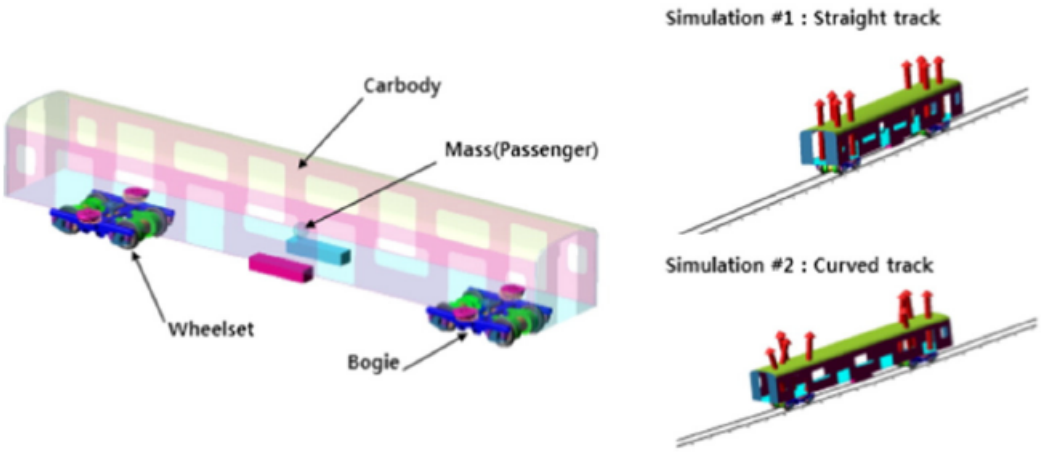

Figure 2.22: Multi-body dynamic simulation of the K-EMU vehicle model [12].

Active suspensions to suppress vibrations by computer control have also been developed. An example of an active suspension system is shown in Figure 2.23. A pneumatic actuation suspension system was implemented on the series E2 Shinkansen trains of JR East in 2001 [1].

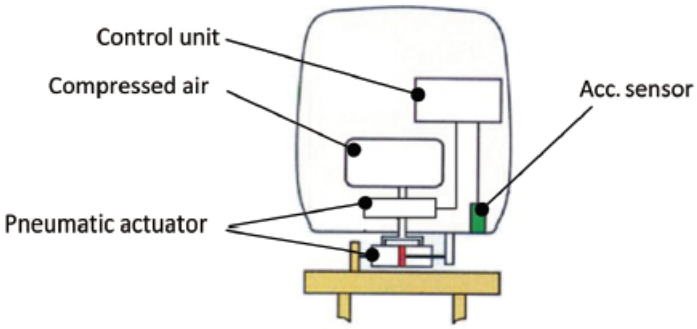

Figure 2.23: Structure of active suspension system [1].

Also, semi-active suspensions to suppress vibration have been developed. They work by changing the damping capacity of oil dampers.

2.1.12 Environment-related Problems

2.1.12.1 Noise and Vibration

Figure 2.24 shows two types of noise-damping wheels.

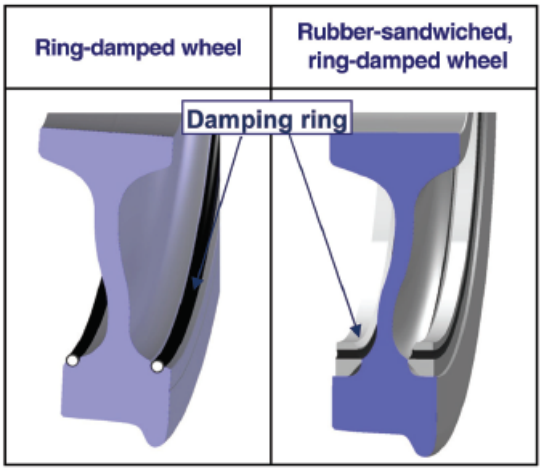

Figure 2.24: Noise-damping wheels [1]

2.1.12.2 Energy Saving

Saving electricity, weight reduction and decreasing mechanical losses are typical measures for saving energy.

One of the new challenges concerning railway vehicles is the adoption of composite materials. This comes along with the philosophy of energy-efficient railway vehicles. They enable a reduction on vehicles' mass. However, there are some difficulties related with their usage that needs further studies and experiments as these materials have an anisotropic behaviour and are very difficult to machine [35].

2.1.13 Maintenance of Railway Vehicles

A philosophy of preventive maintenance should be adopted. Nowadays, all components of vehicle's are constantly monitored and inspections/repairs are conducted when a symptom of a failure is detected.

Figure 2.25: Track condition monitoring bogie [1].

The derailment coefficient (Q/P) is measured with a test train equipped with special wheel sets (Figures 2.25 and 2.26). Tracks are constantly dislocated gradually as trains pass. Also, tracks' conditions change depending on the temperature, humidity, rail/wheel lubrication, and the condition of rail surfaces.

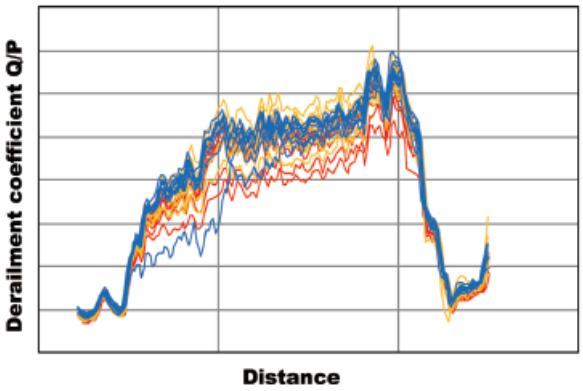

Figure 2.26: Derailment coefficient measured using track condition monitoring bogie (1 week) [1].

Power spectral density (PSD) functions can be used to generate random track irregularities. Federal Railroad Administration of the United States of America (FRA) classifies railway tracks from 1 (the worst) to 6 (the best) in terms of surface irregularities [39].

2.2 A Review on Fatigue

There are many challenges associated with fatigue analysis:

1. Prediction of fatigue under variable amplitudes as it was proven that Miner calculations and local-strain approach haven't produced accurate results;
2. Corrosion fatigue since there is still no explanation for many effects that are observed;
3. Multi-axial fatigue stresses [35].

Concerning fatigue analysis, the critical parts of railway axles are the wheel seats, gear seats, brake disc seat and its surroundings. The study of critical details is of extreme importance. Figures 2.27 and 2.28 depict the distribution of stresses on areas of interests of wheel set assemblies.

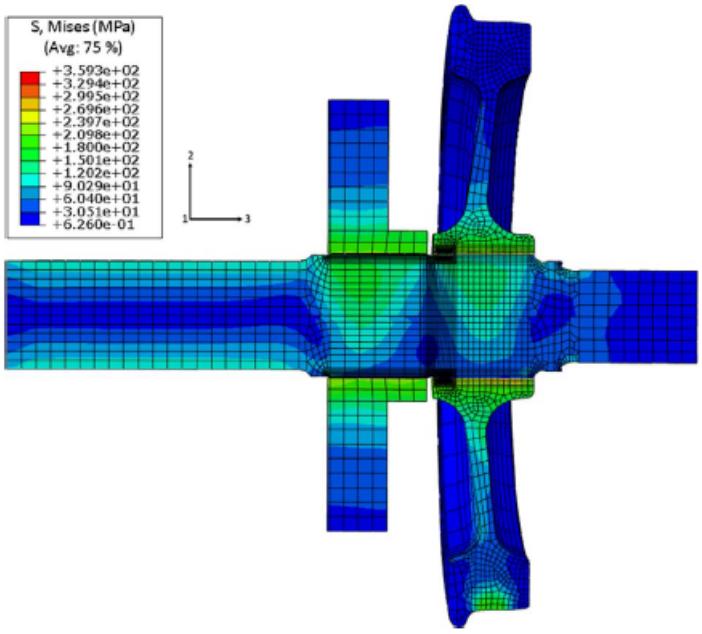

Figure 2.27: Distribution of Von-Mises' stress on the press-fitted and loaded axle [13].

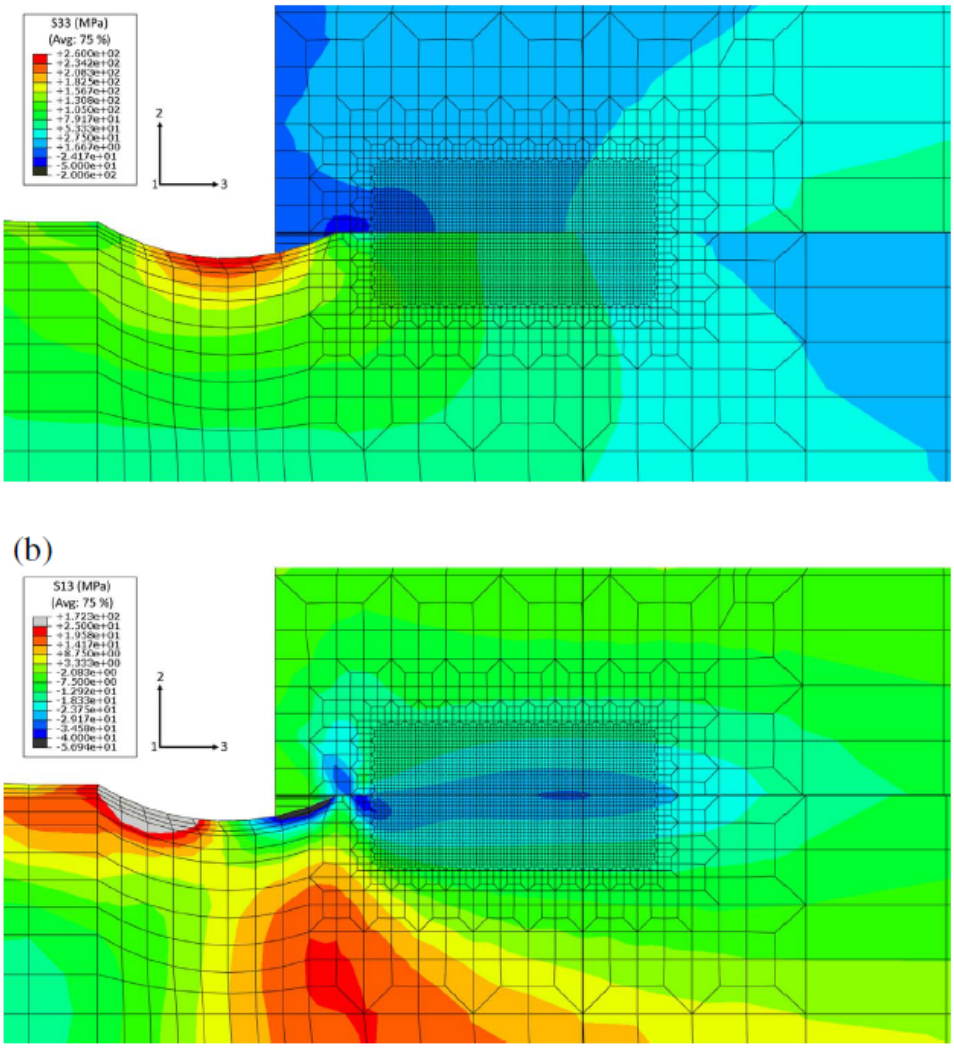

Figure 2.28: Distribution of shear and longitudinal stresses on the area of interest (a) longitudinal stress, (b) shear stress (S13) [13].

2.2.1 Fatigue Limits of Steels for Railway Axles

The fatigue limits have to be derived from knowing the value of S, the security coefficient. Knowing the fatigue limits, the maximum admissible stresses are known. For calculating the safety parameter S, the notch sensitivity coefficient has to be determined. The notch effect q is obtained with the values of R_{fL} and R_{fE}. R_{fL} is the fatigue limit determined from smooth surface small test piece and R_{fE} is the fatigue limit determined from notched small test piece. From evaluated fatigue limit R_{fL} and standard deviation, a probabilistic curve of fatigue strength can be drawn. Figure 2.29 shows a distribution of fatigue test results of a small scale specimen.

$$q = R_{fL}/R_{fE} \tag{2.1}$$

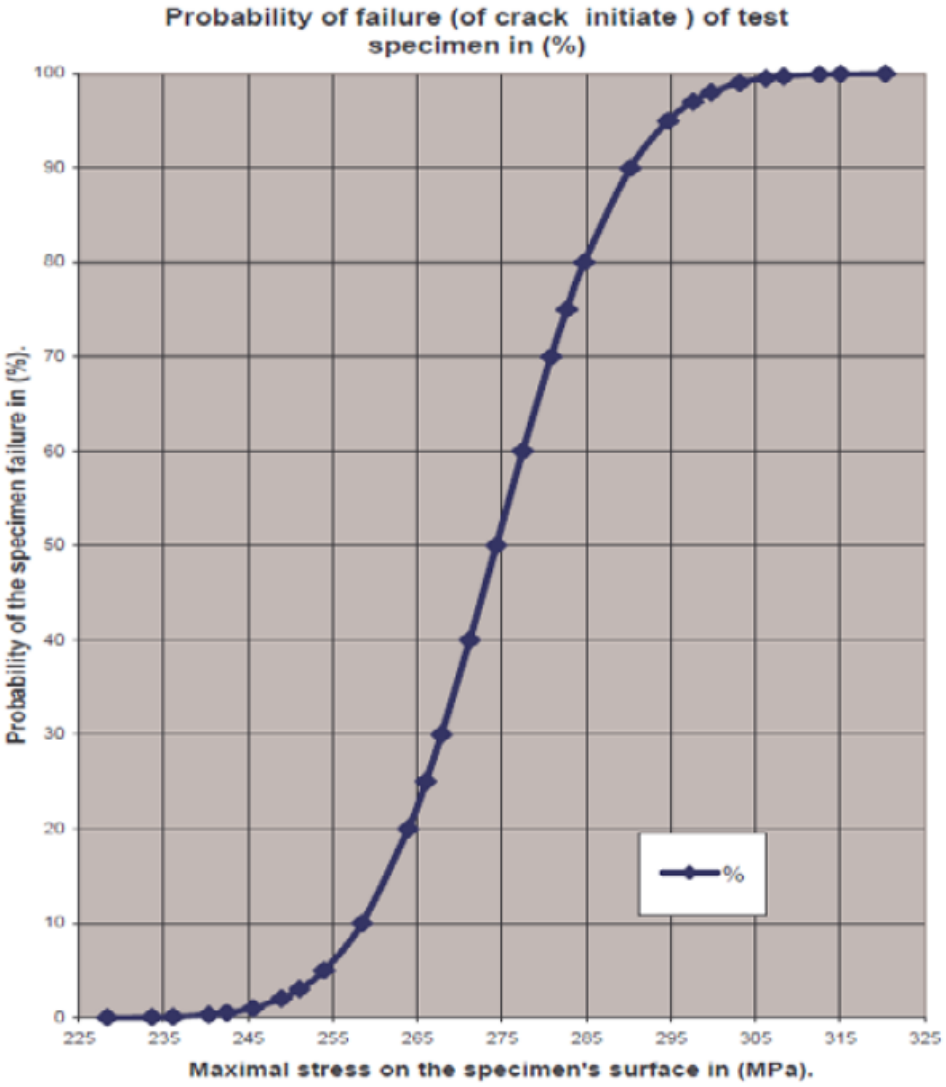

Figure 2.29: Distribution of fatigue test results of a small scale specimen (steel grade EA1N) [14].

2.2.2 Calculation Process for Fatigue Analysis of Rail Axle Vehicles

The calculation process involves the following tasks:

1. Checking the forces on the interfaces of the structure;
2. Combining these forces in load cases;
3. Analysing stress values for all load cases;
4. Comparing stress values with acceptable stress limits.

In order to evaluate local stress conditions, the biaxiality ratio (λ) can be was used, where σ_1 is the maximum principal stress and σ_2 is the minimum principal stress.

$$\lambda = \frac{\sigma_2}{\sigma_1} \tag{2.2}$$

As it was already explained before, the standards consider two different approaches for fatigue calculation:

- Endurance Limit (Goodman diagram)
- Cumulative damage (S-N curve and Miner rule)

2.2.3 Low Cycle Fatigue (LCF) and High Cycle Fatigue (HCF)

The difference between LCF and HCF has to do with deformations. Plastic deformation is associated with LCF, while elastic deformation is associated with HCF. The transition between LCF and HCF, transition between plastic and elastic deformations, has to do with the stress level (Figure 2.30).

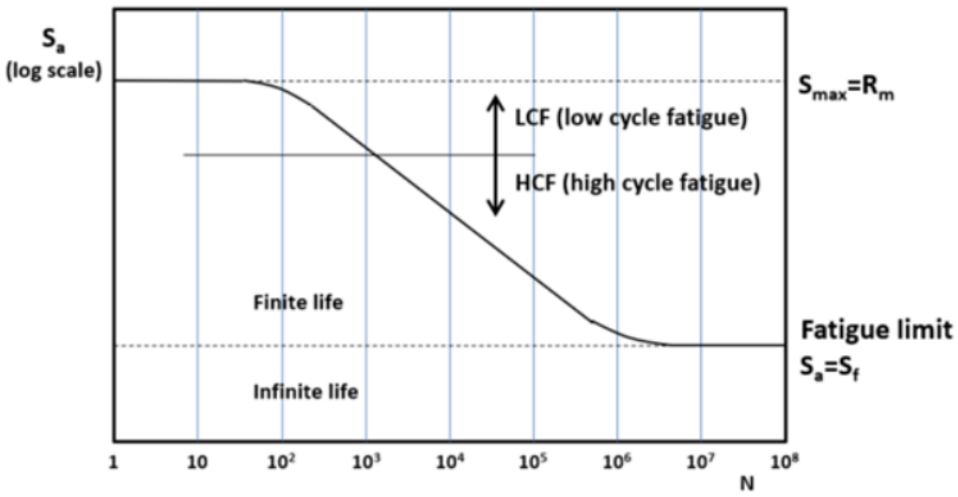

Figure 2.30: LCF and HCF [15].

2.2.4 Fretting Damage

Fretting fatigue is typical high cycle fatigue which is due to repeated occurrence of a microslip between contact surfaces. The relative movement between wheel's internal bore and the press-fit seat is responsible for the appearance of fretting fatigue. Fretting fatigue occurs when movements are within 3-20 μm range and it is characterized by the formation of a "stick-slip" boundary within the press-fit seat [13]. When there is no load, the axle and press-fitted wheels look like a completely solid thing. However, when there is a rotational bending load, the wheel deformation does not follow up the axle bending deformation. Consequently, a micro relative slip is induced due to the difference in deformation. The micro slip occurs near the end of the press-fitted part, as it can be seen in Figure 2.31 [11].

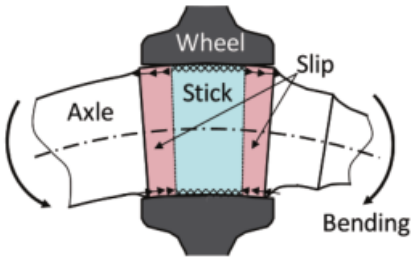

Figure 2.31: Schematic illustration of bending deformation on press-fitted part of an axle [11].

It is necessary to test for more than 10^8 cycles to find the fatigue strength under fretting conditions. Figure 2.32 shows the results of fretting fatigue tests using press-fitted axle assemblies of 50 *mm* axle diameter. Fretting fatigue cracks initiate during service.

A stress relief groove can me implemented as a countermeasure to the above crack initiation. Due to fretting wear, there is a stress redistribution. The introduction of a stress relief groove influences the fretting wear and fatigue. The fatigue limit of the press-fitted part can be raised with the application of a groove [9] [40].

As expected, the depth and with of the wear scar increases with and increase in fretting cycles. Stress concentration at the contact edge is relieved due to fretting wear, while a new stress concentration appears at the edge of wear scar. This leads to an increase of the edge scar which moves towards the inner side of the contact area. Stress concentration in the inner side is considered to cause the fatigue crack initiation [40].

Increasing groove depth or decreasing groove radius can reduce fretting wear and improve fretting fatigue strength [40].

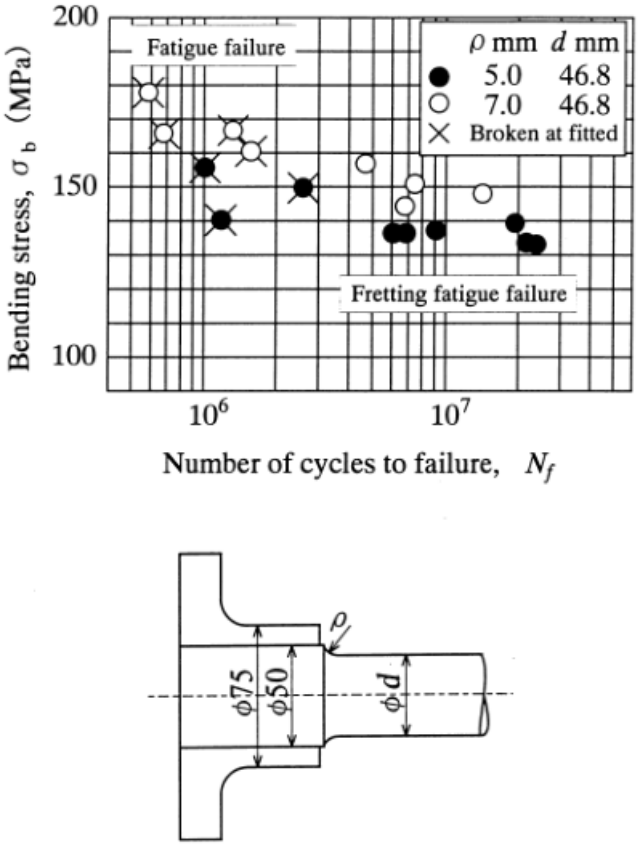

Figure 2.32: Typical feature of fretting fatigue [9].

When fretting occurs for a long period of time, brown powder (cocoa) can accumulate at contact surfaces. This phenomenon is the so called fretting corrosion [11].

The shape of the axle portion near the end of each press-fitted part strongly influences the axle fretting fatigue. The main parameters of the shape of that portion are the diameter ratio, D/d, where D is the diameter of the press-fitted portion and d is the diameter of the non-press-fitted portion, as well as the overhang distance δ. High fatigue strength can be achieved by setting D/d to 1.1 or more and by turning δ to a positive value [11].

Fatigue crack initiation at the press-fit seat region is related with shear stress gradient across the boundary. Fatigue damage begins with the removal of the oxide layer. Then, adhesion of surface asperities surges in form of cold-welds. This will cause the rise of the friction coefficient. While fretting fatigue proceeds, plastic deformation and oxidation of near-surface field occur in the second stage. Cyclic ratcheting of the deformed surface layer leads to the formation of small fretting cracks. Sub-surface cracks can also appear. Entrapped debris have an abrasive effect and they also cause the friction coefficient to decrease. At the last stage, small fretting cracks reaching the critical size limit begin to propagate by influence of surface stresses.

The crack growth rate is governed by the major bending stress and the surface shear.

Fretting fatigue cracks nucleate simultaneously at multiple origins. Coalescence of individual small fretting cracks lead to the formation of major circumferential cracks.

Fretting crack growth rate and the cumulative fretting damage are responsible for miscalculation of the remaining fatigue life and consequently, the premature failure of the axle. It was reported in the literature that a decrease in fatigue life up to 60% can happen due to fretting fatigue [13].

2.2.5 Foreign Object Damages (FOD)

FODs have become the most dangerous defect for high-speed railway axles. The middle of the axle is the most affected area by FODs [41].

They can be a significant stress increaser and it is believed that they have a strong impact on high cycle fatigue failure. FOD can trigger premature crack initiation and subsequent crack propagation [41].

FOD defects can be flying ballast, rain pits, scratches bumps and visible mechanical damages [41].

2.2.6 Fatigue Tests

Fatigue tests can be classified in the following way:

- Classification based on the sequence of stress amplitudes
  - Constant-amplitude test;
  - Variable-amplitude test.
- Classification based on the nature of the test-piece
  - Specimens;
  - Component.
- General Classification of Fatigue Testing
  - Material type test;
  - Structural type test;
  - Actual service type test.

The equipment used for fatigue testing can include actuators for vertical load, actuators for transverse load and actuators for twist load.

2.2.6.1 Constant/Variable Amplitude Tests

Methods of fatigue testing can be classified according to the sequence of stress amplitudes.

- *Constant-amplitude test*

  This sequence consist in applying reversals of stress of constant-amplitude to test-pieces and it stops when failure occurs (see Figure 2.33).

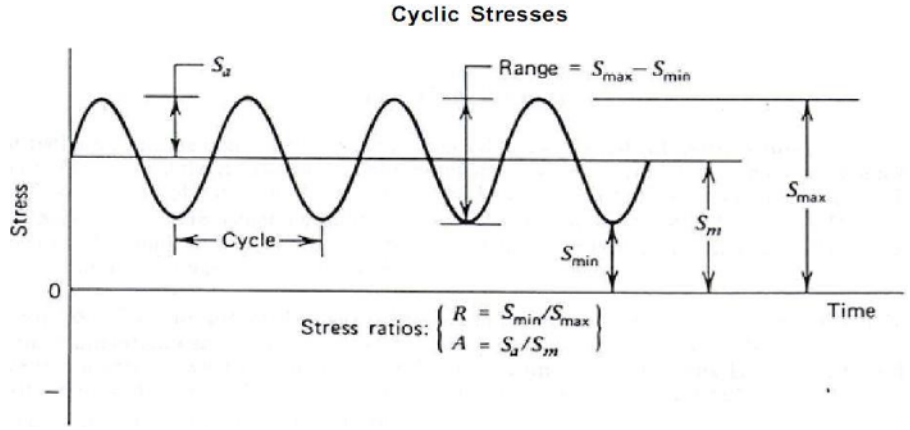

Figure 2.33: Scheme illustrating cyclic loading parameters [16].

  Constant-amplitude tests can be divided according to the choice of stress levels:

  - Routine test - specimens are expected to last between 10^4 to 10^7 cycles;
  - Short-life test - stress levels are suited above the yield stress;
  - Long-life test - stress levels are suited below or slightly above the fatigue limit.

- *Variable-amplitude test*

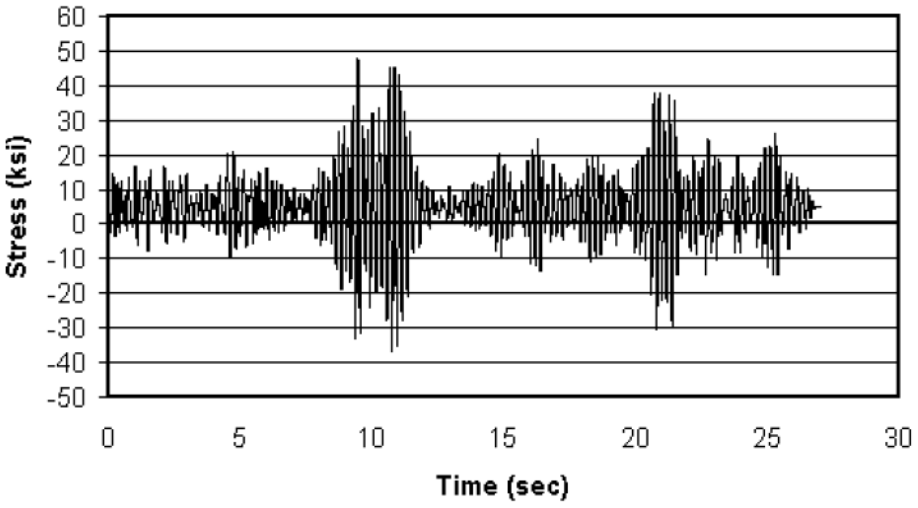

Figure 2.34: Variable-amplitude loading [16].

Figure 2.34 contains a variable-amplitude loading spectrum. Variable-amplitude tests can be divided into:

- Cumulative damage test - its main goal is to study cumulative damage theory and usually the sequences are more simple;
- Service simulating test - these tests comprehend a more elaborate pattern which is similar to service conditions.

2.2.6.2 Specimens or Full Scale Tests

Methods of fatigue testing can also be classified based on the nature of the test-piece. Test pieces are divided into two categories:

- *Specimens*

  A test-piece of small size with a simple shape (standardized) is used. There are different types of fatigue test specimens, like it can be seen on Figure 2.35. The test-piece has to be carefully prepared and posses an adequate surface finish. The choice of such test-piece does not have to do with costs, but with reducing the variability of the product and to maintain different factors under control [16].

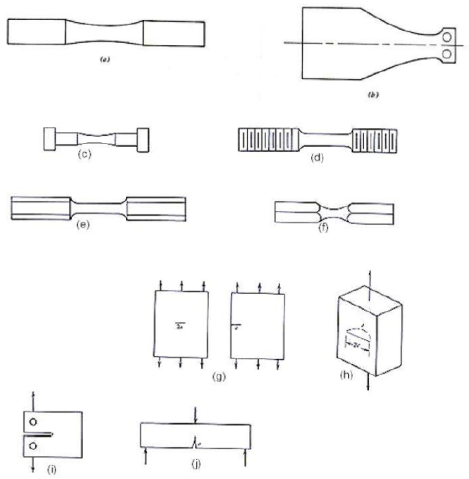

Figure 2.35: Fatigue Test Specimens [16].

Test-pieces are extremely useful for testing the material and collecting its fatigue properties. Nevertheless, these components do not represent the actual component design and fabrication. Therefore, it is also demanding to do tests with full-scale components, exactly as they are used during service [16].

- *Component or full-scale tests*

  Even though these tests are really necessary do conduct in certain cases, they are very expensive and the set-up for doing a full-scale test is much more complex like it can be seen on Figure 2.36. Figure 2.37 presents the results of a full-scale fatigue analysis.

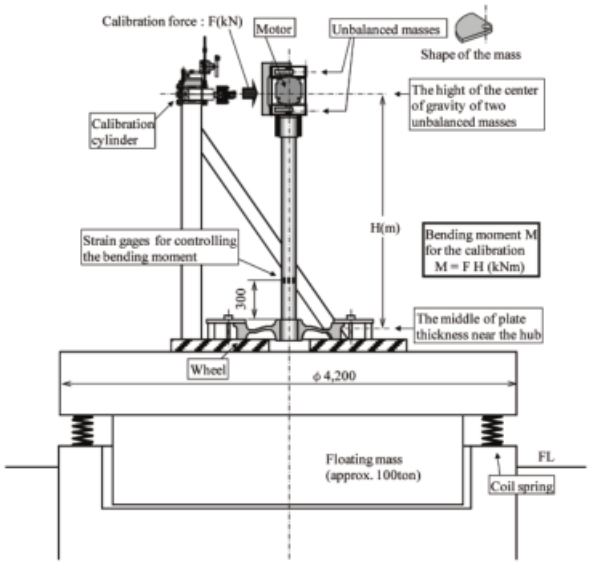

Figure 2.36: Structure of a fatigue testing machine for full-scale wheel and axle assembly [11].

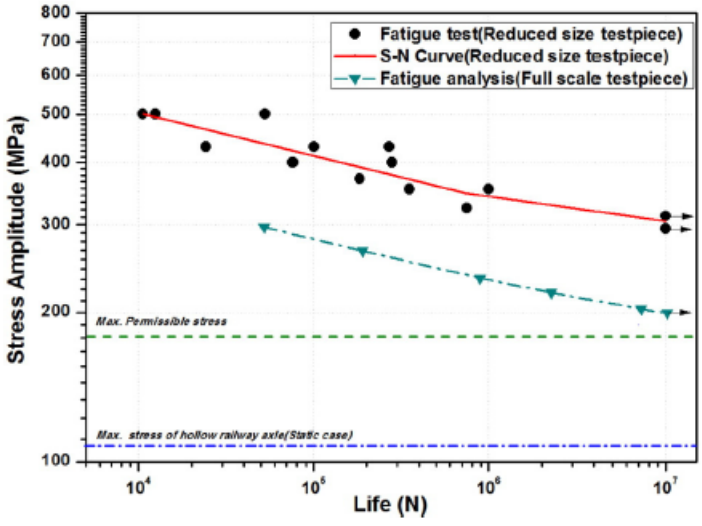

Figure 2.37: Full-scale fatigue analysis result (5% failure) [12].

2.2.6.3 Material/Structural/Actual Service Type Tests

Fatigue tests can also be classified according to the objective of the test:

- *Material type test*

  These tests can be useful for:

  - Comparing the behaviour of different materials subjected to repeated stresses;
  - Understanding the effects of different manufacturing processes;
  - Studying the behaviour of materials in diverse environments;
  - Understanding the influence of geometrical factors such as different sizes and shapes of notches and different surface finishes;
  - Studying the effect of surface treatments on materials' fatigue properties (case-hardening, decarburization, nitriding, shot-peening and plating) [16].

- *Structural type test*

  Structural type tests can be convenient for a comparison of components made from different materials, of different design and fabricated by different procedures [16].

- *Actual service type test*

  Typically, the purpose of these tests is fault finding or verifying a new component in the machine or structure [16].

2.2.7 Fatigue Testing Machines

Fatigue testing machines can be classified according to the purpose of the test (most important one), type of stress, ways of producing the load, operation characteristics, type of load and others [16].

The classifications of fatigue testing machines are the following:

- General purpose;
- Special purpose;
- Equipment for testing parts and assemblies.

In academic environment, general purpose fatigue testing machines are the most commonly used ones. They can be further divided into:

- *Rotating bending machines*

  Rotating beam fatigue tests (Figure 2.38) following the procedures on ISO1143:2010 standard can be used to assess the fatigue limit of the axle material. They are used to generate an S-N curve by turning the motor at constant rotational speed or frequency. In order to lead the specimens to failure, a constant-stationary force is applied on the specimen. Therefore, a constant bending moment is generated. When a stationary moment is applied to a rotating specimen, stress at any point on the outer surface will go from zero to a maximum tension stress. Then, back to zero and after that to a compressive stress [16].

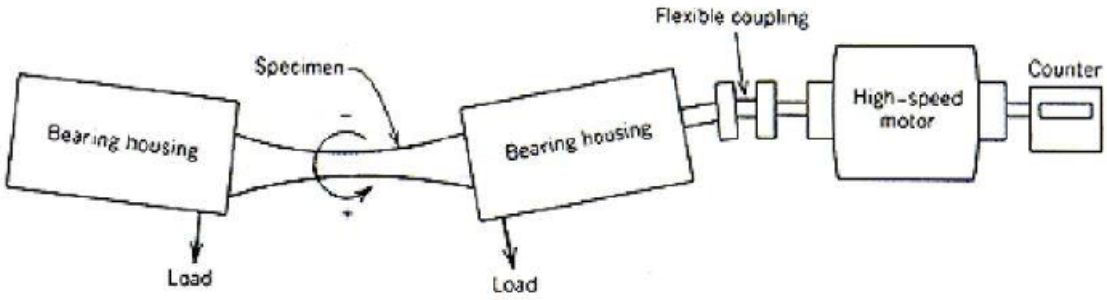

Figure 2.38: Rotating Bending Testing Machine [16].

- *Reciprocating bending machines*

  Have a look at Figure 2.39. A tension-compression and strain controlled fatigue S-N curve is generated. This kind of device is of zero mean cyclic stress [16].

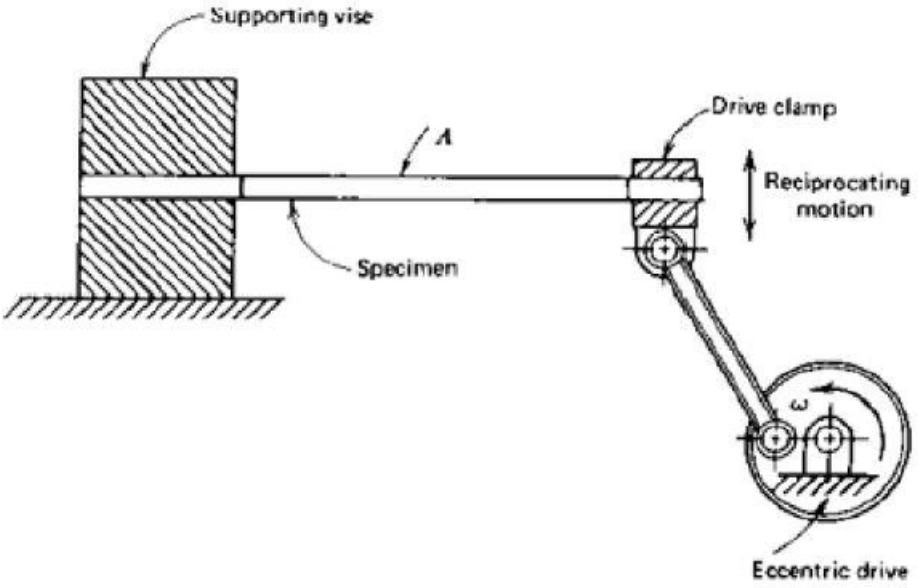

Figure 2.39: Reciprocating Bending Testing Machine [16].

- *Axial loading (push-pull) type fatigue tester*

  The specimen is subject to pure axial loading, tensile or compressive (Figure 2.40). Sometimes these devices can also perform bending and torsion fatigue tests. For this purpose, conversion attachments have to be used. Typically, universal-testers have this characteristic [16].

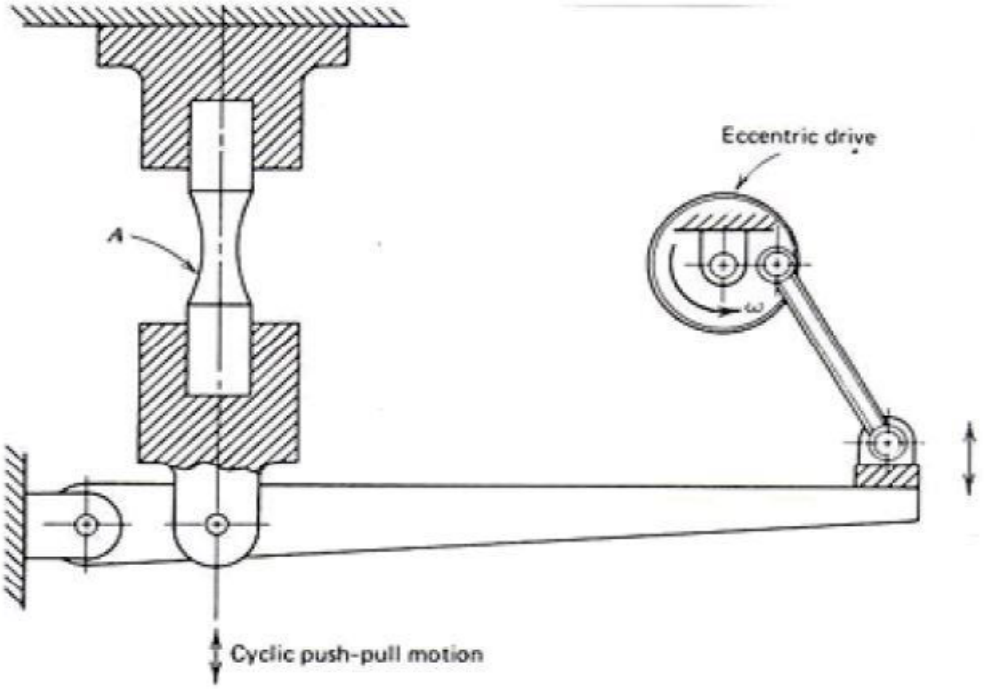

Figure 2.40: Direct-Force Fatigue Testing Machine [16].

Other types of fatigue tests:

- Torsion loading fatigue tester;
- Combined bending and torsion fatigue tester;
- Bi-axial and tri-axial loading fatigue tester [16].

Machines can also be classified according to the principle behind the source of the test-force. Loading can be produced by means of:

- Mechanical deflection;
- Dead weight or constant spring force;
- Centrifugal force;
- Electromagnetic force;
- Hydraulic force;
- Pneumatic force [16].

The choice of the load source relies on multiple factors like the needed frequency, the amount of force required, available control system, cost and how close the test is to be simplified to the actual working loading in service [16].

The components of a fatigue testing machine are the following:

- Load-producing mechanism;
- Load-transmitting member (grips, guide fixtures, flexure joints, ect.);
- Measuring devices to set upper and lower load limits;
- Control devices to control loading throughout the test and automatically correct variations of force/displacement using feedback techniques;
- Counter and shut-off apparatus to count the number of stress reversals and to stop the test after a pre-defined number of cycles, when fracture occurs or at a pre-assigned change in deformation or frequency;
- Framework which supports the various parts of the machine and, if needed, can be set up to reduce the vibrations transmitted to the foundation [16].

2.2.8 Countermeasures for Avoiding Fatigue Occurrence

Techniques such as shot peening, case hardening, and coating can be used to retard the starting of cracks [13].

2.2.8.1 Hardening

Induction hardening can prevent the appearance of fretting damage in axles that are subject to large loads during operation [11].

Residual stresses are elastic tensions that exist in a body without the existence of external loads and temperature gradients. In welded structures, they can achieve very high values. Residual stresses can play a significant role on fatigue behaviour, superimposing to stresses due to external loading (σ_{ext}) and increasing σ_m, the cycle mean stress. Normally, an increase of σ_m leads to a reduction of fatigue life.

Besides increasing the hardness of the axle, induction hardening also produces a large compressive residual stress. Compressive residual stresses restrain the propagation of fretting fatigue cracks by keeping them from opening. The next figure shows the relation between surface residual stress and fretting fatigue limit [11].

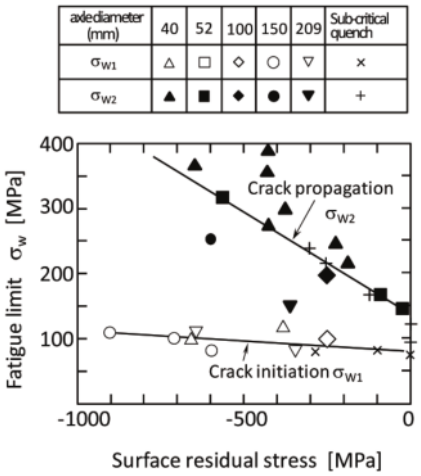

Figure 2.41: Relationship between surface residual stress and fretting fatigue limit [11].

The larger the compressive residual stress, the higher is the value of the fatigue limit for crack propagation (Figure 2.41). Fatigue limit for crack initiation is almost not affected by residual stress [11].

2.2.9 Safe Life and Damage Tolerance Concepts

Design and operation of railway axles are based on a two-stage safety concept that comprehends safe life and damage tolerance methods.

Issues concerning the topic that are important to discuss:

1. Limiting projected lifetime because of events such as damage accumulation, potential very high cycle fatigue and corrosion. A specific concept is the "one-million miles axle". It is based on a worst case scenario including fatigue crack propagation;

2. Improving the reliability of NDT - Probability of Detection (PoD) issues.

Figure 2.42 contains some safety assessment steps for railway axles.

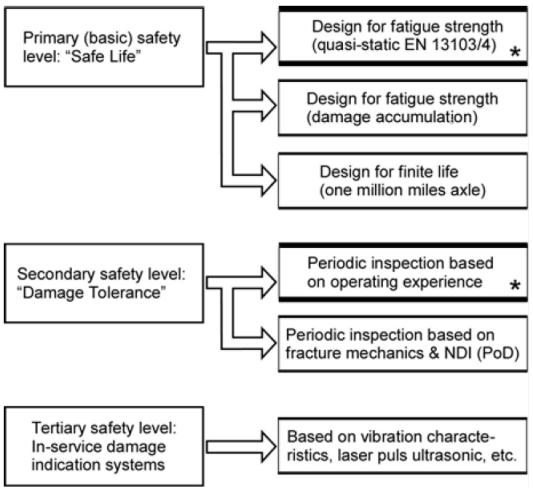

Figure 2.42: Safety assessment steps for railway axles. All options not marked with * refer to present or future development [17].

2.2.9.1 Limiting the Projected Lifetime

The design rules used for rail axles are addressed in the EN13103 and EN13104 standards (see Figure 2.43 (a)). It does not account for a possible reduction of the admissible stresses below the fatigue limit because of VHCF. Also, if corrosion phenomenons are present there might be also some reduction of the admissible stresses but this is not taken into account in the referred standards. Nevertheless, in such cases the standard EN13261 specifies a value of 60% of the maximum admissible stresses on EN13103 and EN13104 standards.

In Figure 2.43 (b), VHCF is taken into account. The fatigue limit is replaced by a sloping curve beyond the knee-point. In the article "Course of SN-curves especially in the high-cycle fatigue regime with regard to component design and safety", Sonsino proposes a change to the fatigue diagram, considering a decrease of 5% per decade loading cycles in logarithmic scales for steels.

In Figure 2.43 (c) a design stress spectrum is compared with an S-N curve with a correction for damage accumulation. Modified Palmgren-Miner rule is used. The drop of the

S-N curve beyond the knee-point is due to damage accumulation and not due to VHCF as it happens for Figure 2.43 (b).

A damage accumulation analysis is employed for obtaining a damage-equivalent constant stress amplitude in Figure 2.43 (d) and this is used like the maximum stress amplitude of Figure 2.43 (a).

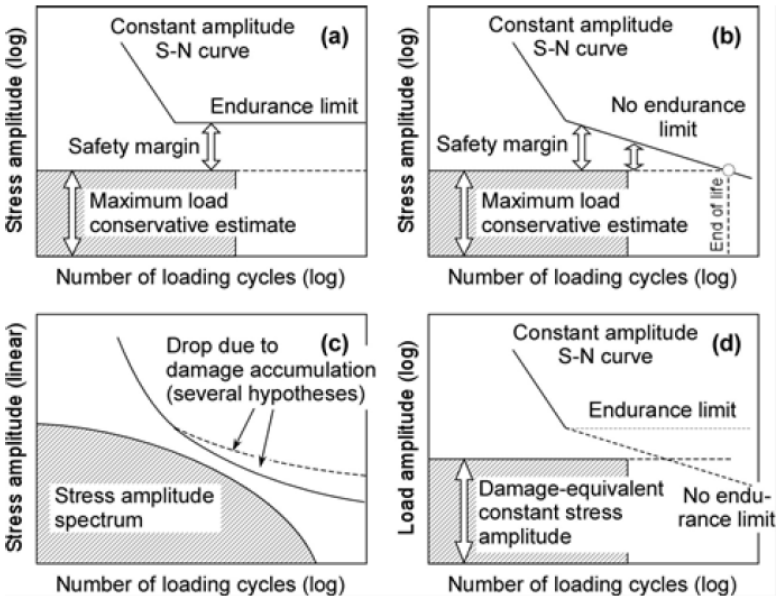

Figure 2.43: Potential concepts of fatigue strength analysis.

2.2.9.2 Reliability Issues of Non-Destructive Testing

Non-Destructive Testing (NDT) can be performed by means of Ultrasonic testing (US) testing or Magnetic Particle Inspection (MPI) testing, for example (Figure 2.44). MPI seems to be the most cost-effective NDT technique for a bare axle (wheels, bearing and brake discs are removed). Nevertheless, risk of scratching during dismantling should be taken into account and fatigue cracks may be initiated and propagate until failure occurs in a shorter amount of time than needed to wear out the wheels. Costly and disruptive axle inspections in between overhauls have to be carried out. Both US and MPI should be used because they allow a compromise between limited intrusiveness and PoD [17].

Ultrasonic inspection types are the following ones:

- Far end scan - inspection from the end of the axle to mid-span or further;
- Near end scan - inspection from the end of the axle to an adjacent seat;
- High angle scan - inspection from the axle body across the seat;
- Inspection from the outer surface in solid axles and from the bore in hollow axles;
- Manual or automatic tests;

- Standard/sophisticated test and analysis methods - phase array, Synthetic Aperture Focusing Technique (SAFT) and others [17].

PoD of a specific inspection becomes larger when cracks are more extended and when the PoD-crack size curve is steeper.

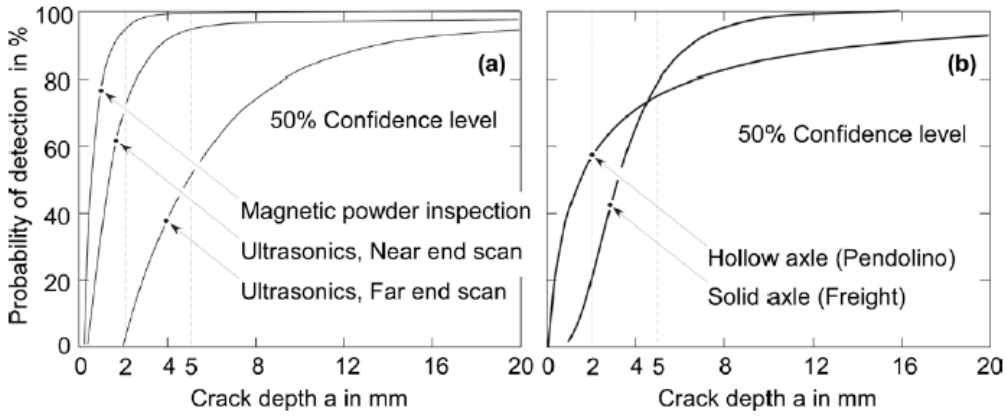

Figure 2.44: Probability of detection (PoD) of cracks as a function of crack depth. (a) Data obtained by magnetic particle inspection and ultrasonic techniques (solid axle); (b) Comparison between ultrasonic near end scan data for solid axles and ultrasonic data obtained from the bore of hollow axles [17].

2.3 A Review on Fracture Mechanics

A fail-safe design for axles is not available. Reviewing and analysing the causes of failure in railway axles can be used to improve axle manufacture and also to improve in service inspection. August Wöhler studied the relationship between material fatigue and fracture/cracks in railway axles [42].

2.3.1 Stress Intensity Factor

The fracture-mechanics-based evaluation assumes that a crack exists and the possibility of propagation of that crack is evaluated by using the Stress Intensity Factor, ΔK.

The stress intensity factor (SIF) is the parameter characteristic of the local stress at the crack tip. This parameter is a function of the crack size, a, of the nominal stress, $\Delta\sigma$, and the adimensional shape function, Y [43].

$$\Delta K = Y\Delta\sigma\sqrt{\pi a} \tag{2.3}$$

The crack size can be measured. The nominal stress can also be evaluated from loads estimations. Therefore, the shape function, Y, is the only unknown parameter. For that, there are two options. Either it is evaluated by finite element modelling (FEM) of the cracked component or by analytical calculations [43].

2.3.2 Crack Propagation

Fatigue crack growth can be divided in three steps (see Figure 2.45). The first step corresponds to the threshold region. The second step corresponds to the Paris region. The third and last step lasts until fracture happens. The three steps are presented below:

- I: Low crack growth rates;
- II: The so-called Paris region, where crack growth can be predicted with the Paris equation:

$$\frac{da}{dN} = C(\Delta K)^m \tag{2.4}$$

  Where a represents the crack length, $\frac{da}{dN}$ is the crack growth, N represents the number of cycles, ΔK is the stress intensity factor (SIF) and C and m are material constants obtained experimentally. The stress intensity factor range, ΔK, is given by:

$$\Delta K = K_{max} - K_{min} \tag{2.5}$$

- III: Unstable crack growth until full fracture.

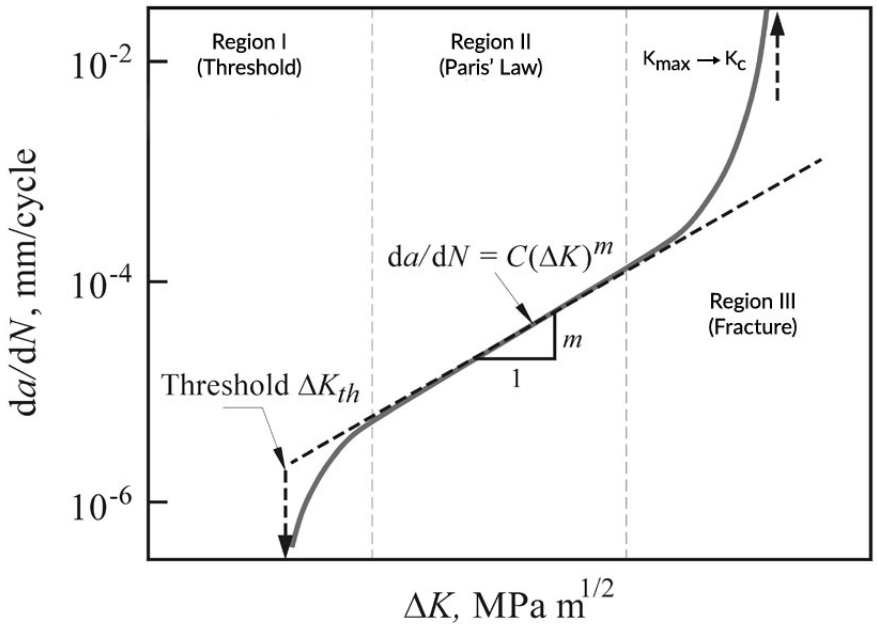

Figure 2.45: Fatigue crack growth rate [18].

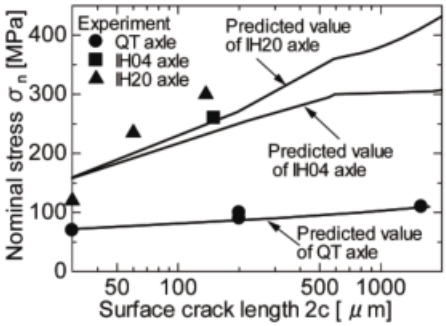

Figure 2.46: Relationships between surface crack length inspected and test stress amplitude [11].

Some conclusions can be drawn from taking a look at Figure 2.46. When nominal stress increases, the crack length increases too. Moreover, induction hardening improves the resistance to crack propagation. It can also be said that the stress required for crack propagation for axles with induction hardening is higher compared with quenched and tempered axles [11].

In the following figure (Figure 2.47), the threshold stress intensity factor range, ΔK_{th}, as a function of crack depth is represented. The threshold stress intensity factor range is basically the range of stress intensity factor that represents the non-propagating limit of crack [11]. It can be seen that ΔK_{th} of microcracks depends on crack size.

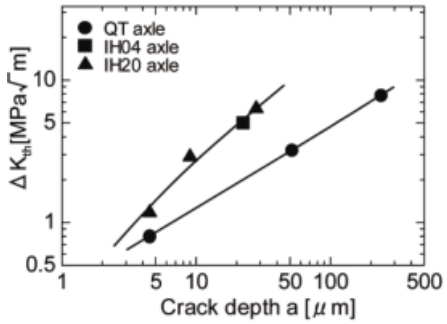

Figure 2.47: Relationship between ΔK_{th} and crack depth [11].

As it was mentioned before, ΔK_{th} increases with the increase in compressive residual stress by induction hardening, for instance. Crack propagates when ΔK is larger than ΔK_{th}, as well as when they are equal to each other. When stress reaches a certain point, ΔK and ΔK_{th} no longer intersect. This critical stress is expected to be the fracture fatigue limit which corresponds to σ_{w2} as shown in Figure 2.48.

Table 2.2 shows that the predicted and experimental values obtained for the fracture fatigue limit agree fairly well.

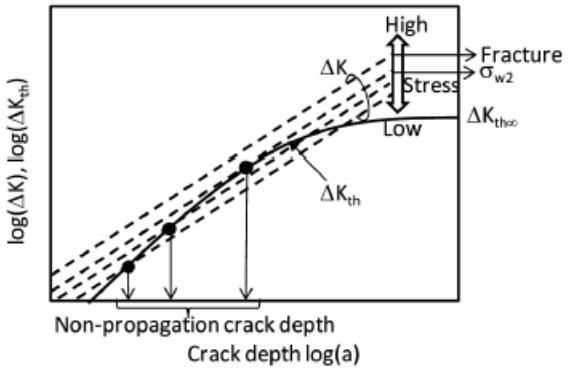

Figure 2.48: Schematic illustration indicating how to predict non-propagation crack size and fatigue limit [11].

Table 2.2: Comparison between predicted and experimental values for the fracture fatigue limit [11].

Class.	Experimental σ_{w2} (MPa)	Predicted σ_{w2} (MPa)
QT	110	110
IH04	270	310
IH20	>320	540

2.3.2.1 LCF Cracks

The fatigue crack initiation period is of major importance. The propagation of cracks can be elimiated by high wear rates between the wheel and the rail. Yet, it is not desirable to have high wear rates. Therefore, there needs to be a balance between LCF cracks and wear rates so that the material is worn right before LCF cracks occur. Besides the interface contact load, wheels exposed to thermo-mechanical cycle loading because of braking can also exhibit LCF [35].

LCF crack initiation can be determined using the Smith–Watson–Topper (SWT) law:

$$\sigma_{max}\varepsilon_a = \frac{\sigma_f'^2}{E}(2N_f)^{2b} + \sigma_f'\varepsilon_f'(2N_f)^{b+c} \tag{2.6}$$

Where σ_{max} is the maximum principal stress in a plane, ε_a is the strain amplitude, N is the number of cycles, E is the Young's modulus, σ_f' is the axial fatigue strength, ε_f' is the axial fatigue ductility coefficient, b' and c' are the fatigue strength and fatigue ductility exponent, respectively.

The Coffin-Manson-Basquin equation can also be used for crack initiation:

$$\frac{\Delta\varepsilon_{EP}}{2} = \frac{\sigma_f'}{E}(2N)^b + \varepsilon_f'(2N)^c \tag{2.7}$$

2.3.2.2 Fretting Cracks

The initiation and propagation of small fretting cracks is highly affected by the microstructure and mechanical properties of the axle steel [13]. The number of cycles to achieve the appearance of the small fretting cracks depends on the following factors:

- Material properties;
- Surface characteristics;
- Press-fitting parameters;
- Dynamic loading conditions.

This means that fretting cracks may nucleate and quickly propagate due to poor machining quality, material defects, improper metallurgical treatments or changes in the service conditions [13]. Results have shown that the initiation of small fretting cracks is driven by the local shear stress and plastic deformations. Though, the effect of shear stress and rubbing between the crack walls reduce as fretting cracks propagate [13].

2.3.2.3 Rolling Contact Fatigue (RCF) Cracks

Shelling, also referred to as tread shelling, is a surface defect that can lead to a subsurface crack and is due to RCF (have a look at Figure 2.49). It is related with the appearance of voids on the surface of trains' wheels. This defect causes high impact force from the non-round portions of the wheel tread and as a result more stresses will be generated. It can be further influenced by a reduction in material strength associated with elevated temperature due to braking.

Figure 2.49: Shelling [10].

2.3.2.4 Inclusions

Non-metallic inclusions can lead to the initiation of fatigue cracks. Inclusions differ from the matrix in multiple aspects:

- Different elastic constants (stiffness mismatch);
- Different strength, different hardness properties and different thermal contraction coefficients [17].

ISO4967 establishes rules for maximum tolerable inclusion dimensions.

2.4 A Review on Probabilistic Prediction Models

In mathematics, a deterministic system is one in which no randomness influences the development of future states of a system. Therefore, a deterministic model always produces the same output no matter the initial conditions.

A stochastic process consists in a family of random variables representing the evolution of a system of numerical values through time. It is the probabilistic counterparty of a deterministic process. For a stochastic process, even though the initial conditions are known, there are multiple (sometimes infinite) possible outcomes.

Knowing the mean value of fatigue limit (with 50% probability of crack initiation) and the standard deviation, the probability of fatigue failure for a particular steel grade can be estimated (see example of Figure 2.50).

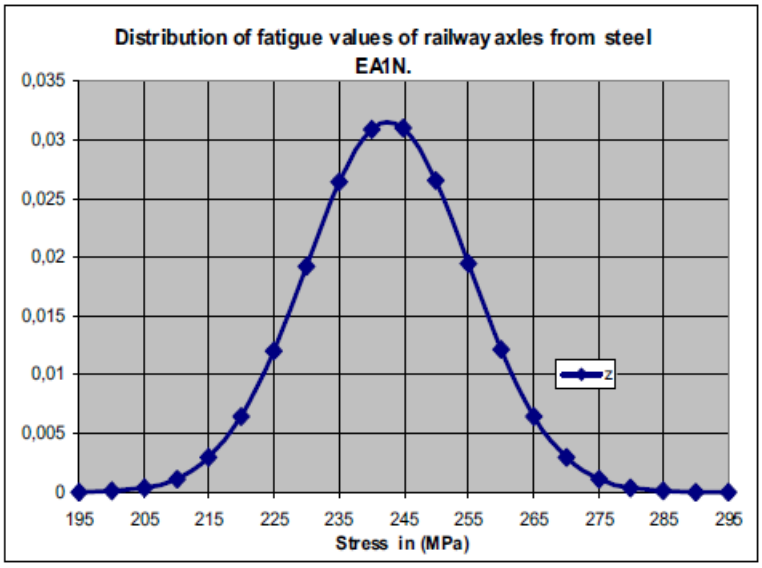

Figure 2.50: Example of distribution of fatigue values of full-scale railway axles from steel EA1N [14].

2.4.1 Bayesian Data Analysis

Nowadays, Bayesian statistics has become very popular. The computational revolution that resulted from the rediscovery of Markov chain Monte Carlo techniques had a very important contribution for this trend. Bayesian statistics allows to satisfactorily combine multiple sources of information into a common model. Therefore, statistical models can be developed even for complex problems [44]. The advantages of Bayesian Data Analysis are the following:

1. Directly tells what are the plausible values for the parameter being analysed;
2. There are no confidence intervals as it focuses only on the central area that contains 95% of distribution;
3. Predictions are easy to make;
4. Suitable for decision analysis, risk analysis and cost-effectiveness analysis;
5. Previous experience/evidence is taken into account [44].

And its disadvantages are the following ones:

1. It requires information about the prior distribution;
2. It allows a quantitative subjective judgement in the analysis;
3. Analysis can be more complex compared to traditional techniques;
4. Computation can be harder;
5. There are no established standards [44].

2.4.1.1 Bayes Theorem

The Bayes Theorem can be expressed by the following equation:

$$P(A|B) = \frac{P(B|A)P(A)}{P(B)} \tag{2.8}$$

Where $P(A)$ is the marginal probability of A, $P(B)$ is the marginal probability of B, $P(A|B)$ is the conditional probability of A given B and $P(B|A)$ is the conditional probability of B given A [44].

Equation 2.9 represents the theorem of total probability [19].

$$P(B) = \sum_{i=n}^{n} P(A_i)P(B|A_i) \tag{2.9}$$

Combining equation 2.8 and 2.9 the following relation is obtained [19]:

$$P(A_i|B) = \frac{P(A_i)P(B|A_i)}{\sum_{i=n}^{n} P(A_i)P(B|A_i)} \tag{2.10}$$

2.4.1.2 Bayesian Inference

One should distinguish between observable and unknown quantities. Data fits in the group of observable quantities. On the other hand, unknown quantities can be statistical parameters, missing data, predicted values and others. In Bayesian inference, probability statements are used to model parameters [44].

Assuming that y represents observed data and θ refers to unknown quantities, the following sampling model where $p(y|\theta)$ is the likelihood function and $p(\theta)$ is the prior distribution can be established [44]:

$$p(y|\theta) \tag{2.11}$$

The full probability model is given by Equation 2.12:

$$p(y,\theta) = p(y|\theta)p(\theta) \tag{2.12}$$

The Posterior distribution for θ is obtained as it is shown in Equation 2.13.

$$posterior \propto likelihood \times prior \tag{2.13}$$

When the prior and posterior come from the same family of distributions, the prior is said to be conjugate to the likelihood.

Assuming that data y_1 is obtained and the posterior $p(\theta|y_1)$ is formed. Then, data y_2 is also collected. The posterior based on y_1, y_2 results:

$$p(\theta|y_1,y_2) \propto p(y_1,y_2|\theta) \times p(\theta) \tag{2.14}$$

As it can be clearly seen, "today's posterior is tomorrow's prior" [44].

2.4.2 Kernel Density Estimation (KDE)

The Kernel density estimation is a non-parametric method to estimate the probability distribution function (PDF) of a random variable. It is used for data smoothing. Being a non-parametric method, it enables less restrictions and less assumptions. The PDF of a Kernel can be written as:

$$\hat{f}(x_i h) = \frac{1}{nh}\sum_{i=1}^{n} K((x-x_i)/h) \tag{2.15}$$

The Kernel function is represented by K and h is associated with the bandwidth.

2.4.2.1 Kernelization for Making Predictions

Kernelization can be a useful tool for building efficient algorithms. This algorithms are obtained with a preprocessing stage that uses smaller inputs called a kernel.

$$y = w^T \phi(x) \tag{2.16}$$

In the previous equation, w refers to a weights' vector and x is the input base feature vector of the test subject. To make predictions, the true nature of ϕ does not have to be obligatory known.

2.4.2.2 Inference of Proportions using a Continuous Prior

Assuming r positive responses out of n patients and considering that patients are independent, with θ being the common response rate, the following equation can be established [44]:

$$p(r|n,\theta) = \binom{n}{r} \theta^r (1-\theta)^{n-r} \propto \theta^r (1-\theta)^{n-r} \tag{2.17}$$

Here, θ is taken as a continuous parameter. If it is assumed that values for θ are equally likely before the data is observed, one has that follows a uniform distribution, $\theta\ Unif(0,1)$.

The posterior can be written as:

$$p(\theta|r,n) \propto \theta^r (1-\theta)^{n-r} \times 1 \tag{2.18}$$

The posterior has a form of the kernel of a Beta$(r+1, n-r+1)$ [44].

External evidence can show that some response rates are more likely than others. Therefore, it is useful to use a Beta(a,b) for the prior distribution [44].

$$p(\theta) \propto \theta^{a-1} (1-\theta)^{b-1} \tag{2.19}$$

Then, the posterior can be re-written as:

$$p(\theta, r|n) = \theta^{r+a-1} (1-\theta)^{n-r+b-1} \propto \theta^r (1-\theta)^{n-r} \tag{2.20}$$

2.4.3 Reliability Analysis

Reliability is basically the probability of a product performing its intended function under specified conditions during a certain period of time [45].

There is always a considerable amount of unknown and uncontrollable factors that result in a large scatter in fatigue life even on test-pieces which would supposedly be similar. Sometimes, the distributions of some random variables is not precisely known. Only intervals are known. In these cases, there is a mixture of random and interval variables [23].

Reliability analysis should use the worst combinations of interval variables. The results from worst case reliability based design (RBD) are more conservative than traditional RBD and the efficiency of these two methods can be said to be the same [23].

In many engineering applications it is too difficult to estimate the reliability of a system. However, it can be easier to estimate the reliability of its components. Knowing the components' reliability and the logical relations between them and the system, systems' reliability can be calculated [19].

The probability of failure is the complement of the reliability (Figure 2.51). Nowadays, reliability can be computationally evaluated with physical equations (models) or computer simulations that specify the state of failure [19].

When the performance reaches a certain value, the state of the component/system changes from safety to failure. The threshold value is called a limit state [19]:

$$Y = g(X) \tag{2.21}$$

If a design has reliability less than required level, conceptually, there are several strategies to improve reliability or decrease the probability of failure [19]:

- Shrinking the distribution;
- Shifting the distribution;
- Both of them.

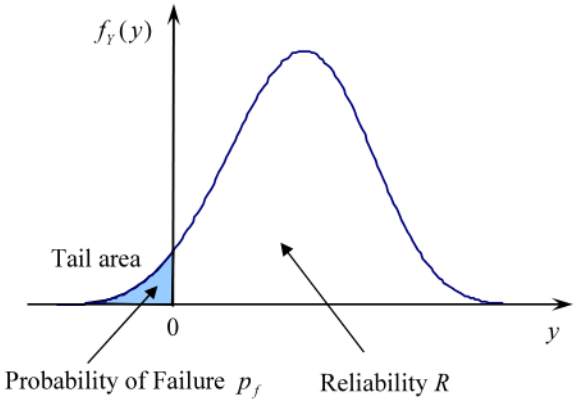

Figure 2.51: Reliability concept [19].

2.4.3.1 Time-Dependent Reliability Analysis by a Sampling Approach to Extreme Values of Stochastic Processes

Almost all engineering systems are both uncertain and time-variant. As so, it is appropriate to use a time-dependent reliability methodology. For example, the material strength can deteriorate with time and the loadings of a structure can also vary with it [19].

In these cases, the limit-state functions change with time. The longer the time interval, the lower the reliability [46].

$$G = g(X, Y(t), t) \tag{2.22}$$

The variable X is of random nature and Y represents a stochastic process. If R represents the reliability, it can be written that

$$R(0, t_s) = Pr\{g(X, Y(t) < 0, \ for\, any\, t \ \in [0, t_s]\} \tag{2.23}$$

The challenges of these methodologies are the following ones:

- The distribution of extreme values of $g(.)$ over $[0, t_s]$ has to be known;
- Monte Carlo Simulation is too expensive;
- The method that is typically used is inaccurate - the upcrossing rate method [47].

The methodology proposed by Hu and Du assumes [47]:

$$G = g(X, Y(t)) \tag{2.24}$$

- Decomposition of Y into Y_R and Y_S:
  - Y_R: Generalized strength variables;
  - Y_S: Generalized stress variables;
- Worst case over $[0, t_s]$ with:
  - Minimum Y_R and maximum Y_S;
- Time-dependent becomes time-independent.

2.4.3.2 Uncertainty Analysis

Uncertainty can be said to be the difference between the present state of knowledge and the complete knowledge (see Figure 2.52) [20].

Uncertainties can be variations in dimensions, material properties and other parameters that do not change with time. On another hand, stochastic loadings vary with time. [46]

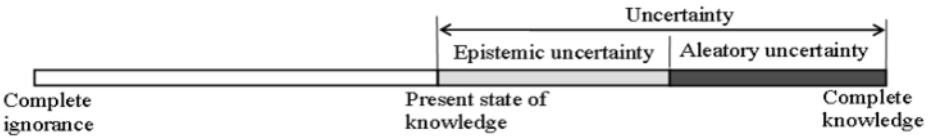

Figure 2.52: Uncertainty [20].

There are different types of uncertainty:

1. Aleatory type, which is related with variation due to randomness;

2. Epistemic type, related with the lack of knowledge [20].

Sometimes is too difficult (or even impossible) to obtain a theoretic or numerical solution. Therefore, an approximation methodology is needed [21].

$$F_Y(y) = Prg(X) < y = \int_{g(\mathbf{x})<y} f_x(\mathbf{x}) d\mathbf{x} \tag{2.25}$$

Given: distributions of input variables **X**

- Joint pdf $f_x(x)$

Find: cumulative distribution function of Y

- $F_Y(y) = Prg(\mathbf{X}) < y$

Figure 2.53 depicts an analysis model for uncertainty analysis.

There are multiple methods than can be used for uncertainty analysis:

1. First Order Reliability Method (FORM);

2. Second Order Reliability Method (SORM);

3. First Order Saddlepoint Approximation (FOSPA);

4. Second Order Saddlepoint Approximation (SOSPA).

Figures 2.54 to 2.57 illustrate the probability of integration in X-space and U-space, respectively.

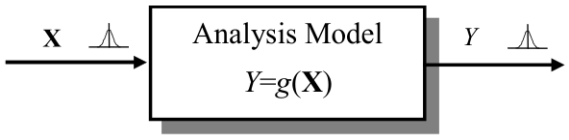

Figure 2.53: Analysis model for uncertainty analysis [21].

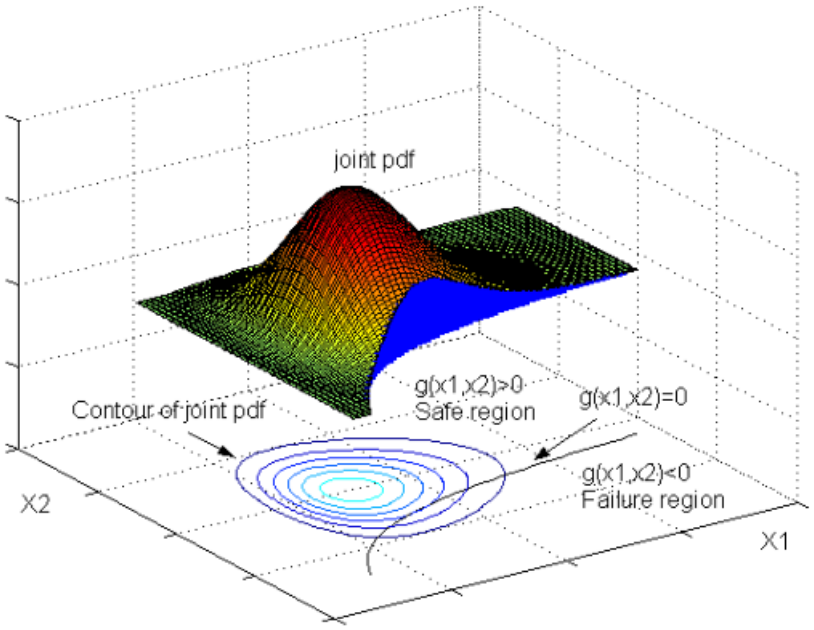

Figure 2.54: Probability integration [21].

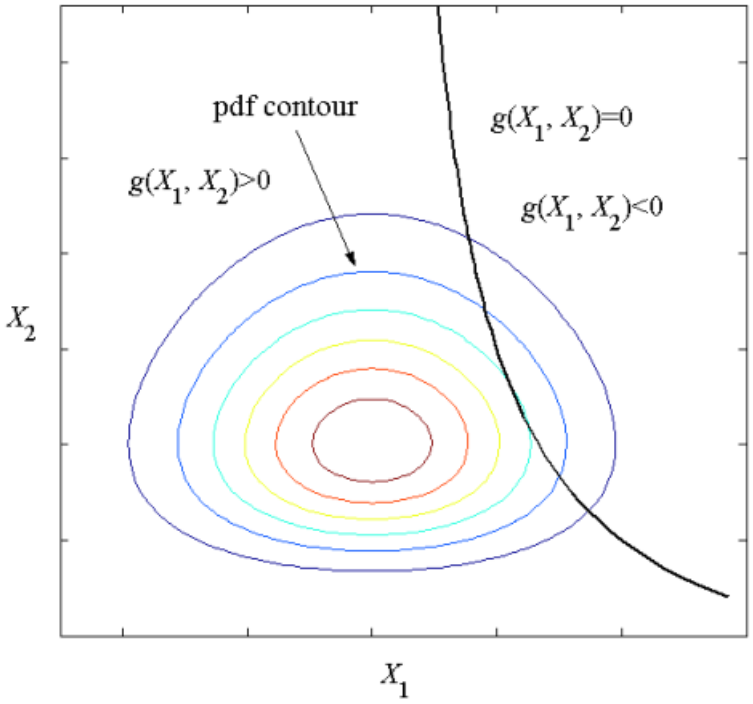

Figure 2.55: Probability integration in X-Space [22].

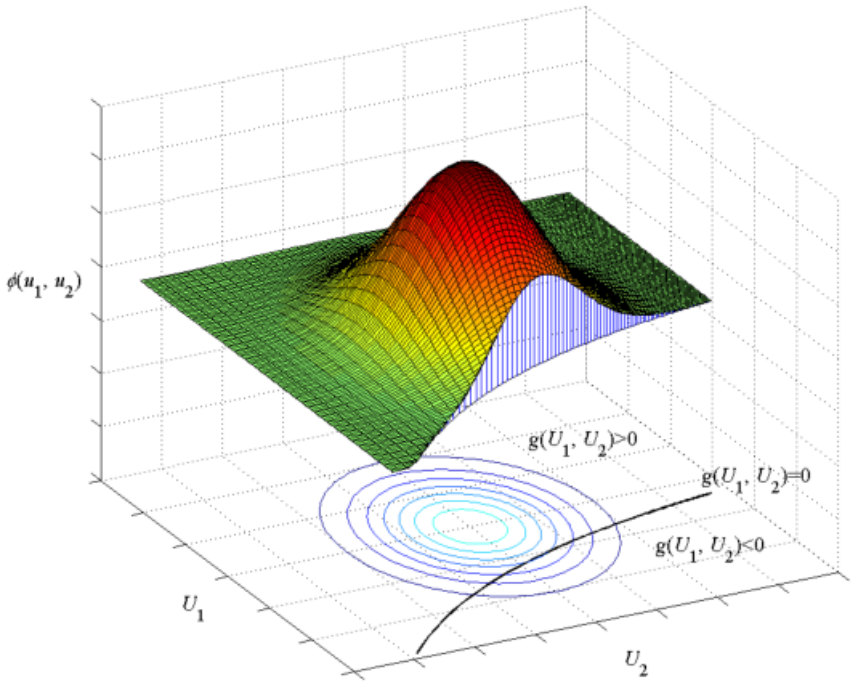

Figure 2.56: Probability integration after the transformation [22].

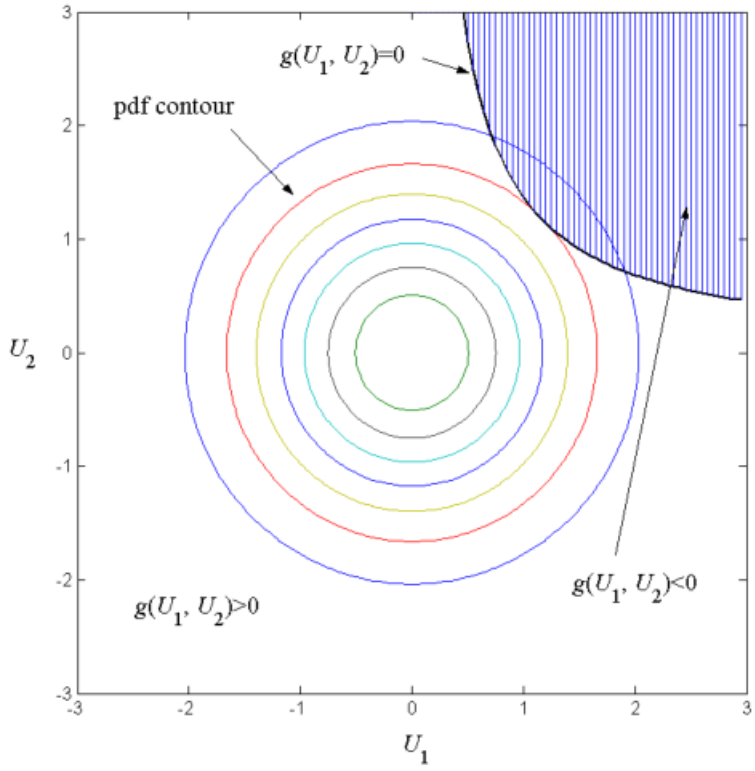

Figure 2.57: Probability integration in U-space [22].

2.4.3.3 Statistical staircase method

Results of fatigue tests can be evaluated by statistical staircase method. According to the original staircase method, the first specimen is subjected to a stress corresponding to the expected average fatigue strength. Then, if the specimen survives 10^7 cycles, it is discarded. The next specimen is subjected to a stress that is one increment above the previous. The increment should be chosen to correspond to the expected level of the standard deviation. If a specimen fails prior to reaching 10^7 cycles, the obtained number of cycles is collected and the next specimen is subjected to a stress that is one increment below the previous one. Following this approach, the sum of failures and run-outs is equal to the total number of specimens. This original staircase method is only suitable when a high number of specimens is available (25 specimens should lead to a sufficient accuracy in the result)[48].

2.4.3.4 Monte Carlo Simulation Technique (MCST)

MCST is typically used when the total number of possible outcomes is too large for computation. The name of this technique is inspired on casinos in Monte Carlo (Monaco), that used similar techniques to understand their profits. It is very useful when multi-variable integration is being done.

2.4.3.5 First Order Reliability Method

Using FORM, the stochastic variables can be the axle load, speed, number of train wagons, volume of traffic per month and material properties of the rail [49]. Figure 2.58 depicts the probability integration methodology in FORM.

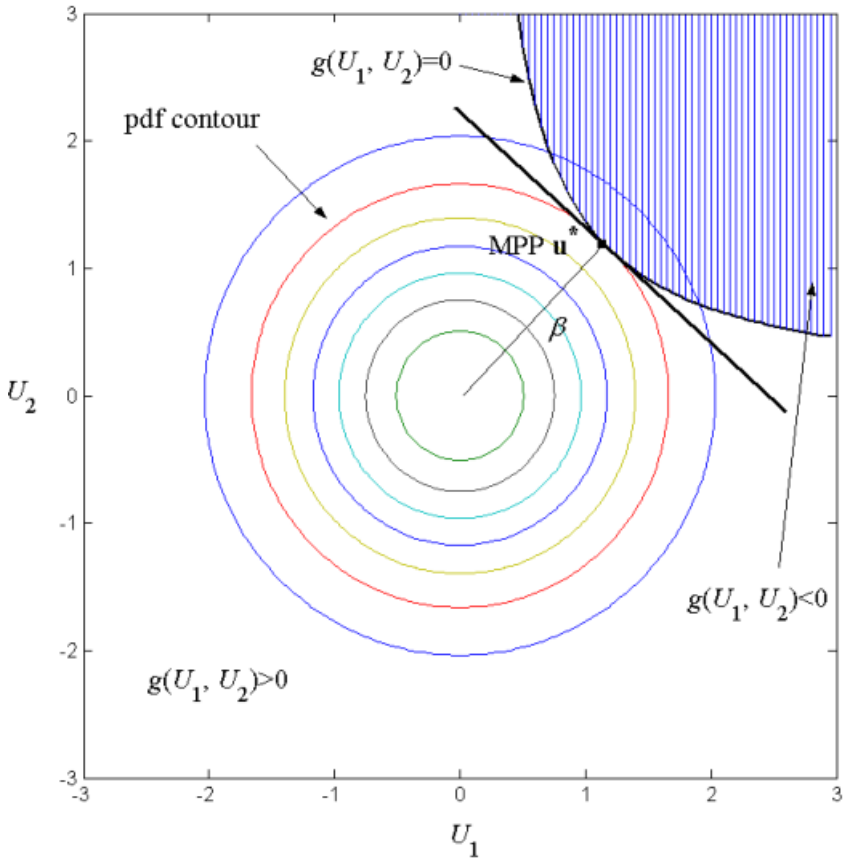

Figure 2.58: Probability integration in FORM [20].

2.4.3.6 Worst Case R-Percentile Performance by FORM

Inverse reliability is a technique that can also be employed. Given reliability R, the corresponding response z can be found.

$$\begin{cases} \text{minimize } \mathbf{u} \text{ and } \mathbf{y}, & g(\mathbf{u},\mathbf{y}) \\ \text{subject to,} & ||u|| = \phi^{-1}(R) \end{cases} \tag{2.26}$$

The variable $\mathbf{u}$ represents random variables transformed from x space to standard normal space. The worst case Most Probable Point (MPP) is represented by u^{MPP} and y^{worst} represents the worst case combination of $\mathbf{y}$. The worst case R-percentile performance results:

$$z^R = g(u^{MPP}, y^{worst}) \tag{2.27}$$

2.4.3.7 RBD Formulation

Reliability based design problems can be solved with single-loop or double-loop procedures. Have a look at Figure 2.59. This is a double-loop procedure [23].

$$\begin{cases} \text{min d}, & \text{h}(\mathbf{d}, \mu_x, \bar{y}) \\ \text{subject to}, & z^{R_i}_{worst,i} = g_i(\mathbf{d}, \mathbf{u}^{MPP,R_i}_{worst,i}, \mathbf{y}_{worst,i}) \geq 0, i = 1,2,...,m \end{cases} \tag{2.28}$$

The objective function is represented by h and **d** represents the design variables.

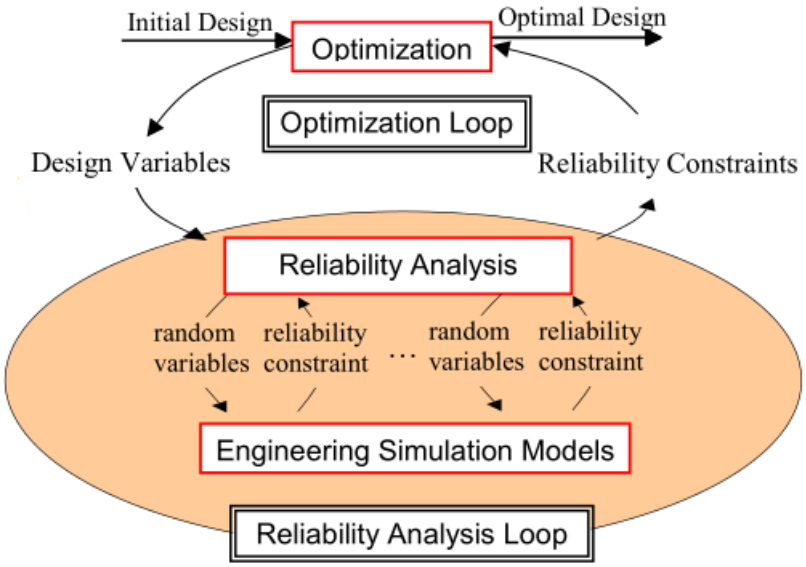

Figure 2.59: Reliability Analysis Loop [23].

2.4.3.8 Sequential Optimization and Reliability Assessment (SORA)

SORA is a single-loop procedure where there is a decouple of optimization from reliability analysis (see Figure 2.60). It is highly efficient [23].

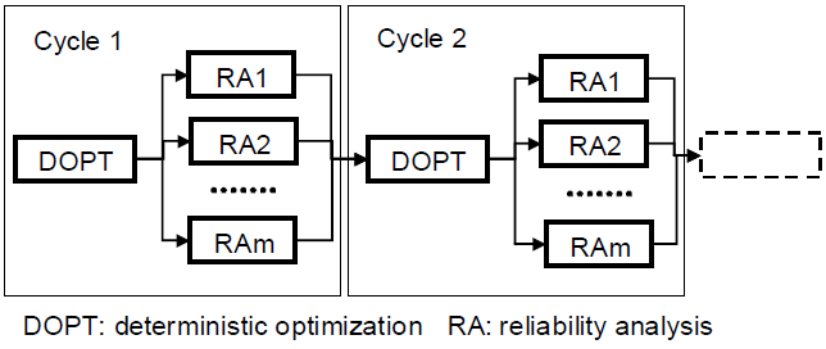

Figure 2.60: Procedure for SORA [23].

2.4.4 Sensitivity analysis

Sensitivity analysis enables to understand how the uncertainty in the output of a mathematical model or system can be split and related to different sources of uncertainty in its inputs. Sensitivity analysis makes possible to identify the most important uncertain variables [20].

2.4.5 Robustness

The robustness of a system/component (Figure 2.61) is the degree to which its properties are not influenced by the uncertainties of input variables or uncertainties of environmental conditions. It measures the insensitivity to parameter variation and uncertainties in environment [19].

Robustness is typically measured with the variance or standard deviation of the performance function $Y = g(\mathbf{X})$ [19].

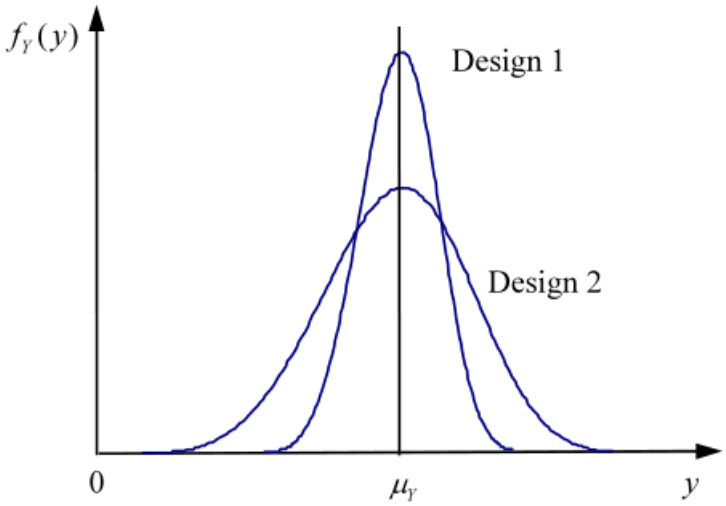

Figure 2.61: Robustness of two designs [19].

Reliability and robustness are conceptually different (Figure 2.62):

- Reliability is concerned with the performance distribution at the tails of the PDF and robustness with the performance distribution around the mean of the performance function;
- Reliability is more related to safety to avoid catastrophic events, while robustness deals with everyday fluctuations and for the avoidance of quality loss [19].

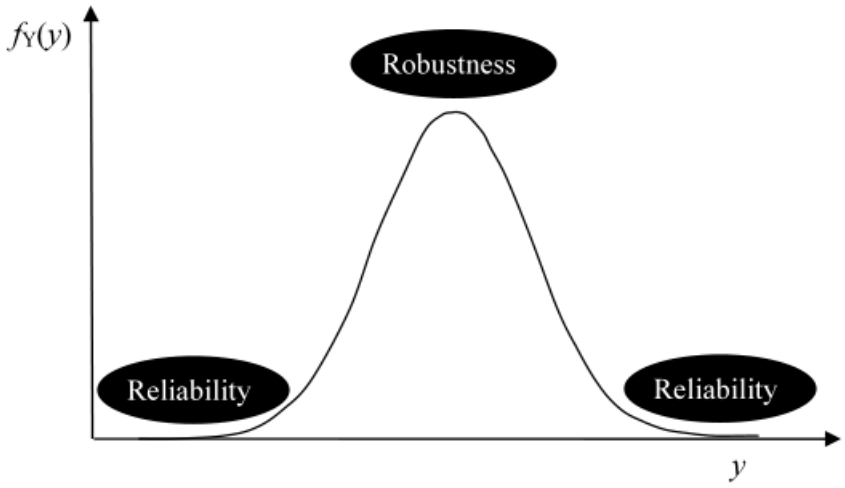

Figure 2.62: Reliability versus Robustness [19].

2.5 Fatigue evaluation of old rail axles design

2.5.1 Introduction

For economic reasons and from the perspective of vehicle fleet management, some old design axles cannot be replaced. Therefore, a fault-tolerant approach is needed. For some cases, it can be said that loads assumed in standards do not fully reflect actual service loads.

The approach developed by *Mazzola et al.* [50] consists in creating a suitable non-destructive testing (NDT) inspection periodicity. A precise evaluation of service loads using multi-body simulation shall be made as well as validated crack propagation models.

According to *Mazzola et al.* [50], all the studied axles were made of 30NiCrMoV12 steel (high strength steel).

2.5.2 Finite element analyses

Normally, the stress calculations involve two steps:

- An axisymmetric model was used to calculate the stresses from the non-linear contact at the interference fit;
- 3D bending stresses were calculated - these stresses result from forces at the bearing journals and are responsible for the dynamic behaviour of the wheelset [50].

A press-fit originates an increase in the mean stress. However, it has no impact on the alternate longitudinal stress component. The SCFs along each fillet were evaluated in a pure bending mode for the two test cases.

Current standards recommend a safety factor of 1.5 for motor axles and 1.2 for non-powered axles.

2.5.3 Fatigue resistances assessment based on current codes

Current standards [31] propose a simple calculation approach. For a generic geometry axle, it considers an equilibrium of the forces acting in the vertical and lateral directions. The effects of traction and braking are taken into consideration in a simplified way. Considerations of EN13104 are the following:

- All contributions for the bending moment are considered except for forces in the longitudinal direction at contact;
- The fatigue limit for the axle body is different from the fatigue limit for wheel seat spots;
- SF equal to 1.5 for motor axles and 1.2 for non-powered axles.

Safety indices lower than one can be encountered. However, the respective railway axles did not fail during more that 30 years of continuous operation. As so, maybe European Standards EN13103/13104 are too conservative [50].

2.5.4 Fatigue analysis and crack propagation assessment - Alternative approach

In order to define an axle's lifetime, two different approaches can be followed:

- Fatigue analysis by means of fatigue damage calculations (simpler one);
- Damage-tolerant lifetime assessment based on crack propagation simulations.

2.5.4.1 Assessment based on fatigue damage

Haibach hypothesis can be followed [50]. A fatigue curve with a knee set at 2×10^6 cycles with slopes k can be assumed for the finite life region. Below the knee, instead of k, $2k-1$ can be assumed.

Damage index for a given stress spectrum:

$$D_{sp} = \frac{n_i}{N_i} \tag{2.29}$$

Axle life:

$$L = \frac{D_{crit}}{D_{sp}} \times L_{sp} \tag{2.30}$$

Where the variable D_{crit} represents the damage index at failure. Values for S_D and k were extracted from Traupe et al. Values of 34CrNiMo6 steel were used because it has fatigue properties pretty similar to NiCrMoV12 steel. Two different values were suggested by *Mazzola et al.* [50] for the damage index - Grubisic and Fischer suggested 0.5 and Hanel et al. suggested 0.3 (more conservative value) [50].

2.5.4.2 Damage-tolerant lifetime assessment based on crack propagation simulations

To calculate the residual lifetime of the axles, a crack propagation algorithm was built by *Mazzola et al.* [50]. In this study, load interaction effects were neglected and Shiratori's weight functions were used.

Stress profiles for rotating bending and residual stresses can be interpolated with the following type of polynomials:

$$\sigma(\xi) = A\xi^3 + B\xi^2 + C\xi + D \tag{2.31}$$

Where ξ is equal to $1 - y/a$, with y representing the thickness of the plate and a the crack depth.

SIF stands for Shiratori stress intensity factor. Terms K_I can be evaluated by interpolating Shiratori's tabular solutions for the four polynomial terms.

$$K_I = AK_3 + BK_2 + CK_1 + DK_0 \tag{2.32}$$

SIF values can be independently determined for the two different stress conditions, rotating bending and press-fit, and then superimposed in order to obtain, at each crack tip, K_{max} and K_{min} (as $DK = K_{max} - K_{min}$). Crack growth rate was afterwards modelled with NASGRO 3.0 propagation equation.

$$\frac{da}{dN} = C\left[\left(\frac{1-f}{1-R}\right)\Delta K\right]^n \times \left((1-\Delta K_{th}/\Delta K)^p / (1-\Delta K_{max}/\Delta K_c)^q\right) \tag{2.33}$$

R is the stress ratio calculated as K_{min}/K_{max}; f is the Newman's closure function; K_c is the fracture toughness; C, n, p and q are material parameters determined by interpolating experimental data and ΔK_{th} is the threshold SIF range.

$$\Delta K_{th} = \Delta K_{th} \times \frac{1}{[(1-f)(1-A_0)(1-R)]^{(1-C_{th}R)}} \tag{2.34}$$

Variable ΔK_{th0} is the threshold SIF range at $R = 0$ and C_{th} is a material parameter.

In the study developed by *Mazzola et al.* [50], the shape of the initial crack was established as being semi-elliptical, with a depth $a_0 = 2$ *mm* and the ratio $a/c = 0.6$. Normally, damage tolerance calculations are carried out considering a defect with a probability of detection (PoD) of 50%. *Mazzola et al.* [50] recognized that their 2 *mm* assumption is conservative, taking into account the fact that the critical sections are not necessarily located near the axle end. The block load sequence was constantly applied up to failure or to an equivalent distance of 10^7 *km*. The braking procedure has a major impact on life predictions. There was no direct correlation between the calculated safety index, which reflects the design procedure of European Standards, and the estimated lifetime predictions based on the simulated loading spectra.

2.5.5 Proposal for a relevant parameter representative of the 'expected service life'

Based on the studies conducted by *Mazzola et al.* [50] a better indicator for prospective service life is the ratio between the maximum SIF and the threshold, here called the propagation index (PI), was proposed.

$$PI = \frac{\Delta K_{max}}{\Delta K_{th,R_{max}}} \tag{2.35}$$

ΔK_{max} is the maximum applied SIF range for the simulated service spectrum considering an initial crack of 1 *mm* and $\Delta K_{th,R_{max}}$ is the threshold SIF.

2.6 Fatigue reliability analysis based on a stress approach applied to a rail fastening spring

2.6.1 Abstract

In the study conducted by *Mohammadzadeh et al.* [24], axle load, speed and material properties are taken as random variables. A dynamically analysis was made for both track and train models so that the displacement throughout time can be obtained. Then, using a FE software, variable amplitude of stresses can be acquired. Rain-flow method and Palmgren-Miner linear damage rule were employed to calculate crack nucleation. FORM and Monte Carlo simulation were used for reliability index estimations. The influences of multiple random variables on the probability of failure is verified through sensitivity analysis. Results obtained by *Mohammadzadeh et al.* [24] demonstrate that the equivalent stress range and the material parameter have a significant influence on fatigue crack nucleation [24].

2.6.2 Introduction

Spring clips usually allow a flexible connection between rail and sleepers (a sleeper, also known as railroad tie or crosstie, is a rectangular support for the rails which is normally placed perpendicular to them). Spring clips also enable to suppress vibrations generated by traffic impacts and preserve the transverse slope and track gauge in acceptable tolerance. They can be classified as rigid or elastic types depending on their flexibility [24]. Figure 2.63 shows a Vossloh spring clips-type SKL14.

Figure 2.63: Vossloh spring clips-type SKL14 [24].

Reliability analysis is relevant when there are random and cyclic excitations caused by traffic loading. In this article, a reliability analysis of spring clips subject to fatigue loads is made.

2.6.3 Problem definition according to *Mohammadzadeh et al.*

In the studied developed by *Mohammadzadeh et al.* [24], cycle counting with rain-flow method was implemented over the stress-time history. The rain-flow counting algorithm was used for fatigue analysis. It allows the conversion of a spectrum of varying stress into an equivalent set of simple stress reversals. A reasonable probability space shall be obtained and then a stress probability distribution. The associating S-N curve and a Miner cumulative damage rule are used for fatigue damage estimations [24].

Fatigue stresses, fatigue strength parameter, critical value of cumulative damage index and the error factor applicable in random loading were taken as random variables. FORM and MCS techniques were employed for reliability analysis (Figure 2.64). Then, influences of these variables on the probability of failure were studied by means of a sensitivity analysis [24].

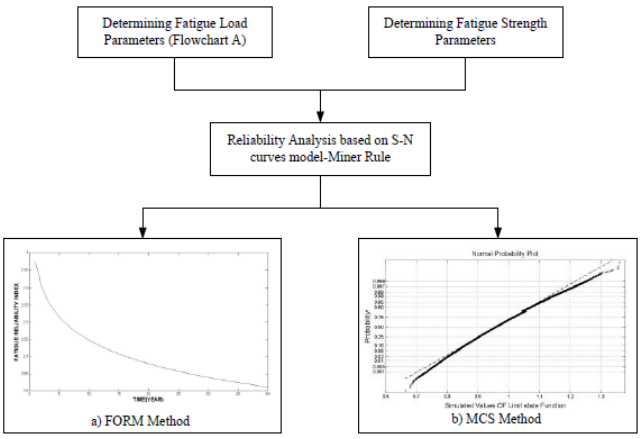

Figure 2.64: Flowchart for the determination of the reliability index using FORM and MCS methods [24].

2.6.4 Numerical analysis of spring clip type Vossloh SKL14

The variables that most significantly affect the stress values in spring clips are the following:

- Train speed (Figure 2.3);
- Axial load (Figure 2.3);
- Number of car-bodies;
- Roughness of the rail and wheel;
- Ballast stiffness [24].

Table 2.3: Probability distribution of speed and axial load in Iranian stations [24].

Random variable	Probability Distribution	Mean	Standard Deviation
Speed(m/s)	Normal	14.09	2.53
Axial load(kg)	Lognormal	22500	3750

2.6.5 Fatigue Reliability Analysis

Variable L represents loading and variable R represents resistance. If the random parameters match with L and R, the limit state function (LSF) can be written as:

$$g(Z) = R - L \tag{2.36}$$

The LSF establishes the boundaries between safety and failure modes. The probability of failure can be expressed by:

$$P(f) = P(g(Z) < 0) \tag{2.37}$$

Reliability index β can be written as:

$$\beta = -\Phi^{-1}(P(f)) \tag{2.38}$$

Φ^{-1} is the inverse standard normal distribution function (CDF). In the work developed by *Mohammadzadeh et al.* [24], the limit state function was formed by a stress based concept in order to evaluate the probabilistic analysis of fatigue life under random loading. The data of the stress range histogram was collected by rain-flow counting method from results of FEM analysis (see Figure 2.65). The equivalent stress range histogram was obtained using the Weibull and log-normal PDF [24].

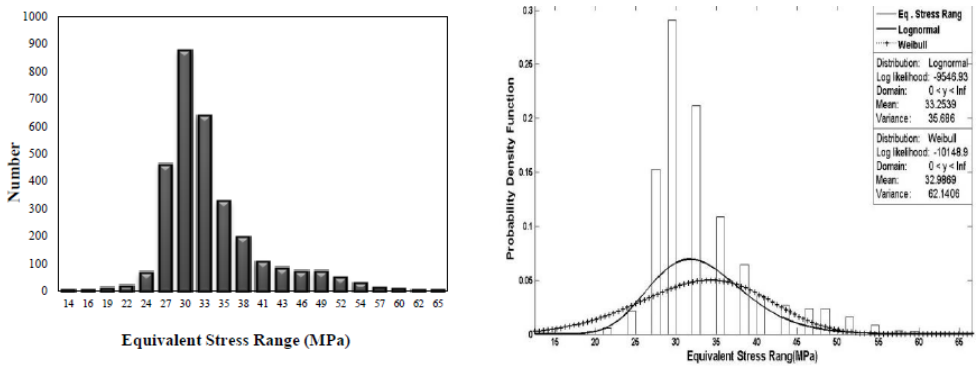

Figure 2.65: Histogram of equivalent stress range fitting process with PDF [24].

Basquin's relation is utilized to predict fatigue life as follows:

$$A = N_f S^m \tag{2.39}$$

Estimation of fatigue damage is assumed to follow the cumulative damage Miner method is given by:

$$D_i = \frac{1}{N_{fi}} \tag{2.40}$$

Where N_{fi} represents the number of cycles to failure at stress range S_i. In this way, the damage rule is represented by:

$$D = \sum_{i=1}^{n} \frac{1}{N_{fi}} = \sum_{i=1}^{n} \frac{S_i^m}{A} \tag{2.41}$$

Stress range is a random variable. Therefore, $\sum_{i=1}^{n} S_i^m$ is also of random nature. If n is enough large, the uncertainty associated with $\sum_{i=1}^{n} S_i^m$ becomes very small. As so, the following relationship can be established:

$$E\left[\left|\sum_{i=1}^{n} S_i^m\right|\right] = E[n]E[S_i^m] \tag{2.42}$$

$$D = \frac{1}{A} E[n]E[S_i^m] \tag{2.43}$$

Failure occurs when the summation of damage approaches a critical value of Δ.

$$g(X,t) = \Delta - eD \tag{2.44}$$

For the authors of this paper, *Mohammadzadeh et al.* [24], Δ is the critical cumulative damage index and e is the error factor applicable in random loading.

$$g(X,t) = \Delta - e\frac{nS_{re}^m}{A} \tag{2.45}$$

In this research, if sufficient information is not available, log-normal distribution with mean value of 1 and coefficient of variation (COV) of 0.3 can be reasonable for steel metals (Kwon and Frangopol, 2010; Ayala-Uraga and Moan, 2007). Variable A is a fatigue based coefficient which contains all the uncertainty values in simulation. As so, its COV was assumed to be very large. So, this value is obtained from the empirical data (Bannantine et al., 1990). The equivalent stress range was obtained using the histogram and results:

$$S_{re} = \left[\sum \frac{n_i}{N_{Total}} S_{ri}^m\right]^{\frac{1}{m}} \tag{2.46}$$

Table 2.4 contains the probability distribution of random variables with the respective mean and COV.

In this research work, FORM and Monte Carlo simulation were two different approaches that could be used to determine the reliability index.

Table 2.4: Probability distribution of random variables with the mean and coefficient of variation [24].

Random variable	Probability Distribution	Mean (μ)	C.O.V
Miner's critical damage accumulation index(X_1)	Lognormal	1	0.30
Fatigue constant (X_2)	Lognormal	2.33e30 (MPa)	0.50
Error factor (X_3)	Lognormal	1	0.30
Equivalent stress range (X_4)	Lognormal Weibull	33.25 (MPa) 32.98 (MPa)	1.07 1.88

The reliability index of spring clips SKL14 was close to 3 in first operation year (see Figure 2.66). Then, there was a steady fall to 2.65 in 40 years of operation time. Based on survival probability of 95% a target reliability index was set to 1.65. Therefore, the remaining life time of Vossloh spring clips estimated 100 years [24].

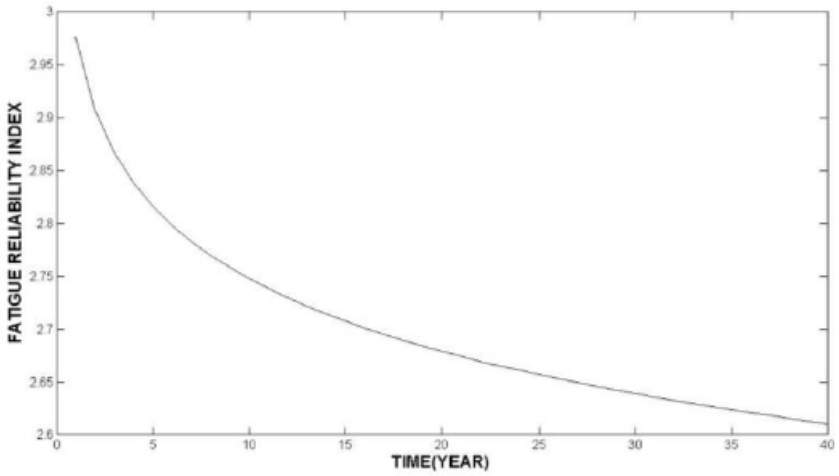

Figure 2.66: Fatigue reliability evaluation of Vossloh type SKL14 [24].

2.6.6 Sensivity analysis

Sensivity analysis was made in order to evaluate influences of random variables on the reliability index (Figures 2.67 and 2.68).

The effect of daily cycle variation was also studied.

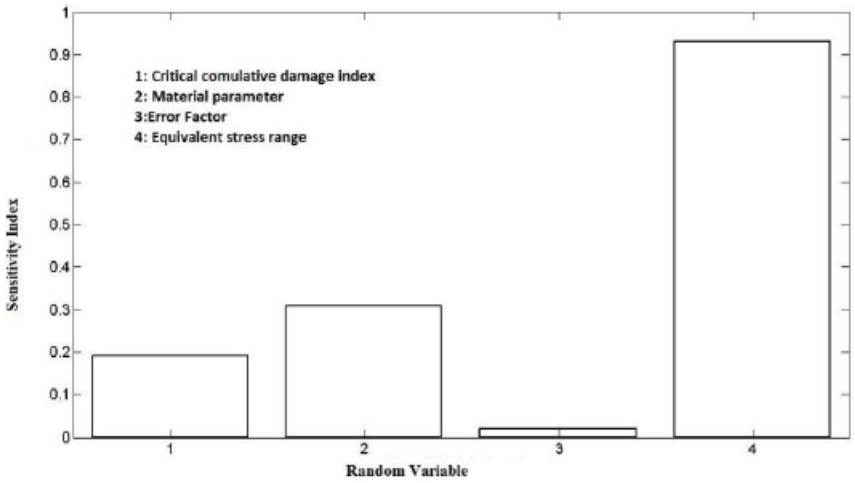

Figure 2.67: Sensitivity Analysis of random variables [24].

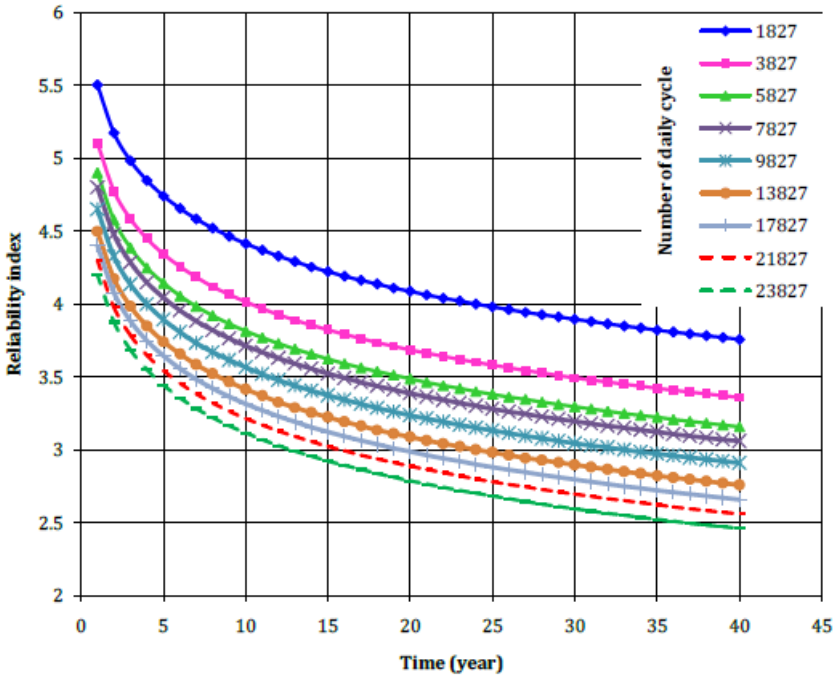

Figure 2.68: Effect of daily cycles variation on the reliability index during lifetime [24].

2.6.7 Conclusion

In the work presented by *Mohammadzadeh et al.* [24], the conclusions that were drawn were the following.

- The equivalent stress range follows a log-normal distribution function;
- It was found that the value of reliability index decreased from 3 to 2.6 for 40 years of operation and fatigue life can be expected as infinite;
- Based on the conducted sensitivity analysis, between the four random variables, the equivalent stress range has proved to have the largest influence on the reliability index;
- With an increase of the number of daily cycles from 1828 to 23828 the reliability index value drops from 5 to 4.30 in the first year of operation.
- With an increase of the equivalent stress range from 30 to 80 MPa, the reliability index decreases from 7 to 2 in the first year of operation.

2.7 Fatigue performance and residual life of railway axles with inside axle boxes

2.7.1 Introduction

In the research conducted *by Wu et al.* [25], an intercity railway system was studied, where the axle boxes placed on the axle leaded to a noticeable difference in the longitudinal stress distribution. This way, standardized strength design method and operation maintenance were recommended to be retaught and updated in order to consider the possibility of inside axle boxes based wheelsets [25]. The total lifetime from an evolved semi elliptical crack (aspect ratio $a/c = 0.8$) located at the middle of the axle was numerically acquired by means of a newly-proposed crack growth model - LAPS.

2.7.2 Material characterization

The microstructure of steel EA4T that is showed on Figure 2.69 is mixed. A mix of lamellar bainitic and lath martensite from the mid-thickness region of hollow axles according to EN13261. It has a hardness of approximately 206HV and slightly conservative properties. Average grain size is 7.2 μm. Having fined grains normally implies a good deformation capacity and good fatigue short crack resistance. As a consequence of fatigue cycles, crack propagates from the notch root. Crack increment Δa and required total cycles N can be recorded.

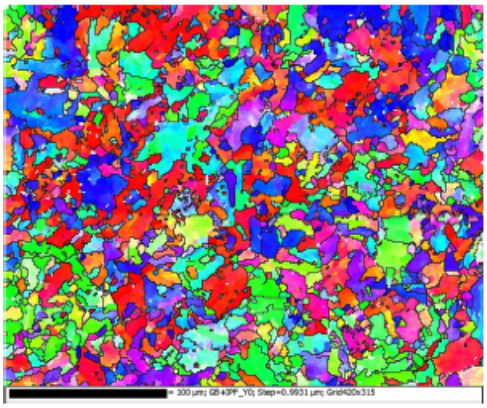

Figure 2.69: Electron backscattered diffraction based grain orientation and texture of EA4T matrix from the mid-thickness axle [25].

2.7.3 Background on fatigue strength and safety

Normally, the fatigue strength and safety are taken into account by:

$$\sigma_{as1} = K_t \frac{32 M_{rbm} D_{ral}}{\pi (D_{ral}^4 - d_{ral}^4)} \leq \frac{\sigma_{lim,rb}}{\eta} \tag{2.47}$$

Where η is a security factor that has to do with uncertainties. Variables α, β, ε and C_{lot} are empirically-determined factors - α for the reliability coefficient, β has to do with surface quality, ε with geometry and C_{lot} with loading type of small-scale specimens.

Scatter denoted by α should be considered to correct the fatigue limit of EA4T specimens. The fatigue diagram with survival probability P_{fal} can be reduced to derive remaining life for equivalent full-scale axles.

$$\alpha = 1 + \phi^{-1}(1 - P_{fal}) CV_{lfs} \tag{2.48}$$

Variable ϕ corresponds to the standard normal cumulative distribution function and CV_{lfs} is the variation coefficient for the fatigue limit at a knee.

Nowadays, it is known that stress levels below the fatigue strength have to be taken into account for fatigue damage issues. They lead to a finite life of materials and structures and must not be neglected. Their contribution is more evident for for VA loading. Giga cycle fatigue should also be considered.

FCG rate curve $da/dN \quad \Delta K$ is used to evaluate residual life and resultant inspection intervals.

The axle is subjected to rotating bending ($R = -1$) which means that a cyclic plastic zone ahead of the growing crack is gradually consolidated prior to unloading. On the other hand, there is a load interaction phenomenon that appears due to complex dynamic stress. This phenomenon induces local plasticity close to the crack tip. A crack opening function f can be employed to modify ΔK and ΔK_{th} so that the plasticity-induced crack closure

effect can be contemplated. Figure 2.70 contains the wheelsets configuration, finite element meshes and loaded locations of a railway hollow axle with inside axle boxes. Variable f is a Newman function.

Critical crack depth or the stopping criterion for the damage tolerance are 25 *mm* or risky 50% of net cross section in the simulation.

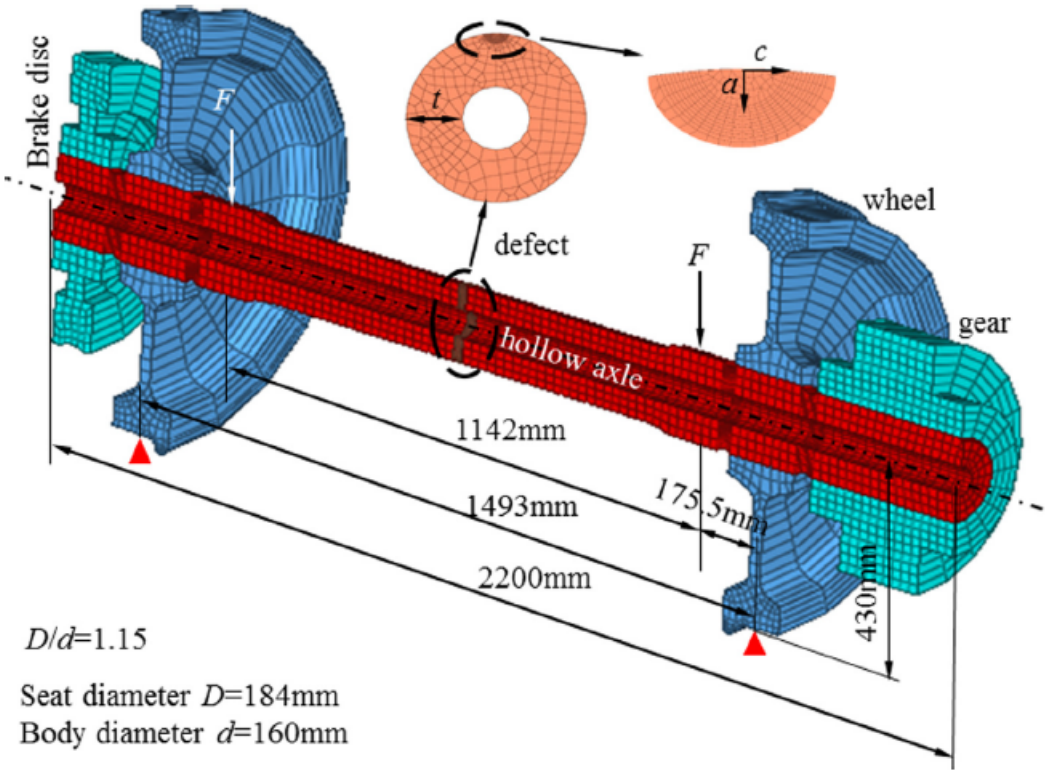

Figure 2.70: The wheelsets configuration, finite element meshes and loaded locations of railway hollow axles with inside axle boxes in case of a defect [25].

In the study conducted by *Wu et al.* [25], it was found that placing axle boxes between two wheels can lead to better dynamic and curve performance. A presumed crack was assumed exactly at the middle of the hollow axle or free body, clearly far way from the stress concentrated region and press fits. It was understood that an acceptable or constant SIF prediction could be nearly acquired with an element size around the crack tip between 1–10% of the evolved crack depth.

In the study conducted by *Wu et al.* [25], boundary conditions to constrain the two wheels were also of extreme importance. They can allow a perfect attachment between the axle and components connected to it - wheels, gears and disc. Vertical loading F was restrained at the middle plane of the bearing journals. In this study, lateral and brake loads were not taken into account due to the track excellent conditions. Vertical load F series conjugates different stress levels that might or might not exceed fatigue limits (VA loading). A 5-stage load spectrum was assumed (Figure 2.71).

Crack closure phenomena can happen very often. Also, parts of the central axle can be subjected to fully reversed loading. All these factors can lead to an increased crack growth resistance partially from the overload. This way, FCG models have to consider fatigue crack closure correction. The main contribution of loading levels is that the extreme loads can easily retard the initiation of a small cracks (even if load frequency is relatively small).

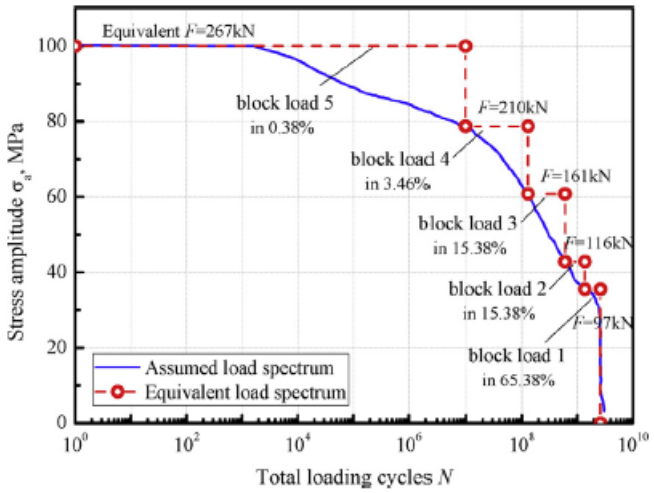

Figure 2.71: Definition of a selected 5-stage block loads used into fracture mechanics assessment corresponding to different service conditions [25].

2.7.4 Results and discussions

Critical stress range had to be determined. It is widely known that the stress relief groove and the geometrical transition are the critical areas. For low carbon steel axles used by Shinkansen, the critical safety section is at the wheel seat (because of small diameter ratio). For classical axles with press-fits and outside axle boxes, the critical safety region of the axle was at the transition between the wheel and the gear seat (peak load of 267 kN), as it can be recognized by taking a look at Figure 2.72. For inside axle boxes, the peak stress region was always at the central area of the axle. It has been shown that because of external axle boxes, critical stress location is caused by an integrated action from rotating bending and press-fit loading, whereas for internal axle boxes the press-fit component does not have a significant contribution. Different fatigue strength for different axle zones should be specified when designing an axle [25].

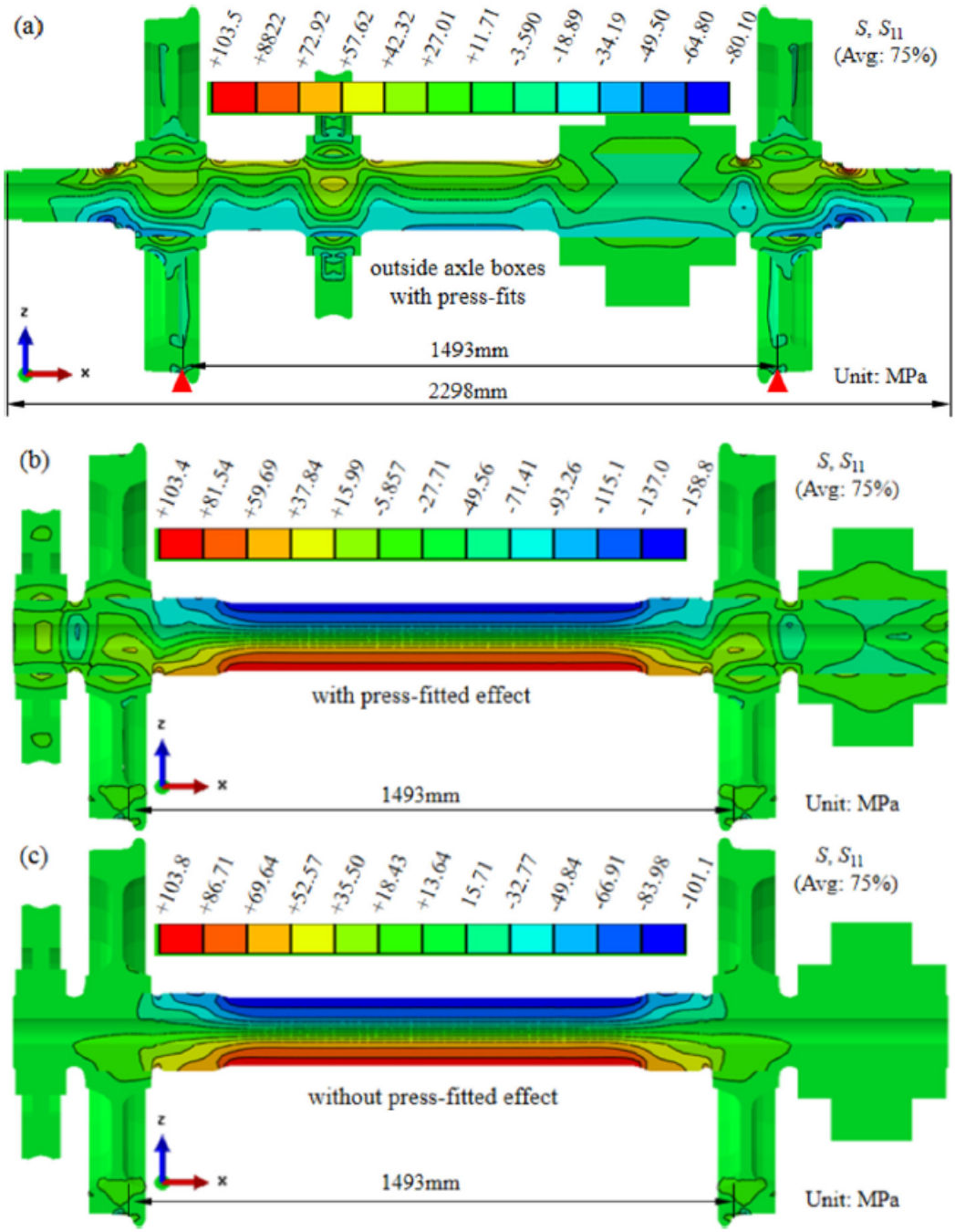

Figure 2.72: Longitudinal stress plots under the same peak loading. (a) for the classical axle with press-fits, (b) and (c) for the assembled inside axle boxes with and without press-fits [25].

2.7 Fatigue performance and residual life of railway axles with inside axle boxes

Fatigue performance can be evaluated by means of axial tension-compression and rotating bending fatigue tests (see Figures 2.73 and 2.74).

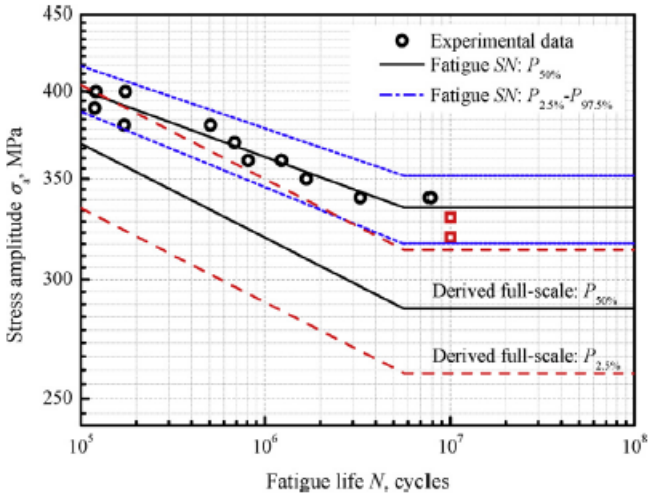

Figure 2.73: Axial TC fatigue SN curves with the failure probability of 2.5%, 50% and 97.5% for small-sized and derived full-scale EA4T specimens [25].

Statistical results of axle failures also showed that the majority of axles failed at surface flaws before the estimated 30 years of service life.

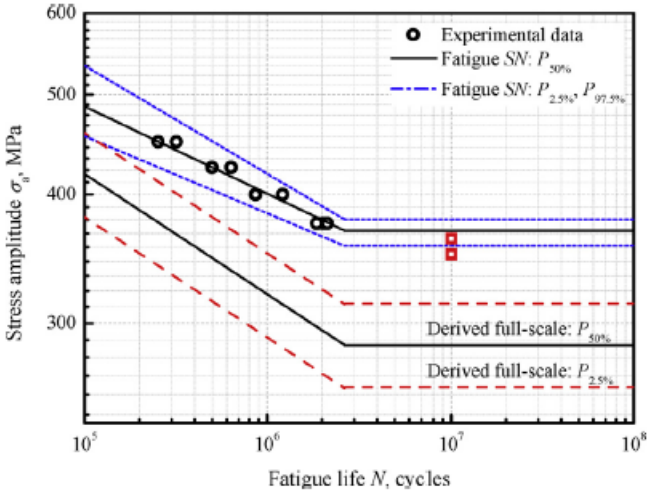

Figure 2.74: RB fatigue SN curves with the failure probability of 2.5%, 50% and 97.5% for small-sized and full-scale EA4T specimens [25].

LAPS and NASGRO were found to estimate well the fatigue crack growth near the threshold region, even though LAPS prediction can be slightly conservative. Moreover, NASGRO can sometimes accumulate a considerable life error as it can be seen in Figure 2.75.

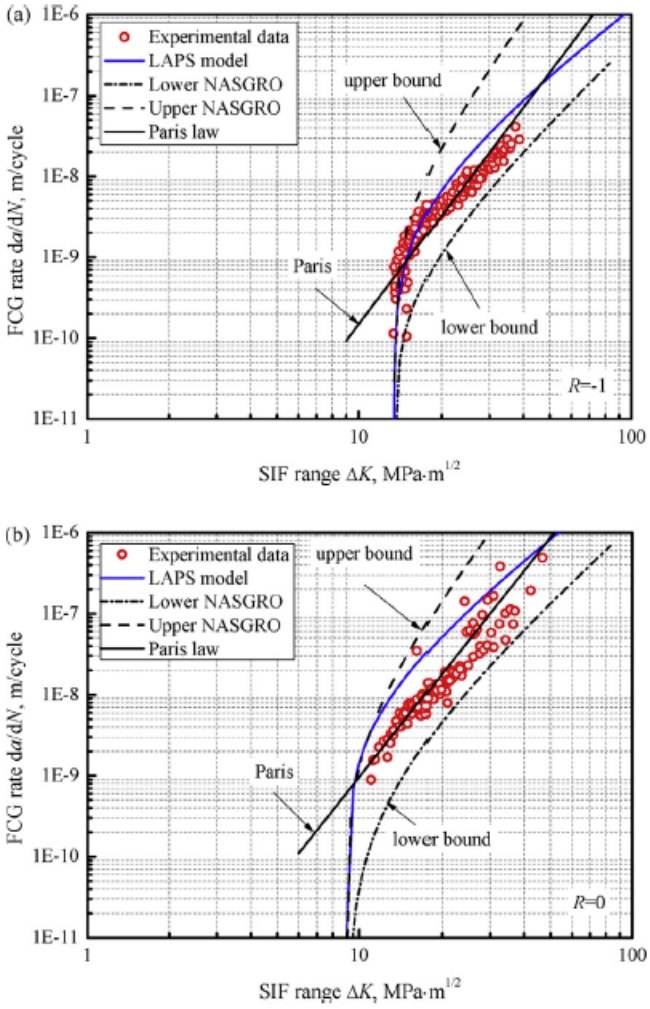

Figure 2.75: Comparisons of predicted FCG curves via LAPS, NASGRO and classical Paris with those of experimental data of EA4T steel grade: (a) under R=-1; (b) under R=0 [25].

In the research conducted by *Wu et al.* [25], the critical crack dimension can be estimated by:

$$\alpha = \frac{1}{\pi}\left(\frac{2\Delta K_{th,lc}}{F \cdot \sigma_{a,th}}\right)^2 - \alpha_{0,H} \tag{2.49}$$

2.8 Fatigue crack growth of railway axles

Experimental works on fatigue crack growth of railway axles were conducted by *Luke et al.* [26]. So, the range of stable crack propagation and near the threshold were experimentally determined for 25CrMo4 (EA4T) and 34CrNiMo6+QT axles. These axles were heat-treated. Experiments were conducted under constant amplitude and variable amplitude loading. Most of the loading cycles were fully reversed cycles with $R = 1$. Obtained results can be used for predicting fatigue crack growth in shafts and in a fillet zone near a press fit [26].

Figures 2.76 and 2.77 present a fracture mechanics assessment concept and a scheme of loading conditions of a railway axle, respectively.

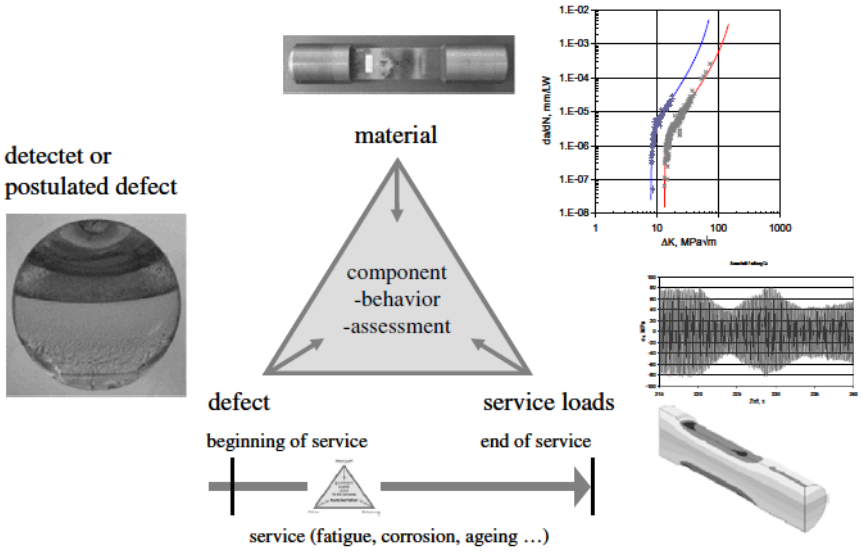

Figure 2.76: Fracture mechanics assessment concept [26].

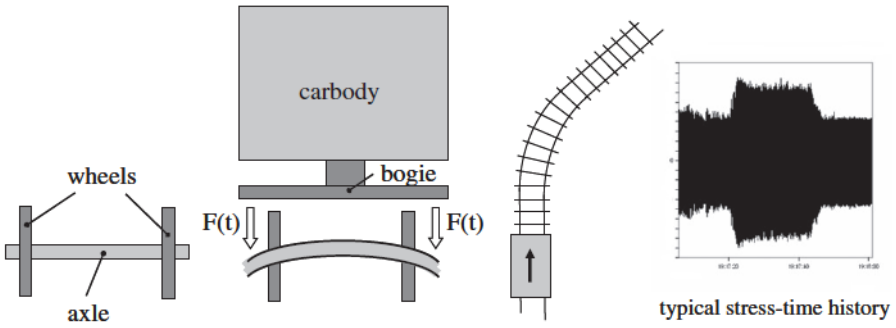

Figure 2.77: Schematic of loading condition for a railway axle [26].

In order to perform fatigue crack growth calculations, stress state in the crack free component has to be obtained. These stresses were linearly distributed across the axle cross

section of the shaft. However, a non-linear stress distribution is obtained for filleted areas where there is a pronounced two-dimensional pattern even in the absence of press-fits (Figure 2.78).

Complexity of a stress state in a fillet increases in the vicinity of press-fits (Figure 2.79).

The R_K ratio is given by:

$$R_K = \frac{K_{min}}{K_{max}} \tag{2.50}$$

R_K typically differs from the stress ratio at the surface and it also varies during crack propagation.

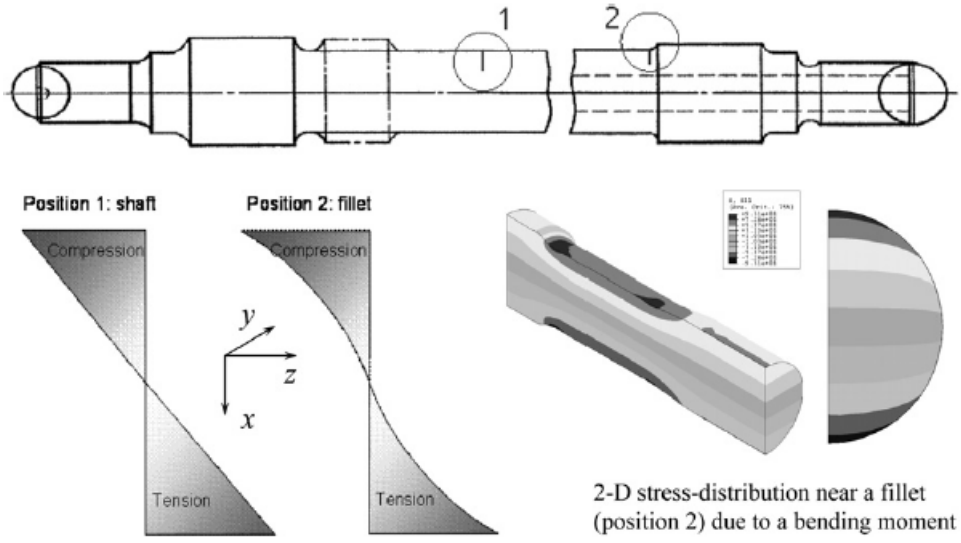

Figure 2.78: Scheme representation of stress distributions at different cross-sections [26].

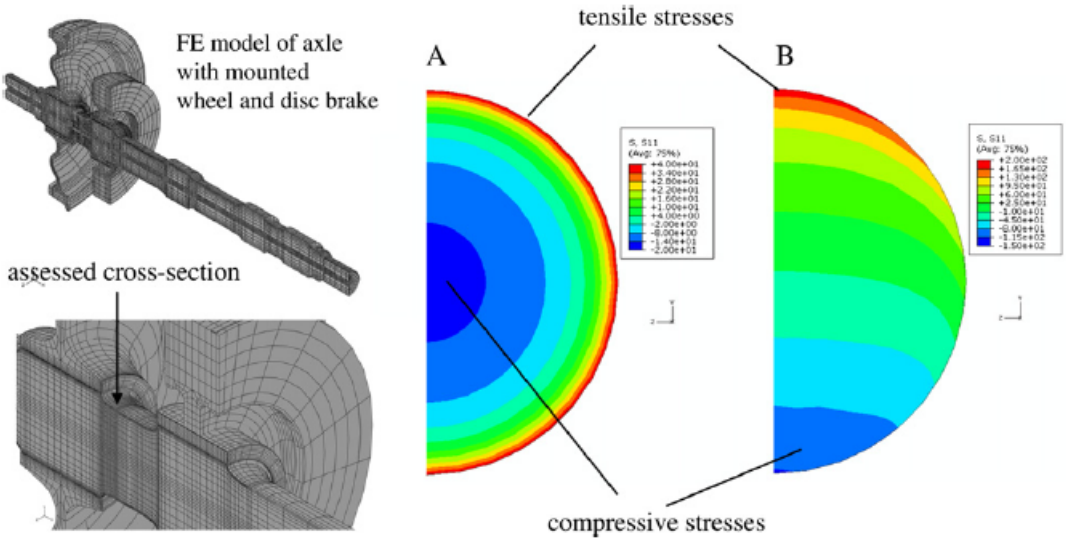

Figure 2.79: Axial stress distribution in a fillet due to press-fitting (A) and at superimposing stresses due to press-fit and bending (B) [26].

For the work being analysed, material was subjected to asymmetric loading cycles with the R-ratio depending upon the load level in the spectrum. This leads to asymmetry of the crack driving force.

In the Figure 2.80, a scheme to the definition of inspection intervals is presented, where the variable L represents the crack growth phase and it is important for the determination of inspection intervals. L is bounded by a characteristic crack depth, a_0, which can be obtained with NDT with a corresponding aspired or required probability of detection, and is also bounded by a final crack depth, a_{End}, that should not exceed $a_{Fracture}$. L_{insp} is determined by dividing L by a safety factor (SF) that considers the reliability of the NDT. Input data, generally subjected to uncertainties and scatter, is to be defined in such a way that a conservative result balancing safety and economical issues can be achieved.

For the determination of crack growth rates under constant amplitude loading, stress ratios $R = -1$ and $R = 0.1$ were used by *Luke et al.* [26]. Stress ratio $R = 0.1$ enables the estimation of the mean stress effect.

ΔK is the full range of the stress intensity factor and was obtained by:

$$\Delta K = K_{max} - K_{min} \tag{2.51}$$

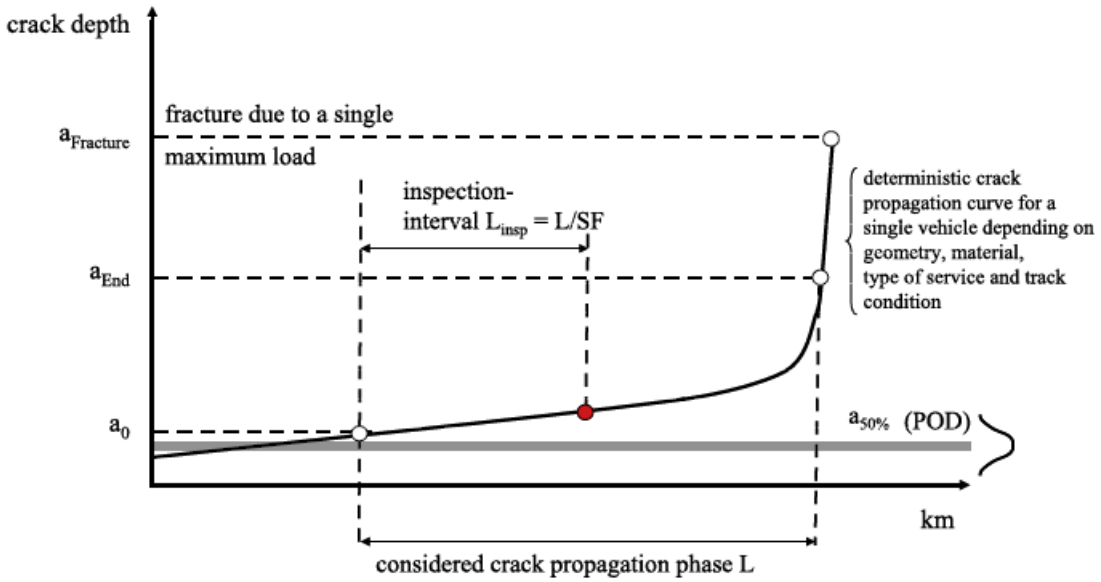

Figure 2.80: Scheme to the definition of inspection intervals [26].

In the research proposed by *Luke et al.* [26], the influence of overloads on fatigue crack propagation was studied. For single overloads, the retardation is probably due to an increase of the plastic zone at the crack tip, related crack closure and crack tip blunting effects. Multiple overloads can lead to crack acceleration.

2.8.1 Fatigue crack growth rates under block sequence loading

Under low or moderate stress levels, overload cycles usually result in crack retardation. This is typically attributed to plasticity induced compressive residual stresses, crack tip blunting, crack closure or plastic zone shielding. However, at high levels of applied loading, overload cycles seem to produce severe material damage ahead of the crack tip. This leads to an accelerated crack propagation.

The stress intensity factors solution for cracks in solid axles was computed using the assumptions proposed in Figure 2.81. This figure shows a semi-elliptical surface crack which is normally considered as a representative crack model for surface cracks in round bars. Axial stress distribution in a fillet zone is typically characterized as a two-dimensional function (coordinates x and y). Stresses induced by the press-fit considerably accelerate the crack growth as it can be seen in Figure 2.82.

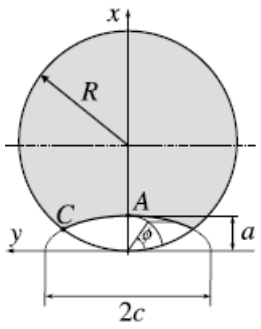

Figure 2.81: Semi-elliptical surface crack which is normally considered as a representative crack model for surface cracks in round bars [26].

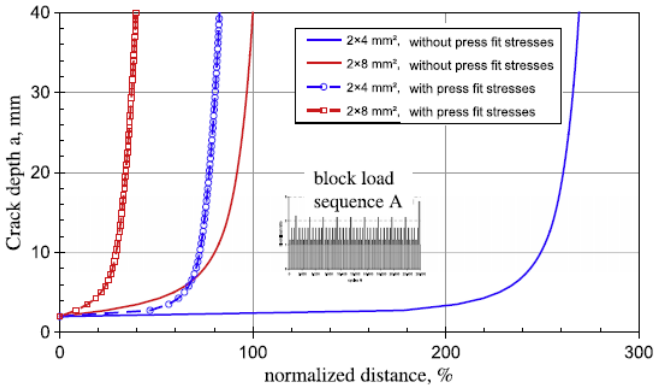

Figure 2.82: Influence of stresses due to press-fitting on fatigue crack propagation in a fillet, material EA4T, block loading sequence A [26].

2.9 Cyclic plastic strain-based damage tolerance for railway axles

For the cycle plastic strain-based damage tolerance, considering the effects of crack closure and load ratio, based on plastic strain energy and modified Rice-Kujawski-Ellyin (RKE) solution in the tip of a growing fatigue crack for a plane stress condition, a new crack closure based fatigue crack growth rate model - LowGRO - for low cycle fatigue behavior and improved threshold stress intensity factor range at different loading ratios was proposed by *Wu et al.* [27]. For railway steel axles such as 25CrMo4 and 34CrNiMo6, the results predicted by LowGRO correlated well with the experimental data.

Reversed cyclic loading is one of the main causes of failures of railway structures. Other studies have shown that a local highly strained region along the crack tip is the reason for the fatigue crack initiation for reversed cyclic loading [27].

Other fatigue crack growth rate models have been proposed, but the majority of them do not take into consideration the effects of loading ratios and fatigue crack closure that are a characteristic of rotating bending components like a railway axle. Therefore, reliability and validity of engineering design and assessment are affected [27].

The Standard NASGRO equation has been widely employed to establish to formulate the integrated FCG curve of railway axles. Yet, it is necessary to conduct very complex and expensive fracture mechanics tests. Those FCG curves depend on the following aspects:

- Testing machine;
- Applied stress;
- Operation experience;
- Test specimen geometry.

Moreover, in order to rebuild the FCG data, there are some parameters and constants that are required to fit the experimental data with a significant scatter and uncertainty. Frequently, this results in large deviations from real components/structures [27].

In the research conducted by *Wu et al.* [27], a new FCG model based on cyclic plastic strain behaviour and on the influence of stress ratios and crack closure was proposed. The first step consists in formulating the cyclic stress and strain fields ahead of a fatigue crack tip. The theoretical solutions of the Rice-Kujawski-Ellyin singularity stress field from a modified form of Rice's solution for the anti-plane shear under plane stress condition were used. Next, material elements around the crack tip were assumed to be subjected to strain-controlled reversed uniaxial loading. Then, the plastic strain energy (PSE) was chosen as the failure criteria and integrated inside the cyclic plastic zone adjacent to a stable growing fatigue crack [27].

2.9.1 Crack-tip based damage modelling

In Figure 2.83, it can be seen that a monotonic plastic zone is formed near the crack tip. This zone maintains the crack open until crack arrest. A fatigue process zone appears because of the non-proportional plasticity and crack tip blunting. The crack then develops inside the fatigue process zone [27].

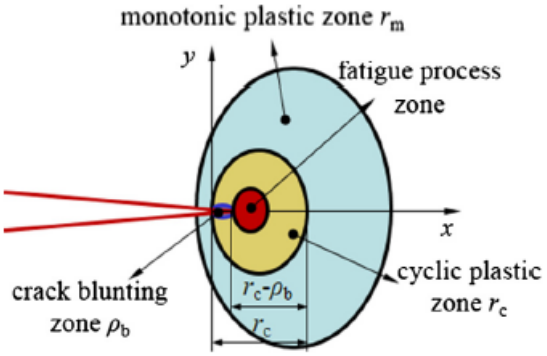

Figure 2.83: Various plastic regions near the crack tip under blunting and cyclic loading [27].

2.9.1.1 Plasticity-induced crack closure

Stresses that are developed on railway axles range from positive to negative stress ratios. This happens mainly beneath the press fits, stress relief and axle shaft areas. Consequently, the reversed plastic zone is generated with ease [27].

The plasticity-induced crack closure effect causes the decreased strain range ahead of the crack tip and resultant reduced fatigue crack driving force. In order to formulate the FCG model with the crack closure effect, the cyclic SIF $\Delta K = K_{max} - K_{min}$ range is frequently replaced by an effective value [27]:

$$\Delta K_{eff} = K_{max} - K_{op} = \left(\frac{1-f}{1-R}\right)\Delta K \tag{2.52}$$

The variable f represents the crack opening function expressed by K_{op}/K_{max} for the fatigue long crack.

2.9.1.2 Cyclic stress-strain behaviour

For remote cyclic loading, unloading and reloading, Rice's plastic superposition theory is used with Rice-Kujawski-Ellyin field at the tip of a growing crack under plain stress states [27].

For strain hardening materials, the cyclic stress range $\Delta\sigma_t$ and plastic strain range $\Delta\varepsilon_{pt}$ are theoretically obtained from RKE field.

The cyclic plastic zone size r_c and a critical blunting size ρ_b are taken as:

$$r_c = \frac{\Delta K^2}{4\pi(n'+1)\sigma_y^2} \tag{2.53}$$

$$\rho_b = \frac{\Delta K_{th}^2}{4\pi(n'+1)\sigma_y^2} \tag{2.54}$$

Then, the plastic strain energy inside the fatigue plastic zone can be obtained by:

$$\int_0^{r_c-\rho_b} \Delta\sigma_t \cdot \Delta\varepsilon_{pt} dr = 4K'(\varepsilon_{yc})^{(n'+1)} r_c ln\left(\frac{r_c}{\rho_b}\right) \tag{2.55}$$

2.9.1.3 Low cycle fatigue behaviour

The cyclic plastic zone contains a large strain. Therefore, most of the damage accumulation is in this zone. The stress-strain field and its critical size are the most important parameters to monitor the fatigue cracking rate from low cycle fatigue responses near the crack tip [27].

The Manson-Coffin equation from smoothed specimens can be employed to experimentally describe the fatigue life with the mean stress σ_m:

$$\Delta\varepsilon_{pe} = 2\varepsilon_f'(2N_f)^c \tag{2.56}$$

$$\Delta\sigma_e = 2(\sigma_f' - \sigma_m)(2N_f)^b \tag{2.57}$$

$\Delta\varepsilon_{pe}$ represents the cyclic plastic strain range and $\Delta\sigma_e$ represents the cyclic stress range.

Following the Neuber micro-support concept ahead of the crack tip:

$$\frac{da}{dN} = \frac{r_c - \rho_b}{\Delta N} = \frac{\Delta K_{eff}^2 - \Delta K_{th}^2}{4\pi\,(n'+1)\,\sigma_{yc}^2 \Delta N} \tag{2.58}$$

A modified crack opening function f is further described in this paper.

The current LowGRO model is very similar to the NASGRO one. The main difference is that the remaining life of cracked axles is inferred mainly by LCF tests of smoothed scaled specimens rather than standard fracture mechanics experiments [27].

2.9.1.4 Results and discussion

Table 2.5 contains the LCF properties of railway axle used steels.

Table 2.5: The LCF properties of railway axle used steels [27].

The material	σ_{yc}, MPa	K', MPa	n'	σ'_f, MPa	b	ε'_f	c
25CrMo4	380	892	0.11	900	−0.072	0.90	−0.69
34CrNiMo6	713	843	0.10	1184	−0.055	0.47	−0.61

The next two figures (Figures 2.84 and 2.85) compare current LowGRO with experimental data.

The experimental data was mainly collected near the threshold because *Wu et al.* attempted to focus on physically short crack effects [27].

Current LowGRO provides a slightly conservative prediction at $R < 0$ and, to some extent, a slightly dangerous prediction at $R \geq 0$ due to crack closure compared with standard NASGRO model and experimental data [27].

Based on LCF properties and crack closure effects, the newly-proposed LowGRO model enables a very good FCG prediction without the need of expensive fracture mechanics tests [27].

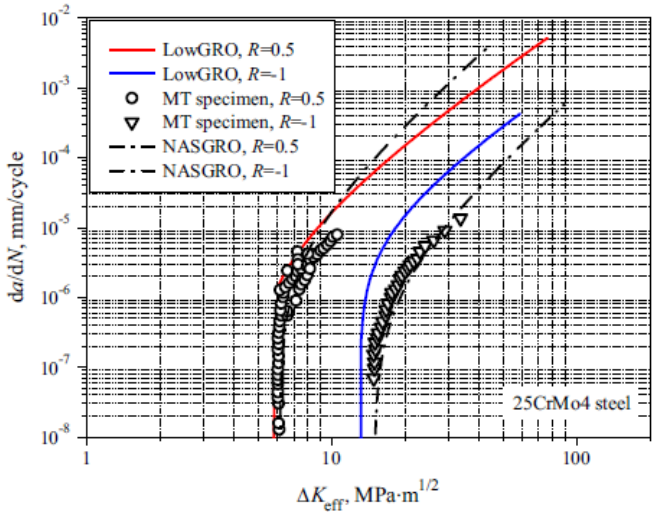

Figure 2.84: Comparisons of experimental FCG data with predicted curves from the LowGRO and NASGRO under load ratios of R = 0.5 and -1 for 25CrMo4 steel [27].

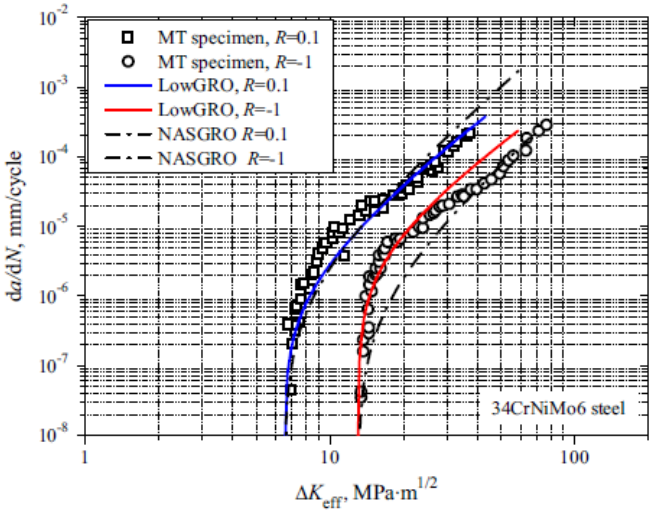

Figure 2.85: Comparisons of experimental FCG data with predicted curves from the LowGRO and NASGRO under load ratios of R = 0.1 and -1 for 34CrNiMo6 steel [27].

2.10 Probabilistic modelling of damage accumulation for time-dependent fatigue reliability analysis

Predicting the failure of railway axles is extremely important. This way, fatigue fractures can be prevented.

In the research conducted by *Zhu et al.* [28], a combination of a non-linear damage accumulation model, a probabilistic S-N curve and a one-to-one probability density function transformation technique were carried out to develop a probabilistic methodology to model damage accumulation. This way, the time-dependent fatigue reliability of railway axle steels can be studied [28].

Damage accumulation was represented as a distribution in a general degradation path. There is a non-linear damage accumulation phenomenon for variable-amplitude loading conditions. Mean and variability change over time. Taking into account an estimation of the evolution and probabilistic distribution of fatigue damage over time, a strategy for fatigue reliability assessments and service life prediction was given [28].

Materials ageing is a key factor for reliability and safety studies of railway/axle components [28].

Current models treat fatigue damage accumulation in railway axles/components as a deterministic process. Yet, it is known that fatigue damage accumulation under service operations is of stochastic in nature. Stochasticity derives from an inherent variability in materials' fatigue resistance as well as the statistical nature of service loads acting on the components. A conventional method for analysing fatigue damage accumulation considering a stochastic loading is to define an equivalent stress range based on the Palmgren–Miner rule and deterministic S-N curves. The principal disadvantages of this method are the non consideration of variability, loading sequence effects, load interaction effects and uncertainty [28].

For real engineering components, the damage process is typically of non-linear nature.

Two factors have to be taken into account for the probabilistic modelling of fatigue damage accumulation:

- Accurate physics-based damage accumulation model;
- Appropriate uncertainty modelling technique.

The uncertainty modelling process typically comprehends complex mathematical calculations. In this article, a simple approach is developed to study the stochastic nature of fatigue damage accumulation.

The main focus of the research work developed by *Zhu et al.* [28] was to study the way how damage accumulation can be measured in terms of fatigue life distributions adopting the probability distribution function (PDF) transformation technique.

2.10.1 Probabilistic modelling of fatigue damage accumulation

A variation on the loads acting on railway axles/components leads to a cumulative failure mechanism which is an irreversible degradation process. Cumulative damage ultimately causes failure. Fatigue, creep, corrosion, wear and erosion are examples of types of cumulative damage that are used to measure degradation.

Degradation analysis consists in a probabilistic modelling process of a failure mechanism degradation path (Figure 2.86). Degradation paths evolve in the space of a degradation measure (indicator) and this indicator evolves toward the failure threshold. The behaviour under cumulative damage can be predicted to be used for structural safety analysis, decisions concerning inspection times and design criteria. Reliability manifested as the degradation measure is deteriorating probabilistically with time, as shown in the next figure. D_0 is the initial damage, D_C is the critical threshold value that depends on the studied components/specimens. Therefore, a probabilistic threshold value is more appropriate.

The variability of a degradation measure increases with time. The cumulative fatigue damage can be seen as a random variable that follows a probability distribution. There is an increase on its mean value and variability over time.

A new probabilistic approach for modelling fatigue damage accumulation was proposed by *Zhu et al.* [28].

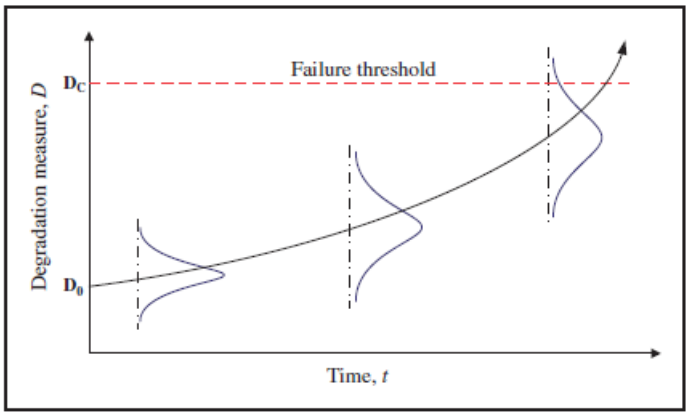

Figure 2.86: Degradation path example [28].

2.10.2 Modelling the mean value of cumulative fatigue damage

A constant amplitude loading was applied to a railway axle/component. Ignoring environmental and frequency-based effects on $D(n)$, it can be said that the rate of damage accumulation depends on D_0 and on the loading stress amplitude, S. For engineering problems, the dependency on the actual damage state can be characterized in terms of the loading cycles, n. A non-linear relationship between the damage accumulation and the number of loading

cycles can be more suitable for some situations depending on the nature of the fatigue failure. The general form of the cumulative fatigue damage curve in the previous figure can be written as:

$$D(n) = D_0 + f(S, D_0)n^a \tag{2.59}$$

Where $f(S, D_0)$ is the rate of damage accumulation associated with cyclic loading. Moreover, parameter a is a damage accumulation exponent and it depends on the amplitude of alternating stress. Function $f(S, D_0)$ is established based on the boundary conditions and failure criterion. It is considered that failure occurs when the cumulative damage, $D(n)$, equals the critical threshold damage, D_C, and the number of loading cycles, n, equals the constant amplitude fatigue life, N_f.

$$f(S, D_0) = \frac{D_c - D_0}{N_f^a} \tag{2.60}$$

Substituting Equation 2.61 in 2.60:

$$D(n) = D_0 + (D_c - D_0)\left(\frac{n}{N_f}\right)^a \tag{2.61}$$

The equation that translates the relationship between N_f and S given by the $S-N$ curve is:

$$N_f S^m = C \tag{2.62}$$

Where C is a fatigue strength constant and m corresponds to the slope of the $S-N$ curve.

Combining equations 2.61 and 2.62, the following equation can be written:

$$D(n) = D_0 + (D_c - D_0)\left(\frac{S^m}{C}\right)n^a \tag{2.63}$$

Figure 2.87 provides an example of possible damage accumulation curves as a function of loading cycles as described in the above equation.

Assuming that there is no initial damage and that failure occurs when $D_C = 1$, the following equation can be written:

$$D(n) = \sum_{i=1}^{j} = \sum_{i=1}^{j}\left(\frac{S_i^m}{C}\right)^{a_i} n_i^{a_i} \tag{2.64}$$

This last equation represents a load-dependent damage model with non-linear evolution. With Equations 2.63 and 2.64, the mean value of the cumulative fatigue damage can be calculated for constant and variable amplitude loading, respectively.

2.10.3 Distribution of cumulative fatigue damage

Despite the existence of several models to describe regular or typical fatigue damage accumulation, individual fatigue damage accumulation paths may diverge considerably from the mean.

Figure 2.87 shows a probabilistic interpretation of a general damage accumulation curve. It can be seen how to obtain the PDF of the damage accumulation based on the known PDF for fatigue life at any given stress level.

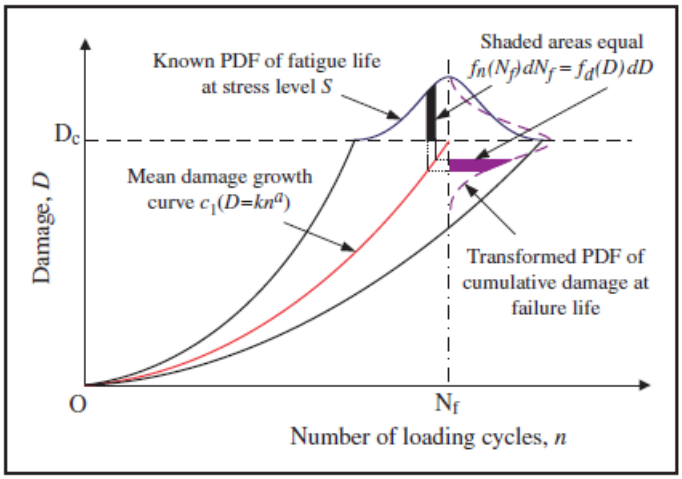

Figure 2.87: One-to-one PDF transformation under cyclic loading [28].

Curve c_1 represents the trendline of the mean cumulative damage as given by Equation 2.63 at a given stress level S. It is clear the non-linear evolution of the cumulative damage depending on the number of loading cycles.

Considering $D_0 = 0$, the previous equation can be written as:

$$D(n) = kn^a \tag{2.65}$$

$$k = D_C \left(\frac{S^m}{C}\right)^a \tag{2.66}$$

According with the PDF transformation methodology developed by Benjamin and Cornell, when a random variable is related to another random variable, the unknown PDF of that variable can be reached using the known PDF of the other. To derive the distribution of $D(n)$ there has to be a clearly defined relation between cumulative damage, $D(n)$, and loading cycles, n. Variability of the fatigue failure life N_f can be described by a log-normal distribution. Its mean is $\mu_{(N_f)}$ and standard deviation is $\sigma_{(N_f)}$. The PDF of N_f is defined as:

$$f_n(N_f) = \frac{1}{N_f \sigma_{N_f} \sqrt{2\pi}} exp\left(-\frac{1}{2}\left(\frac{lnN_f - \mu_{N_f}}{\sigma_{N_f}}\right)^2\right) \tag{2.67}$$

In order to get the PDF of cumulative damage $D(n)$, the cumulative distribution function must be first obtained and then differentiated.

The relationship between the PDF of the cumulative damage, $f_d(D)$, and that of the fatigue failure life can be derived with the help of the following equation:

$$f_d(D) = f_n(N_f)dN_f \tag{2.68}$$

The above equation can be graphically derived from the equal-shaded areas shown in the figure 2.87.

Substituting equations 2.65 and 2.67 in Equation 2.68, one has:

$$f_d(D) = \frac{1}{Da\sigma_{N_f}\sqrt{2\pi}} exp\left(-\frac{1}{2}\left(\frac{ln(D) - ln(k) - a\mu_{N_f}}{a\sigma_{N_f}}\right)^2\right) \tag{2.69}$$

2.10.4 Modelling the trend curve of the variance

Variability/standard deviation of cumulative damage increases monotonically with an increasing number of loading cycles whereas the variability of fatigue lives increases with decreasing stress levels [28].

Using a geometric reasoning technique proposed in Rathod et al., the rate of change in variability as a function of the number of loading cycles can be interpreted as it can be seen in Figure 2.88.

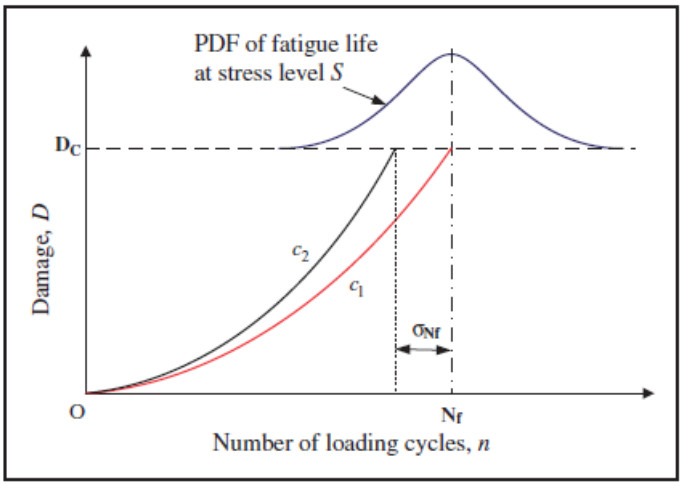

Figure 2.88: Graphical interpretation of the rate of change in variability as a function of the number of loading cycles [28].

Variable c_1 is the mean cumulative damage trend line and c_2 is the $(1-\sigma)$ curve of fatigue life distribution.

The rate of change of the standard deviation r_σ of loading cycles can be written as:

$$r_\sigma = \frac{\sigma_{N_f}}{ln(N_f)} \tag{2.70}$$

The standard deviation of the number of loading cycles n can be obtained:

$$\sigma_n = \left(\frac{\sigma_{N_f}}{ln\left(N_f\right)} \right) ln(n) \tag{2.71}$$

The standard deviation of the cumulative damage D can be obtained as:

$$\sigma_D = a \left(\frac{\sigma_{N_f}}{ln(N_f)} \right) ln(n) \tag{2.72}$$

Equation 2.72 can be used to capture the variability in the cumulative damage under constant amplitude loading. Equation 2.72 can also be extended to obtain the total variability in the cumulative damage $D(n)$ at the time of fatigue failure for components under multi-level stress loading if assuming that damage is accumulated stochastically and independently under each level stress loading.

$$\sigma_D = \sqrt{\sum_{i=1}^{j} \left(a_i \left(\frac{\sigma_{N_{fi}}}{ln\left(N_{fi}\right)} \right) ln\left(n_i\right) \right)^2} \tag{2.73}$$

2.10.5 A framework for time-dependent reliability analysis

The probabilistic estimation of damage accumulation consists of both physics-based and data-driven-based techniques, as it can be seen in Figure 2.89.

The physics-based predictive model combined with the data-driven based probabilistic mode aims to perceive the remaining useful life and reliability in a projected future state. The deterministic physics-based predictive model is based on a non-linear fracture mechanics and/or continuum damage mechanics model and the data-driven one is based on a stochastic approach [28].

Figure 2.89 contains a simplified flow diagram for life prediction and reliability assessment of engineering components.

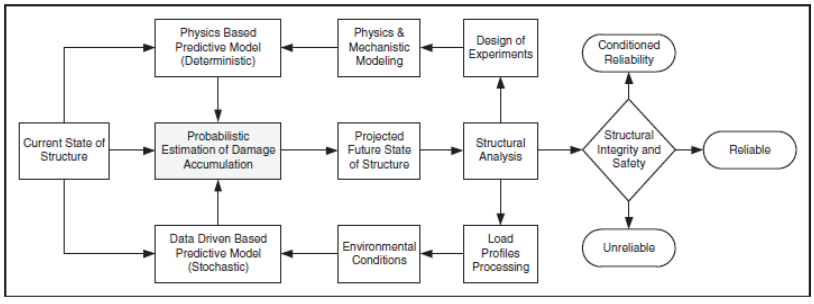

Figure 2.89: A simplified flow diagram for life prediction and reliability assessment of engineering components [28].

The damage state of a structure/component follows a distribution that is not deterministic due to the uncertainty in fatigue damage accumulation. Initial damage size, loading spectrum and environmental conditions be considered for making the analysis [28].

The main goal of the analysis is to compute the reliability for a given service time.

In the paper being analysed, it is assumed that the critical threshold damage has the same distribution as the cumulative damage measure. It is also assumed that at the fatigue failure point, the variability $\sigma^2_{D_C}$ of D_C is equal to that of cumulative damage measure σ^2_D.

The limit state function for fatigue reliability analysis is $G(n)$ which can be expressed as:

$$G(n) = D_C - D(n) \tag{2.74}$$

Assuming a log-normal distribution for cumulative fatigue damage, given the model for $D(n)$, it is possible to derive the reliability of a component in terms of the general damage accumulation curve:

$$R = Pr\left[G(n) > 0 = 1 - \phi\left(-\frac{\mu_{D_C} - \mu_D)}{\sqrt{\sigma^2_{D_C} + \sigma^2_D}}\right)\right] \tag{2.75}$$

2.10.5.1 Validation and discussion

Fatigue life (for constant amplitude loading) was assumed to follow a log-normal distribution. The variability of the threshold damage at fatigue failure life needs to be predicted.

Variable a is the damage accumulation exponent. It is an experimentally fitted function of the stress amplitude. It accounts for loading sequence effects.

Statistics of experimental data of 45 steel and LZ50 steel are presented on Table 2.6.

Table 2.6: Statistics of constant amplitude S-N curve data [28].

			Statistics of fatigue life ($\ln N_f$)	
Material	Reference	Stress amplitude S_i (MPa)	Mean	Standard deviation
45 steel-1	Zheng and Wei [40]	525	5.33	0.32
		500	5.50	0.34
		475	5.59	0.29
		450	5.82	0.35
		400	6.15	0.26
45 steel-2	Yan et al.[41]	750	4.49	0.15
		650	5.00	0.14
		630	5.04	0.12
		590	5.24	0.10
		520	5.65	0.24
LZ50 steel	Wang et al.[42]	320	10.48	0.36
	Yan et al.[43]	305	11.62	0.26
		290	12.40	0.37
		280	13.08	0.36
		275	13.44	0.83

Fitting the S-N curve model in Equation 2.62 one has that $m = 2.43604$ and $C = 9.85123 \cdot 10^8$.

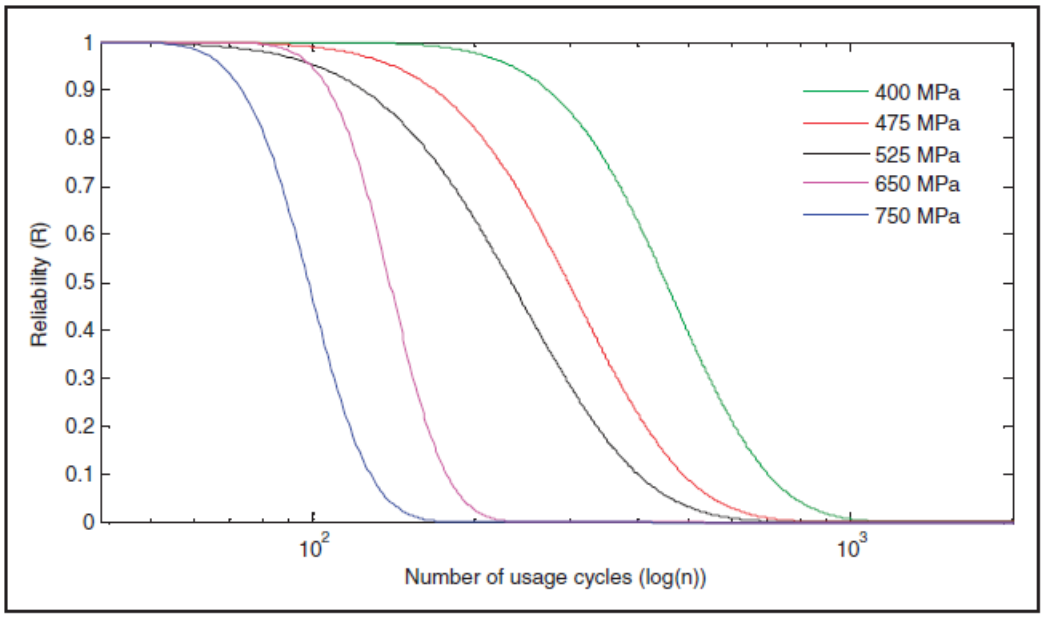

Figure 2.90: Time-dependent reliability plot for 45 steel at different stress levels [28].

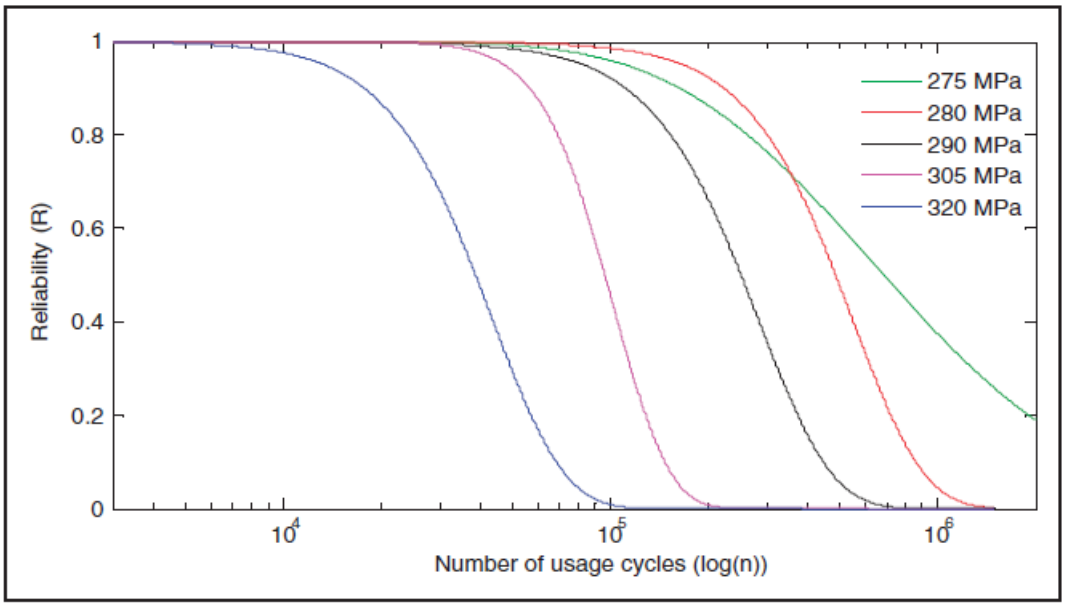

Figure 2.91: Time-dependent reliability plot for LZ50 steel at different stress levels [28].

Analysing Figures 2.90 and 2.91 it is understandable that reliability lessens with an increase in time or number of loading cycles. The high and stable reliability phase represents the crack initiation period and the reliability loss phase corresponds to the crack propagation period. A faster loss of reliability along the crack propagation period indicates a faster degradation or higher rate of damage accumulation that took place for these materials.

Analysing Figure 2.92, it can be seen that the predicted results closely agree with the experimental ones.

The approach proposed in this paper is suitable and valid for deterministic variable amplitude loading of railway axle steels.

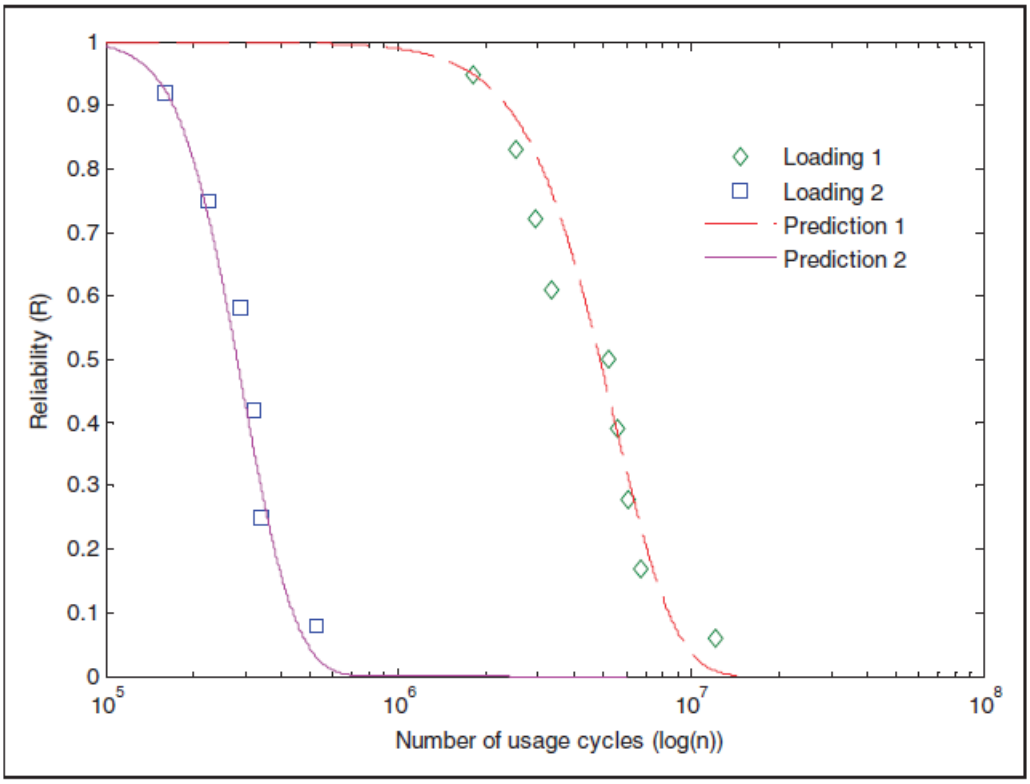

Figure 2.92: Fatigue reliability variation in predicted and experimental results for 45 steel [28].

2.11 Fatigue resistance assessment of railway axles: experimental tests and damage calculations

Filippini et al. suggested an experimental program based on small scale specimens [29]. Small scale tests were made in order to determine the S-N curve and the Miner index for fatigue damage assessment.

The consistent ("konsequent") version of Miner's rule (following FKM-Guidelines) proved to be a good choice as a design criterion. It also enabled a good transferability of small scale fatigue tests to full scale.

The German FKM guideline was released in 2001 as a result of activities sponsored by the Research Committee on Mechanical Engineering [51]. It considers aspects such as special effects at cyclic loading, mixed mode loading, dynamic (impact) loading, stress corrosion cracking and probabilistic aspects in fracture mechanics calculations.

The consistent form of the Miner rule takes into account the gradual decline in fatigue strength with increasing damage. This means that the Wöhler line is lowered. This procedure is only possible iteratively.

The consistent Miner rule was used together with an allowable damage sum $D_{crit} = 0.3$ combined with a 2.5% percentile of the S-N curve derived by experiments made with small specimens.

Then, EA4T and EA1T steels were tested with both constant and amplitude variable loading. The main goal of these tests was to determine the critical damage sum leading to a conservative fatigue assessment.

2.11.1 Constant amplitude fatigue tests

The specimens were design for tension-compression axial fatigue tests. Axles cut-up plan and specimens preparation can be observed in Figure 2.93.

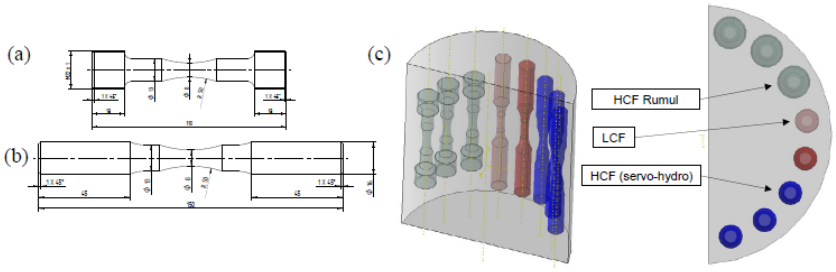

Figure 2.93: a) Details of fatigue experiments, b) shape and dimension of HCF specimens; c) positions of the specimens in the railway axles segments [29].

In this study, fatigue tests characteristics were the following:

- Constant amplitude (load controlled) high cycle fatigue tests;

- Sinusoidal loading;
- $R = S_{min}/S_{max} = -1$;
- Runout test was fixed at 10^7 cycles;
- Staircase procedure was used.

Figure 2.94 contains a S-N diagram with a uniform scatter band. An S-N curve of small specimens of EA1N steel can be observed in Figure 2.95).

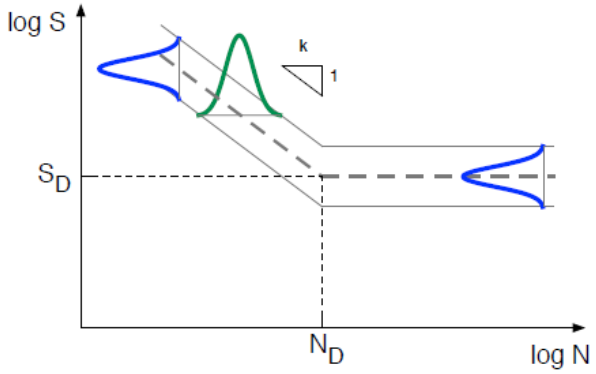

Figure 2.94: Schematic of the S-N diagram with a uniform scatter band [29].

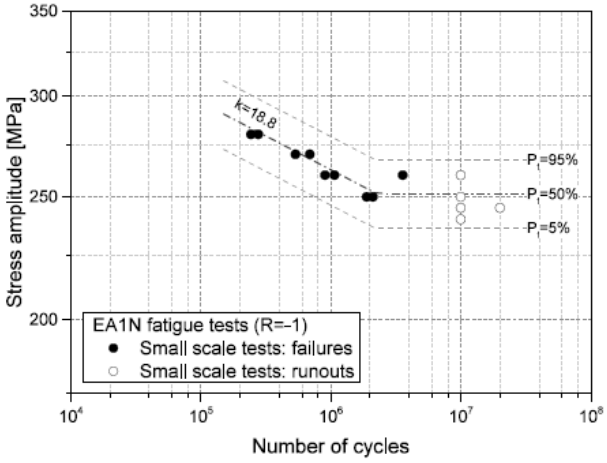

Figure 2.95: S-N curve of small specimens of EA1N steel.

2.11.2 Variable amplitude fatigue tests

In service loading spectrum was normalized by the maximum bending moment amplitude and discretized in blocks (Figure 2.96). Then, the consistent Miner rule was applied to the fatigue test spectrum in order to derive the allowable damage sum (2.97).

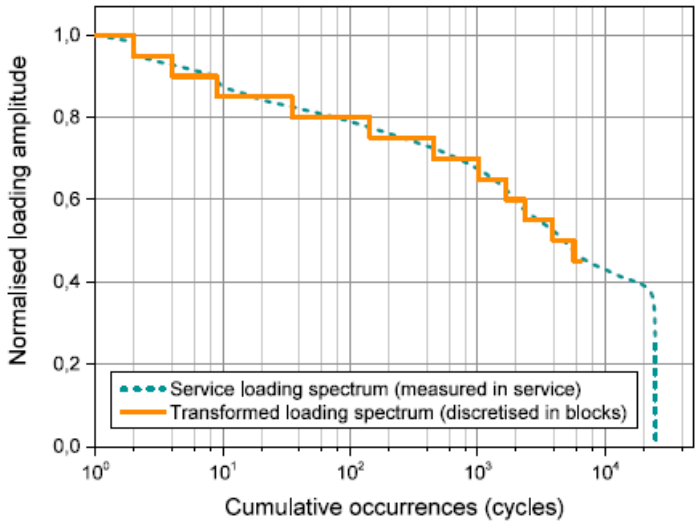

Figure 2.96: From the loading spectrum measured in service to the shortened (accelerated) spectrum to be used in the fatigue tests with variable amplitudes with small specimens [29].

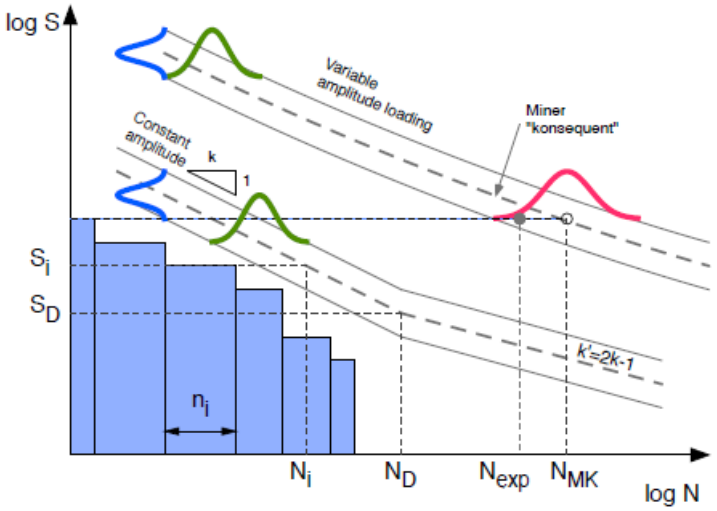

Figure 2.97: Application of the Miner consistent ("konsequent") rule to the fatigue test spectrum for deriving the allowable damage sum [29].

2.11.3 Damage calculation

The first method by Haibach provides a nice approximation of life estimates that could be obtained with Miner "konsequent" method as illustrated in the FKM guideline [51]. Also, this method is simpler to apply [29].

$$D = \frac{1}{S_D^k \cdot N_D} \cdot \sum_{S_i \geq S_D} n_i \cdot S_i^k + \frac{1}{S_D^{k'} \cdot N_D} \cdot \sum_{S_i \geq S_D} n_i \cdot S_i^{k'} \tag{2.76}$$

The second method enables to calculated a fatigue life N_{MK} under the following assumptions:

- Stresses above the fatigue limit cause a reduction of the fatigue limit for the subsequent cycles;
- The reduction of fatigue strength can be calculated starting from the largest stress amplitude;
- Failure occurs when the damage hits value D_m [29].

There is also a modified version of Miner's rule that takes into account the contribution to fatigue damage of loading amplitudes below the fatigue limit [29].

Critical Miner Index has been calculated adopting an S-N curve with 50% failure probability.

The obtained average critical damage D_{crit} was lower than 1 as it's commonly and in most cases wrongly assumed. Also, there was no dependence on the maximum stress level of the spectrum [29].

The values of D_{crit} calculated with the Haibach's modified Miner rule and Miner "konsequent" method were very similar. They followed a log-normal distribution [29].

In this paper, it was chosen to follow the format of the FKM guidelines (S-N diagram with $P_f = 2.5\%$ and a critical damage sum $D_{min} = 0.3$). This is simple a assessment rule which provides conservative estimates for the variable amplitude that were done. These results were already utilized by Beretta and Regazzi (2016) in order to determine the minimum safety factor for the design of railway axles under variable amplitude loading [29].

Chapter 3

Numerical Analysis of a Railway Axle with Outside Axle Boxes

3.1 Finite Element Model

The State Key Laboratory of Traction Power (TPL) on Southwest Jiaotong University developed numerical models for railway axles with both inside and outside axle boxes. These models were built to support studies such as "On the fatigue performance and residual life of intercity railway axles with inside axle boxes" [25]. These models were gently provided by the TPL and used to support the work carried on during this master's thesis.

The numerical model of the railway axle with outside axle boxes was more relevant for the scope of these thesis, as this configuration is the most common one on Portuguese trains. These same model consists of a railway axle, two wheels, the gear box and the brake disc (see Figures 3.1 to 3.5 and Table 3.1). Special attention was paid to the relief groove between the wheel and the gear box. This section proved to be the critical stress region for the classical axle configuration with press-fits. As so, it was built separately and then assembled to the rest of the axle in order to understand better the stress distribution along this section and make it possible to study crack propagation. Previous studies have demonstrated that the critical stress location results from an integrated action of the rotating bending and press-fit loading.

Stress integrity can be calculated by means of the Finite Element Method based on a predefined crack length. The direction of the crack growth can be modelled assessing the direction vectors of the maximum principal stresses predicted within the FE analysis.

Table 3.1: Dimensions of the axle with outside axle boxes.

	Dimensions [*mm*]
Diameter of the critical stress region	180
Axle body diameter	170
Inner diameter of the axle	60

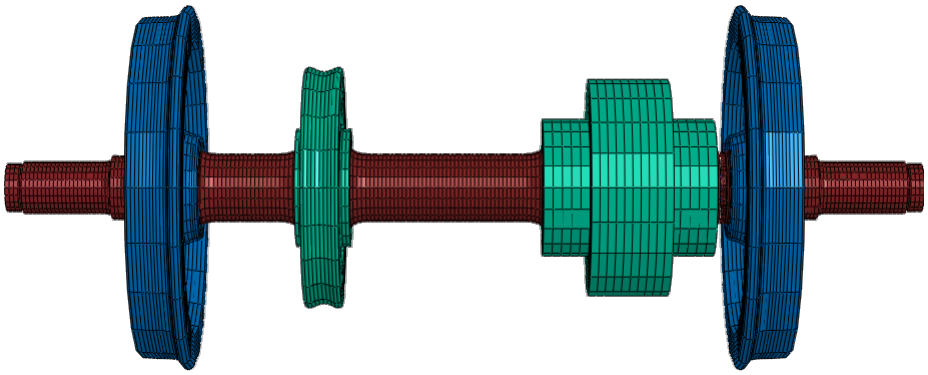

Figure 3.1: Front view of the numerical model of the axle with outside axle boxes.

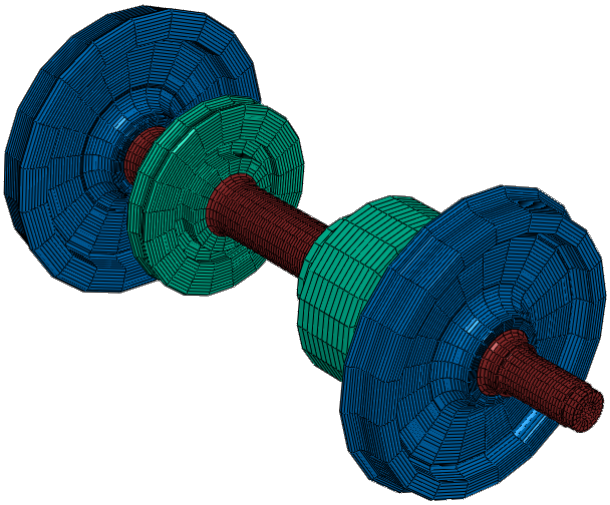

Figure 3.2: Isometric view of the numerical model of the axle with outside axle boxes.

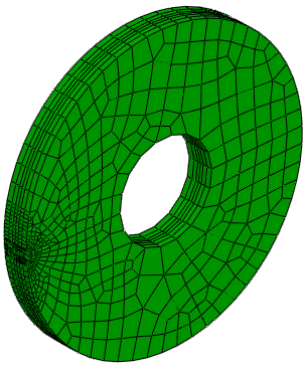

Figure 3.3: Isometric view of the critical stress region of the numerical model of the axle with outside axle boxes.

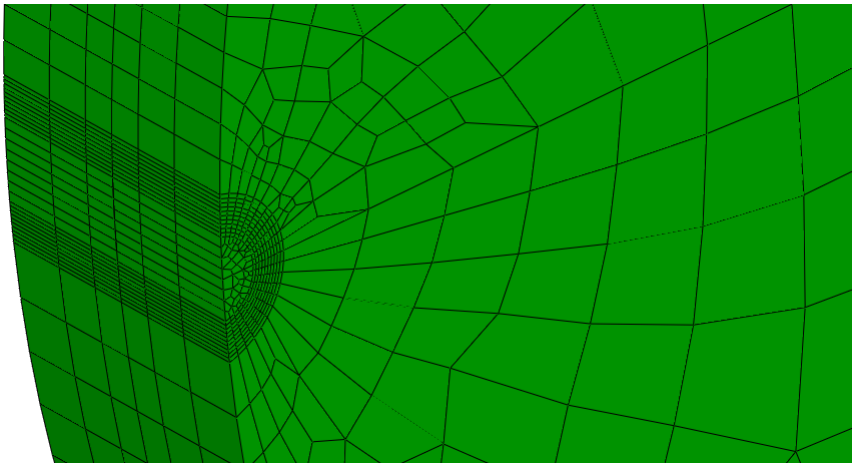

Figure 3.4: Zoom on the critical stress region to better observe the mesh.

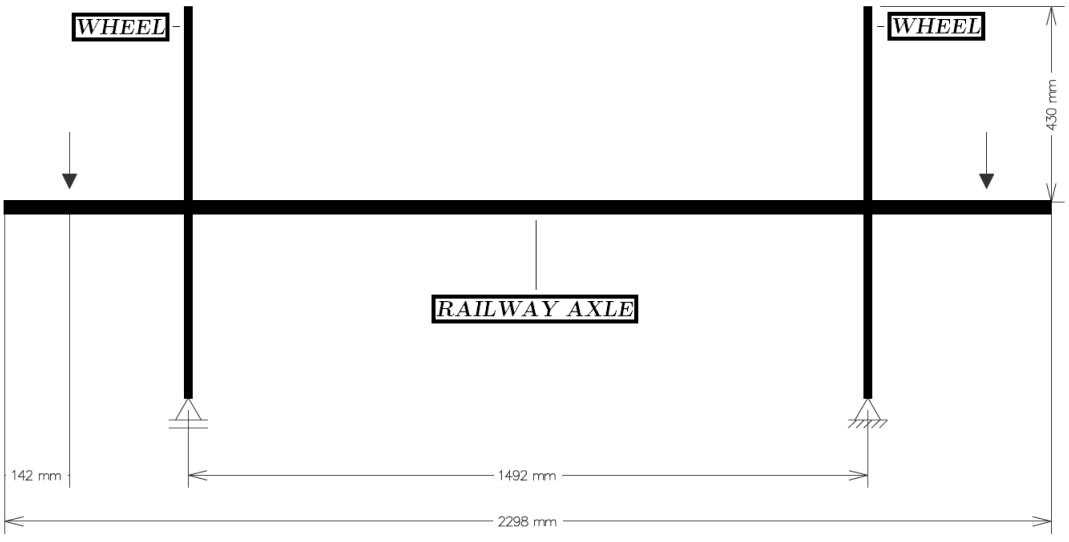

Figure 3.5: Scheme showing some dimensions of the numerical model of the axle with outside axle boxes.

3.1.1 Description

The numerical models which supported these thesis were built in ABAQUS software package. The element type used in these models was the C3D8R type which relates to structural 8-node solid brick elements with reduced integration.

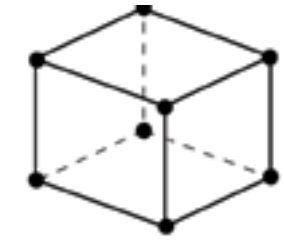

Figure 3.6: C3D8R element type [30].

3.1.1.1 Contact Analysis

The wheels, the gear box and the brake disc are press-fitted to the axle. As so, the bonding of these components to the axle is a very important aspect. The radial interference, ν, and the friction coefficient, μ, are key parameters of the fitting interference. They are of extreme importance to correctly predict the maximum stress and corresponding residual life for the crack-tip stress calculations. In the present work, ν was taken as -0.1 and μ as a constant value of 0.6 in order to achieve a good balance between efficiency and accuracy of highly non-linear contact analysis [25].

Master-slave contact (surface to surface based tie contact approach) was used to assemble the components and to ensure stress and strain continuity. The inner surface of the gear, disc and wheels are taken as master surfaces and the outer surface of the axle as the slave surface.

3.1.1.2 Constraint and Loading

Boundary conditions allow to constrain the two wheels and they also enable to accomplish a correct attachment between the axle and the wheels, gear and disc. First of all, the contact areas between the wheels and track were restricted through the displacements in three directions. Spring elements were used to connect the wheels, gear and disc to the axle with satisfactory stability and to build the residual stress field generated by the press-fits. The stiffness of the spring elements was set to unity, having no real physical meaning. Afterwards, the spring elements should be disconnected to assure that the press-fits would not disturb the deformation of the axle [25].

For strength assessment purposes, the axle box bearing system is normally substituted by an equivalent force F (vertical force resulting from the bogie and train) at the middle plane of the bearing journals. As the track conditions were assumed to be of the highest standard, lateral and brake loads were neglected [25].

The loading process should be divided into a step-by-step loading mode. For each step, the load increases linearly. This helps on obtaining better convergence, accuracy and computational efficiency [25].

A five stage load spectrum extracted from other papers was adopted by Wu et al. [25]. However, in order to generate the RB fatigue SN curve for the classical axle with press-fits, higher loads were taken into account. This way, it was possible to obtain points on the LCF and HCF regimes.

It should be mentioned that crack closure effect can sometimes be encountered, as different load levels constitute the load spectrum.

3.1.2 Material

The material picked for the axle is the well known EA4T steel (25CrMo4) which is widely used in trains all over Europe and China. Firstly, the EA4T steel was taken as a linear elastic body with Young's modulus $E = 206\ GPa$ and Poisson's ratio $\nu = 0.3$. Then, the elastoplastic behaviour was also studied.

True stress-strain curve can be obtained with the following equations:

$$\sigma_{true} = \sigma_{eng}(1 + \varepsilon_{eng}) \tag{3.1}$$

$$\varepsilon_{true} = ln(1 + \varepsilon_{eng}) \tag{3.2}$$

The variables σ_{eng} and ε_{eng} correlate the current state of the steel specimen with its original undeformed state (through initial cross section and length). On other hand, σ_{true} and ε_{true} correlate the current deformed state with the history of previously performed states and not the original undeformed ones.

3.2 Monotonic Tension Behaviour

The values for the 0.2% offset proof yield strength, $R_{p0.2}$, the ultimate tensile strength, R_m, and the tensile fracture elongation were extracted from the paper "On the fatigue performance and residual life of intercity railway axles with inside axle boxes" (Table 3.2) [25].

Table 3.2: Mechanical properties obtained from monotonic tensile testing.

$R_{p0.2}$ $[MPa]$	590
R_m $[MPa]$	704
Tensile fracture elongation [%]	18

Data concerning the plastic behaviour (engineering curve) of the EA4T steel was collected. Based on the relations between engineering and true-stress strain data, values for the logarithmic true plastic strain were obtained (see Tables 3.3, 3.4 and 3.5).

Table 3.3: Engineering stress and its respective plastic strain.

Stress $[MPa]$	Plastic strain
558.48	0
600.11	0.00651
650.49	0.01794
700.57	0.02980
740.30	0.04393
769.26	0.06237
782.07	0.08020

A plot relating true stress and true plastic strain (both in logarithmic coordinates) can be drawn. In order to avoid necking influence, only values between the yield strength and ultimate strength portions of the engineering stress-strain curve are considered ($\sigma =$ 600.113371, $\sigma = 650.4910673$ and $\sigma = 700.5682074$).

Table 3.4: Engineering stress-strain data.

σ_{eng} $[MPa]$	ε_{eng}^{el}	ε_{eng}^{pl}	$\varepsilon_{eng}^{total}$
600.11	0.00291	0.00651	0.00942
650.49	0.00316	0.01794	0.02110
700.57	0.00340	0.02980	0.03320

In the previous table, the values for the elastic component of the engineering strain were obtained dividing the respective stress by the Young's modulus $E = 206$ GPa of the material. Summing the elastic and the plastic components, the total engineering strain can be obtanied.

Table 3.5: True stress-strain data.

σ_{true} $[MPa]$	$\varepsilon_{true}^{total}$	ε_{true}^{el}	ε_{true}^{pl}
605.77	0.00938	0.00294	0.00644
664.22	0.02088	0.00322	0.01766
723.83	0.03266	0.00351	0.02915

The trend line relating true stress and true plastic strain can now be drawn (Figure 3.7). The trend line is represented by a power function, in which n corresponds to the strain hardening exponent (expresses the material's work hardening behaviour) and K corresponds to the strength coefficient:

$$\sigma = K\left(\varepsilon_{pl}\right)^{n} = 1070.9\left(\varepsilon_{pl}\right)^{0.1141} \tag{3.3}$$

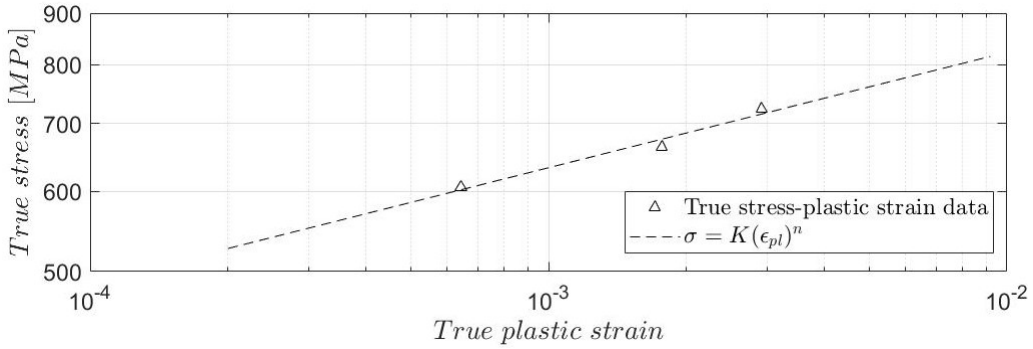

Figure 3.7: True stress versus true plastic strain.

At this point, the monotonic tensile behaviour can be plotted based on the Ramberg-Osgood relationship. True stress-strain data will be used. The Ramberg-Osgood relationship can be written as:

$$\sigma = \frac{\sigma}{E} + \frac{\sigma}{K}^{(1/n)} \tag{3.4}$$

The stress-strain data for the monotonic behaviour characterization of the EA4T steel can be found in the Appendix. In this section, only the true stress-strain curve is presented (Figure 3.8).

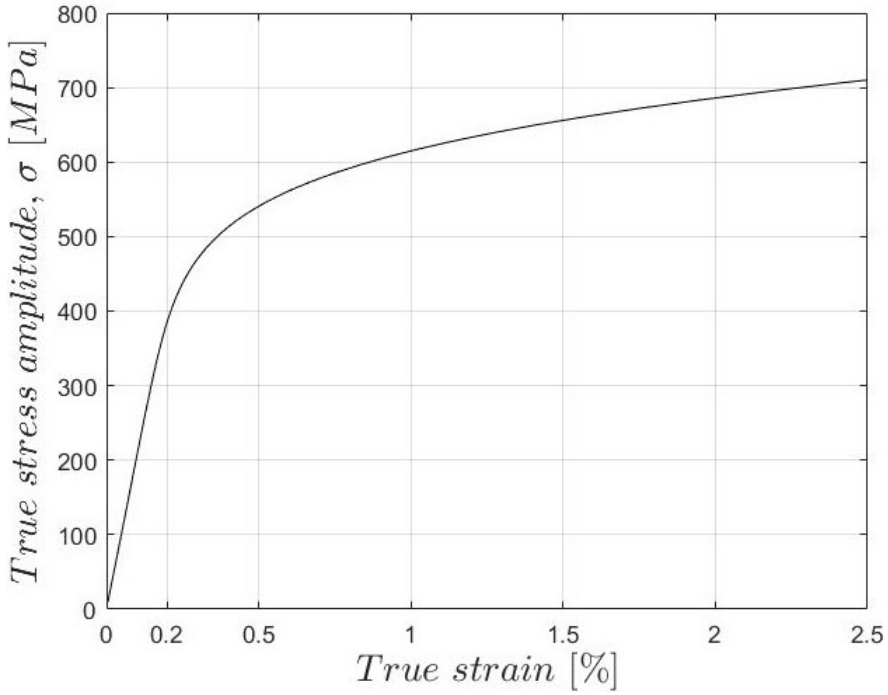

Figure 3.8: Monotonic tensile curve for the EA4T steel used for hollow axles with outside axle boxes.

3.3 Cyclic Stress-Strain Behaviour

The cyclic plastic parameters such as the cyclic yield strength, σ_{yc}, the strain hardening exponent, n', and the strength coefficient, K', were also taken from the paper "On the fatigue performance and residual life of intercity railway axles with inside axle boxes" (see Table 3.6) [25].

Table 3.6: Cyclic plastic parameters.

σ_{yc} $[MPa]$	385.2
n'	0.102
K' $[MPa]$	806.30

For cyclic stress-strain behaviour, usually there is no distinction between true and engineering values. The reasons for these are the following ones:

- The differences between engineering and true curves during the tension and compression stages of the cycle are opposite to each other and consequently they cancel out;
- Strain levels for cyclic loading applications are typically small when compared to the monotonic ones. For cyclic loading applications, strain levels are normally less than 2% [52].

The cyclic stress-strain curve can be plotted using once more the Ramberg-Osgood relationship (Figure 3.9). Again, the stress-strain data for the cyclic behaviour of the EA4T steel can be found in the Appendix.

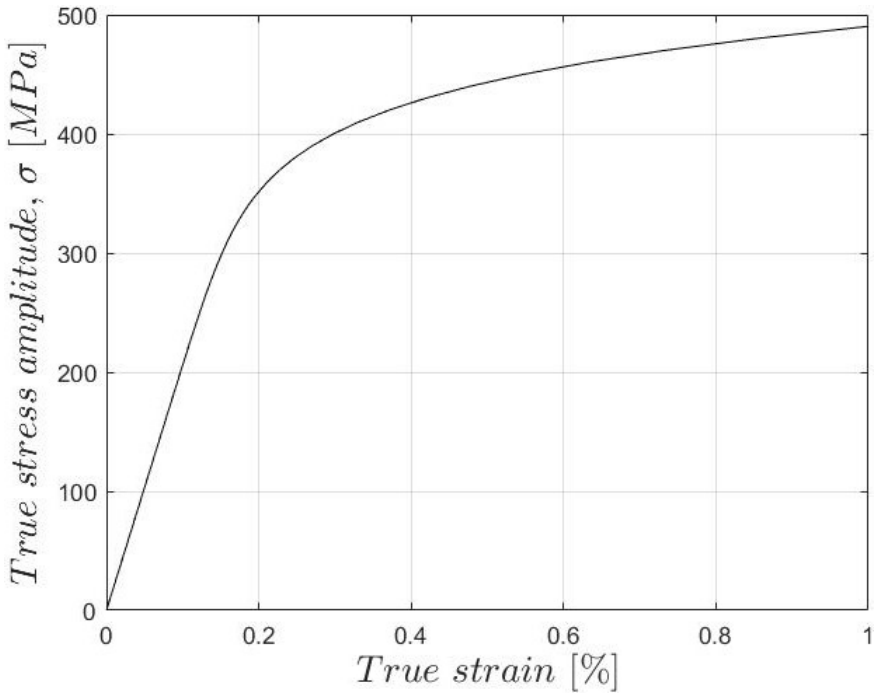

Figure 3.9: Cyclic curve for the EA4T steel used for hollow axles with outside axle boxes.

In order to have a better understanding about the monotonic and cyclic curves, a plot is presented containing both of them. The solid line represents the monotonic behaviour and the dashed line represents the cyclic one.

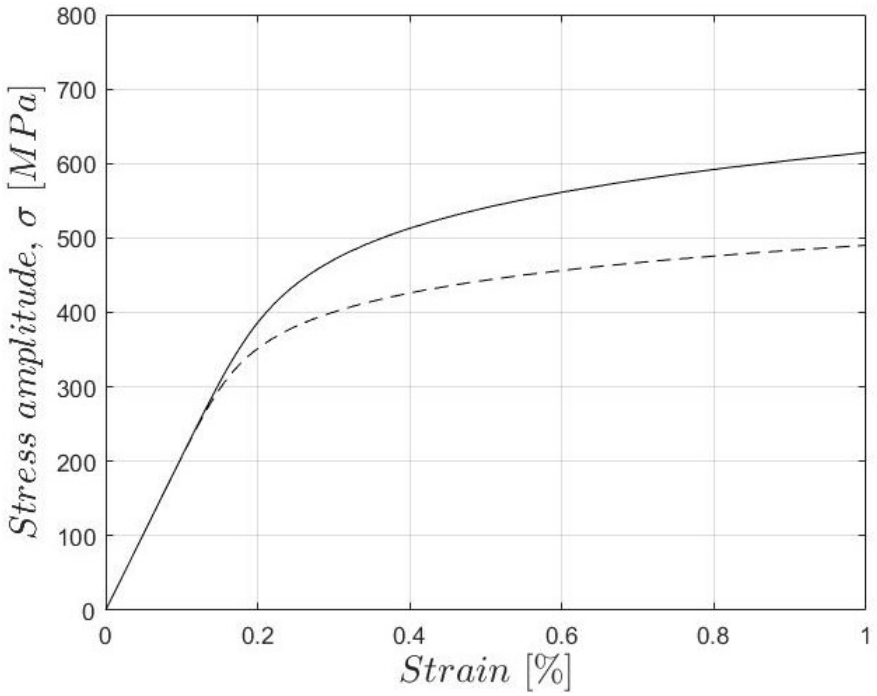

Figure 3.10: Monotonic tensile and cyclic stress-strain curves for the EA4T steel used for hollow axles with internal axle boxes.

Analysing Figure 3.10, it can be seen that the cyclic curve is below the monotonic curve. Therefore, it can be said that cyclic softening exists. Cyclic hardening would be present if the cyclic curve would be above the monotonic curve [52].

In the numerical model, monotonic properties were used for a cyclic loading application. Nevertheless, these should be done in a very careful way because if cyclic softening exists it can lead to an underestimation of the extent of plastic strain [52].

3.4 Elastoplastic Stress Analysis based on Numerical Solutions Combined with the Neuber Rule

3.4.1 Introduction

The numerical model was used to calculate stresses along the classical wheelset with outside axle boxes. There was a special focus on the stress relief groove between between the wheel and the gear box, as this region is one of the critical areas in terms of stress. Furthermore, sometimes fatigue cracks initiate, propagate and eventually lead to failure in this same area.

To ensure good convergence, accuracy and computational efficiency, the loading process should also be carefully set to a step-by-step loading mode.

The standard EN13104 demands that:

- All the contributions to the bending moment (masses, braking and travelling in a curve) should be taken into consideration (except for the longitudinal direction at contact);
- The axle body and the wheel seat spots have different fatigue limits;
- The safety factor should be equal to 1.5 for motor axles and 1.2 for non-powered ones.

Nevertheless, as the track conditions were assumed to be superb, only the equivalent vertical forces at the middle plane of the bearing journals were considered for strength assessment purposes.

The stress relief groove between the gear and the wheel, where the cross-sectional area is not constant, experiences a local increase in terms of stresses. This can be measured by the elastic stress concentration factor, K_t.

$$K_t = \frac{\sigma_{loc}}{\sigma_{nom}} \tag{3.5}$$

The SCF is basically the ratio between the highest stress and a reference stress of the cross-section. Elastic SCF can be obtained from:

- Numerical models;
- Elasticity theory;
- Experimental works.

Typically, the best way to obtain stress concentration factors is using numerical models. However, a fine mesh in the locations of steep stress gradients is mandatory.

3.4.2 Numerical Modelling

For linear elastic analysis, the only inputs that have to be inserted in Abaqus concerning the material behaviour are the Young's modulus, E, and the Poisson's ratio, ν.

First of all, four steps (not including the initial one) were defined in the numerical model. The first step did not comprehend any external loading. Only the interference phenomena was taken into account for observing the stress distributions along the wheelset. Besides the interference fit, the following steps - step 2, 3 and 4 - also included the equivalent vertical forces applied on the external bearing journals, F. Each step comprehends several load increments. For step number 2, vertical force F was set to a value of 500 kN on its last increment. For step number 3, a value of 1000 kN was chosen. Lastly, for step number 4, 1500 kN was picked.

At the end of the simulation, the values of the maximum principal stresses on the critical stress section were observed. Principal stresses/strains are nothing but eigenvalues of the stress/strain tensor.

3.4.3 SCF Analysis

The SCF proved to be the one of the most difficult parameters to estimate. Analysing all the increments since the beginning of step 2 on the FE software until the end of step 4, an important occurrence seemed to be happening. The SCF, calculated by dividing the Maximum Principal stress obtained with the FE software by the respective nominal stress was not remaining constant. The reason for this occurrence is expected to be the interference fit on the surroundings of the critical stress section. Therefore, the distribution of the SCF as a function of the nominal stress or the applied vertical load was evaluated and can be seen on Table 3.8 and Figures 3.16 and 3.17.

The values for the range of nominal stresses were carefully chosen. First, eight load cases were considered, each one with different values for the equivalent vertical forces, F. Then, a static analysis was conducted do determine the bending moment distribution along the railway axle. It consisted on a two-dimensional scheme of the railway axle with a roller support on the left wheel and a pinned support on the right wheel. This scheme can be observed in Figure 3.5. Then, by diving the values of the bending moments by the section modulus for the critical stress region, the values for the range of nominal stresses were finally obtained (3.7). Equation 3.6 was used to calculate the section modulus.

$$W = \frac{\pi\left(D^4 - d^4\right)}{32D} = \frac{\pi\left(0.18^4 - 0.06^4\right)}{32 \cdot 0.18} = 565487 \ \left[mm^3\right] \tag{3.6}$$

Table 3.7: Range of nominal stresses.

External load [*kN*]	Bending moment [*Nm*]	Range of nominal stresses [*MPa*]
1125	293600	519.20
1000	261000	461.55
875	228400	403.90
750	195800	346.25
625	163100	288.42
500	130500	230.77
375	97900	173.13
267	69700	123.26

Figures 3.11 to 3.15 contain a colour map for the Maximum Principal stress obtained by FE analysis, for different load steps.

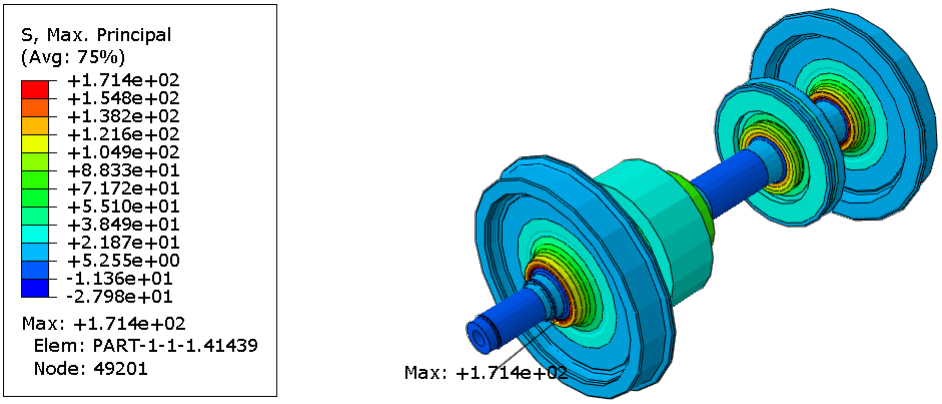

Figure 3.11: Colour map for the Maximum Principal stress [*MPa*] obtained by FE analysis (step 1 - no external loading, just the press-fit exists).

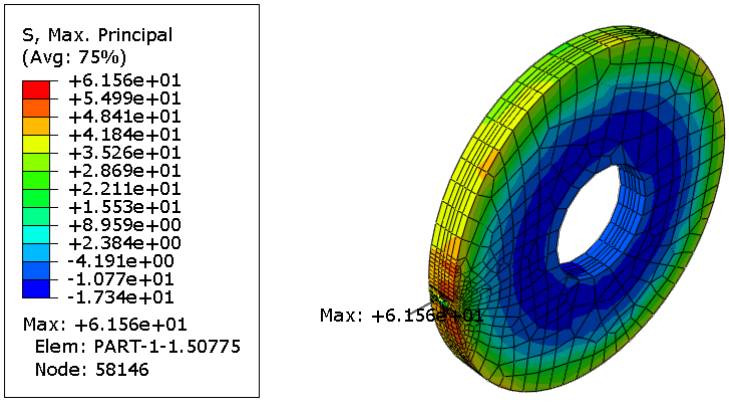

Figure 3.12: Colour map for the Maximum Principal stress [*MPa*] obtained by FE analysis at the critical stress region (step 1: no external loading, just the press-fit exists).

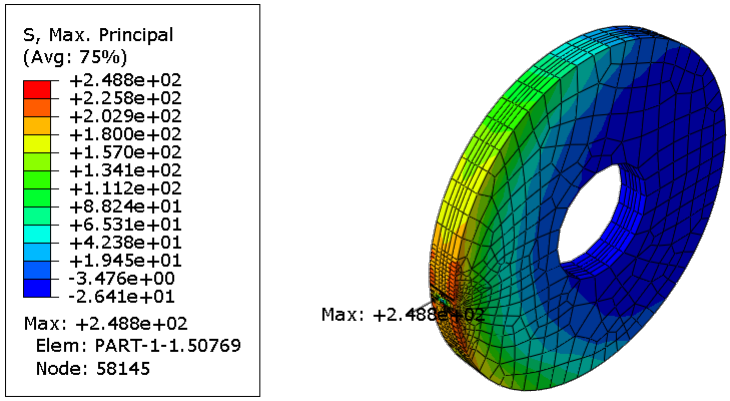

Figure 3.13: Colour map for the Maximum Principal stress [*MPa*] obtained by FE analysis at the critical stress region (step 2: $F = 500$ [*kN*]).

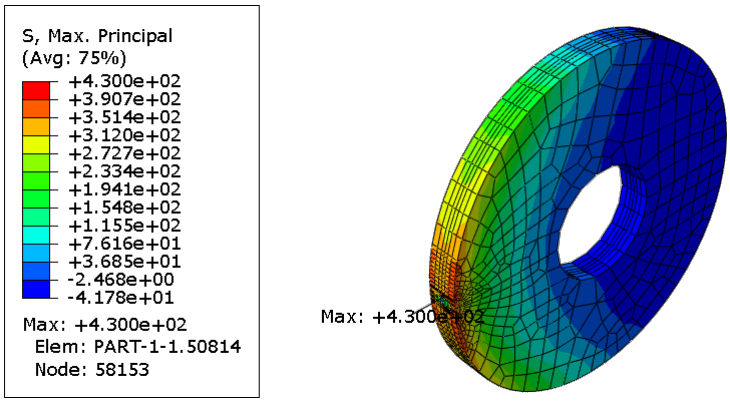

Figure 3.14: Colour map for the Maximum Principal stress [*MPa*] obtained by FE analysis at the critical stress region (step 3: $F = 1000$ [*kN*]).

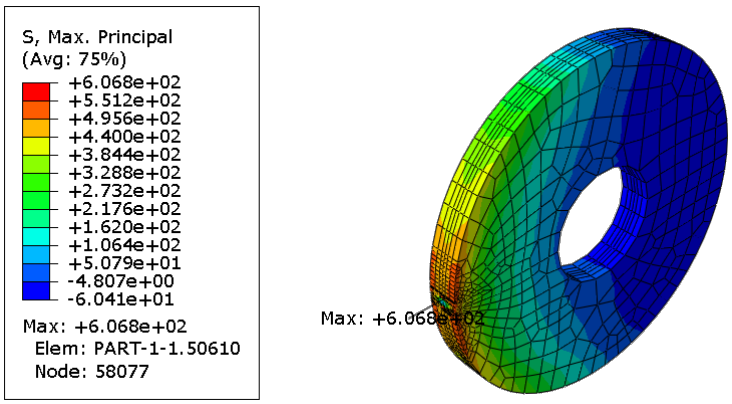

Figure 3.15: Colour map for the Maximum Principal stress [*MPa*] obtained by FE analysis at the critical stress region (step 4: $F = 1500$ [*kN*]).

It should be mentioned that the values for the Maximum Principal stress that can be observed in Figures 3.13, 3.14 and 3.15 are different from the ones presented on Table 3.8.

The values on Table 3.8 were the highest values found for the Maximum Principal stress at the last load increment of each step. Each load increment can be divided into multiple sub-increments. The FE software only jumps from one load increment to another when convergence is achieved. Therefore, the values of Figures 3.13, 3.14 and 3.15 show the average Maximum Principal stress and Table 3.8 contains the highest value found for the Maximum Principal Stresses by comparing all the sub-increments of the last load increment of each step.

Table 3.8: SCF values for each load step.

Vertical force, F $[kN]$	σ_{nom}	$\sigma_{Max.Principal}$	K_t
100	46.15	104.43	2.26
175	80.77	133.99	1.66
288	132.70	178.14	1.34
456	210.58	244.00	1.16
500	230.77	260.00	1.13
550	253.85	280.03	1.10
600	276.93	299.02	1.08
675	311.55	327.41	1.05
788	363.47	369.80	1.02
956	441.36	432.94	≈ 1
1000	461.55	449.22	≈ 1
1050	484.63	467.78	≈ 1
1100	507.70	486.29	≈ 1
1175	542.32	513.96	≈ 1
1288	594.24	555.24	≈ 1
1456	672.13	616.64	≈ 1
1500	692.32	632.42	≈ 1

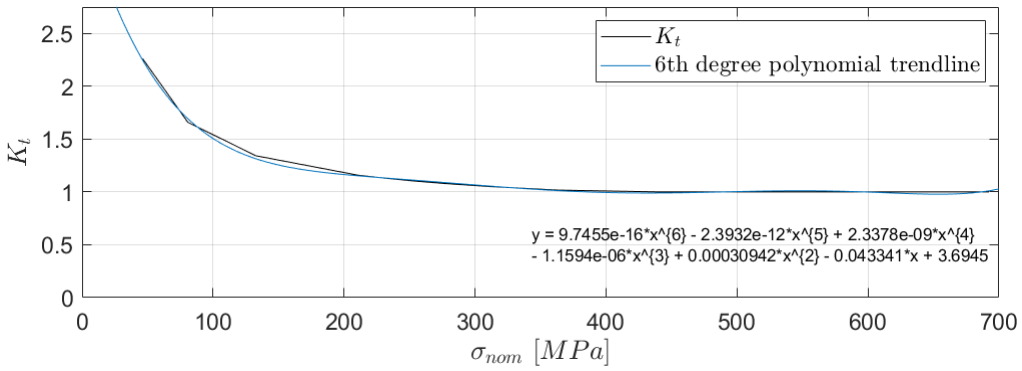

Figure 3.16: K_t as a function of the nominal stress, σ_{nom} $[MPa]$.

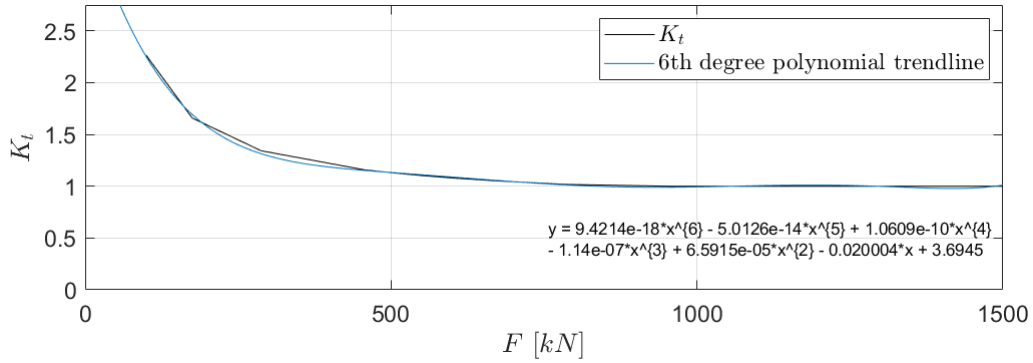

Figure 3.17: K_t as a function of the applied vertical force, F $[kN]$.

The values of K_t that were taken into account when the Neuber rule was applied are the ones presented at Table 3.9. The average value of the SCF represented by $K_{t_{avg}}$ is calculated with the values of K_t from $F = 100$ to $F = 787.5$ kN.

Table 3.9: Values of the SCF to be used with the Neuber procedure.

$K_{t_{max}}$	2.26
$K_{t_{avg}}$	1.31
$K_{t_{power}}$	Equation 3.7

$$K_t = 9.7455 \cdot 10^{-16} {\sigma_{nom}}^6 - 2.3932 \cdot 10^{-12} {\sigma_{nom}}^5 + 2.3378 \cdot 10^{-9} {\sigma_{nom}}^4 \\ -1.1594 \cdot 10^{-6} {\sigma_{nom}}^3 + 3.0942 \cdot 10^{-4} {\sigma_{nom}}^2 - 4.3341 \cdot 10^{-2} \sigma_{nom} + 3.6945 \tag{3.7}$$

3.4.4 Neuber's Rule

The Neuber's rule was used to obtain the rotating bending fatigue S-N curve for the classical axle with press-fits.

Neuber's rule establishes that the product of nominal stresses and strains is proportional to the to the product of the local elastoplastic stresses and strains. With Neuber's rule, nominal stresses/strains can be either elastic or elastoplastic.

For the present case, nominal stresses S come from elastic calculations. As so, the following formulation can be used (even if real stresses are above the yield strength):

$$(K_t S)^2 = E \sigma \varepsilon \tag{3.8}$$

For cyclic loading, instead of S one should use ΔS.

$$\frac{(K_t \Delta S)^2}{E} = \Delta \sigma \Delta \varepsilon \tag{3.9}$$

Combining Equation 3.9 with the cyclic stress-strain curve, the stress at the notch root, $\Delta\sigma$, can be obtained. After this, the range of local strains, $\Delta\varepsilon$, can be obtained too.

$$\frac{(K_t\Delta S)^2}{E} = \frac{\Delta\sigma^2}{E} + 2\Delta\sigma\left(\frac{\Delta\sigma}{2K'}\right)^{\left(\frac{1}{n'}\right)} \tag{3.10}$$

This equation can be solved with an iterative process or numerical techniques.

3.4.5 Strain-Based Approach to Life Estimation ($\varepsilon - N$)

$$\frac{\Delta\varepsilon_{EP}}{2} = \frac{\Delta\varepsilon_e}{2} + \frac{\Delta\varepsilon_p}{2} \tag{3.11}$$

The elastic behaviour can be transformed to Basquin's equation and the relation between plastic strain and life is the Coffin-Manson relationship [52].

The slopes of the elastic and plastic lines are b (fatigue strength exponent) and c (fatigue ductility exponent), respectively [52].

Therefore, the number of cycles to failure can be calculated according to the following equation [52]:

$$\frac{\Delta\varepsilon_{EP}}{2} = \frac{\sigma'_f}{E}(2N)^b + \varepsilon'_f(2N)^c \tag{3.12}$$

But first, parameters such as the fatigue ductility properties, the range of nominal stresses and the SCF had do be determined (the Young's modulus is also needed, but that has already been assessed previously, with E being equal to 206 [GPa]).

The fatigue ductility properties were extracted from the paper "On the fatigue performance and residual life of intercity railway axles with inside axle boxes" (Table 3.10) [25].

Table 3.10: Fatigue ductility properties for the EA4T steel.

σ'_f [MPa]	b	ε'_f	c
811.1	-0.069	0.658	-0.641

3.5 Elastoplastic Stress Analysis based on Numerical Modelling

The results obtained for the range of local elastoplastic stresses and strains with the Neuber's rule (for K_t varying with the nominal stress) are going to be compared with the results obtained with the numerical model (see Figure 3.18).

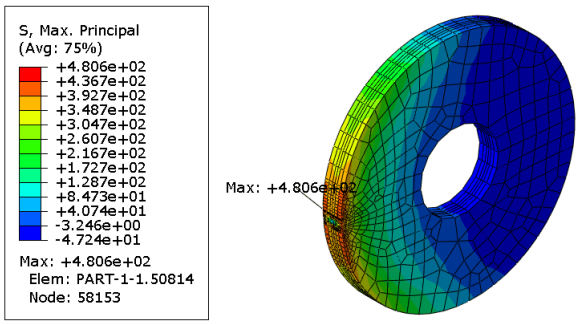

Figure 3.18: Colour map for the Maximum Principal stress [MPa] obtained by FE analysis at the critical stress region (elastoplastic analysis, $F = 1500$ [kN]).

Table 3.11: Comparison of the results obtained for the range of local elastoplastic stresses with the Neuber's rule (for K_t varying with the nominal stress) and with the numerical model.

	Range of local stresses EP [MPa]		
External load [kN]	Neuber's rule	FE software	Error (%)
1125	521.82	501.35	3.92
1000	458.78	452.06	1.46
875	401.92	403.89	0.49
750	355.40	356.21	0.23
625	311.05	308.79	0.73
500	261.72	261.16	0.21
375	208.73	213.31	2.19

Table 3.12: Comparison of the results obtained for the range of local elastoplastic strains with the Neuber's rule (for K_t varying with the nominal stress) and with the numerical model.

	Range of local strains EP		
External load [kN]	Neuber's rule	FE software	Error (%)
1125	0.00256	0.00215	16.02
1000	0.00224	0.00194	13.39
875	0.00195	0.00174	10.77
750	0.00173	0.00153	11.56
625	0.00151	0.00133	11.92
500	0.00127	0.00113	11.02
375	0.00101	0.00093	7.92

Analysing the results of Tables 3.11 and 3.12, it can be concluded that the results obtained with the numerical model agree very well with the ones obtained with the Neuber's rule. Even though a maximum error of 16% and an average error of 11.8% were found for the range of local elastoplastic strains, these errors are not as serious as they might seem at first sight as we are on the presence of very small values of strain.

3.6 Fatigue Modelling based on Local Stress Approaches

The Neuber rule and the Coffin-Manson relation were used to calculate the residual life for each stress level.

At this point, the rotating bending fatigue S-N curves for the classical axle with press-fits can be obtained. A different plot is generated for each K_t chosen for the Neuber procedure (See Tables 3.13 to 3.15 and Figures 3.19 to 3.21).

Table 3.13: Rotating bending fatigue S-N data for the classical axle with press-fits based on the Neuber's rule for $K_t = 2.26$ (data obtained by an iterative process).

Range of nominal stresses [MPa]	Range of local stresses EP [MPa]	Range of local strains EP	Number of cycles N_f
519.20	849.70	0.00787	4.81E+03
461.55	815.90	0.00647	8.98E+03
403.90	773.03	0.00523	2.06E+04
346.25	714.94	0.00416	6.79E+04
288.42	631.26	0.00327	4.38E+05
230.77	518.52	0.00255	7.68E+06
173.13	391.08	0.00190	4.52E+08
123.26	278.65	0.00135	6.12E+10

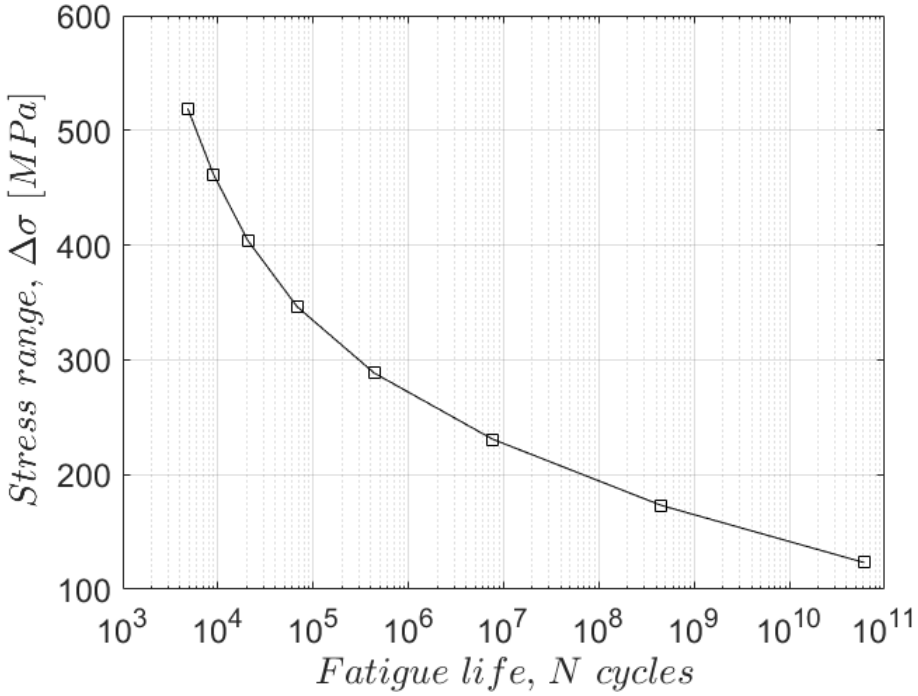

Figure 3.19: RB fatigue S-N curve for the classical axle with press-fits with $K_t = 2.26$.

Table 3.14: Rotating bending fatigue S-N data for the classical axle with press-fits based on the Neuber's rule for $K_t = 1.31$ (data obtained by an iterative process).

Range of nominal stresses [MPa]	Range of local stresses EP [MPa]	Range of local strains EP	Number of cycles N_f
519.20	652.03	0.00344	2.71E+05
461.55	593.34	0.00299	1.09E+06
403.90	525.65	0.00259	6.31E+06
346.25	452.79	0.00221	5.44E+07
288.42	377.76	0.00184	7.46E+08
230.77	302.30	0.00147	1.88E+10
173.13	226.89	0.00110	1.20E+12

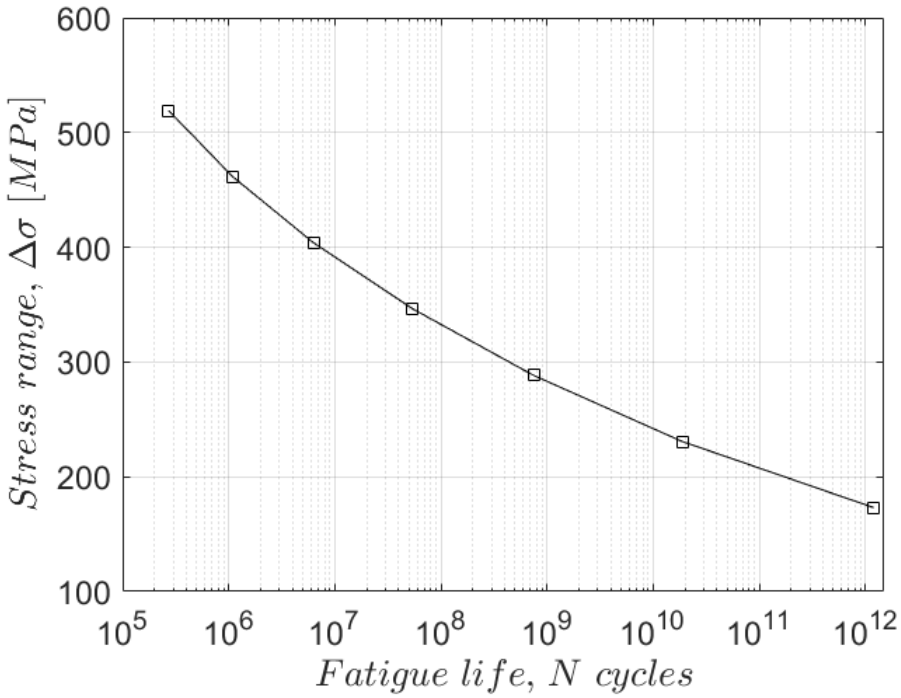

Figure 3.20: RB fatigue S-N curve for the classical axle with press-fits with $K_t = 1.31$.

Table 3.15: Rotating bending fatigue S-N data for the classical axle with press-fits based on the Neuber's rule for K_t as a function of the nominal stress (data obtained by an iterative process).

Range of nominal stresses [MPa]	Range of local stresses EP [MPa]	Range of local strains EP	Number of cycles N_f
519.20	521.82	0.00256	7.01E+06
461.55	458.78	0.00224	4.50E+07
403.90	401.92	0.00195	3.04E+08
346.25	355.40	0.00173	1.80E+09
288.42	311.05	0.00151	1.24E+10
230.77	261.72	0.00127	1.52E+11
173.13	208.73	0.00101	4.03E+12

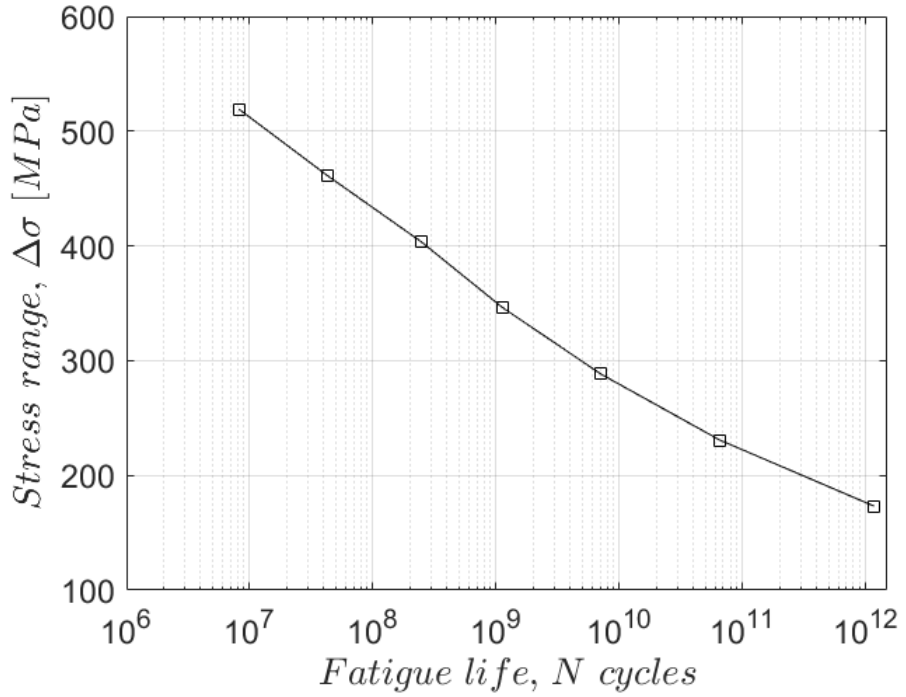

Figure 3.21: RB fatigue S-N curve for the classical axle with press-fits with K_t as a function of the nominal stress.

3.7 Admissible stress levels for different sections of railway axles

Based on standards EN13103/EN13104, another methodology could be used to identify the admissible stress levels. Admissible stress levels for different critical stress sections of railway axles can be derived by considering the respective stress concentration factor k_t:

$$\sigma_{admissible} = K_t \frac{32 M_{rb} D}{\pi (D^4 - d^4)} \leq \frac{\sigma_{lim,rb}}{\eta} \tag{3.13}$$

Variable M_{rb} and $\sigma_{lim,rb}$ correspond to the bending moment and fatigue limit for full-scale axles. The seat and bore diameters are represented by variables D and d, respectively. The security factor is represented by variable η.

According to the EN13104 standard, the fatigue limits for hollow axles are the following ones:

- 240 [MPa] outside the fitting;
- 132 [MPa] beneath fitting, except bearing journal;
- 113 [MPa] outside fitting on the bearing journal;
- 96 [MPa] for the surface of the bore.

The security coefficient, η, value by which the fatigue limits have to be divided to obtain the maximum permissible stresses is calculated as follows:

$$\eta = 1.3 \ (or \ 1.5) \times \frac{q_{other \ steel}}{q_{steel \ EA1N}} \tag{3.14}$$

For powered hollow axles with press-fit driving gear or pinion of steel grade EA4T, the value of the security coefficient, S, should be derived as follows:

$$R_{fl} = 350 \ [MPa] \tag{3.15}$$

$$R_{fe} = 215 \ [MPa] \tag{3.16}$$

$$q = R_{fl}/R_{fe} = 350/215 = 1.63 \tag{3.17}$$

$$\eta = 1.5 \times \frac{1.63}{1.47} = 1.66 \tag{3.18}$$

One should realize that 1.66 corresponds to a minimum value for the security coefficient.

Intended use of the axle	Security coefficient S [a]	Zone 1 [b] N/mm²	Zone 2 [c] N/mm²	Zone 3 [d] N/mm²	Zone 4 [e] N/mm²
Powered axle with press-fit driving gear or pinion	1,66	145	80	68	58
Other cases	1,44	167	92	78	67

[a] Minimum value, unless measurements exist that demonstrate the loads are more precisely defined than those defined in this standard within an appropriate maintenance regime which maintains the track conditions, whereby a lower value of security coefficient S may be used if agreed between the designer and vehicle operator. However the security coefficient value S shall not be less than 1,33.

[b] Zone 1: axle body, plain bearing seats, fillets.

[c] Zone 2: all seats except journals and plain bearing seats.

[d] Zone 3: journal (beneath the rolling bearing).

[e] Zone 4: bore.

Figure 3.22: Maximum permissible constraints for hollow axles of steel grade EA4T (S is the same as η) [31].

3.8 Conclusions

The numerical model proved to be a great tool to perform linear elastic stress analysis.

Nevertheless, the issue regarding the variation of the stress concentration factor, K_t, should be further explored. It was observed that the interference fits would lead to the appearance of non-linearities in the numerical model. These non-linearities have leaded to a non-constant SCF as the vertical load increased.

Analysing the three RB fatigue S-N curves presented in this chapter, it can be concluded that the values assumed for K_t in the critical stress region have a notorious influence on the life estimation for the classical axles with press-fits:

- If the maximum value of the SCF, $K_t = 2.26$, is assumed for all the load steps, the impact on the residual life is severe. The fatigue limit is close to $200/2 = 100$ $[MPa]$ (the variable on the vertical axis is stress range and not stress amplitude).

- If an average value of the SCF is assumed for all load steps, $K_t = 1.31$, the fatigue limit is around $400/2 = 200$ $[MPa]$ which is the double of the value obtained for $K_t = 2.26$.

- Assuming a variation of K_t according to the applied load (or nominal stress) leads to significantly different results. If Figure 3.21 is observed, it can be seen that the fatigue limit for a variable K_t is around $500/2 = 250$ $[MPa]$ which is 2.5 times higher than the value obtained for $K_t = 2.26$.

The numerical analysis used to predict fatigue life will be compared with an S-N probabilistic evaluation for the rail axle being studied. Furthermore, the numerical model presented in this chapter will be used together with reliability analysis to predict a S-N probabilistic field based on statistical distributions for material's properties.

Chapter 4

Probabilistic Fatigue Analysis of Railway Axles based on Small-Scale Fatigue Data

An experimental campaign was carried out at the State Key Laboratory of Traction Power, in China, to study fatigue behaviour and fracture mechanics of EA4T hollow axles by doing rotating bending and axial fatigue tests. The results of these fatigue tests were provided by the TPL in order to support the work developed in this thesis. In this Chapter, the experimental results are going to be analysed through a probabilistic analysis and using the EN13103/EN13104 method.

4.1 Rotating Bending High Cycle Fatigue Tests

4.1.1 Introduction

Fatigue fracture is one of the main mechanical problems of high-speed railway axles. Ensuring that fatigue fracture does not happen is demanding to guarantee safety, reliability and long service life (30 years of service or 10^9 cycles). There will be a focus on the rotating bending fatigue tests as they are more relevant for the scope of this thesis.

4.1.2 Test Material - EA4T Steel Composition and Properties

The chemical composition of medium strength EA4T steel grade is presented on Table 4.1.

Table 4.1: Main chemical compositions of medium strength EA4T steel grade (wt.%).

Cr	Mo	Cu	Or	V	C	Si	Mn	P	S
0.90-1.20	0.15-0.30	0.30	0.30	0.06	0.22-0.29	0.15-0.40	0.50-0.80	0.02	0.015

The mechanical properties of the EA4T steel should be $R_{p0.2} \geq 420$ *MPa*, $R_m \geq 650$ *MPa*, and the tensile fracture elongation should be $\geq 18\%$ [32].

4.1.2.1 Monotonic Data

Prior to conducting the fatigue tests, the monotonic behaviour was also obtained by monotonic tensile testing. The data obtained is summarized on Table 4.2.

Table 4.2: Monotonic tensile properties [32].

Axle type	Location of the samples	E [*GPa*]	$R_{p0.2}$ [*MPa*]	R_m [*MPa*]	$\varepsilon_{fracture}$ [%]
Powered	Exterior surface	225.03	590.66	722.46	17.45
	Core area	214.01	555.30	703.76	18.90
	Inner surface	214.58	538.87	693.20	16.96
Non-powered	Exterior surface	200.49	587.26	728.81	20.39
	Core area	201.60	555.42	707.93	20.32
	Inner surface	203.67	520.15	677.99	21.20

4.1.3 Samples

Taking into consideration that the heat treatment process can result in a different material performance on the outer surface, mid-section and inner surface, samples needed to be extracted from these three different regions [32].

Figure 4.1 shows the hollow axle from where the specimens were extracted.

Rounded dog-bone samples were extracted from these three different locations of the axle (Figures 4.2 to 4.4).

Figure 4.1: Railway vehicle hollow axle from where the specimens were extracted (EA4T steel) [32].

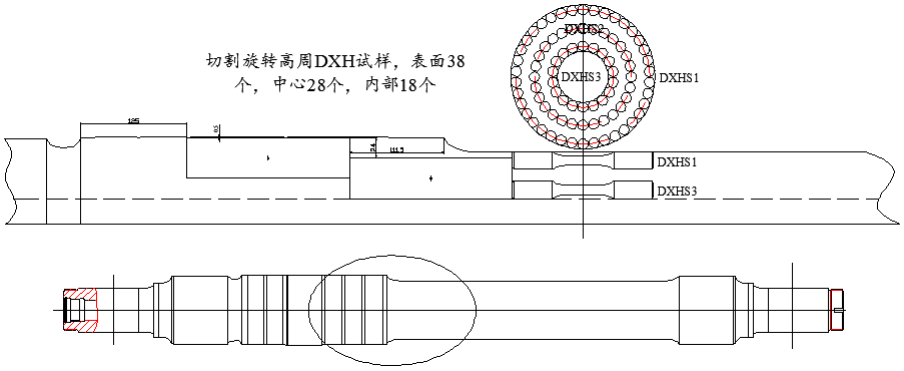

Figure 4.2: Regions from where the samples were extracted for rotating bending fatigue tests [32].

Figure 4.3: Extraction of samples [32].

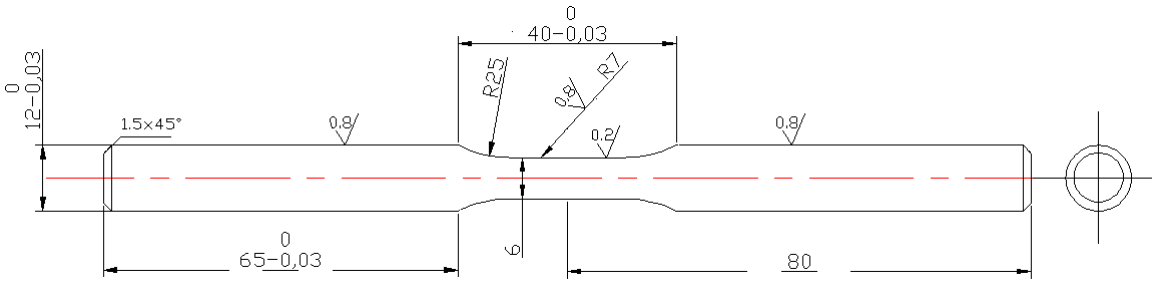

Figure 4.4: Dimensions of the samples used for rotating bending fatigue tests.

4.1.4 Test Basis

In order to perform these fatigue tests the standard GB/T 4337-2008 was taken into account. This standard applies to metallic materials fatigue tests. It specifies the metallic material rotating rod bending fatigue test methods.

4.1.5 Test Equipment

The equipment for carrying out the rotating bending fatigue tests was a PQ-6 rotary bending fatigue testing machine (Figure 4.5). The frequency chosen for the RB fatigue tests was 50 *Hz*.

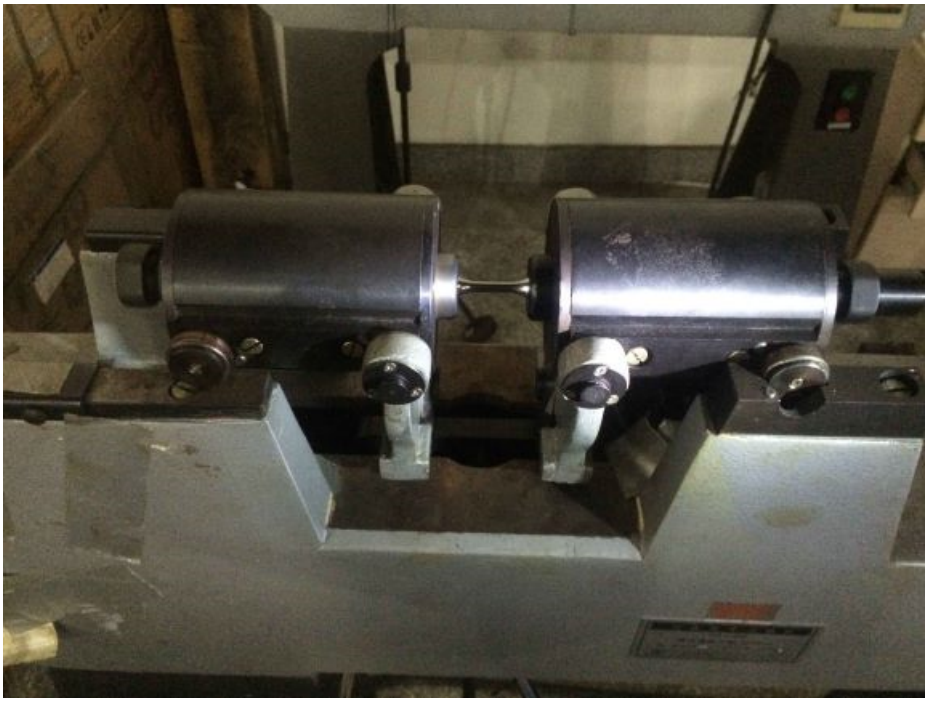

Figure 4.5: PQ-6 rotary bending fatigue testing machine [32].

4.1.6 Test Results

The stress ratio for the rotating bending experiments was always set to $R = -1$. This means that the minimum stresses were equal to the maximum stresses in terms of absolute value. This also means that the mean stress was zero. Tables 4.3, 4.4 and 4.5 contain the results of the rotating bending tests.

Table 4.3: Rotating bending test results for samples extracted from the region close to the outer surface.

Sample	Stress, σ_b [MPa]	Diameter [mm]	Load [N]	Cycles to failure, N_f
DHS1-1#	425	5.98	178.9	198929
DHS1-2#	400	6.00	169.6	1215085
DHS1-3#	450	6.01	191.8	318082
DHS1-4#	375	6.01	159.8	2027358
DHS1-5#	350	6.00	148.4	10^7 (unbroken)
DHS1-6#	375	6.03	161.4	2133338
DHS1-7#	425	5.98	178.7	634104
DHS1-8#	475	6.01	202.4	93343
DHS1-9#	362.5	6.03	155.7	10^7 (unbroken)
DHS1-10#	375	6.00	159.0	1869301
DHS1-11#	400	5.97	167.5	863540
DHS1-12#	450	6.00	190.8	252354

Table 4.4: Rotating bending test results for samples extracted the from mid-section region.

Sample	Stress, σ_b [MPa]	Diameter [mm]	Load [N]	Cycles to failure, N_f
DHS2-1#	375	5.99	157.9	1810404
DHS2-2#	400	6.01	170.0	365387
DHS2-3#	425	5.99	180.0	344534
DHS2-4#	375	6.03	161.3	1104765
DHS2-5#	350	6.02	149.7	2308748
DHS2-6#	337.5	6.01	143.6	10^7 (unbroken)
DHS2-7#	337.5	6.02	144.6	10^7 (unbroken)
DHS2-8#	350	6.01	149.2	2625910
DHS2-9#	400	6.03	171.9	519334
DHS2-10#	425	6.02	182.0	267326
DHS2-11#	350	6.01	149.2	10^7 (unbroken)
DHS2-12#	375	6.04	161.5	944797

Table 4.5: Rotating bending test results for samples extracted from the region close to the inner surface.

Sample	Stress, σ_b [MPa]	Diameter [mm]	Load [N]	Cycles to failure, N_f
DHS3-1#	400	6.04	173.1	374939
DHS3-2#	375	5.98	157.4	850834
DHS3-3#	350	6.01	149.1	1877726
DHS3-4#	325	6.01	137.8	10^7(unbroken)
DHS3-5#	337.5	6.01	143.9	1688560
DHS3-6#	337.5	5.99	142.0	10^7 (unbroken)
DHS3-7#	350	5.99	147.9	1333456
DHS3-8#	375	6.02	160.2	457858
DHS3-9#	400	6.01	170.3	331812
DHS3-10#	425	6.02	182.0	208918
DHS3-11#	425	6.00	180.2	183485
DHS3-12#	350	6.00	148.4	2282416
DHS3-13#	337.5	5.97	141.0	1900077

4.2 Fatigue design assessment based on the EN13103/EN13104 method

In order to account for the transferability between laboratory specimens and full-scale axles for the same loading conditions, the nominal stress amplitude of laboratory specimens has to be modified:

$$\sigma_{a,fs} = \sigma_{a,ls}\alpha\beta\varepsilon C_{lot}/K_t \tag{4.1}$$

Where α, β, ε and C_{lot} are empirically-determined factors for the reliability coefficient, surface quality, geometry and loading type of small-scale specimens, respectively.

Scatter denoted by α should be considered to correct the fatigue limit of EA4T specimens.

$$\alpha = 1 + \phi^{-1}(1 - P_{fal})CV_{fs} \tag{4.2}$$

Where ϕ corresponds to the standard normal cumulative distribution function and CV_{fs} is the variation coefficient for the fatigue limit at a knee.

4.3 Procedures of ASTM E739-91 (2004)

Sometimes, the amplitude of the stress or strain is not constant during the whole duration of fatigue tests. When this happens, effective (equivalent) values of S or ε should be used.

In $S-N$ tests, the fatigue life N is the dependent (random) variable and S is the independent (controlled) one.

The distribution of fatigue life is not known, no matter the test. Actually, in some situations the distribution can be quite complex. For simplifying the analysis, this standard assumes that the logarithms of fatigue lives follow a normal distribution. It is also assumed that the variance of the logarithmic life is constant. In other words, the scatter in logN is assumed to be the same for low and high levels of stresses or strains [36].

$$\mu_{Y|X} = A + BX \tag{4.3}$$

In the previous equation, $\mu_{Y|X}$ represents the expected value of Y given X.

Regarding the samples, a random sample is mandatory to state that the specimens are representative of the conceptual universe about which statistical and engineering inference is made.

This standard also establishes the minimum number of specimens required on S-N testing according to the type of test (Table 4.6).

Table 4.6: Minimum number of specimens required on S-N testing according to the type of test [36].

Type of test	Minimum number of specimens
Preliminary and exploratory (exploratory research and development tests)	6 to 12
Research and development testing of components and specimens	6 to 12
Design allowable data	12 to 24
Reliability data	12 to 24

Table 4.7: Percent replication according to the type of test [36].

Type of test	Percent replication
Preliminary and exploratory (exploratory research and development tests)	17 to 33 min
Research and development testing of components and specimens	33 to 50 min
Design allowable data	50 to 75 min
Reliability data	75 to 88 min

The percent replication represents the portion of the total number of specimens tested that can be used to obtain an estimate of the variability of replicate tests (Table 4.7).

$$\%replication = 100 \times \left(\frac{Total\ number\ of\ different\ stress/\ strain\ levels\ tested}{Total\ number\ of\ specimens\ tested} \right) \quad (4.4)$$

Assuming a constant variance is typically reasonable for notched and joint specimens with a number of cycles to failure up to 10^6. Normally, the variance of unnotched specimens increases with decreasing stress level.

4.3.1 Estimated S-N curve of a component based on ultimate tensile strength

There are techniques for estimating an S–N curve when only limited information is available.

For the HCF region, the slope of the S–N curve is denoted as b. Each of the variables used to calculate b can be fully understood by analysing Figure 4.6.

$$b = \frac{logS_{1000} - logS_{be}}{logS_{10^3} - log10^6} = -\frac{1}{3} log \left(\frac{S_{1000}}{S_{be}} \right) \quad (4.5)$$

The inverse slope of the curve is represented by k.

$$k = -\frac{1}{b} \quad (4.6)$$

If fatigue behaviour is dominated by the crack propagation stage (welded joints, sharp notched components and others), the S–N curve typically possesses a steeper slope ($b \approx 3$; $k \approx 3$). If fatigue behaviour is dominated by the crack initiation mode (smooth and blunt notched components, for instance), the S–N curve has a flatter slope ($b \approx -0.15$; $k \approx 7$).

There are a few factors that influence the fatigue behaviour and therefore, directly influence S-N curves. These factors are the reliability coefficient, surface quality, geometry effect and loading type factors.

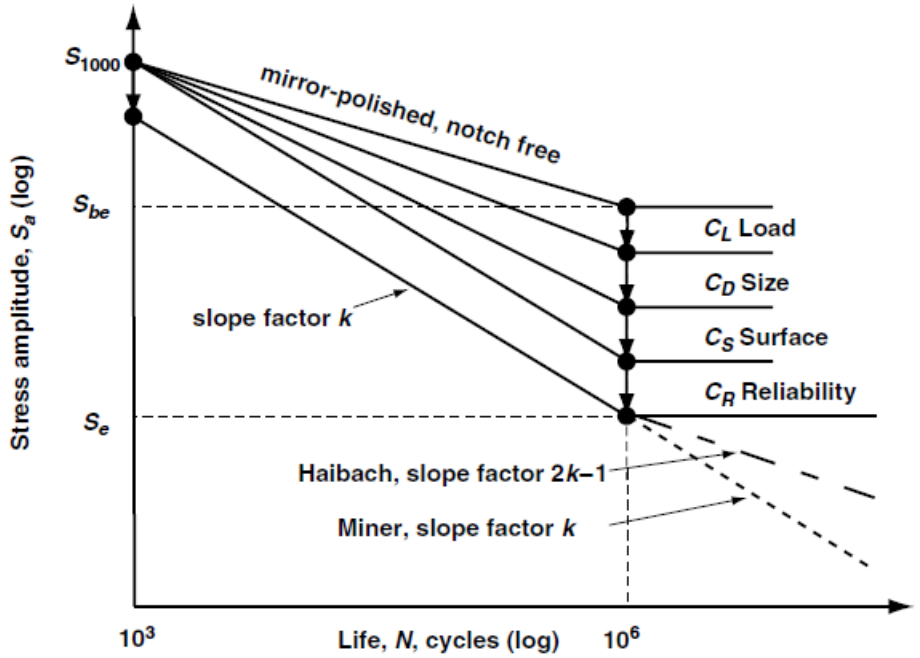

Figure 4.6: Modified S–N curves for smooth components made of steels [33].

4.3.2 Estimated Fatigue Limit

When fatigue tests have to be ended at a specific large number of cycles (10^7, for example), this non-failure stress amplitude is assumed as the endurance limit.

For ultimate tensile strengths below 1400 *MPa*, the bending fatigue limit, S_{be}, at 10^6 for steels can be estimated as half of the ultimate tensile strength.

The fatigue limit S_e can be estimated by multiplying the bending fatigue limit by four factors:

- Loading factor (C_L);
- Surface finish (C_S);
- Size (C_D);
- Reliability level (C_R).

$$S_e = S_{be} \times C_L \times C_S \times C_D \times C_R \tag{4.7}$$

4.3.3 Modifying Factor for the Type of Loading (C_L) at the Fatigue Limit

Table 4.8 contains the values for the modifying Factor according to the type of loading.

Table 4.8: Load Factors, C_L [33].

Type of Loading	C_L	Comments
Pure axial loading	0.9	
Axial loading (with slight bending)	0.7	
Bending	1.0	
Torsional	0.58	For steels
Torsional	0.8	For cast iron

4.3.4 Modifying Factor for the Surface Finishing (C_S) at the Fatigue Limit

Most of fatigue cracks initiate at the free surface of a material. Therefore, the surface condition of a test sample is of extreme importance. Two factors are used to characterize the surface condition:

- Notch-like surface irregularities or roughness;
- Residual stress in the surface layer.

Figures 4.7 and 4.8 show how to obtain the modifying factor for the surface finishing Factor, C_S.

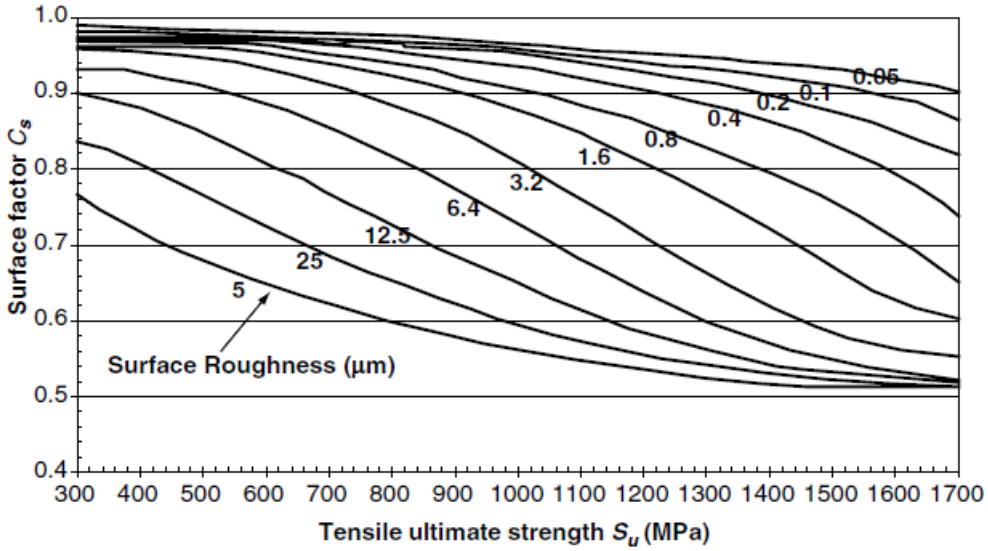

Figure 4.7: Qualitative description of C_S surface finish factor [33].

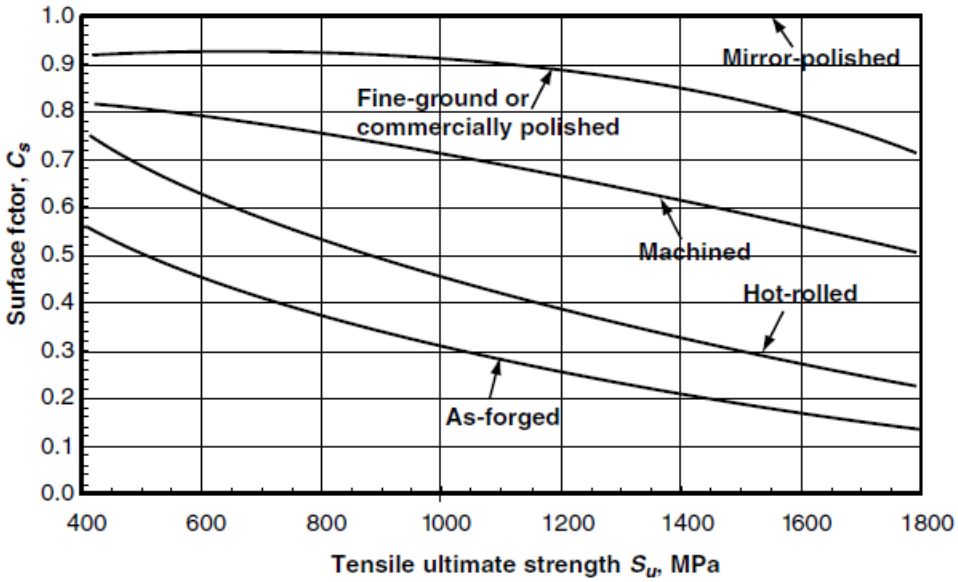

Figure 4.8: Qualitative description of C_s surface finish factor [33].

Normally, the surface finish is more critical for high-strength steels in a HCF regime where crack initiation dominates the fatigue life. For short lives, the crack propagation stage dominates the fatigue life and the effect of surface finish on fatigue strength is not so important.

4.3.5 Modifying Factor for the Specimen Size (C_D) at the Fatigue Limit

Figure 4.9 contains the values for the modifying Factor according to the type of loading

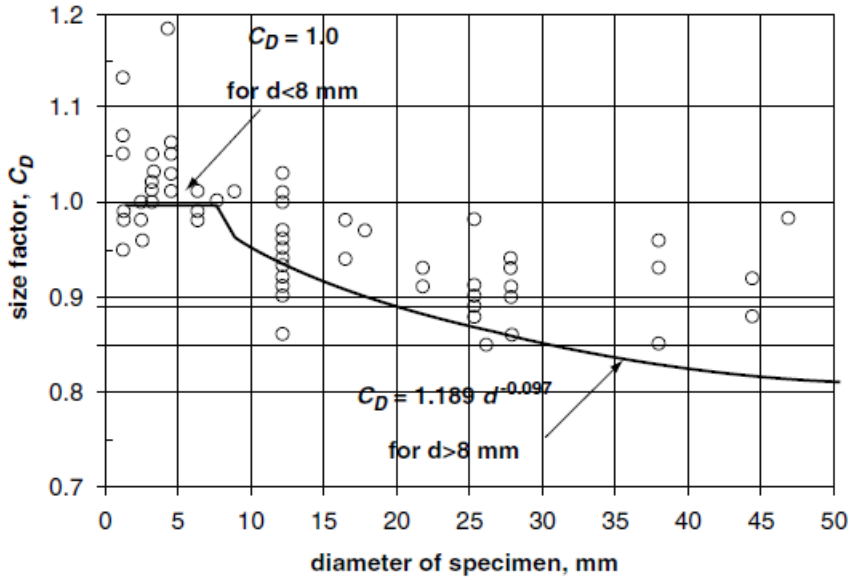

Figure 4.9: Quantitative description of the size factor (C_D) [33].

4.3.6 Modifying Factor for Reliability, C_R, at the Fatigue Strength at 10^3 Cycles

If statistical scatter of fatigue data is taken into account, the fatigue strength of a component would be changed from the median baseline S–N data for a certain reliability level.

The reliability factors presented on the Table 4.10 can also be used for estimating the fatigue strength at the fatigue limit.

Table 4.9: Estimates of S_{1000} [33].

Type of Material	Type of Loading	S_{1000}
All	Bending	$0.9 \times S_u$
All	Axial	$0.75 \times S_u$
Steel	Torsion	$0.9 \times S_{us} = 0.72 \times S_u$
Nonferrous	Torsion	$0.9 \times S_{us} = 0.63 \times S_u$
Cast iron	Torsion	$0.9 \times S_{us} = 1.17 \times S_u$

Table 4.10: Reliability factors (C_R) [33]

Reliability	C_R
0.50	1.000
0.90	0.897
0.95	0.868
0.99	0.814
0.999	0.753
0.9999	0.702
0.99999	0.659
0.999999	0.620

4.3.7 Derivation of reliability factors, C_{S_e}

$$S_{e,R} = C_R \times \mu_{S_e} \tag{4.8}$$

The fatigue limit with a reliability R can be establish as:

$$S_{e,R} = \mu_{S_e} - \phi^{-1}(1-R) \times (\sigma_{S_e}) = \mu_{S_e} - \phi^{-1}(1-R) \times C_{S_e} \times \mu_{S_e} \tag{4.9}$$

Table 4.11 contains the reliability factor for $R = 0.90$, $R = 0.95$ and $R = 0.99$.

Table 4.11: Reliability factors [33].

R	$1-R$	$\phi^{-1}(1-R)$	C_R
0.90	0.1	−1.282	0.897
0.95	0.05	−1.645	0.868
0.99	0.001	−2.326	0.814

The fatigue performance of the axle surface is greater than the core region and the inner hole. And the fatigue performance of the core region is greater than the inner hole. This indicates that the axle fatigue strength is distributed along the radial direction. Specimens extracted close to the outer surface have higher fatigue limits. Also, the specimens extracted from the mid-section region have higher fatigue limits than the ones extracted closer to the inner surface. This means that as the distance from the outer surface increases, the S-N curves move downwards.

4.4 Probabilistic S-N Fields

At this point, the experimental data presented before can be used to generate the probabilistic rotating bending fatigue S-N curves for both small-scale and derived full-scale axles based on ASTM E739-91 standard.

The values adopted for the reliability coefficient α, the surface quality β, the geometry effect ε and the loading coefficient C_{lot} are the same used in the paper "On the fatigue performance and residual life of intercity railway axles with inside axle boxes" (see Table 4.12) [25].

Table 4.12: Correction factors for converting small-scale data into full-scale data.

α	β	ε	C_{lot}
0.91	0.90	0.86	1.00

RB fatigue S-N curves with failure probability of 50%, 5%-95% and 2.3%-97.7% were generated for small-sized and derived full-scale EA4T specimens, with confidence intervals of 75%. The difference between Figures 4.10 and 4.11 has to do with the value of K_t chosen to derive the probabilistic curves for the full-scale axles. Figure 4.10 corresponds to $K_t = 2.26$ and Figure 4.11 to $K_t = 1.31$.

The data obtained for the RB fatigue S-N curves for the classical axle with press-fits based on Neuber's rule is also present in Figures 4.10 and 4.11 and these values agree well with the probabilistic ones. As so, it can be stated that the numerical-analytical analysis described on Chapter 3 provided good results.

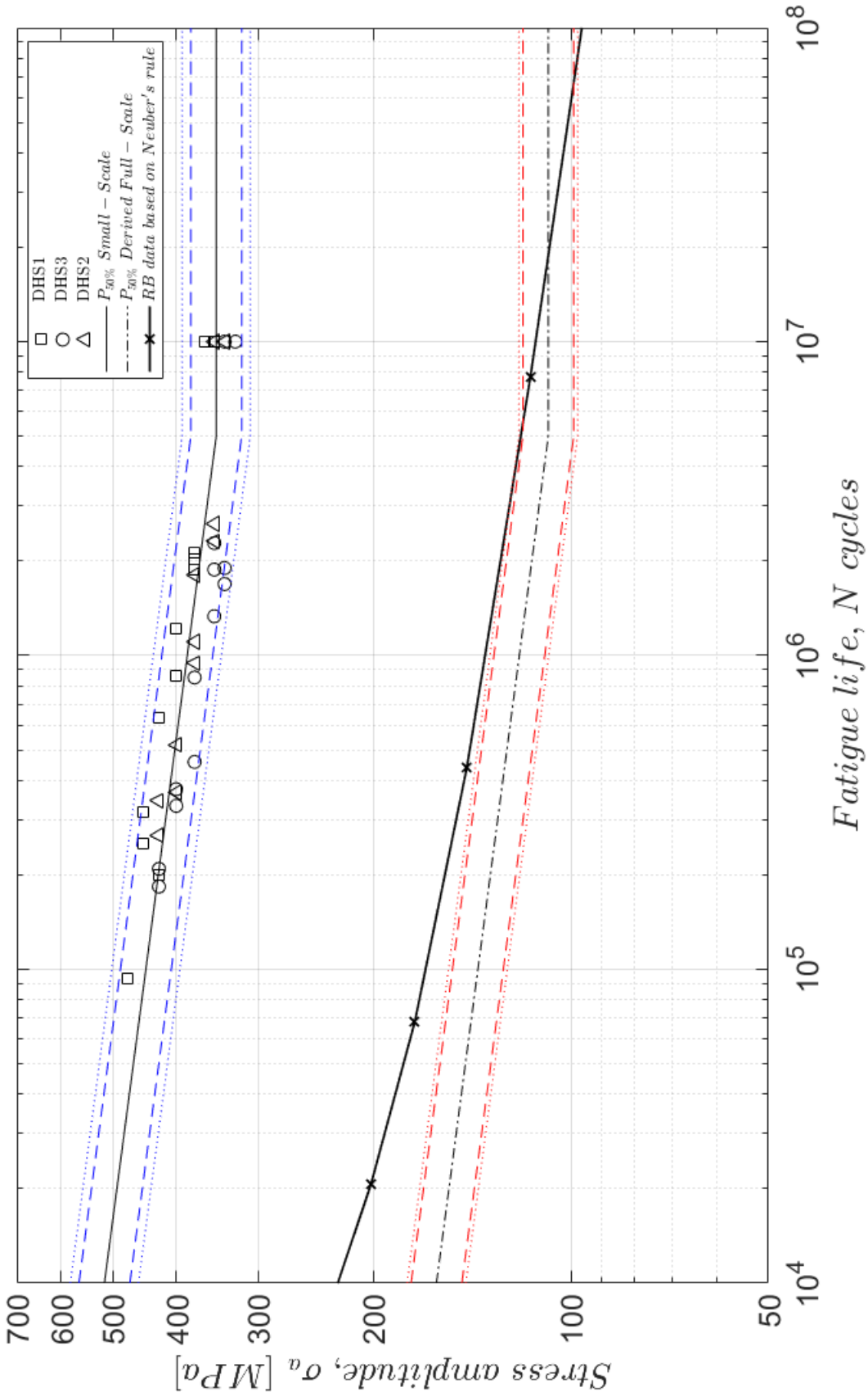

Figure 4.10: RB fatigue S-N curves with failure probability of 50%, 5%-95% and 2.3%-97.7% for small-sized and full-scale EA4T specimens with $K_t = 2.26$.

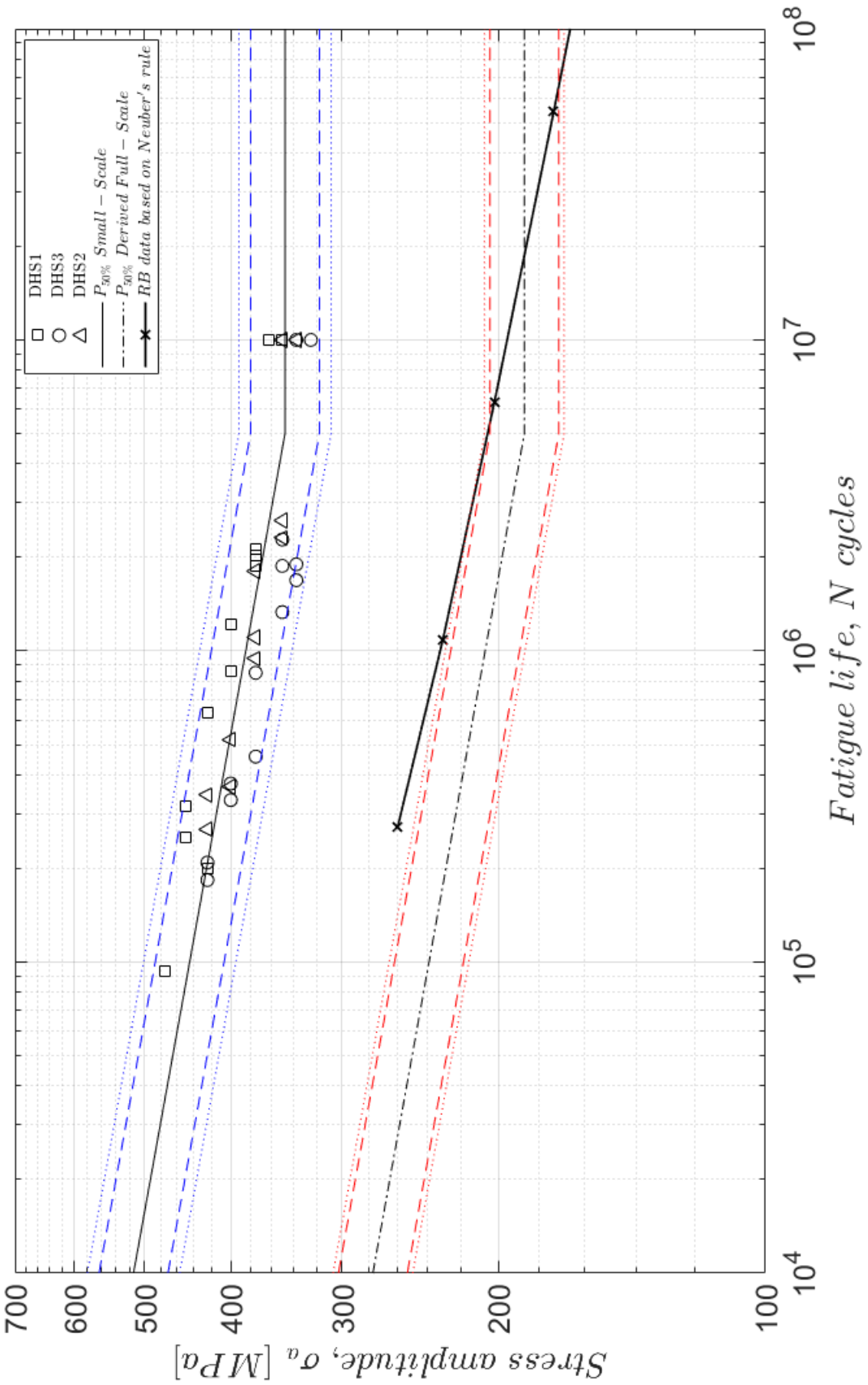

Figure 4.11: RB fatigue S-N curves with failure probability of 50%, 5%-95% and 2.3%-97.7% for small-sized and full-scale EA4T specimens with $K_t = 1.31$.

Chapter 5

Residual Fatigue Life of a Railway Axle

5.1 Introduction

In this study, it is intended to establish the mean curve for da/dN *vs* ΔK using the Paris law, in order to evaluate the residual life for different nominal stress levels.

As so, the stress intensity factor (SIF), ΔK, is determined for different levels of nominal stress using the standard BS7910. This way, based on the integration of the Paris law and using a fracture mechanics approach, using also the initial crack length, a_i, and imposing the critical stress intensity factor, K_C, the residual life can be evaluated.

5.2 Fatigue Crack Growth Characterization of the EA4T steel

Fatigue crack growth data was as well provided by the State Key Laboratory of Traction Power in order to help in the research conducted during this master's thesis.

Fatigue crack growth rate tests are employed to establish the relationship between crack growth (da/dN) and the stress intensity factor (ΔK) in the Paris region. The Paris law can be written as:

$$da/dN = C\Delta K^m \tag{5.1}$$

Several fatigue tests were done for mode I fatigue crack growth rate. In mode I, the propagation of the crack happens in the normal direction of the loading plane, due to normal tensile stresses that appear in the tip of the crack. Four different stress ratios were chosen: -1, 0, 0.1 and 0.5 (Figures 5.2 to 5.6). For stress ratios $R = 0.5$ and $R = -1$, it was necessary to start the tests with lower stress ratios in order to excite the force. Also, middle tension specimens (MT) were used for these (see Figure 5.1).

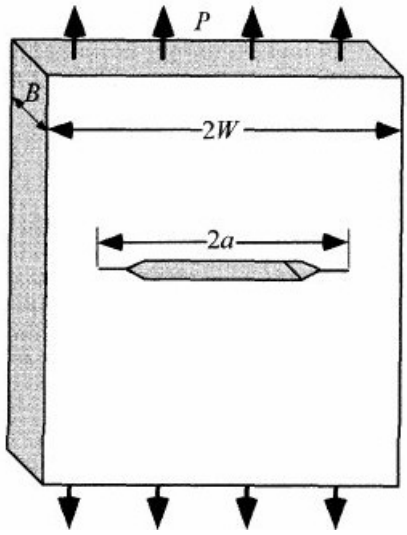

Figure 5.1: Standardized fracture mechanics test specimen: middle tension (MT) specimen [34].

For the present analysis, the dimension W of the test specimens was typically around 48 *mm* and B around 6 *mm*.

For each one of the stress ratios, plots were built relating the fatigue crack growth with the stress intensity factor range for data belonging to the Paris region. Then, power regressions were applied in order to calculate parameters C and m. Afterwards, plots containing the relevant data and the Paris law were built for each stress ratio.

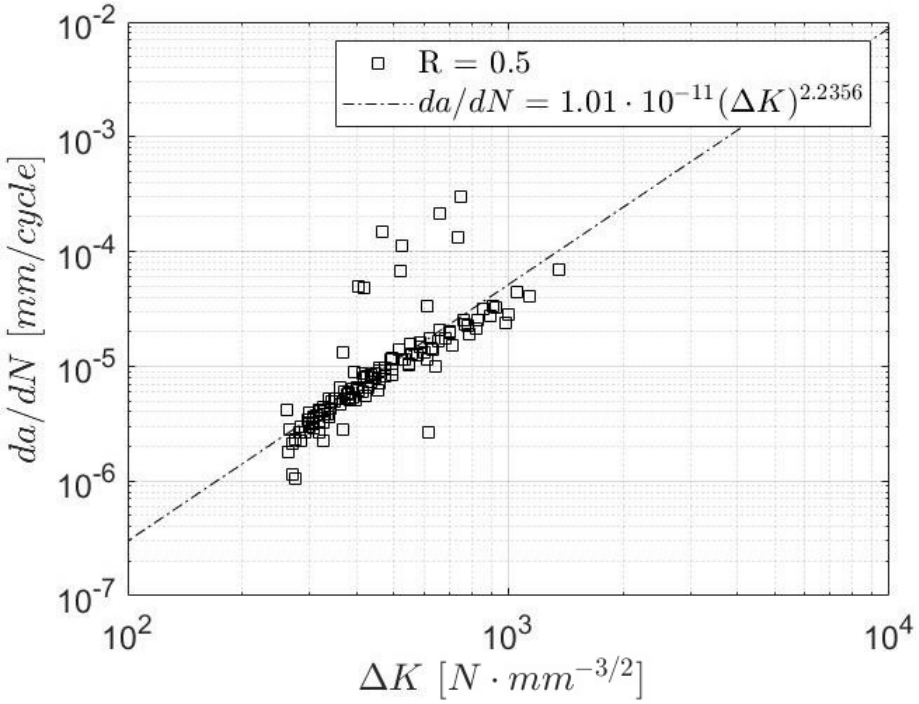

Figure 5.2: Fatigue crack growth data for the EA4T steel with $R = 0.5$.

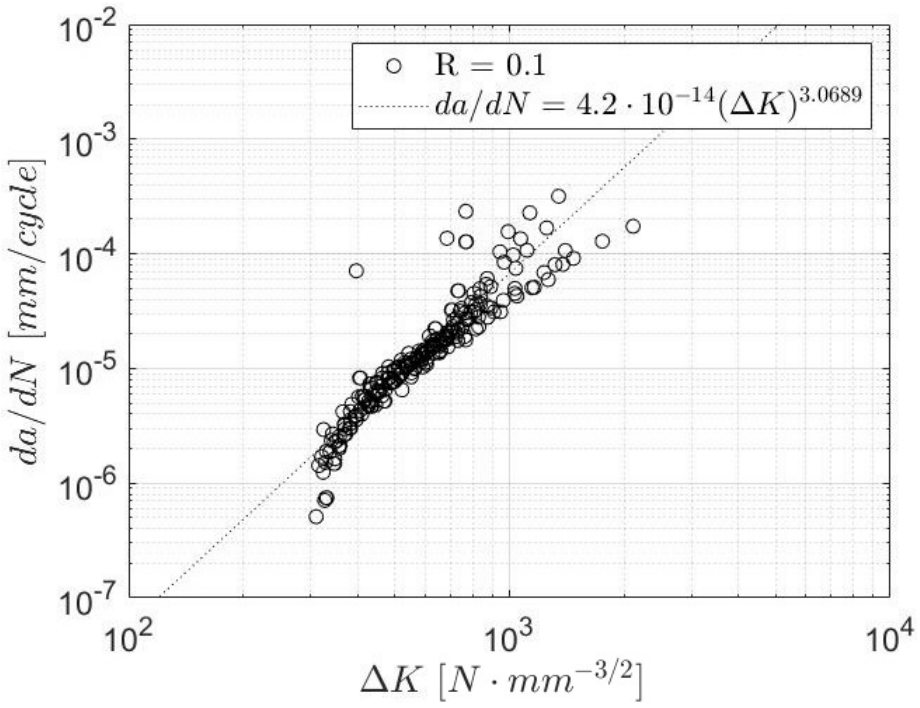

Figure 5.3: Fatigue crack growth data for the EA4T steel with $R = 0.1$.

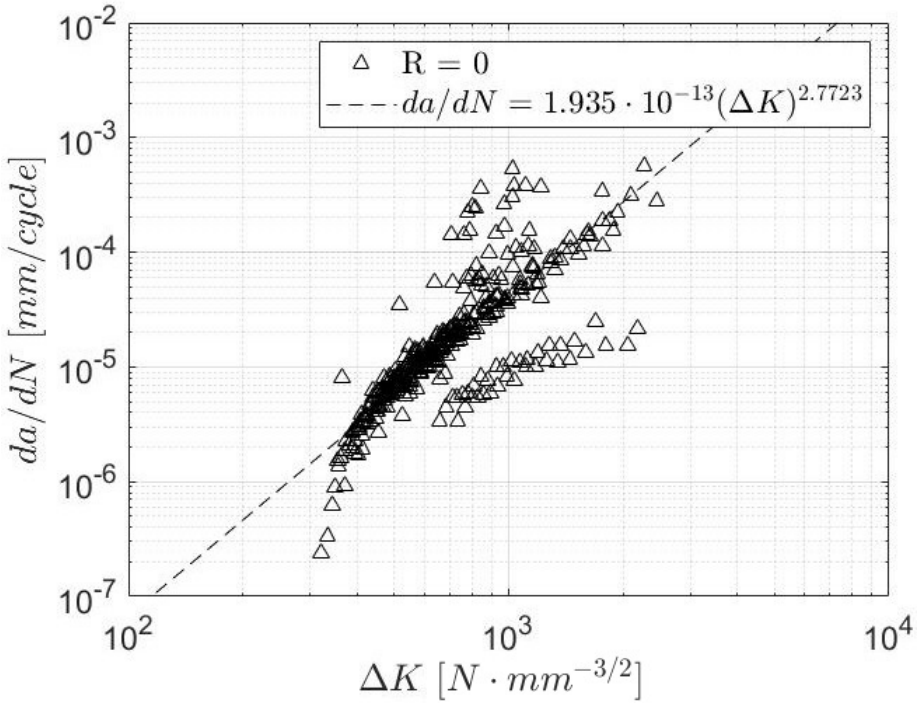

Figure 5.4: Fatigue crack growth data for the EA4T steel with $R = 0$.

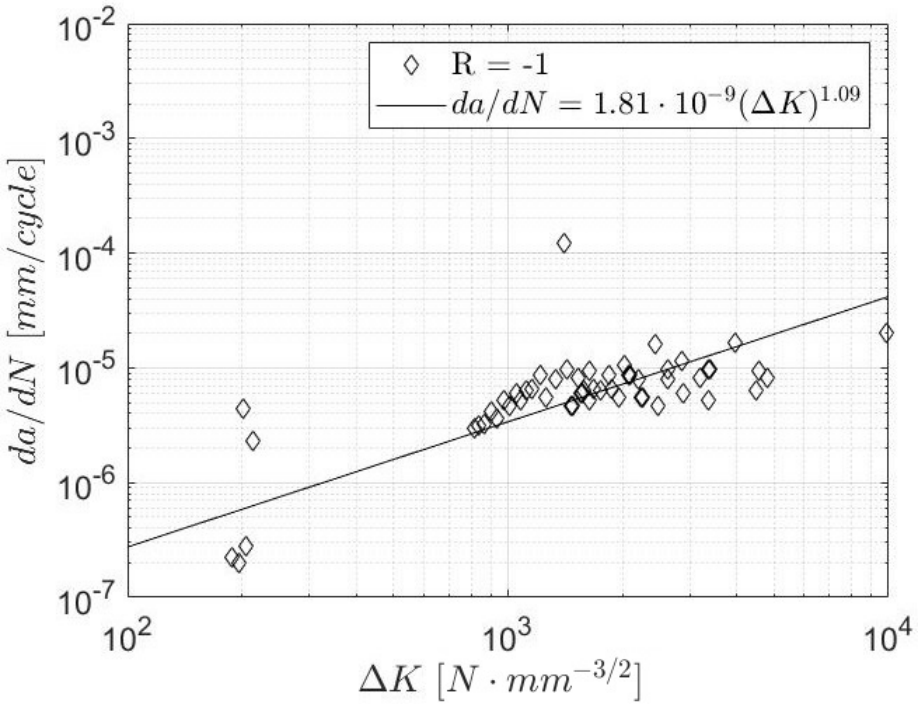

Figure 5.5: Fatigue crack growth data for the EA4T steel with $R = -1$.

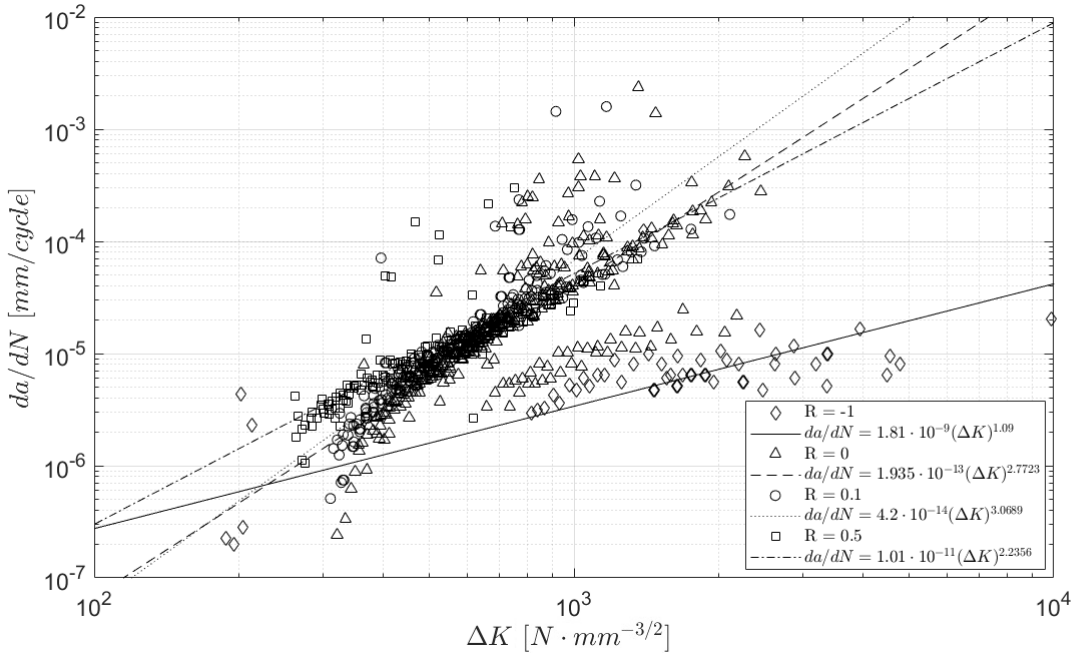

Figure 5.6: Fatigue crack growth data for the EA4T steel for various stress ratios.

It can be concluded that for a positive stress ratio, the effect on the residual life is not significant. The same cannot be said about negatives stress ratios, $R < 0$, where the effect of average stresses is clearly seen.

5.3 Fracture Mechanics based Approach

The residual life of a structural component is based on fracture mechanics approach by integrating the Paris law and obtaining the stress intensity factor.

The British Standard BS7910 was used to predict the stress intensity factor solution for an external surface flaw in a cylinder oriented circumferentially.

According to the standard BS7910, the following procedure should be followed:

- Determine the initial crack size: a_i
- Determine the final crack size: a_f / Determine: K_C (K_{max})
- Determine the stress range: $\Delta\sigma$
- Divide the path between a_i and a_f in x steps: $\Delta a = (a_f - a_i)/x$
- For all steps:
  - Calculate ΔK on the beginning of each step
  - Calculate ΔN for each step: $\Delta N = \frac{\Delta a}{C\Delta K^m}$
  - $a_{i+1} = a_i + \Delta a$
  - $N_{i+1} = N_i + \Delta N$
- Summation of ΔN for all steps: $N = \sum \Delta N$

Also, the standard BS7910 states that the solution for flat plates can be adopted to circumferential external surface flaws in cylinders.

Studies have shown that the crack shape based on fractured full-scale axles and small-scale rods is normally a semi-ellipse (Figure 5.7).

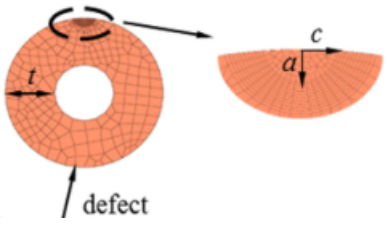

Figure 5.7: Semi-elliptical surface crack in a hollow axle [25].

5.3.1 Stress Intensity Factor Calculation

For fatigue assessments, the SIF can be calculated with the following equation:

$$\Delta K_I = Y(\Delta\sigma)\sqrt{\pi a} \tag{5.2}$$

For surface flaws in plates, $M = 1$ and f_w is given by:

$$f_w = \left[sec\left((\pi c/W)(a/B)^{0.5}\right)\right]^{0.5} \tag{5.3}$$

Concerning fracture assessments, the following equation is applied for the normal procedure - Level 2 (different levels of treatment of flaws are possible):

$$Y\sigma = (Y\sigma)_p + (Y\sigma)_s \tag{5.4}$$

Where $(Y\sigma)_p$ is related with primary stresses and $(Y\sigma)_s$ is related with secondary stresses.

$$(Y\sigma)_p = M \cdot f_w \left[k_{tm} M_{km} M_m P_m + k_{tb} M_{kb} M_b \left(P_b + (k_m - 1) P_m\right)\right] \tag{5.5}$$

$$(Y\sigma)_s = M_m Q_m + M_b Q_b \tag{5.6}$$

For the present case, secondary stresses are not considered which results in $Y\sigma = (Y\sigma)_p$.

For fatigue purposes, the next equation is applied:

$$(Y\Delta\sigma)_p = M \cdot f_w \left[k_{tm} M_{km} M_m \Delta\sigma_m + k_{tb} M_{kb} M_b \left(\Delta\sigma_b + (k_m - 1)\Delta\sigma_m\right)\right] \tag{5.7}$$

As we are not on the presence of welds, $M_{kb} = M_{km} = 1$. Also, $k_m = 1$ because there is no misalignment. Moreover, $k_{tm} = 1$ because there is no membrane loading.

For bending loading, the following conditions are applied:

$$M_b = H \cdot M_m \tag{5.8}$$

$$M_m = \left(M_1 + M_2(a/B)^2 + M_3(a/B)^4\right) g \cdot f_\theta / \Phi \tag{5.9}$$

M_1	=	$1.13 - 0.09(a/c)$	for $0 \le a/2c \le 0.5$
M_1	=	$(c/a)^{0.5}\{1 + 0.04(c/a)\}$	for $0.5 < a/2c \le 1.0$
M_2	=	$[0.89/\{0.2 + (a/c)\}] - 0.54$	for $0 \le a/2c \le 0.5$
M_2	=	$0.2(c/a)^4$	for $0.5 < a/2c \le 1.0$
M_3	=	$0.5 - 1/\{0.65 + (a/c)\} + 14\{1 - (a/c)\}^{24}$	for $a/2c \le 0.5$
M_3	=	$-0.11\,(c/a)^4$	for $0.5 < a/2c \le 1.0$
g	=	$1 + \{0.1 + 0.35(a/B)^2\}(1 - \sin\theta)^2$	for $a/2c \le 0.5$
g	=	$1 + \{0.1 + 0.35(c/a)(a/B)^2\}(1 - \sin\theta)^2$	for $0.5 < a/2c \le 1.0$
f_θ	=	$\{(a/c)^2 \cos^2\theta + \sin^2\theta\}^{0.25}$	for $0 \le a/2c \le 0.5$
f_θ	=	$\{(c/a)^2 \sin^2\theta + \cos^2\theta\}^{0.25}$	for $0.5 < a/2c \le 1.0$

Φ, the complete elliptic integral of the second kind, may be determined from standard tables or from the following solution, which is sufficiently accurate:

$\Phi = \{1 + 1.464(a/c)^{1.65}\}^{0.5}$	for $0 \le a/2c \le 0.5$
$\Phi = \{1 + 1.464(c/a)^{1.65}\}^{0.5}$	for $0.5 < a/2c \le 1.0$

$$H = H_1 + (H_2 - H_1)\sin^q \theta \tag{5.10}$$

where

$$\begin{aligned}
q &= 0.2 + (a/c) + 0.6(a/B) && \text{for } 0 \le a/2c \le 0.5 \\
q &= 0.2 + (c/a) + 0.6(a/B) && \text{for } 0.5 < a/2c \le 1.0 \\
H_1 &= 1 - 0.34(a/B) - 0.11(a/c)(a/B) && \text{for } 0 \le a/2c \le 0.5 \\
H_1 &= 1 - \{0.04 + 0.41(c/a)\}(a/B) + \{0.55 - 1.93(c/a)^{0.75} + 1.38(c/a)^{1.5}\}(a/B)^2 && \text{for } 0.5 < a/2c \le 1.0 \\
H_2 &= 1 + \mathrm{G1}(a/B) + \mathrm{G2}(a/B)^2
\end{aligned}$$

where

$$\begin{aligned}
G_1 &= -1.22 - 0.12(a/c) && \text{for } 0 \le a/2c \le 0.5 \\
G_1 &= -2.11 + 0.77(c/a) && \text{for } 0.5 < a/2c \le 1.0 \\
G_2 &= 0.55 - 1.05(a/c)^{0.75} + 0.47(a/c)^{1.5} && \text{for } 0 \le a/2c \le 0.5 \\
G_2 &= 0.55 - 0.72(c/a)^{0.75} + 0.14\,(c/a)^{1.5} && \text{for } 0.5 < a/2c \le 1.0
\end{aligned}$$

Once again, it is emphasized that membrane loadings are not present in this situation and only bending loadings are considered.

The stress intensity factor can be now calculated at the deepest point on the crack front ($\theta = \pi/2$) as a function of the crack length.

Table 5.1 contains relevant parameters to calculate the SIF as a function of the crack length.

Table 5.1: Relevant parameters to calculate the SIF as a function of the crack length.

a/2c	0.5
B	60 [mm]
θ	$\pi/2$ [rad]
k_{tb}	1.31

The variable B represents the width of the net cross-section. The value taken for k_{tb} was the average value calculated in 3 $K_{t_{avg}} = 1.31$. For an external surface flaw in a cylinder oriented circumferentially, f_w is equal to 1. Variables $G_1 = -1.41$ and $G_2 = -0.03$, always. The SIF can now be obtained as a function of the crack length (see Table 5.2 and Figure 5.8).

Table 5.2: Calculation procedure for ΔK.

a	c	q	a/B	H_1	H_2	H	M_b	$Y\sigma$	ΔK
0.15	0.3	1.20	0.00250	0.99888	0.99665	0.9967	0.04846	0.06349	0.04358
0.2	0.4	1.20	0.00333	0.99850	0.99553	0.99553	0.04854	0.04358	0.0504
0.25	0.5	1.20	0.00417	0.99813	0.99442	0.99442	0.04861	0.06358	0.05644
0.3	0.6	1.20	0.00500	0.99775	0.99330	0.9933	0.04869	0.0504	0.06192
0.35	0.7	1.20	0.00583	0.99738	0.99218	0.99218	0.04876	0.06368	0.06698
0.4	0.8	1.20	0.00667	0.99700	0.99107	0.99107	0.04884	0.05644	0.0717
0.45	0.9	1.20	0.00750	0.99663	0.98995	0.98995	0.04892	0.06378	0.07619
0.5	1	1.21	0.00833	0.99625	0.98883	0.98883	0.04899	0.06192	0.08044
0.55	1.1	1.21	0.00917	0.99588	0.98771	0.98771	0.04907	0.0639	0.08449
0.6	1.2	1.21	0.01000	0.99550	0.98660	0.9866	0.04914	0.06698	0.08839
0.65	1.3	1.21	0.01083	0.99513	0.98548	0.9855	0.04922	0.06398	0.09214
0.7	1.4	1.21	0.01167	0.99475	0.98436	0.98436	0.0493	0.0717	0.09577
0.75	1.5	1.21	0.01250	0.99438	0.98325	0.98325	0.04938	0.06408	0.09929
(...)	(...)	(...)	(...)	(...)	(...)	(...)	(...)	(...)	(...)
28.5	57	1.49	0.47500	0.78625	0.35673	0.35673	0.18938	0.24809	2.34751
29	58	1.49	0.48333	0.78250	0.34533	0.34533	0.19693	0.25798	2.46237
29.5	59	1.50	0.49167	0.77875	0.33391	0.33391	0.20500	0.26854	2.58525
30	60	1.50	0.50000	0.77500	0.32250	0.3225	0.21364	0.27987	2.71700
30.5	61	1.51	0.50833	0.77125	0.31108	0.31108	0.22292	0.29203	2.85860
31	62	1.51	0.51667	0.76750	0.29966	0.29966	0.23292	0.30513	3.01117
31.5	63	1.52	0.52500	0.76375	0.28823	0.28823	0.24371	0.31926	3.17600
32	64	1.52	0.53333	0.76000	0.27680	0.2768	0.25540	0.33457	3.35461
32.5	65	1.53	0.54167	0.75625	0.26536	0.26536	0.26810	0.35121	3.54877
33	66	1.53	0.55000	0.75250	0.25393	0.25393	0.28194	0.36934	3.76058
33.5	67	1.54	0.55833	0.74875	0.24248	0.24248	0.29708	0.38918	3.99254
34	68	1.54	0.56667	0.74500	0.23103	0.23103	0.31373	0.41099	4.24761
34.5	69	1.55	0.57500	0.74125	0.21958	0.21958	0.33211	0.43507	4.52942
35	70	1.55	0.58333	0.73750	0.20813	0.20813	0.35251	0.46179	4.84237

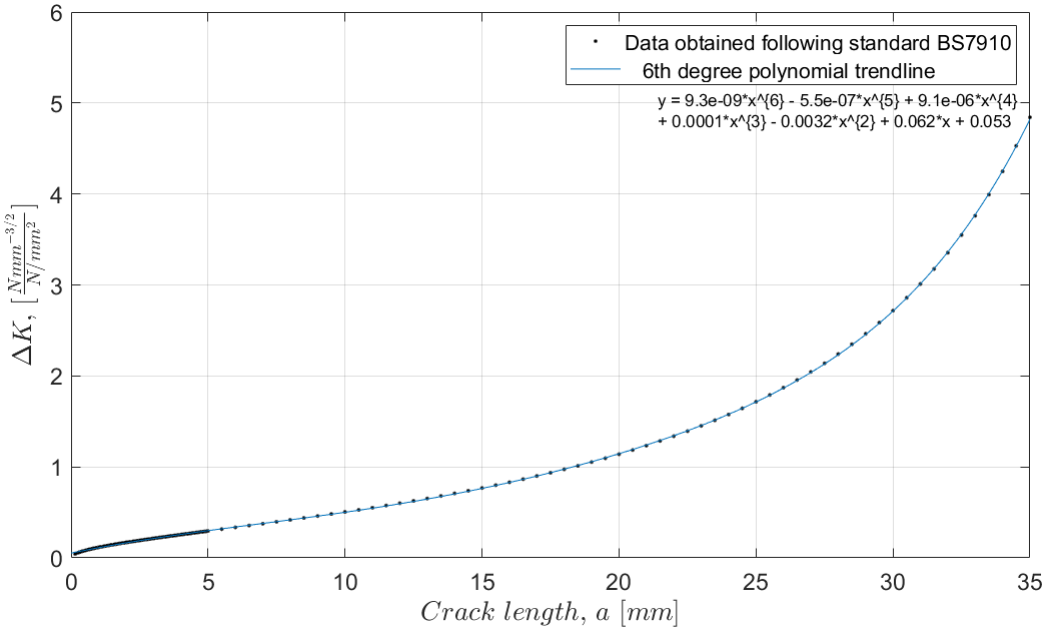

Figure 5.8: SIF as a function of the crack length.

5.3.2 Residual Life Estimation

Now that the SIF was obtained as a function of the crack length, the relation between the stress range, $\Delta\sigma$, and the number of cycles of propagation, N_p, can also be obtained. However, before that, the equation that relates the crack growth (da/dN) and the SIF (ΔK) in the Paris region should be established, for all stress ratios used in the experiments:

$$da/dN = 4.423 \times 10^{-7} (\Delta K)^{2.661} \tag{5.11}$$

Table 5.3 contains the number of cycles of propagation for different stress ranges and different initial crack lengths, $a_i = 0.15$, $a_i = 0.5$ and $a_i = 1$, respectively.

Table 5.3: Number of cycles of propagation for different stress ranges with an initial crack length of $a_i = 0.15$ $[mm]$.)

$\Delta\sigma$ $[MPa]$	N_p
519.20	128
461.55	181
403.90	267
346.25	415
288.42	694
230.77	1287
173.13	2816
123.26	7022

Table 5.4: Number of cycles of propagation for different stress ranges with an initial crack length of $a_i = 0.5$ [mm].)

$\Delta\sigma$ [MPa]	N_p
519.20	75
461.55	109
403.90	162
346.25	256
288.42	433
230.77	812
173.13	1791
123.26	4485

Table 5.5: Number of cycles of propagation for different stress ranges with an initial crack length of $a_i = 1$ [mm].)

$\Delta\sigma$ [MPa]	N_p
519.20	43
461.55	64
403.90	97
346.25	155
288.42	267
230.77	508
173.13	1134
123.26	2855

5.3.3 Conclusions

Analysing these results, it can be concluded that the appearance of cracks is a very serious issue and components should be immediately repaired or substituted.

The fatigue crack propagation phase is not determinant in the fatigue process and for this reason, the identification of cracks can be extremely important.

Chapter 6

Fatigue Reliability Analysis

6.1 Introduction

Structural reliability techniques such as the Monte Carlo Simulation Technique and Artificial Neural Networks were used to the fatigue life prediction of a railway axle.

MCST was found to be powerful tool for the present study, where the total number of possible outcomes was very large.

Concerning the Artificial Neural Network, it had to be calibrated before validation. The stress concentration factor that was used was $K_t = 1.5$. The Artificial Neural Network that was trained also proved to be a very powerful and accurate tool to predict results.

But first, the relevant parameters for fatigue analysis need to be collected. Some of them can be assumed as constant and others can be taken has random variables that are represented by probabilistic distributions.

6.2 Probabilistic Distributions of Fatigue Parameters

The fatigue approach used in this analysis is based on the Neuber rule and Ramberg-Osgood equation combined with the Coffin-Manson relation with aims to make the fatigue life prediction of the railway axle under consideration.

The properties of probabilistic distributions of parameters like K', σ'_f and ε'_f were derived based on the information obtained from the articles "On the fatigue performance and residual life of intercity railway axles with inside axle boxes" [25] and "Fatigue reliability of structural components" [53] (see Table 6.1 and Figures 6.1 to 6.3). In this analysis, the random variables were described by Log-Normal distributions. The probabilistic distributions were obtained based on maximum-likelihood estimation. Parameters such as the Young's modulus, E, the strain hardening exponent, n', the stress concentration factor, K_t, the fatigue strength exponent, b, and the fatigue ductility exponent, c, were assumed as constant.

Table 6.1: Properties of probabilistic distributions of fatigue parameters.

K' $[MPa]$	σ'_f $[MPa]$	ε'_f
Log-Normal	Log-Normal	Log-Normal
Mean = 806.3	Mean = 811.1	Mean = 0.658
COV = 10%	COV = 5%	COV = 10%

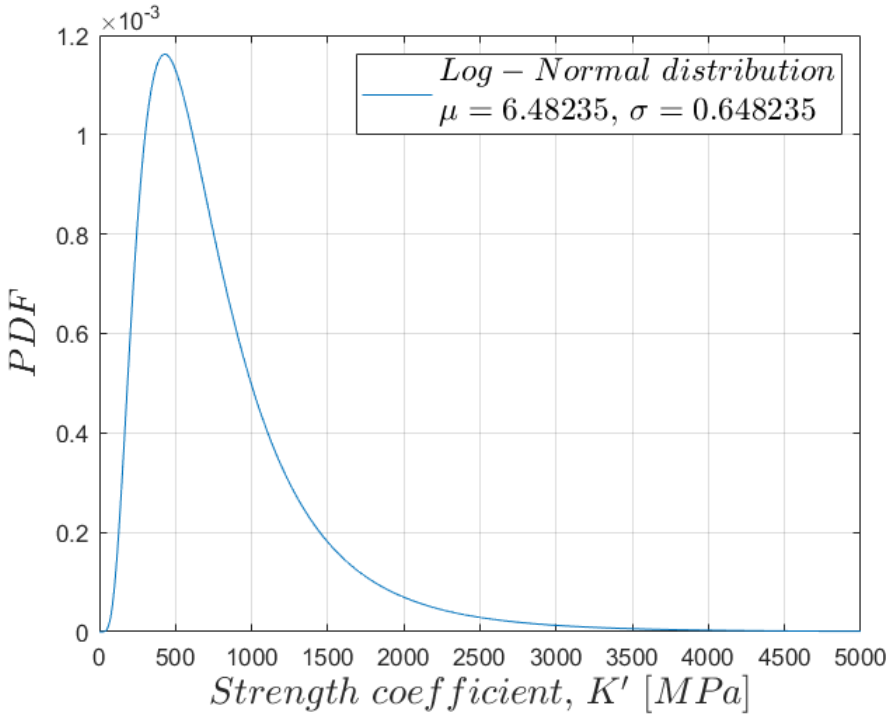

Figure 6.1: Probabilistic distribution function for the strength coefficient, K' $[MPa]$.

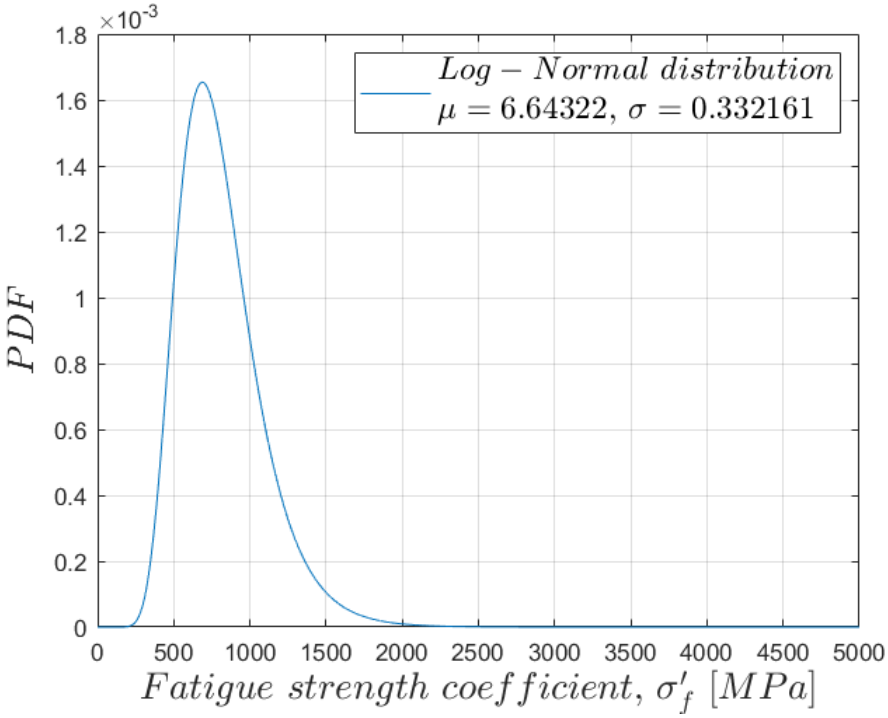

Figure 6.2: Probabilistic distribution function for the fatigue strength coefficient, σ'_f [*MPa*].

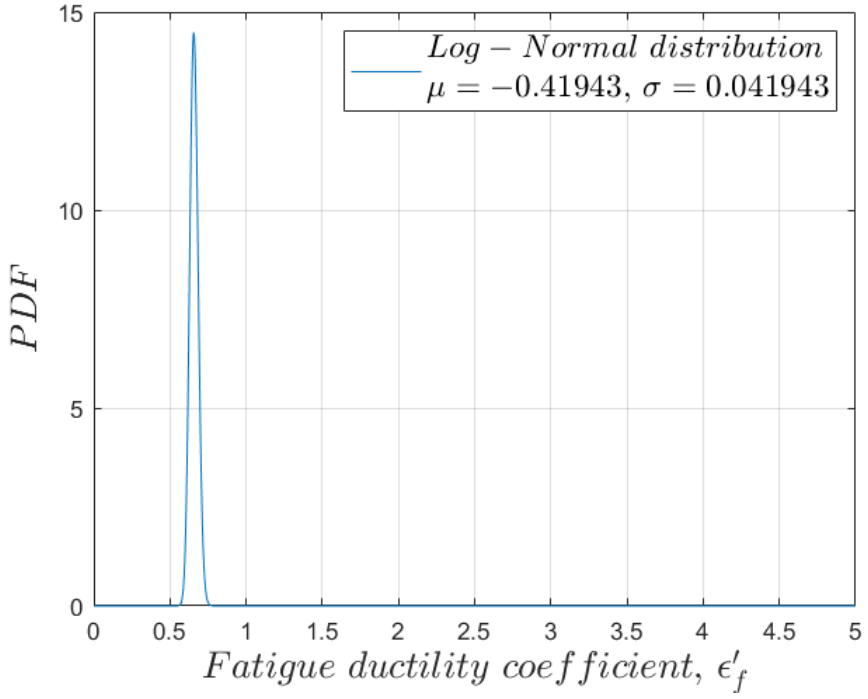

Figure 6.3: Probabilistic distribution function for the fatigue ductility coefficient, ε'_f.

6.3 Fatigue Resistance Analysis based on the Monte Carlo Simulation

6.3.1 Procedure

Figure 6.4 contains a procedure for the probabilistic fatigue life assessment using the Monte Carlo Simulation Technique. This procedure must be followed for each one of the different stress levels.

When an external load is applied in middle plane of the axle bearing journals, a stress distribution is generated along the axle. Taking into account the Neuber rule, the cyclic Ramberg-Osgood equation, the strain-life relation and the results obtained from the numerical simulation, the Monte Carlo simulation can be carried out. This way, the probabilistic distributions of local elastoplastic stresses and strains can be computed. Afterwards, the probabilistic distribution for the number of cycles to failure, N_f, can be computed as well.

Monte Carlo simulation specifications:

- Inputs:
  - $\Delta\sigma_{Nom}$ (resultant from an external load);
  - E, n', b, c, $K_t \rightarrow constant\ parameters$;
  - K', σ'_f, $\varepsilon'_f \rightarrow random\ variables\ w/\ Log-Normal\ distributions$;
- Outputs:
  - $\Delta\sigma_{EP}, \Delta\varepsilon_{EP}, N_f \rightarrow random\ variables\ w/\ Log-Normal\ or\ Weibull\ distributions$;
- Number of simulations: 5000 (for each SCF, nominal stress and output parameter combination).

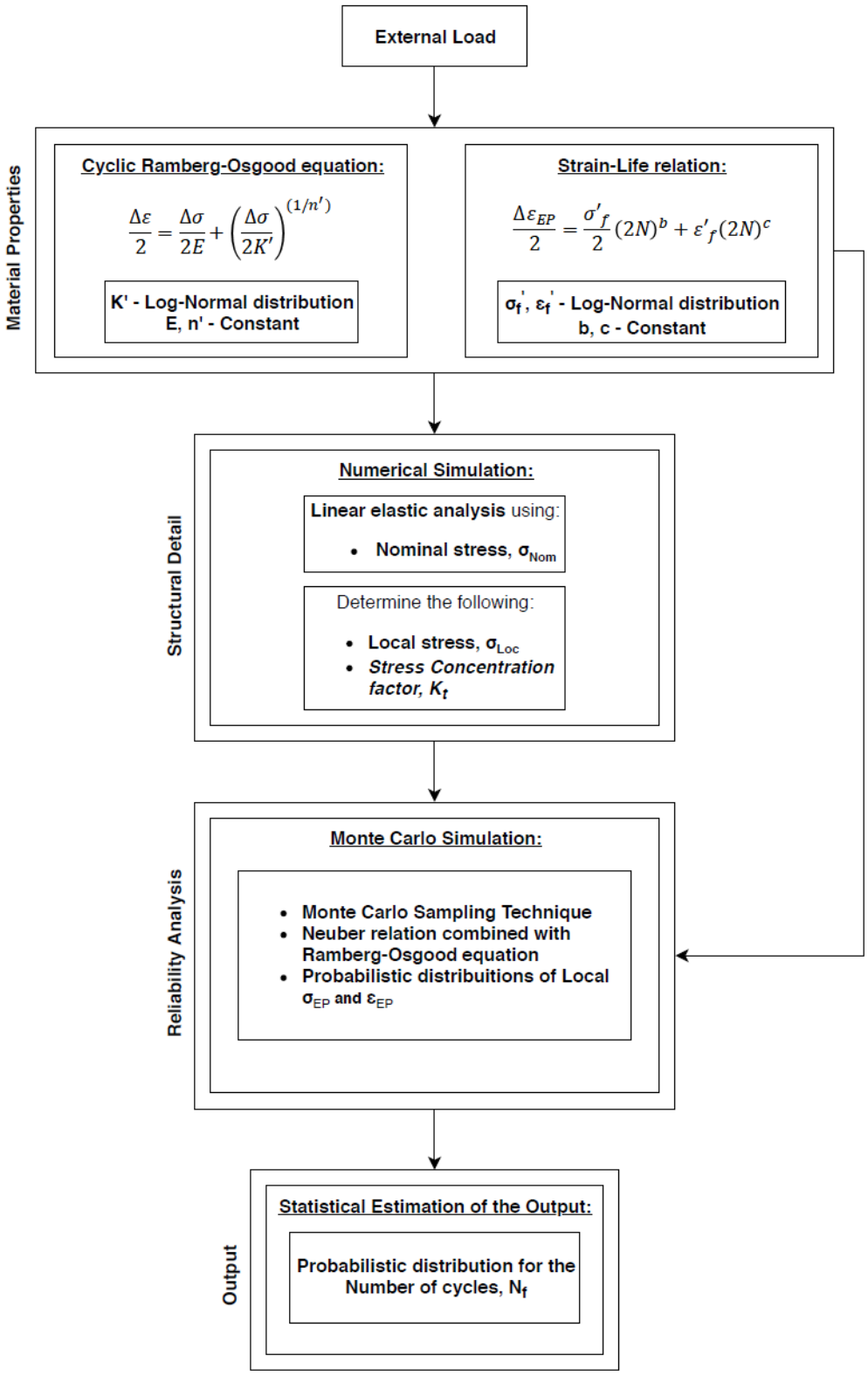

Figure 6.4: Procedure for probabilistic fatigue life assessment using the Monte Carlo Simulation Technique.

In this section, the parameters of the Log-Normal and Weibull distributions obtained with the MCST are presented (Tables 6.2, 6.3, 6.5, 6.6, 6.8, 6.9, 6.11 and 6.12). Furthermore, a statistical test that depicts how good a distribution fits the respective data is also provided (Tables 6.4, 6.14, 6.10 and 6.13). For the present case, the Anderson-Darling statistical test was employed. In addition to all this, plots containing histograms together with simulated Log-Normal and Weibull PDF that fit the histograms' data are also presented (Figures 6.5 to 6.19).

The tables containing the parameters of the Log-Normal and Weibull distributions only concern the number of cycles to failure, N_f. The same can be said about Anderson-Darling statistical test. The data was divided according to the stress concentration factor, K_t. For each of the values depicted for K_t (1.31, 1.5, 2 and 2.26), the data is subdivided according to the nominal stress.

However, histograms were built not only for the number of cycles to failure, N_f, but also for the range of local elastoplastic stresses and strains.

It should be noted that only some of the histograms that were generated are presented in this section. The histograms that are shown in this section are the following ones:

- $K_t = 1.31 \rightarrow \sigma_{Nominal} = 519.199 \rightarrow N_f,\ \sigma_{EP},\ \varepsilon_{EP}$
- $K_t = 1.31 \rightarrow \sigma_{Nominal} = 403.9,\ 288.424,\ 173.15 \rightarrow N_f$
- $K_t = 1.5 \rightarrow \sigma_{Nominal} = 403.9 \rightarrow N_f,\ \sigma_{EP},\ \varepsilon_{EP}$
- $K_t = 2 \rightarrow \sigma_{Nominal} = 288.424 \rightarrow N_f,\ \sigma_{EP},\ \varepsilon_{EP}$
- $K_t = 2.26 \rightarrow \sigma_{Nominal} = 519.199 \rightarrow N_f,\ \sigma_{EP},\ \varepsilon_{EP}$

The obtained results show that the the Log-Normal distribution is the one that fits best the number of cycles to failure and the range of local elastoplastic strains. The Weibull distribution is the one that fits best the range of local elastoplastic stresses.

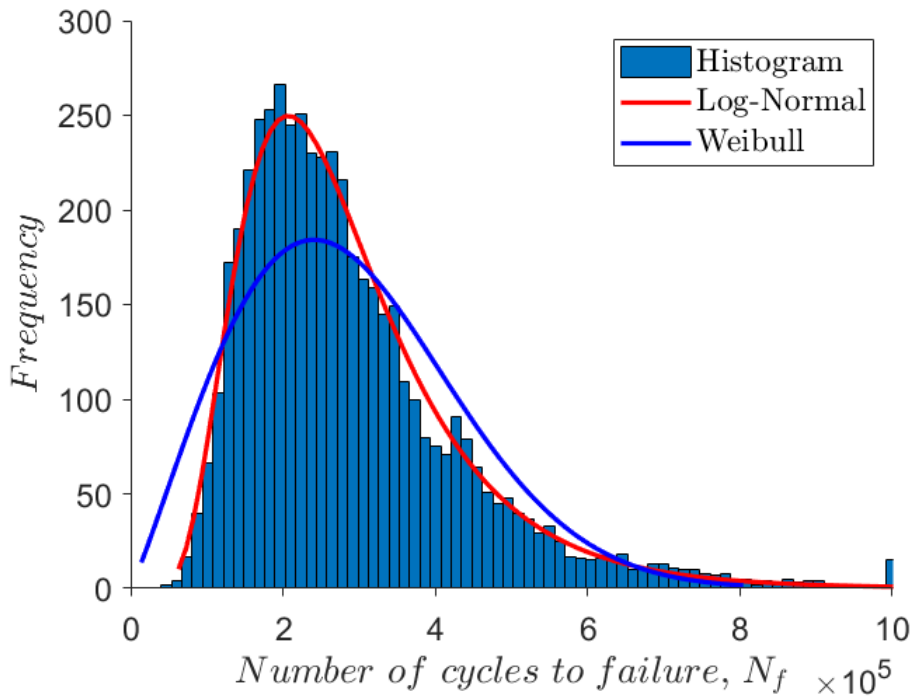

Figure 6.5: Fitting of simulated probabilistic density functions for the the number of cycles to failure with $\sigma_{Nominal} = 519.199$ and $K_t = 1.31$.

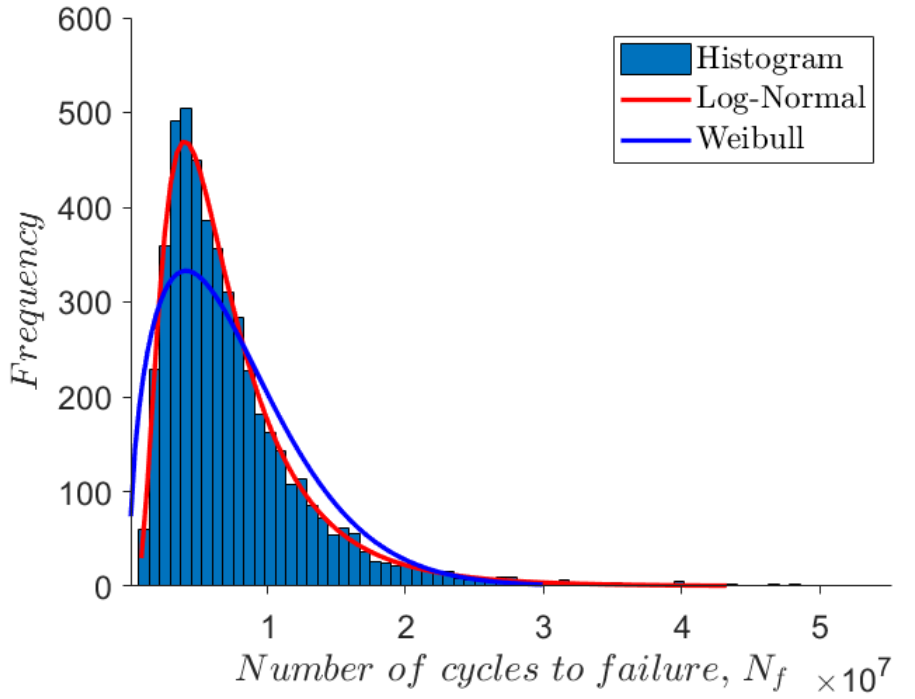

Figure 6.6: Fitting of simulated probabilistic density functions for the the number of cycles to failure with $\sigma_{Nominal} = 403.9$ and $K_t = 1.31$.

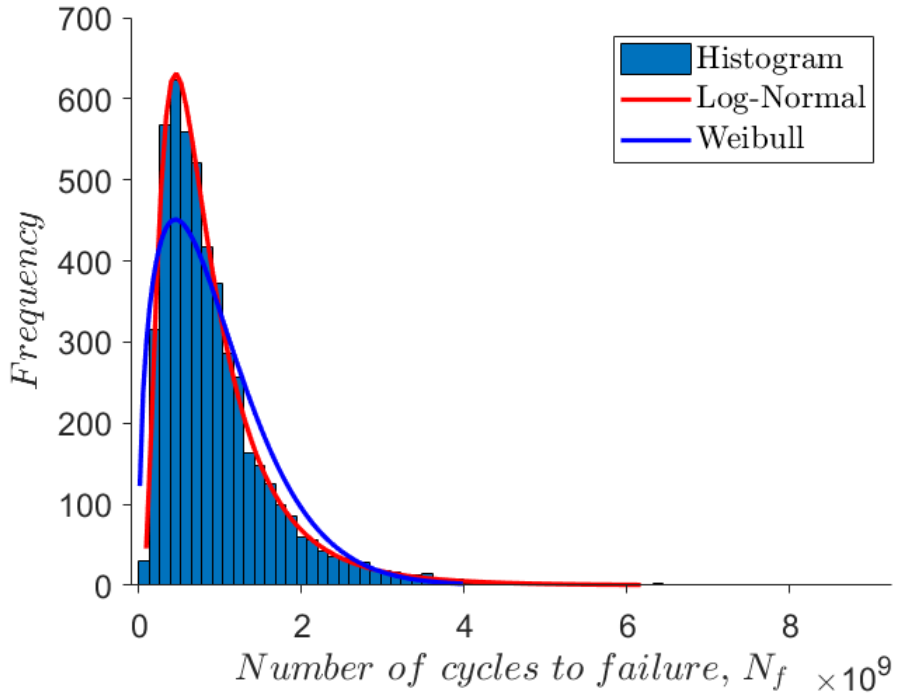

Figure 6.7: Fitting of simulated probabilistic density functions for the the number of cycles to failure with $\sigma_{Nominal} = 288.424$ and $K_t = 1.31$.

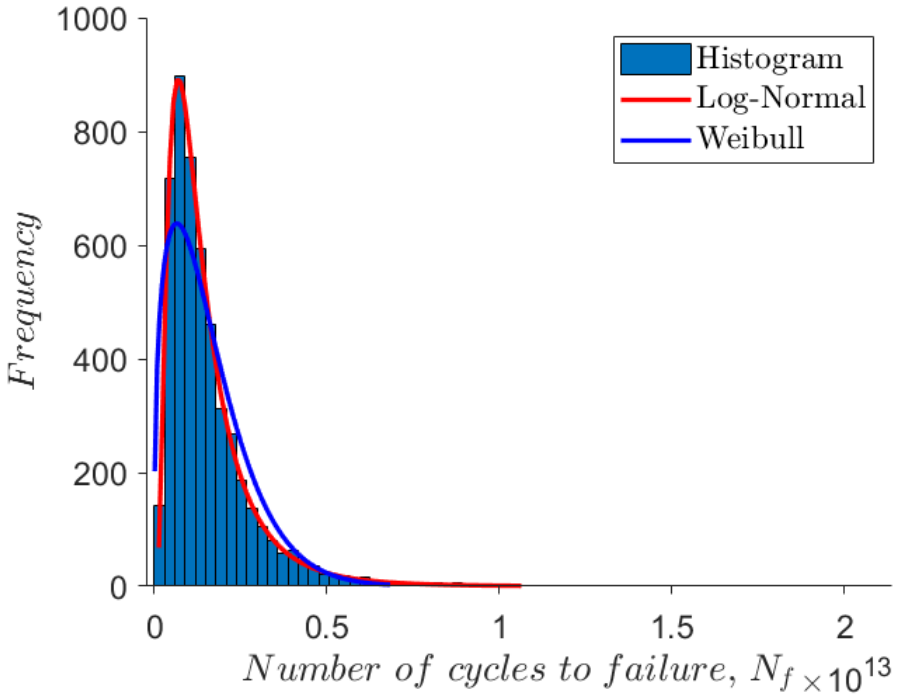

Figure 6.8: Fitting of simulated probabilistic density functions for the the number of cycles to failure with $\sigma_{Nominal} = 173.15$ and $K_t = 1.31$.

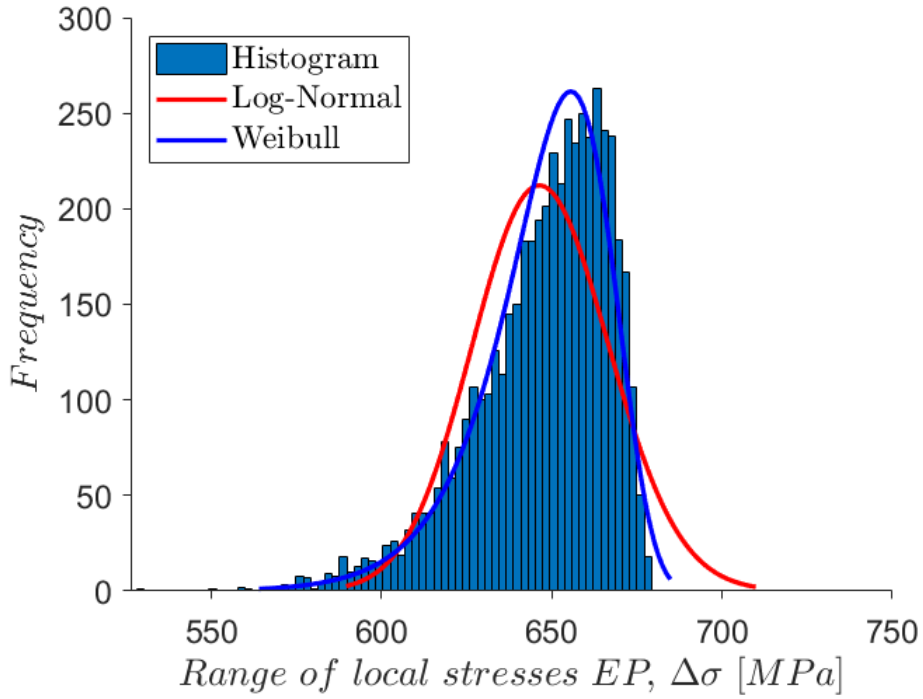

Figure 6.9: Fitting of simulated probabilistic density functions for the the range of local elastoplastic stresses with $\sigma_{Nominal} = 519.199$ and $K_t = 1.31$.

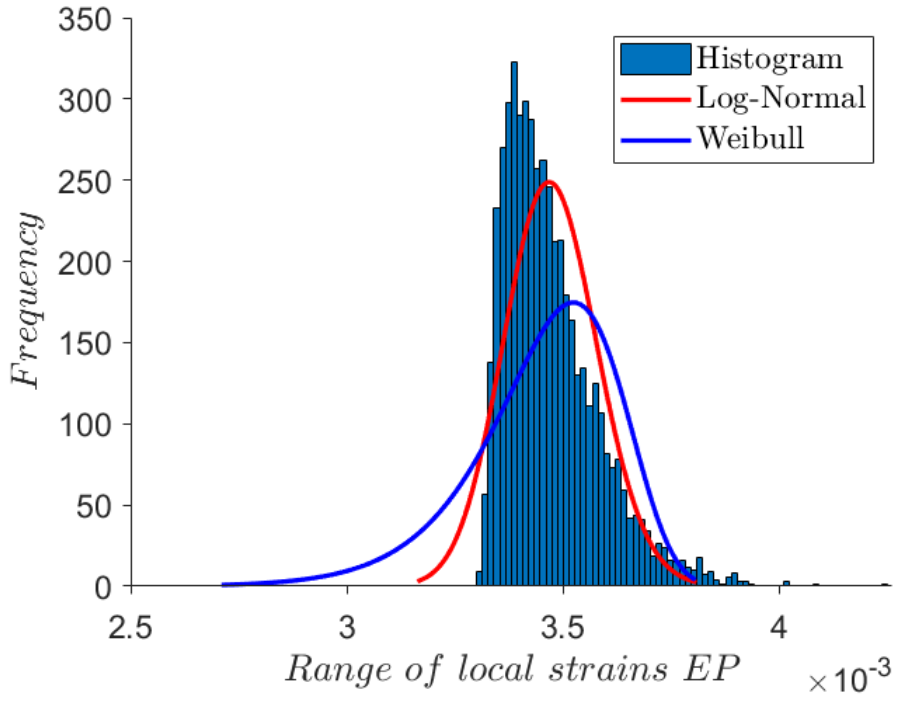

Figure 6.10: Fitting of simulated probabilistic density functions for the the range of local elastoplastic strains with $\sigma_{Nominal} = 519.199$ and $K_t = 1.31$.

Table 6.2: Parameters of the Log-Normal distribution for the number of cycles to failure, N_f, with $K_t = 1.31$.

	Log-Normal distribution for N_f, $K_t = 1.31$			
Nominal stress [*MPa*]	519.199	403.9	288.424	173.125
μ	12.381	15.571	20.422	27.793
σ	0.50831	0.6887	0.70667	0.73831
γ	17512	2.67E+05	-49432	9.72E+09
$P_{5\%}$	1.03E+05	1.86E+06	2.36E+08	3.49E+11
$P_{50\%}$	2.38E+05	5.79E+06	7.55E+08	1.18E+12
$P_{95\%}$	5.50E+05	1.80E+07	2.41E+09	3.96E+12

Table 6.3: Parameters of the Weibull distribution for the number of cycles to failure, N_f, with $K_t = 1.31$.

	Weibull distribution for N_f, $K_t = 1.31$			
Nominal stress MPa	519.199	403.9	288.424	173.125
α	1.7885	1.3337	1.3327	1.2771
β	2.75E+05	7.44E+06	9.81E+08	1.59E+12
γ	45276	8.15E+05	5.47E+07	9.15E+10
$P_{5\%}$	5.23E+04	8.03E+05	1.06E+08	1.55E+11
$P_{50\%}$	2.24E+05	5.66E+06	7.45E+08	1.19E+12
$P_{95\%}$	5.08E+05	1.69E+07	2.23E+09	3.75E+12

Table 6.4: Goodness of fit statistical tests for $K_t = 1.31$.

	Anderson–Darling for N_f, $K_t = 1.31$			
Nominal stress [*MPa*]	519.199	403.9	288.424	173.125
Log-Normal	0.49897	0.32374	0.18802	0.16307
Weibull	41.843	39.412	40.462	41.493

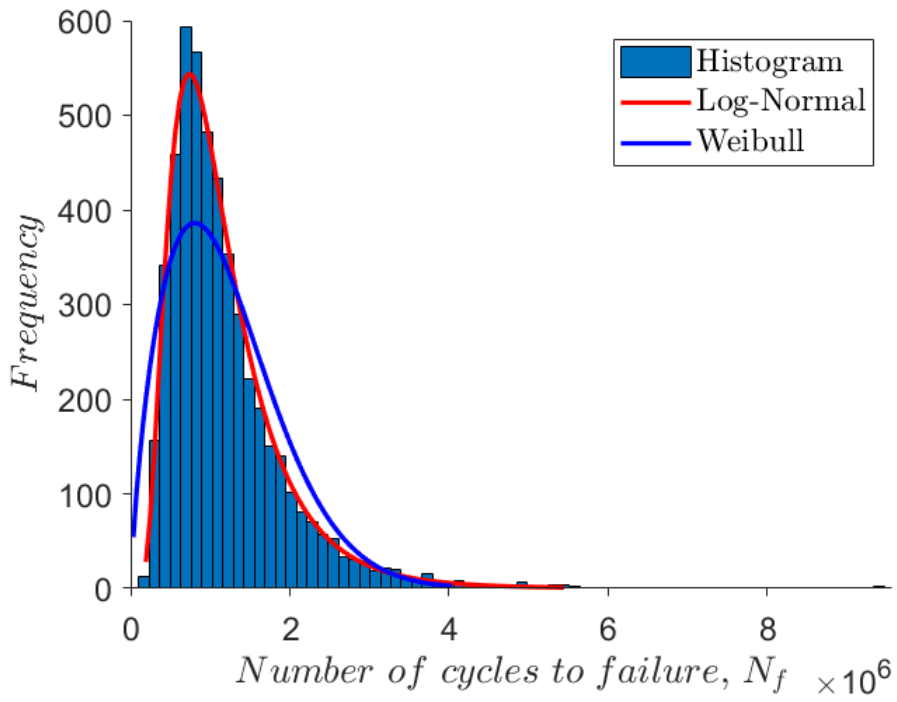

Figure 6.11: Fitting of simulated probabilistic density functions for the the number of cycles to failure with $\sigma_{Nominal} = 403.9$ and $K_t = 1.5$.

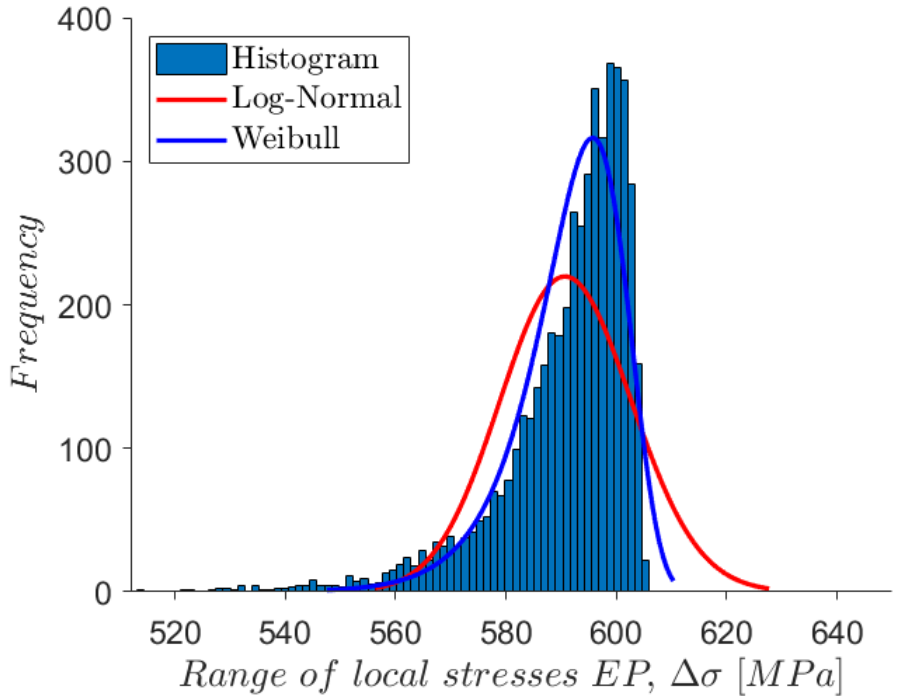

Figure 6.12: Fitting of simulated probabilistic density functions for the the range of local elastoplastic stresses with $\sigma_{Nominal} = 403.9$ and $K_t = 1.5$.

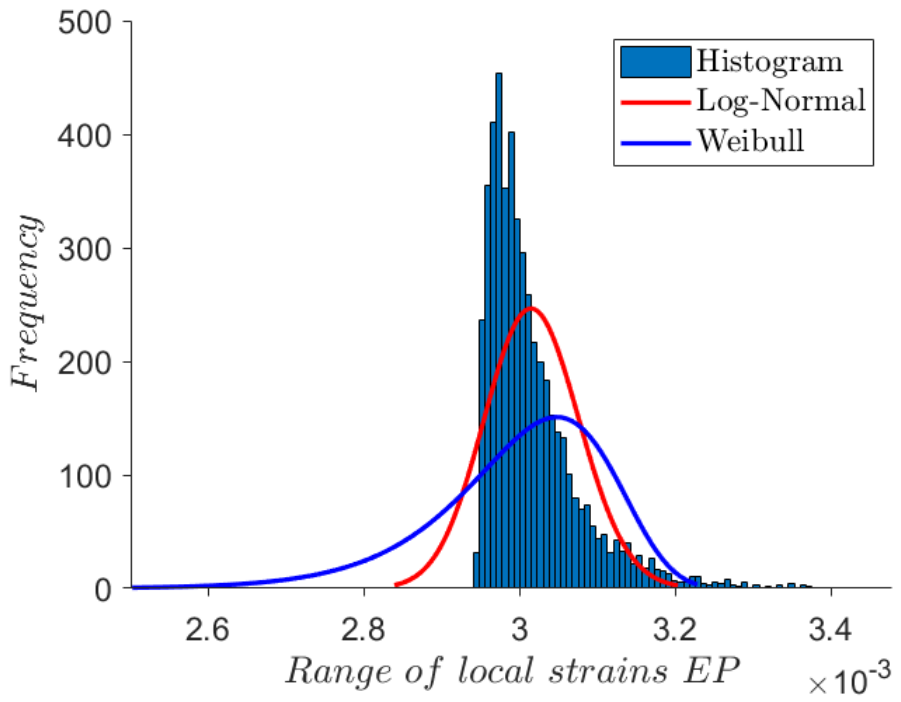

Figure 6.13: Fitting of simulated probabilistic density functions for the the range of local elastoplastic strains with $\sigma_{Nominal} = 403.9$ and $K_t = 1.5$.

Table 6.5: Parameters of the Log-Normal distribution for the number of cycles to failure, N_f, with $K_t = 1.5$.

	Log-Normal distribution for N_f, $K_t = 1.5$			
Nominal stress [*MPa*]	519.199	403.9	288.424	173.125
μ	11.09000	13.74600	18.45400	25.85900
σ	0.41980	0.60680	0.70886	0.70589
γ	2445	63473	761780	-1.9E+09
$P_{5\%}$	3.28E+04	3.44E+05	3.22E+07	5.32E+10
$P_{50\%}$	6.55E+04	9.33E+05	1.03E+08	1.70E+11
$P_{95\%}$	1.31E+05	2.53E+06	3.32E+08	5.43E+11

Table 6.6: Parameters of the Weibull distribution for the number of cycles to failure, N_f, with $K_t = 1.5$.

	Weibull distribution for N_f, $K_t = 1.5$			
Nominal stress [*MPa*]	519.199	403.9	288.424	173.125
α	1.9402	1.4474	1.3321	1.3021
β	6.47E+04	1.11E+06	1.37E+08	2.19E+11
γ	16766	1.87E+05	8.76E+06	1.49E+10
$P_{5\%}$	1.40E+04	1.42E+05	1.47E+07	2.24E+10
$P_{50\%}$	5.35E+04	8.60E+05	1.04E+08	1.65E+11
$P_{95\%}$	1.14E+05	2.37E+06	3.11E+08	5.09E+11

Table 6.7: Goodness of fit statistical tests for $K_t = 1.5$.

	Anderson–Darling for N_f, $K_t = 1.5$			
Nominal stress [*MPa*]	519.199	403.9	288.424	173.125
Log-Normal	0.33112	0.73304	0.16315	0.18139
Weibull	23.892	37.471	36.792	31.737

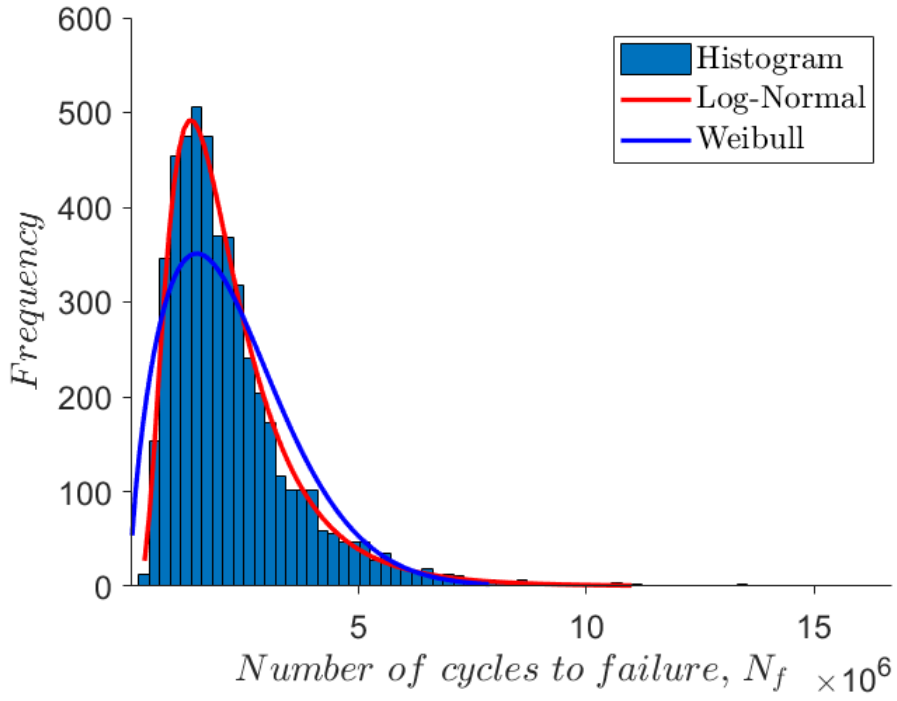

Figure 6.14: Fitting of simulated probabilistic density functions for the the number of cycles to failure with $\sigma_{Nominal} = 288.424$ and $K_t = 2$.

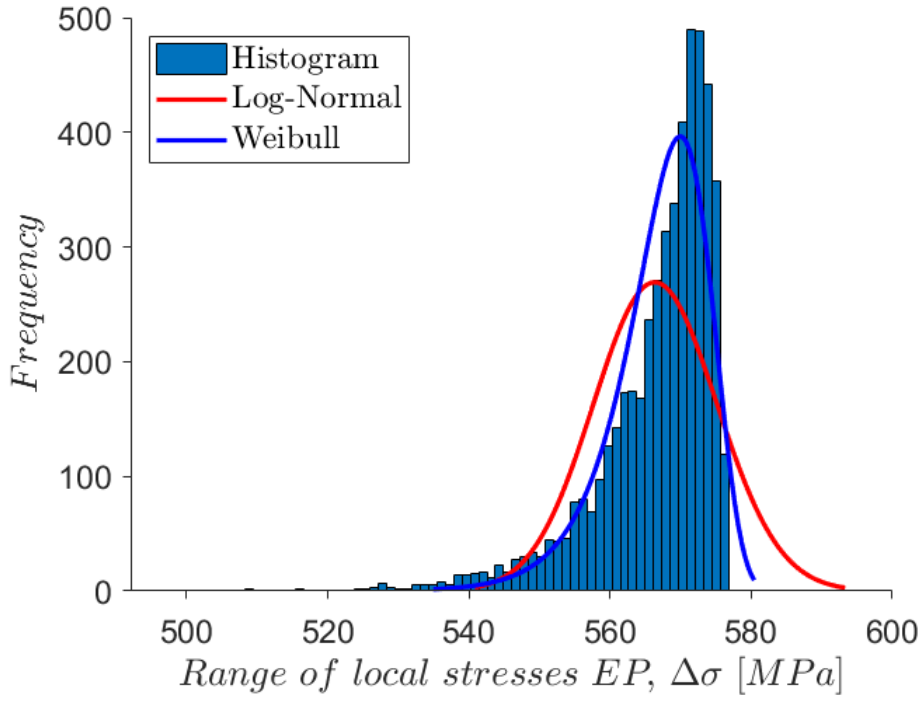

Figure 6.15: Fitting of simulated probabilistic density functions for the the range of local elastoplastic stresses with $\sigma_{Nominal} = 288.424$ and $K_t = 2$.

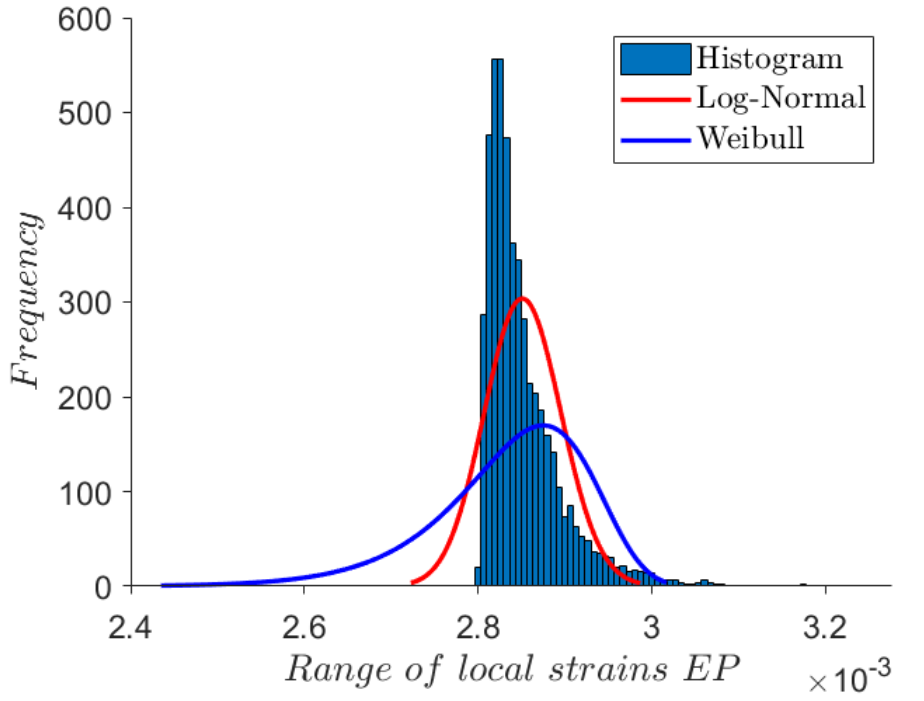

Figure 6.16: Fitting of simulated probabilistic density functions for the the range of local elastoplastic strains with $\sigma_{Nominal} = 288.424$ and $K_t = 2$.

Table 6.8: Parameters of the Log-Normal distribution for the number of cycles to failure, N_f, with $K_t = 2$.

	Log-Normal distribution for N_f, $K_t = 2$			
Nominal stress [*MPa*]	519.199	403.9	288.424	173.125
μ	9.11060	10.82200	14.36700	21.67100
σ	0.29884	0.38617	0.63678	0.70887
γ	0	0	122770	-2.6E+07
$P_{5\%}$	5.54E+03	2.66E+04	6.09E+05	8.04E+08
$P_{50\%}$	9.05E+03	5.01E+04	1.74E+06	2.58E+09
$P_{95\%}$	1.48E+04	9.46E+04	4.95E+06	8.28E+09

Table 6.9: Parameters of the Weibull distribution for the number of cycles to failure, N_f, with $K_t = 2$.

	Weibull distribution for N_f, $K_t = 2$			
Nominal stress [*MPa*]	519.199	403.9	288.424	173.125
α	2.2707	2.0225	1.4972	1.3339
β	7.11E+03	4.73E+04	2.25E+06	3.42E+09
γ	3178.3	12210	2.35E+05	1.69E+08
$P_{5\%}$	1.92E+03	1.09E+04	3.09E+05	3.68E+08
$P_{50\%}$	6.05E+03	3.95E+04	1.76E+06	2.59E+09
$P_{95\%}$	1.15E+04	8.14E+04	4.68E+06	7.77E+09

Table 6.10: Goodness of fit statistical tests for $K_t = 2$.

	Anderson–Darling for N_f, $K_t = 2$			
Nominal stress [*MPa*]	519.199	403.9	288.424	173.125
Log-Normal	0.30291	0.1215	0.34049	0.21594
Weibull	17.396	25.635	45.395	38.022

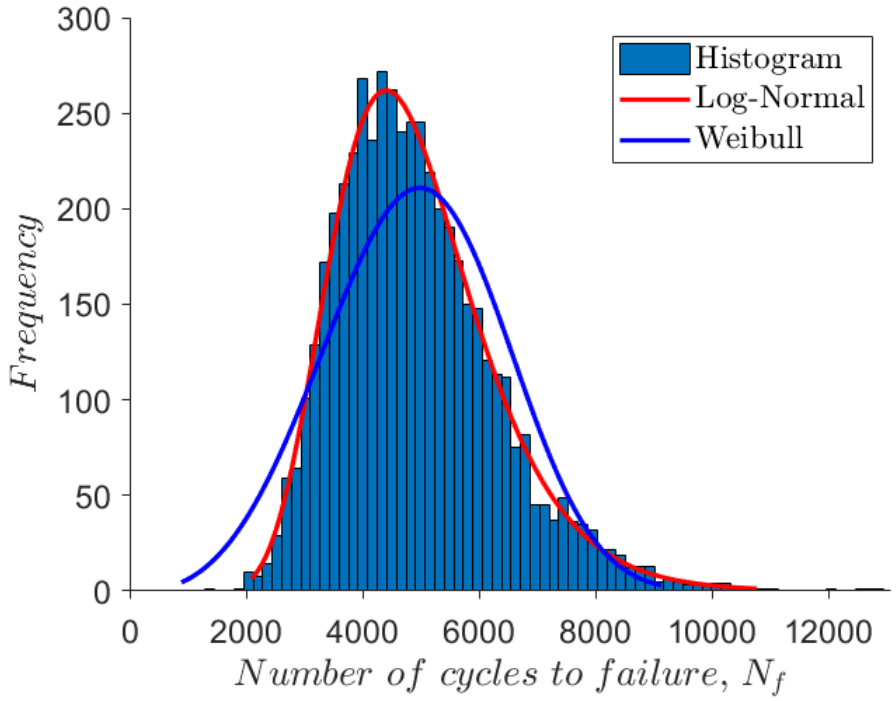

Figure 6.17: Fitting of simulated probabilistic density functions for the the number of cycles to failure with $\sigma_{Nominal} = 519.199$ and $K_t = 2.26$.

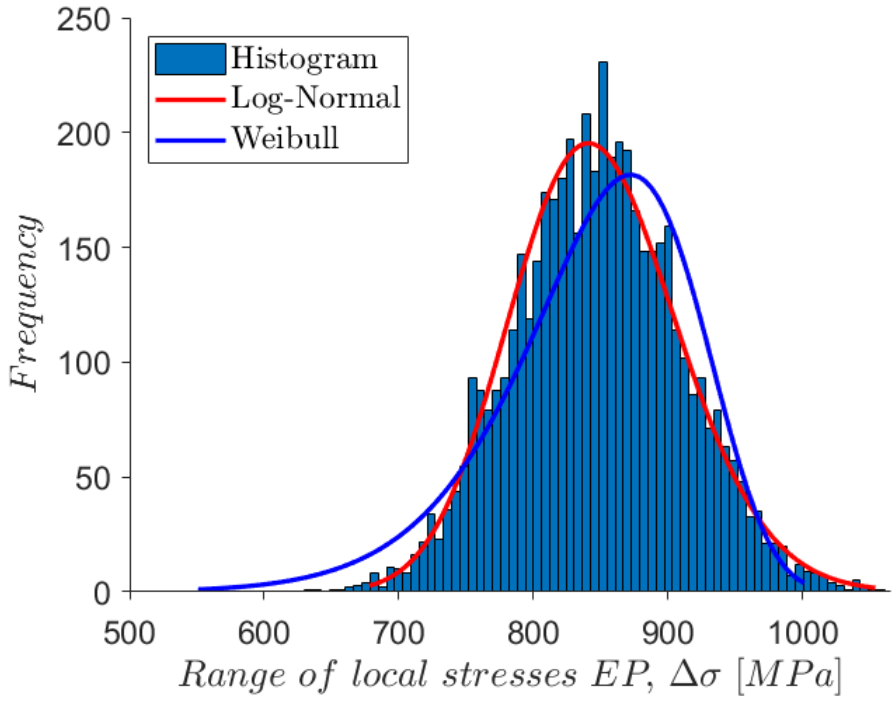

Figure 6.18: Fitting of simulated probabilistic density functions for the the range of local elastoplastic stresses with $\sigma_{Nominal} = 519.199$ and $K_t = 2.26$.

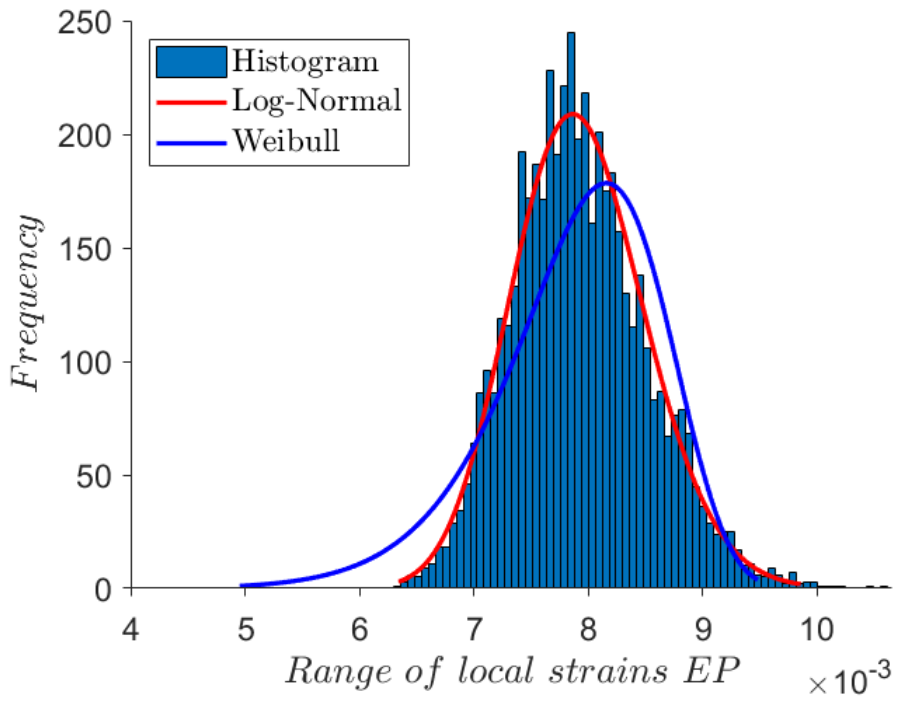

Figure 6.19: Fitting of simulated probabilistic density functions for the the range of local elastoplastic strains with $\sigma_{Nominal} = 519.199$ and $K_t = 2.26$.

Table 6.11: Parameters of the Log-Normal distribution for the number of cycles to failure, N_f, with $K_t = 2.26$.

	Log-Normal distribution for N_f, $K_t = 2.26$			
Nominal stress [*MPa*]	519.199	403.9	288.424	173.125
μ	8.46430	9.88700	12.88100	19.87900
σ	0.27327	0.33399	0.54319	0.73316
γ	0	475.69	19817	5905600
$P_{5\%}$	3.03E+03	1.14E+04	1.61E+05	1.29E+08
$P_{50\%}$	4.74E+03	1.97E+04	3.93E+05	4.30E+08
$P_{95\%}$	7.43E+03	3.41E+04	9.60E+05	1.44E+09

Table 6.12: Parameters of the Weibull distribution for the number of cycles to failure, N_f, with $K_t = 2.26$.

	Weibull distribution for N_f, $K_t = 2.26$			
Nominal stress MPa	519.199	403.9	288.424	173.125
α	2.7697	2.2322	1.6451	1.2777
β	4.07E+03	1.70E+04	4.62E+05	5.71E+08
γ	1295.7	6214.2	64752	4.14E+07
$P_{5\%}$	1.39E+03	4.50E+03	7.60E+04	5.59E+07
$P_{50\%}$	3.57E+03	1.45E+04	3.70E+05	4.29E+08
$P_{95\%}$	6.05E+03	2.78E+04	9.00E+05	1.35E+09

Table 6.13: Goodness of fit statistical tests for $K_t = 2.26$.

	Anderson–Darling (for N_f, $K_t = 2.26$)			
Nominal stress [MPa]	519.199	403.9	288.424	173.125
Log-Normal	0.2237	0.40331	0.43397	0.14464
Weibull	31.4	20.953	45.276	35.485

6.3.2 Results and Discussion

The probabilistic fatigue fields resultant from the Monte Carlo simulation procedure can be plotted and compared with the results for the probabilistic fields previously presented on Chapter 4 for the RB fatigue S-N curves with failure probability of 50%, 5%-95% and 2.3%-97.7% for full-scale EA4T specimens obtained with the standard ASTM E739-91.

As the Log-Normal distribution was found to be the one that best fits the data for the number of cycles to failure, only this results are going to be considered in this comparison.

Analysing Figures 6.20 and 6.21, it can be seen that the results obtained with the MCST agree well with the data for full-scale EA4T specimens obtained with the standard ASTM E739-91, even though it can be seen that the results obtained with the standard are slightly more conservative.

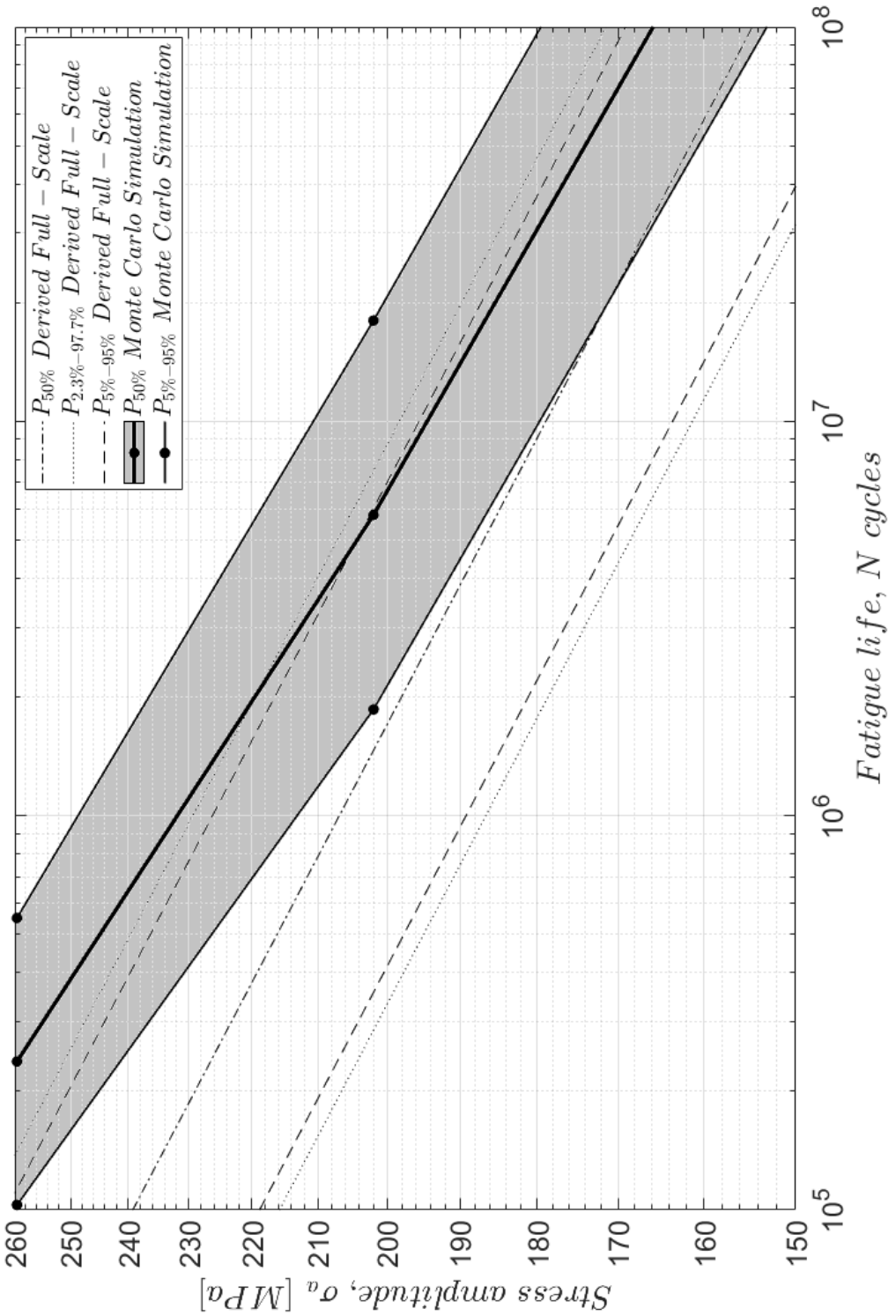

Figure 6.20: Comparison of Monte Carlo simulation probabilistic fields (Log-Normal distribution) for $K_t = 1.31$ with the RB fatigue S-N curves with failure probability of 50%, 5%-95% and 2.3%-97.7% for full-scale EA4T specimens obtained with the standard ASTM E739-91.

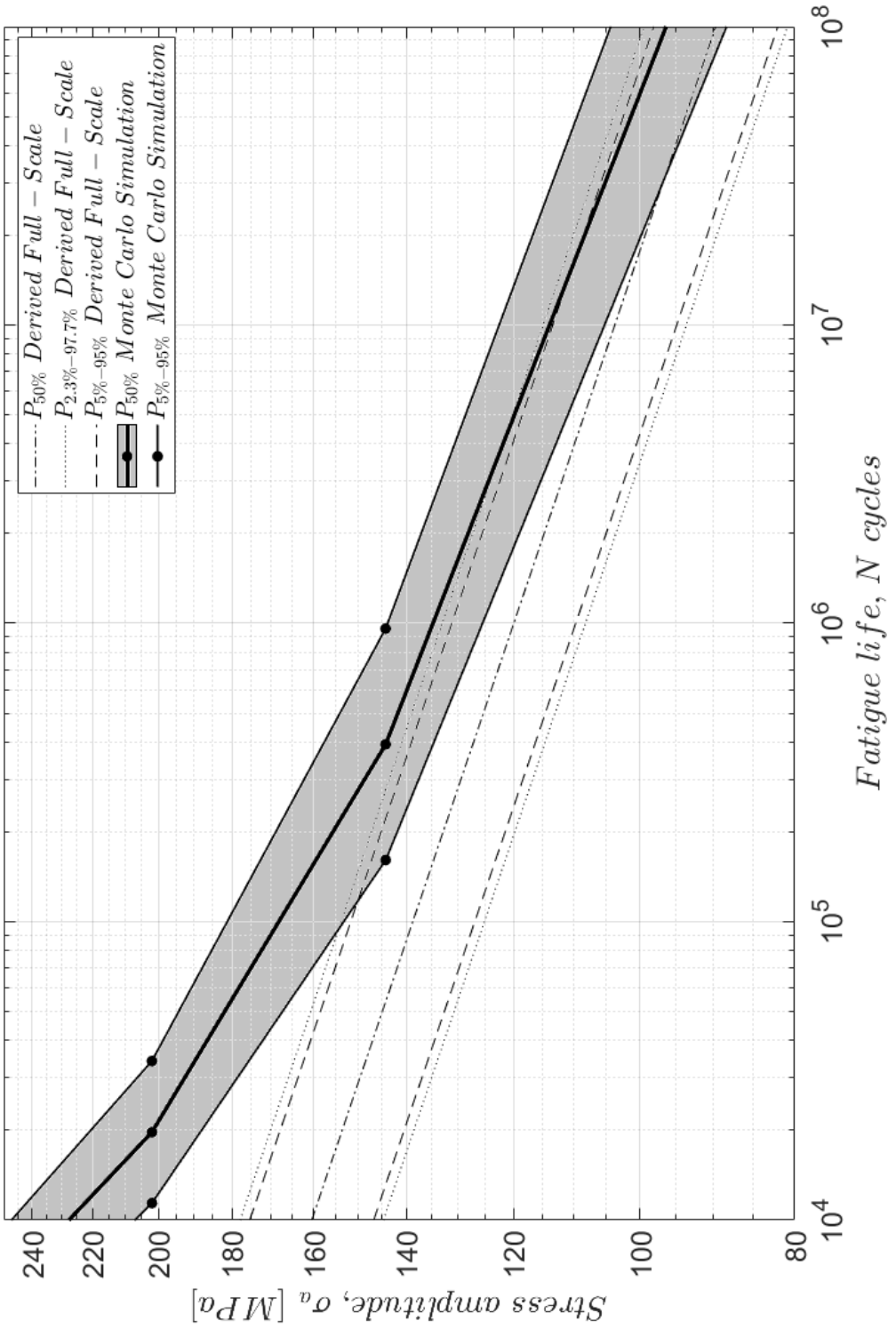

Figure 6.21: Comparison of Monte Carlo simulation probabilistic fields (Log-Normal distribution) for $K_t = 2.26$ with the RB fatigue S-N curves with failure probability of 50%, 5%-95% and 2.3%-97.7% for full-scale EA4T specimens obtained with the standard ASTM E739-91.

6.4 Fatigue Resistance Analysis based on Multilayer Neural Network (MLNN) Data

6.4.1 Procedure

In the procedure for the analysis of fatigue resistance, multiple input data can be jointed to a non-linear response of structures with complex analytical process using artificial neural networks (ANN). ANN consist on a computational machine learning approach to enable the highly non-linear mapping between two main data sets - input variables and output response. ANN can be normally used for acceptable classification or regression problems which are the complex mathematical relations with continuous or discontinuous forms [54].

The multilayer neural network is a prediction tool which consists on three main layers:

- Input;
- Hidden;
- Output layers.

Each layer involves multiple nodes:

- For the input layer, nodes (neurons) are associated with the input variables such as load and nominal stress;
- Concerning the hidden layer, the number of nodes is given by trial and error;
- For the output layer, the node is associated with the response of the structures such as the number of cycles to failure, for instance.

In the MLNN, the approximated function to predict the number of cycles to failure is given by:

$$Y = b + \sum_{j=1}^{M} w_j \phi_j \tag{6.1}$$

In the previous equation, variable b represents bias. The bias is like the intercept added in a linear equation. In a neural network, the bias node is always "on". The bias value allows the activation function to be shifted to the left or to the right right in order to better fit the data. Concerning w_j, it represents the weights for the output layer. Variable ϕ_j is the response of node j of the hidden layer which can be defined with a non-linear map as a sigmoid function. For the present case, the non-linear map is given by:

$$\phi_j = \frac{1}{1 + exp\left[-\left(b_j + \sum_{i=1}^{n} w_{ji} x_i\right)\right]} \tag{6.2}$$

On Equation 6.2, b_j is the bias for the j-th hidden node and w_{ji} represents the weights for the connection between j-th hidden node and i-th node from the input layer.

Figure 6.22 contains a scheme of a MLNN structure. Between 2 to 10 hidden nodes were tested using trial and error to determine the best results for MLNN model.

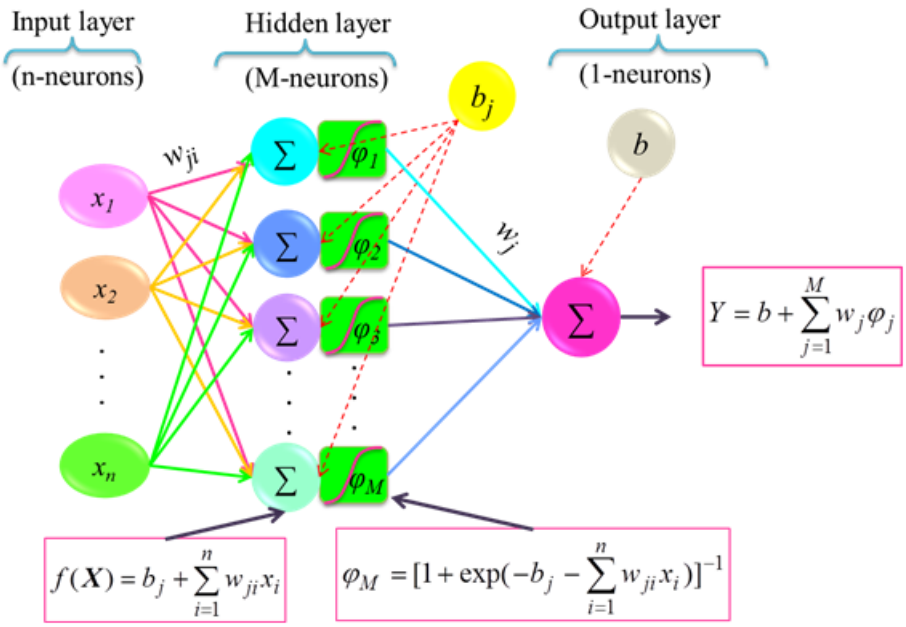

Figure 6.22: Structure of a MLNN (n-M-1).

To achieve the best connections between input and output layers, the learning approach for computing the optimal conditions of weights w and biases b is even more important. It enables accurate predictions of MLNN.

The back-propagation (BP) approach for ANN is a common training methodology that provides the non-linear mapping between the input variables and respective response [55]. Gradient-based optimization methods and non-gradient-based heuristic optimization methods can be used for BP in the training stage of ANN.

The gradient methods are efficient computational approaches. However, the iterative process is formulated based on a complex formula and reaching the optimal conditions can be difficult (slow convergence rates for highly non-linear relations with complex data or even no-converge for some specific engineering problems).

Therefore, the meta-heuristic optimization methods can be used to train MLNN with n-nodes in the input layer and M-nodes in the hidden layer. The coefficient vector should be defined as $\boldsymbol{\theta} = \{\boldsymbol{b}, \boldsymbol{w}\}$ for weights and biases. The best conditions for the unknown coefficient vector lead to an accurate non-linear relation for the number of cycle to failure in the fatigue life analysis.

The particle swarm optimization (PSO) as an evolutionary computational technique-based meta- heuristic algorithm can be applied to train the MLNN model by minimizing the error between the observed and predicted response of the structure as shown by the

optimization model presented below [56]:

$$min\ MSE = \frac{1}{N}\sum_{i=1}^{M}[O_i - Y_i]^2 \tag{6.3}$$

On Equation 6.3 the variables N and O represent the number of train data points and the observed fatigue life response, respectively.

The best calibration for the unknown coefficients is provided when the mean square error (MSE) is minimized based on MLNN model. The PSO updating formulations are utilized to achieve the optimal results as follows [57]:

$$\boldsymbol{\theta}_{i+1} = \boldsymbol{\theta}_i + \mathbf{V}_{i+1} \tag{6.4}$$

$$\mathbf{V}_{i+1} = \eta_i \mathbf{V}_{i+1} + c_1 \times rand() \left[\boldsymbol{\theta}_i^{best} - \boldsymbol{\theta}_i\right] + c_2 \times rand() \left[\boldsymbol{\theta}_i^{best} - \boldsymbol{\theta}_i\right] \tag{6.5}$$

Where, $\mathbf{V}$ is the velocity of the particle and η is a reduction factor which is calculated as:

$$\eta_i = \eta_{max} - \frac{\eta_{max} - \eta_{min}}{NI} i \tag{6.6}$$

In which i is the current iteration, NI represents the total number of iterations, η_{max} and η_{min} are the maximum and minimum reduction factors. Coefficients c_1 and c_2 are acceleration coefficients and $rand()$ denotes generated random number between 0 and 1. The coefficient vector θ_i is adjusted using updating velocity which relies on the best results of iterative results.

In order to compute the best coefficient vector in the training stage of a MLNN, the parameters of PSO are given as: $c_1 = c_2 = 2$, $NI = 1000$, number of particles $NOP = 30$, $\eta_{max} = 0.9$, $\eta_{min} = 0.3$, $V_0 = 0.3 rand()$ and $\theta_0 = 1 - 2 rand()$.

A MATLAB code was developed to train the MLNN-based PSO. Its framework is presented in Figure 6.23. In this current work, the number of hidden layers is obtained as $M = 4$. The non-linear relation between computed weight and biases is presented below:

$$\hat{N}_f = exp[10Y + 20] \tag{6.7}$$

$$Y = 0.102 + [0.246\ 0.814\ 1.797\ 0.123] \times f\left(\begin{bmatrix} -0.341 \\ 1.875 \\ -0.883 \\ 0.1447 \end{bmatrix} + \begin{bmatrix} -0.403 & 1.349 \\ -0.576 & -1.495 \\ -0.087 & -1.288 \\ -0.390 & 0.227 \end{bmatrix} \times \begin{bmatrix} \hat{P} \\ \hat{\sigma}_n \end{bmatrix}\right) \tag{6.8}$$

$$\hat{P} = (P - 500)/1250 - 1 \tag{6.9}$$

$$\hat{\sigma}_n = (\sigma_n - 150)/200 - 1 \tag{6.10}$$

Where $\hat{N}$ represents the predicted number of cycles, Y are the evaluated normalized values for the number of cycles to failure, f is the active sigmoid function, P and σ_n are the load and nominal stress (input variables). Its normalized values, $\hat{P}$ and $\hat{\sigma}_n$, are used in the modelling process.

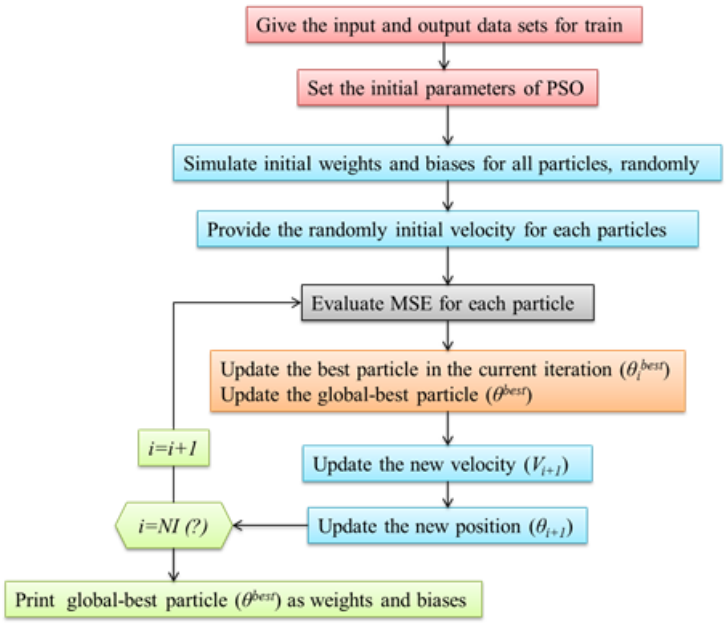

Figure 6.23: Framework of a MLNN-based PSO.

6.4.2 Training the Artificial Neural Network with a Multi Layer Neural Network-based Particle Swarm Optimization

In order to train the neural network, 3 points on the finite life region and 1 point on the infinite life region were chosen.

First, the neural network was calibrated and afterwards it was validated. In order to validate it, results were predicted for the points that were not used to calibrate the neural network.

Neural network specifications:

- Inputs: E, K', n', σ'_f, b, ε'_f, c, K_t, $\Delta\sigma_{Nom}$;
- Outputs: N_f.

The neural network was trained for the mean values of K', σ'_f and ε'_f. Also, the value taken for the stress concentration factor, K_t, was equal to 1.5.

6.4.3 Results and Discussion

The artificial neural network that was trained proved to be a very powerful and accurate tool to predict results, as it can be proved by the determination coefficient that was obtained, $R^2 = 0.9999926$ which is practically equal to 1 (see Figure 6.24).

Table 6.14 contains the results predicted by the MLNN-PSO.

Table 6.14: MLNN-PSO predicted results.

	Number of cycles, N_f	
Range of nominal stresses [MPa]	Predicted results	Observed results
521.85	59480	59399
480.12	127939	128293
445.99	275814	277210
396.65	1103015	1107560
350.67	5566510	5487524
268.80	2.36126E+08	2.37128E+08
192.75	2.86770E+10	3.00605E+10
161.98	3.57658E+11	3.57836E+11

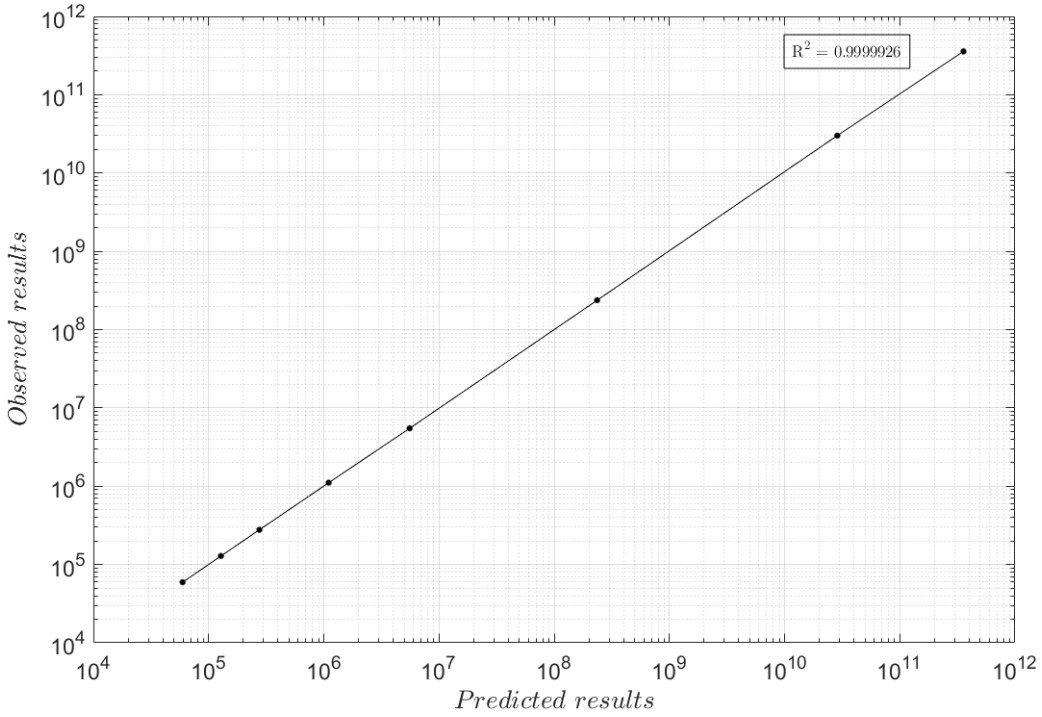

Figure 6.24: Correlation between predicted and observed results for the number of cycles, N_f.

Chapter 7

Conclusions and Future Work

7.1 Conclusions

In this dissertation, an extensive review on railway, fatigue, fracture mechanics and probabilistic prediction models was carried out. After that, fatigue strength characterization and fatigue life prediction of a railway axle made in EA4T steel based on a numerical analysis using the finite element method and the Neuber rule were done. Furthermore, rotating bending high cycle fatigue tests' data was used to generate the probabilistic rotating bending fatigue S-N curves. Besides, fatigue crack growth characterization was also addressed. Finally, structural reliability techniques (MCST and ANN) were used for fatigue analysis.

The results obtained with the Neuber rule for local elastoplastic stresses and strains are very similar to the ones obtained with finite element modelling.

The value of the SCF for a transition whose design is fully complaint with the current standards is 1.2. However, this value seems to be excessively lower when compared to the values for the SCF obtained with the analysis of the stress relief groove in the numerical model. For instance, a maximum value of $K_t = 2.26$ was encountered.

The standard procedure to obtain the S-N design curve of a railway axle taking into consideration the rotating bending high cycle fatigue experimental results of small-scale samples proved to be very efficient when compared with the mean S-N curve obtained using the Neuber rule, the Ramberg-Osgood equation and the Coffin-Manson relation.

The fatigue resistance analysis based on local approaches allowed to obtain the mean rotating bending S-N curve for the classical axle with press-fits which correlates well with the probabilistic fields obtained following the standard ASTM E739-91.

The initiation stage is predominant. This stage is of crucial importance because for higher loads the propagation stage only comprehends a very small number of cycles, rapidly leading components to failure. This means that when cracks are detected, components should be immediately repaired or substituted. Therefore, crack detection is important.

The structural reliability techniques used for fatigue analysis proved to be very useful in the probabilistic S-N fields prediction for a railway axle.

7.2 Future Work

The future works can be summarized as:

- Fatigue tests of rail axle steels used in the railway vehicles;
- FCG tests of rail axle steels used in railway vehicles;
- Development of a consistent methodology for fatigue analysis to obtain an S-N curve of railway axles using local approaches and its comparison with the assumptions of standards EN13103/EN13104;
- Neural networks could also be used for the fatigue crack propagation phase;
- The artificial neural network could be combined with reliability analysis in order to obtain probabilistic S-N fields;
- The propagation stage could also be evaluated in terms of reliability analysis;
- Initiation and propagation stages can both be included to obtain a global S-N curve based on reliability analysis.

References

[1] Satoshi Koizumi, Osamu Goto, Masaharu Ueda, Y Shimokawa, M Mizuno, Taizo Makino, Hiroki Sakai, Makoto Kimura, Yoshinori Okagata, Kazuhiko Saeki, General Manager, Miyuki Yamamoto, Osamu Kondo, Tsutomu Sugiura, Hiroshi Tomono, and Kenji Saita. Advance in Railway Vehicle Technology and Future Prospects Mainly in Relation to Bogie. *NIPPON STEEL & SUMITOMO METAL TECHNICAL REPORT No. 105*, (105):1–2, 2013.

[2] Jung Won Seo, Hyun Moo Hur, Hyun Kyu Jun, Seok Jin Kwon, and Dong Hyeong Lee. Fatigue Design Evaluation of Railway Bogie with Full-Scale Fatigue Test. *Advances in Materials Science and Engineering*, 2017, 2017. doi:10.1155/2017/5656497.

[3] Fatigue limit diagram according to Haigh and Smith - tec-science. URL: https://www.tec-science.com/material-science/material-testing/fatigue-limit-diagram-according-to-haigh-and-smith-creation/.

[4] Explain the S-N curve for fatigue life. URL: https://www.ques10.com/p/21920/explain-the-s-n-curve-for-fatigue-life/.

[5] G Belloni, M Bocciolone, and A Lo Conte. Fatigue test bench for railway bogies and superstructures. (figure 1), 2015.

[6] Amol B. Sapkal and Saurabh S. Sirsikar. Static and fatigue strength analysis of bogie frame. *National Conference in Applied Sciences and Humanities (NCASH 2016)*, 1(March):129–134, 2016.

[7] PRC Rail Consulting Ltd. Bogies | The Railway Technical Website | PRC Rail Consulting Ltd. URL: http://www.railway-technical.com/trains/rolling-stock-index-1/bogies.html.

[8] ITT_Tender Evaluation Criteria_Aluminium Headstocks. URL: https://www.google.com/url?sa=i{&}url=http{%}3A{%}2F{%}2Fpubliccontent.sinpro.cz{%}2FPublicFiles{%}2F2017{%}2F0.

[9] K. Hirakawa, K. Toyama, and M. Kubota. The analysis and prevention of failure in railway axles. *International Journal of Fatigue*, 20(2):135–144, 1998. doi:10.1016/S0142-1123(97)00096-0.

[10] Miyuki YAMAMOTO. NIPPON STEEL & SUMITOMO METAL TECHNICAL REPORT No. 105 DECEMBER 2013.

[11] Taizo Makino and Hiroki Sakai. Fatigue Property of Railway Axles for Shinkansen Vehicles. *Nippon Steel & Sumitomo Metal Technical Report*, (105), 2013.

[12] Seung wan Son, Hyun seung Jung, Tae soo Kwon, and Jin sung Kim. Fatigue life prediction of a railway hollow axle with a tapered bore surface. *Engineering Failure Analysis*, 58(P1):44–55, 2015. URL: http://dx.doi.org/10.1016/j.engfailanal.2015.08.031, doi:10.1016/j.engfailanal.2015.08.031.

[13] G. Gürer and C. H. Gür. Failure analysis of fretting fatigue initiation and growth on railway axle press-fits. *Engineering Failure Analysis*, 84(November 2017):151–166, 2018. URL: https://doi.org/10.1016/j.engfailanal.2017.06.054, doi:10.1016/j.engfailanal.2017.06.054.

[14] Miroslav Novosad and Bohuslav Řeha. Fatigue tests of railway axles. *EAN 2010: 48th International Scientific Conference on Experimental Stress Analysis*, pages 285–292, 2010. doi:10.1016/j.proeng.2010.03.242.

[15] What is the Difference between Low & High Cycle Fatigue? - Fatec Engineering. URL: https://www.fatec-engineering.com/wp-content/uploads/2018/08/S-N-Curve-Low-Cycle-Fatigue-and-High-Cycle-Fatigue.png.

[16] Abass Adeyinka Azeez. Fatigue Failure and Testing Methods. page 32, 2013.

[17] Dietmar Klingbeil, Uwe Zerbst, and Christian Klinger. Safe life and damage tolerance concepts of railway axles. *13th International Conference on Fracture 2013, ICF 2013*, 5:4096–4105, 2013.

[18] Fatigue crack growth rate.

[19] Charter Two. Basic probability theory. *Topics in Safety, Risk, Reliability and Quality*, 18:9–20, 2012. doi:10.1007/978-94-007-4056-3_2.

[20] Xiaoping Du. Unified uncertainty analysis by the first order reliability method. *Journal of Mechanical Design, Transactions of the ASME*, 130(9):0914011–09140110, 2008. doi:10.1115/1.2943295.

[21] Xiaoping Du and Agus Sudjianto. A saddlepoint approximation method for uncertainty analysis. *Proceedings of the ASME Design Engineering Technical Conference*, 1:445–452, 2004. doi:10.1115/detc2004-57269.

[22] Achintya Haldar and Sankaran Mahadevan. First-Order and Second-Order Reliability Methods. *Probabilistic Structural Mechanics Handbook*, (September):27–52, 1995. doi:10.1007/978-1-4615-1771-9_3.

[23] Xiaoping Du, Agus Sudjianto, and Beiqing Huang. Reliability-based design with the mixture of random and interval variables. *Journal of Mechanical Design, Transactions of the ASME*, 127(6):1068–1076, 2005. doi:10.1115/1.1992510.

[24] Saeed Mohammadzadeh. Stress-based fatigue reliability analysis of the rail festening spring under traffic loads. *Latin American Journal of Solids and Structures 11*, 2014. doi:10.1590/S1679-78252014000600006.

[25] S. C. Wu, Y. X. Liu, C. H. Li, G. Z. Kang, and S. L. Liang. On the fatigue performance and residual life of intercity railway axles with inside axle boxes. *Engineering Fracture Mechanics*, 197(April):176–191, 2018. doi:10.1016/j.engfracmech.2018.04.046.

[26] M. Luke, I. Varfolomeev, K. Lütkepohl, and A. Esderts. Fatigue crack growth in railway axles: Assessment concept and validation tests. *Engineering Fracture Mechanics*, 78(5):714–730, 2011. URL: http://dx.doi.org/10.1016/j.engfracmech.2010.11.024, doi:10.1016/j.engfracmech.2010.11.024.

[27] S. C. Wu, S. Q. Zhang, Z. W. Xu, G. Z. Kang, and L. X. Cai. Cyclic plastic strain based damage tolerance for railway axles in China. *International Journal of Fatigue*, 93:64–70, 2016. doi:10.1016/j.ijfatigue.2016.08.006.

[28] Shun-Peng Zhu, Hong-Zhong Huang, Yanfeng Li, Yu Liu, and Yuanjian Yang. Probabilistic modeling of damage accumulation for time-dependent fatigue reliability analysis of railway axle steels. *Proceedings of the Institution of Mechanical Engineers, Part F: Journal of Rail and Rapid Transit*, 229(1):23–33, 2015. URL: https://doi.org/10.1177/0954409713496772, doi:10.1177/0954409713496772.

[29] M. Filippini, M. Luke, I. Varfolomeev, D. Regazzi, and S. Beretta. Fatigue strength assessment of railway axles considering small-scale tests and damage calculations. *Procedia Structural Integrity*, 4:11–18, 2017. doi:10.1016/j.prostr.2017.07.013.

[30] *ABAQUS analysis user's manual*. Pawtucket, RI, USA, version 6. edition, 2010.

[31] Standard EN13104. Railway applications. Wheelsets and bogies. Powered axles. Design method., 2010.

[32] Luo Yan Wu Shengchuan, Xu Zhongwei, Duan Hao, Hu Yanan, Zhang Siqi. Report-T714-wusc. Technical report.

[33] Leenaporn Jongpaiboonkit, William J King, Gary E Lyons, Amy L Paguirigan, W Jay, David J Beebe, and William L Murphy. *and Analysis*, volume 29. 2008.

[34] Malur Srinivasan. *Fracture Toughness of Metal Castings*, pages 285–312. 2012. doi:10.5772/50297.

[35] Shukri Afazov, Willem Denmark, and Anas Yaghi. Modelling aspects of the design of railway vehicle structures and their crashworthiness. *Proceedings of the Institution of Mechanical Engineers, Part F: Journal of Rail and Rapid Transit*, 230(6):1575–1589, 2016. doi:10.1177/0954409715605141.

[36] Standard ASTM E739 - 91. Standard Practice for Statistical Analysis of Linear or Linearized Stress-Life (S-N) and Strain-Life (ε-N) Fatigue Data., 2004.

[37] Analysis of methodologies for fatigue calculation for railway bogie frames. A.Cera 1, G.Mancini 1, V.Leonardi 1, L.Bertini 2. 2006.

[38] CP. Comboios de Portugal. pages 1–25, 2013. URL: http://www.cp.pt/cp/displayPage.do?vgnextoid=96fed5abe2a74010VgnVCM1000007b01a8c0RCRD.

[39] Isao Okamoto. Shinkansen Bogies. *Japan Railway & Transport Review*, 6(March):46–53, 1999. URL: http://www.ejrcf.or.jp/jrtr/jrtr19/pdf/Technology.pdf.

[40] Dongfang Zeng, Yuanbin Zhang, Liantao Lu, Lang Zou, and Shengyang Zhu. Fretting wear and fatigue in press-fitted railway axle: A simulation study of the influence of stress relief groove. *International Journal of Fatigue*, 118(September 2018):225–236, 2019. doi:10.1016/j.ijfatigue.2018.09.008.

[41] S C Wu, Z W Xu, G Z Kang, and W F He. Probabilistic fatigue assessment for high-speed railway axles due to foreign object damages. 117(June):90–100, 2018. doi:10.1016/j.ijfatigue.2018.08.011.

[42] Miroslav Novosad and Rostislav Fajkoš. Procedia Engineering. *Procedia Engineering*, 210:1–10, 2017. doi:10.1016/j.proeng.2010.03.242.

[43] D. Regazzi. Advances in life prediction and durability of railway axles. page 134, 2013.

[44] Regina L. Nuzzo. An Introduction to Bayesian Data Analysis for Correlations. *PM and R*, 9(12):1278–1282, 2017. doi:10.1016/j.pmrj.2017.11.003.

[45] Yao Cheng and Xiaoping Du. System reliability analysis with dependent component failures during early design stage. *ASME International Mechanical Engineering Congress and Exposition, Proceedings (IMECE)*, 11-2015, 2015. doi:10.1115/IMECE201550269.

[46] Zhen Hu. A Mixed Efficient Global Optimization (m- EGO) Based Time-Dependent Reliability Analysis Method Outline • Problem statement • Mixed Efficient Global Optimization (m-EGO) • Time-Dependent Reliability Analysis with m-EGO • Numerical Examples • Conclusio. pages 1–23, 2014.

[47] Zhen Hu Xiaoping Du. Processes, Stochastic. 2012.

[48] Co-ordinating Working Group. Guidance for evaluation of. 2009.

[49] Hasan Keshavarzian and Tayebeh Nesari. Reliability Analysis for Cyclic Fatigue Life Prediction in Railroad Bolt Hole. 11(9):1227–1232, 2017.

[50] Laura Mazzola, Daniele Regazzi, Stefano Beretta, and Stefano Bruni. Fatigue assessment of old design axles: Service simulation and life extension. *Proceedings of the Institution of Mechanical Engineers, Part F: Journal of Rail and Rapid Transit*, 230(2):572–584, 2016. doi:10.1177/0954409714552699.

[51] Igor Varfolomeyev and Brita Pyttel. FKM Guideline "Fracture Mechanics Proof of Strength for Engineering Components": Procedures, Compendiums, Examples, jul 2008. URL: https://doi.org/10.1115/PVP2008-61554, doi:10.1115/PVP2008-61554.

[52] Helmut Herrmann and Herbert Bucksch. Stress-Strain Behaviour. *Dictionary Geotechnical Engineering/Wörterbuch GeoTechnik*, pages 1329–1329, 2014. doi:10.1007/978-3-642-41714-6_198108.

[53] Hieronim Jakubczak, Wojciech Sobczykiewicz, and G Glinka. Fatigue reliability of structural components. *International Journal oF Materials & Product Technology*, 25:64–83, 2006. doi:10.1504/IJMPT.2006.008274.

[54] Kurt Hornik, Maxwell Stinchcombe, and Halbert White. Multilayer feedforward networks are universal approximators. *Neural Networks*, 2(5):359–366, 1989. URL: http://www.sciencedirect.com/science/article/pii/0893608089900208, doi:https://doi.org/10.1016/0893-6080(89)90020-8.

[55] David E Rumelhart, Geoffrey E Hinton, and Ronald J Williams. Learning representations by back-propagating errors. *Nature*, 323(6088):533–536, 1986. URL: https://doi.org/10.1038/323533a0, doi:10.1038/323533a0.

[56] SeyedAli Mirjalili, Siti Zaiton Mohd Hashim, and Hossein Moradian Sardroudi. Training feedforward neural networks using hybrid particle swarm optimization and gravitational search algorithm. *Applied Mathematics and Computation*, 218(22):11125–11137, 2012. URL: http://www.sciencedirect.com/science/article/pii/S0096300312004857, doi:https://doi.org/10.1016/j.amc.2012.04.069.

[57] James Kennedy. *Particle Swarm Optimization*, pages 760–766. Springer US, Boston, MA, 2010. URL: https://doi.org/10.1007/978-0-387-30164-8{_}630, doi:10.1007/978-0-387-30164-8_630.

Appendix A

Table A.1: Stress-strain data for the monotonic behaviour characterization of steel EA4T.

σ_{eng} [MPa]	σ/E	(σ/K)^(1/n)	$\varepsilon_{eng}^{total}$	σ_{true}	$\varepsilon_{true}^{total}$
10	4.85437E-05	1.62476E-18	4.85437E-05	10.00048544	4.85425E-05
20	9.70874E-05	7.06463E-16	9.70874E-05	20.00194175	9.70827E-05
30	0.000145631	2.46829E-14	0.000145631	30.00436893	0.00014562
40	0.000194175	3.07177E-13	0.000194175	40.00776699	0.000194156
50	0.000242718	2.17136E-12	0.000242718	50.01213592	0.000242689
60	0.000291262	1.07324E-11	0.000291262	60.01747573	0.00029122
70	0.000339806	4.14413E-11	0.000339806	70.02378641	0.000339748
80	0.00038835	1.33564E-10	0.00038835	80.03106797	0.000388274
90	0.000436893	3.74974E-10	0.000436894	90.03932042	0.000436798
100	0.000485437	9.44129E-10	0.000485438	100.0485438	0.00048532
110	0.000533981	2.17674E-09	0.000533983	110.0587381	0.00053384
120	0.000582524	4.66654E-09	0.000582529	120.0699035	0.000582359
130	0.000631068	9.41149E-09	0.000631077	130.0820401	0.000630878
140	0.000679612	1.80191E-08	0.00067963	140.0951482	0.000679399
150	0.000728155	3.29866E-08	0.000728188	150.1092282	0.000727923
160	0.000776699	5.80749E-08	0.000776757	160.1242811	0.000776456
170	0.000825243	9.87965E-08	0.000825342	170.1403081	0.000825001
180	0.000873786	1.63043E-07	0.000873949	180.1573109	0.000873568
190	0.00092233	2.61876E-07	0.000922592	190.1752925	0.000922167
200	0.000970874	4.10517E-07	0.000971284	200.1942569	0.000970813
210	0.001019417	6.29563E-07	0.001020047	210.2142099	0.001019527
220	0.001067961	9.46469E-07	0.001068908	220.2351597	0.001068337
230	0.001116505	1.39734E-06	0.001117902	230.2571175	0.001117278
240	0.001165049	2.02906E-06	0.001167078	240.2800986	0.001166397
250	0.001213592	2.90184E-06	0.001216494	250.3041235	0.001215755

σ_{eng} [MPa]	σ/E	(σ/K)^(1/n)	$\varepsilon_{eng}^{total}$	σ_{true}	$\varepsilon_{true}^{total}$
260	0.001262136	4.09221E-06	0.001266228	260.3292193	0.001265427
270	0.00131068	5.6965E-06	0.001316376	270.3554215	0.00131551
280	0.001359223	7.83488E-06	0.001367058	280.3827763	0.001366125
290	0.001407767	1.06561E-05	0.001418423	290.4113427	0.001417418
300	0.001456311	1.43429E-05	0.001470654	300.4411961	0.001469573
310	0.001504854	1.91181E-05	0.001523972	310.4724315	0.001522812
320	0.001553398	2.52515E-05	0.00157865	320.5051679	0.001577405
330	0.001601942	3.30684E-05	0.00163501	330.5395533	0.001633675
340	0.001650485	4.29577E-05	0.001693443	340.5757707	0.001692011
347	0.001684466	5.13582E-05	0.001735824	347.602331	0.001734319
360	0.001747573	7.08926E-05	0.001818465	360.6546476	0.001816814
370	0.001796117	9.0134E-05	0.001886251	370.6979127	0.001884474
380	0.00184466	0.000113866	0.001958526	380.7442401	0.001956611
390	0.001893204	0.000142976	0.00203618	390.7941103	0.00203411
400	0.001941748	0.000178497	0.002120245	400.8480978	0.002118
410	0.001990291	0.000221624	0.002211916	410.9068854	0.002209473
420	0.002038835	0.00027374	0.002312575	420.9712817	0.002309905
430	0.002087379	0.000336436	0.002423814	431.0422402	0.002420882
440	0.002135922	0.000411535	0.002547457	441.120881	0.002544218
450	0.002184466	0.000501122	0.002685588	451.2085148	0.002681989
460	0.00223301	0.000607577	0.002840587	461.3066699	0.00283656
470	0.002281553	0.0007336	0.003015154	471.4171223	0.003010617
480	0.002330097	0.000882256	0.003212353	481.5419292	0.003207204
490	0.002378641	0.001057004	0.003435645	491.6834661	0.003429757
500	0.002427184	0.001261751	0.003688935	501.8444676	0.003682148

σ_{eng} [MPa]	σ/E	(σ/K)^(1/n)	$\varepsilon_{eng}^{total}$	σ_{true}	$\varepsilon_{true}^{total}$
510	0.002475728	0.001500886	0.003976614	512.028073	0.003968728
520	0.002524272	0.001779336	0.004303608	522.2378759	0.004294373
530	0.002572816	0.002102618	0.004675433	532.4779796	0.004664537
540	0.002621359	0.002476894	0.005098253	542.7530569	0.005085301
550	0.002669903	0.002909036	0.005578939	553.0684164	0.005563434
560	0.002718447	0.003406687	0.006125134	563.4300748	0.006106451
570	0.00276699	0.003978336	0.006745326	573.844836	0.006722678
580	0.002815534	0.004633391	0.007448925	584.3203767	0.007421319
590	0.002864078	0.005382263	0.00824634	594.8653408	0.008212525
600	0.002912621	0.006236446	0.009149068	605.4894405	0.009107468
610	0.002961165	0.007208618	0.010169783	616.2035678	0.010118419
620	0.003009709	0.008312733	0.011322442	627.0199139	0.011258823
630	0.003058252	0.009564127	0.012622379	637.9520988	0.012543381
640	0.003106796	0.01097963	0.014086426	649.0153125	0.013988134
650	0.00315534	0.012577684	0.015733024	660.2264656	0.015610543
660	0.003203883	0.01437847	0.017582354	671.6043534	0.017429572
670	0.003252427	0.016404039	0.019656466	683.169832	0.019465772
680	0.003300971	0.018678452	0.021979423	694.9460075	0.021741357
690	0.003349515	0.021227934	0.024577449	706.9584396	0.024280282
700	0.003398058	0.024081029	0.027479087	719.2353608	0.027108314

Table A.2: Stress and strain data for the cyclic behaviour of the EA4T steel.

σ [MPa]	σ/E	(σ/K')^(1/n')	ε^{total}
10	4.85437E-05	2.03637E-19	4.85437E-05
20	9.70874E-05	1.82025E-16	9.70874E-05
30	0.000145631	9.69428E-15	0.000145631
40	0.000194175	1.62707E-13	0.000194175
50	0.000242718	1.45045E-12	0.000242718
60	0.000291262	8.66543E-12	0.000291262
70	0.000339806	3.92764E-11	0.000339806
80	0.00038835	1.45439E-10	0.00038835
90	0.000436893	4.61503E-10	0.000436894
100	0.000485437	1.29652E-09	0.000485438
110	0.000533981	3.30057E-09	0.000533984
120	0.000582524	7.74577E-09	0.000582532
130	0.000631068	1.69773E-08	0.000631085
140	0.000679612	3.5108E-08	0.000679647
150	0.000728155	6.90498E-08	0.000728224
160	0.000776699	1.30003E-07	0.000776829
170	0.000825243	2.35549E-07	0.000825478
180	0.000873786	4.12524E-07	0.000874199
190	0.00092233	7.009E-07	0.000923031
200	0.000970874	1.15892E-06	0.000972033
210	0.001019417	1.86978E-06	0.001021287
220	0.001067961	2.95028E-06	0.001070911
230	0.001116505	4.56173E-06	0.001121067
240	0.001165049	6.92371E-06	0.001171972
250	0.001213592	1.03312E-05	0.001223923

σ [*MPa*]	σ/E	(σ/K')^(1/n')	ε^{total}
260	0.001262136	1.51755E-05	0.001277311
270	0.00131068	2.19702E-05	0.00133265
280	0.001359223	3.1382E-05	0.001390605
290	0.001407767	4.42682E-05	0.001452035
300	0.001456311	6.17216E-05	0.001518032
310	0.001504854	8.51235E-05	0.001589978
320	0.001553398	0.000116206	0.001669604
330	0.001601942	0.000157126	0.001759068
340	0.001650485	0.00021055	0.001861036
347	0.001684466	0.000257114	0.00194158
360	0.001747573	0.000368743	0.002116316
370	0.001796117	0.000482373	0.002278489
380	0.00184466	0.000626514	0.002471174
390	0.001893204	0.000808219	0.002701423
400	0.001941748	0.001035921	0.002977669
410	0.001990291	0.001319662	0.003309953
420	0.002038835	0.001671341	0.003710176
430	0.002087379	0.002105004	0.004192383
440	0.002135922	0.002637166	0.004773088
450	0.002184466	0.003287169	0.005471636
460	0.00223301	0.004077591	0.006310601
470	0.002281553	0.005034688	0.007316241
480	0.002330097	0.006188901	0.008518998
490	0.002378641	0.007575409	0.00995405
500	0.002427184	0.009234746	0.01166193